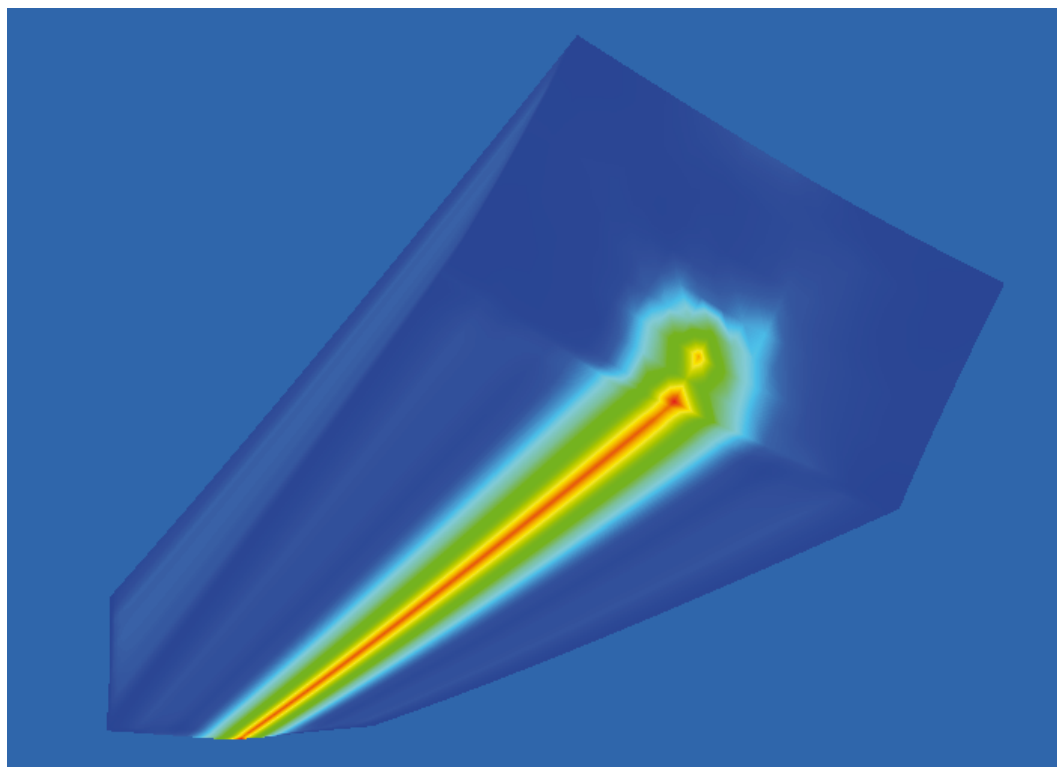
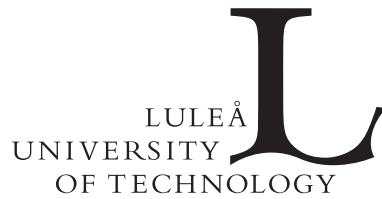


Modelling of Dynamic and Quasistatic Events with Special Focus on Wood-Drying Distortions



by
Mats Ekevad

Luleå University of Technology
LTU Skellefteå
Division of Wood Science and Technology



DOCTORAL THESIS

Modelling of Dynamic and Quasistatic Events with Special Focus on Wood-Drying Distortions

by
Mats Ekevad

Division of Wood Science and Technology
LTU Skellefteå
Luleå University of Technology
S-931 87 Skellefteå, Sweden
<http://www.ltu.se/ske>
2006

Abstract

This thesis deals mainly with computer simulations of wood-drying distortions, especially twist. The reason for this is that such distortions often appear in dried timber, and the results are quality downgrades and thus value losses in the wood value chain. A computer simulation is a way to theoretically simulate what happens in reality when moisture content in timber changes. If the computer simulation model is appropriate and capable of realistic simulations of real events, then it is possible to study what happens with the timber distortions if some parameters in the simulation model are changed. In that way, a good simulation model is a good tool to use when trying to reduce wood-drying distortions by altering some parameters in the process of producing timber. Computer simulations have the comparative advantage over real-world experiments of being cheaper and faster to perform, but the disadvantage that the outcome may be doubtful if the simulation model is bad.

Wood is an anisotropic material that is often modelled as an orthotropic material, i.e., a material that has three orthogonal directions at each point with different material properties. A method to measure the orthotropic directions in wood nondestructively was the subject of paper 1. The method was to calculate the directions from the information in a series of two-dimensional computed tomography (CT) images. Fictitious, small calculation spheres were distributed in the wood material, and the principal directions of inertia of these spheres were calculated using the density information in the CT images. The principal directions were assumed to be the radial, the tangential and the fibre direction at the point in question. Tests of the method on three wood samples showed that the method works, but that there was considerable spread in the results from individual spheres. The spread was reduced by calculating mean values for a number of spheres in the vicinity of each other.

Twist of timber depends on various influencing variables. Traditionally, a formula from the late 50s by Stevens and Johnston, valid for single growth ring cylinders, has often been used to explain which variables influence twist. One interesting influencing variable in this formula is the spiral grain angle; the others are the moisture content change, the coefficient of moisture expansion and the radius of the growth ring cylinder in question. However, real boards are not single growth ring cylinders, and paper 2 deals with the dependence of twist of realistic boards on various influencing variables. Derivations were made on a theoretical and analytical level of the twist of timber, and the result was a formula whose first term corresponds to Stevens and Johnston's original formula; but the formula has also a second term. This second term is proportional to the gradient of the spiral grain angle and is especially important for timber sawn far from pith. The validity of the second term was shown by comparisons with finite element method (FEM) results and also with experimental results.

The first step in simulating wood-drying distortions is to simulate the wood-drying process. The output of this moisture transport simulation is the moisture content of the wood piece as a function of time. This output is then used as input to a second step in which the shrinkage and deformation of the wood piece is simulated. A diffusion model

was used here to simulate moisture transport, and this simulation requires diffusion and mass transfer coefficients. Such values from drying Norway spruce (*Picea abies*) sapwood were measured and reported in paper 3. Measurements of the moisture content during drying of a sample were made with CT, and the diffusion coefficient was evaluated with two methods. The first method used a one-dimensional and the second a two-dimensional diffusion model. No assumptions of the dependence of the diffusion coefficient on any functions or variables were made beforehand. Both methods showed about the same result and dependence on moisture content, but also on depth (distance from surface) of the diffusion coefficient. The depth dependence was only apparent near the surface. Comparisons of the evaluated values of the diffusion coefficient in general terms with other results were made and showed agreement.

Industrial process changes aimed at reducing twist distortions are interesting to study. In paper 4, simulations of drying distortions were conducted, and pretwist during drying as a remedy to overcome twist of boards was tried. Paper 4 also contained results from laboratory experiments on the influence of the spiral grain angle and the degree of restraint and pretwist during drying on twist of boards. Results from an industrial test of the influence of the spiral grain angle and the degree of restraint on twist of boards were also described. The laboratory experiments and the industrial test were simulated with an FEM simulation model in two stages. First, the FEM model was calibrated by adjusting the yield stresses of the wood material in order for the results from the laboratory experiments to agree with the simulation model results. Then in a second stage, the simulation model was used to simulate the industrial test. The results showed that the FEM simulation model was capable of producing realistic results, but that there were some discrepancies between the industrial test results and the simulation results. The discrepancies were assumed to be due to biased measurements, insufficient knowledge of the distribution of the spiral grain angle or other causes.

Keywords: Computed Tomography, CT, Diffusion coefficient, Distortions, Drying, FEM, Finite element method, Timber, Norway spruce, *Picea abies*, Pretwist, Simulation, Spiral grain, Straight, Timber, Twist, Warp, Wood.

Sammanfattning

Denna avhandling handlar främst om datorsimuleringar av torkdeformationer hos sågat virke, och då speciellt om skevhet. Skälet för att intressera sig för torkdeformationer är att dessa innebär problem och ger kvalitetsnedsättningar och värdeförluster i trävärdekedjan. Datorsimuleringar är ett teoretiskt sätt att simulera vad som händer i verkligheten när virke torkas. Med en bra datormodell som är kapabel till realistiska simuleringar av torkprocessen är det möjligt att studera vad som händer med torkdeformationerna när parametrar i torkprocessen ändras. På så sätt är en bra datormodell ett bra verktyg för att förbättra och optimera torkprocessen för sågat virke. Datorsimuleringar har den fördelen jämfört med verkliga experiment att de är billiga och snabba att utföra, medan de har den nackdelen att resultaten kan vara tveksamma om datormodellen inte är bra.

Trä är ett anisotropt material som ofta modelleras som ortotropt. Detta innebär att det har tre ortogonala riktningar i varje punkt och olika egenskaper i varje sådan riktning. I artikel 1 beskrevs en icke-förstörande metod att bestämma de ortotropa riktningarna i trä ur en serie tvådimensionella bilder tagna med datortomografi (CT). Denna metod använder sig av fiktiva, små sfärer i trämaterialiet där sfärens huvudtröghetsriktningar beräknas utifrån densitetsinformationen i CT-bilderna. Huvudtröghetsriktningarna antas vara den radiella, den tangentiella och fiberriktningen i punkten ifråga. Tester av metoden på tre provbitar visade att metoden fungerar, men att resultat från enskilda sfärer uppvisade stor spridning.

Skevhet hos sågat virke beror på ett antal faktorer (variabler). Traditionellt så har ofta en formel från sent 50-tal av Stevens och Johnston för enskilda årsringscylindrar använts för att förklara vad skevhet beror av. I denna formel är fibervinkeln en intressant variabel (de övriga är fuktkvotsförändringen, fuktexpansionskoefficienten och årsringsradien). Men sågat virke är inte enskilda årsringscylindrar, och i artikel 2 behandlades beroendet hos skevheten hos sågat virke av diverse variabler genom en teoretisk och analytisk härledning. Resultatet blev en formel med två termer där den första termen motsvarar Stevens och Johnstons formel. Den andra termen är proportionell mot den radiella gradienten hos fibervinkeln och den kan dominera över den första termen för virke som är sågat långt från mörgen. Giltigheten hos den andra termen visades genom jämförelser med finita element- (FEM) resultat och mätresultat.

Det första steget när man simulerar fuktdeformationer är att simulera torkprocessen. Resultatet av denna simulering är fuktkvoten som funktion av tiden i varje punkt i träbiten i fråga. Andra steget är sedan att simulera krympningen och deformationerna genom att använda fuktkvoten från första steget som indata. I första steget användes en diffusionsmodell för fukttransporten, och då krävs att massövergångstal och diffusionskoefficient är kända. Sådana värden vid torkning av splintved hos gran (Norway spruce, *Picea abies*) uppmättes och rapporterades i artikel 3. Mätningar av fuktkvoten gjordes med hjälp av CT, och diffusionskoefficienten beräknades med två metoder. Den första metoden använde en endimensionell och den andra en tvådimensionell diffusionsmodell. Inga antaganden om diffusionskoefficientens beroende av någon funktion eller några speciella parametrar gjordes på förhand. Båda metoderna

gav närapå likadana resultat och visade på ett beroende hos diffusionskoefficienten av fuktkvoten och avståndet till ytan. Beroendet på avståndet till ytan gällde bara nära ytan. En jämförelse visade på överensstämmelse i generella termer med resultat uppmätta av andra.

Industriella processförändringar syftade att minska skevheten hos det producerade virket är intressanta att studera. I artikel 4 behandlades hur skevheten kan styras hos sågat och torkat virke som varit fastspänt under torkningen på olika sätt. Genom att hålla virket fastspänt i ett rakt läge under torkningen så minskar skevheten jämfört med virke som torkats helt fritt. Genom att hålla virket fast inspänt i ett motvridet läge under torkningen kan man åstadkomma ett helt rakt virke efter torkningen. Med motvridet menas att man vrider virket tvärs emot den förväntade skevheten efter torkning. Den storlek på motvridningen som krävs för att få rakt virke efter torkningen är en funktion av fibervinkeln hos virket. Resultat från laboratorieexperiment på virke som torkats fritt, fast inspänt och motvridet redovisades. Vidare redovisades resultat från industriförsök på sågat virke som torkats fritt och fast inspänt. En simuleringsmodell som använder FEM prövades, och resultaten jämfördes med mätresultaten i två steg. I ett första steg kalibrerades FEM-modellen genom att flytgränser för träet fastställdes för att ge resultat som överensstämde med laboratorieexperimenten. I ett andra steg jämfördes FEM-modellens resultat med resultaten från industriförsöken. Jämförelserna visade att FEM-modellen gav realistiska resultat, men att vissa skillnader mellan FEM-modellens resultat och resultaten från industriförsöken fanns. Skillnaderna antogs bero på oprecisa mätdata och andra skillnader mellan FEM-modellen och det verkliga virket.

Acknowledgement

I express my gratitude to Formas (the Swedish Research Council for Environment, Agricultural Sciences and Spatial Planning) and to the European Regional Development Fund, objective 1, northern part of Sweden, for financial support.

Preface

Although the special focus of this PhD thesis is wood-drying distortions, it also deals somewhat with pole-vaulting. Pole-vaulting was the subject of my licentiate thesis from 1995, *On the Mechanics of Pole Vaulting*, and it is included here as the last appendix. I am aware that some readers may think that drying distortions of wood and pole vaulting have little in common. But on the contrary, I think they have much in common, since both subjects involve dynamic events that are very suitable for finite element simulations. Aside from that, I think it is nice to have my scientific work collected. Also, some readers may wonder: “why model pole-vaulting in the licentiate thesis and wood-drying distortions in the PhD thesis?” Well, if you care about that, here’s the answer: (if you don’t care, stop here, and don’t read the rest of this preface).

I have never really planned to become a scientist or to become a PhD. In fact, I haven’t done much long-term career planning at all, to tell the truth. I believe my career so far has been the result of curiosity, interest, determination and a great deal of coincidence. In school I quickly discovered that I was good at, and interested in, mathematics, physics and those kinds of subjects. One thing led to another, and now, after 25 years of work after graduating as a “civilingenjör” (Master of Engineering) and at the age of 50, I am at the point of defending my PhD thesis. Here is how my career in engineering and science started:

I started working as an engineer back in 1980 for the (on a Swedish scale) relatively large turbine manufacturing company Stal-Laval Turbin AB in Finspång. I came there as a “civilingenjör” and a freshman and I came there directly from LTU (Luleå University of Technology). I didn’t want to stay at LTU as a PhD student, even though I was very interested in mathematics, solid mechanics, computer methods and all the other subjects we were taught at the university. I was offered to stay and commence PhD studies, but I rejected those offers. I was a bit tired of school and instead very eager to see what my knowledge could be used for in industry. I was curious to find out what engineers really worked with in industry, since I think the teachers at the university never told us that (perhaps, I believe, because most of the teachers at universities have little or no industrial experience).

However, I soon found out that my knowledge wasn’t that extensive, since I worked with colleagues who knew a lot more than me about almost everything. I stayed at Stal-Laval for seven years, and I learned a lot, both theoretical and practical stuff, about machine design, finite elements, rotor dynamics, fluid dynamics, fatigue, vibrations, computer programming and so on. This was mainly because of the stimulating work and environment at the research and development department, but also because of my own interest. During the years in Finspång I started taking some PhD courses at Linköping University together with a group of other engineers at Stal-Laval, since we all discovered that our knowledge in mathematics (linear algebra), solid mechanics and dynamics was too limited. We were in the happy situation that our employer let us go to the lectures on our working time. I think my 7 years in Finspång were my most intense period (hitherto) when it comes to learning things, but also when it comes to producing results. Most of the

time, I wrote computer programs and developed methods for strength calculations and dynamical calculations of turbine parts. I think a lot of my work there (and also my colleagues' work) would easily have qualified for publishing in scientific journals, but it was not customary at that time to publish one's work.

After my time in Finspång I wanted to try to work for a small company in order to have at least some experience of marketing and business work in small companies, i.e., things that I knew little about at that time. Thus in 1987 I started working at the Industrial Development Centre (IUC) in Skellefteå, a relatively small (about 50 employees) consulting company. IUC operated on a partly commercial basis, but with financial support from the state and municipality, to do product development for small companies. The plan was that IUC was going to do some marketing work for the new IBM supercomputer that the municipality of Skellefteå had bought and for which IUC was hired. I was employed to show examples of large computer simulations and also to help client companies do their own simulations.

The period in which I was doing these marketing examples of computer simulations (for free) was very interesting; e.g., I simulated downhill skiing, crash protection bars in cars, poles for pole vaulting and other sorts of unusual things. Sometimes we also helped inventors who came to us with their inventions and wanted to simulate something that had to do with the invention. In that way I have gotten requests to simulate horse-wagon wheels, hospital beds, car-towing mechanisms, poles for lighting up roads, electrical contacts, rubber water containers and so on. I also came to meet other interesting people during this period, inventors as I mentioned above, politicians, newspaper people, bureaucrats, real secret detectives from SÄPO, King Carl-Gustav of Sweden, the ambassador of Russia in Sweden, Boris Pankin, who worked for the communist regime in Russia but was nominated in 1991 by Mikhail Gorbachyov as the first foreign minister of the new Russian federation, the prime minister of Sweden, Ingvar Carlsson, one of the famous inventors of the FFT transform back in 1965, Cooley and Tukey (I don't remember which one), the legendary Sergei Bubka and others.

Our purpose with the simulations at that time was mainly to show how a supercomputer could be used in industry for product development. Since we were doing marketing for the supercomputer, we often managed to publish the stories of the small but spectacular simulations in local newspapers or even in national newspapers. In that way my simulation of a pole vault ended up in a large article in *Ny Teknik* in 1988 that caught the eye and interest of Bengt Lundberg, Professor in solid mechanics at LTU, whom I already knew from before. He suggested that we do something more with my simulations, which would lead to some scientific papers and to a licentiate degree for me. I was very interested in that, and after some planning, Bengt and I managed to get some money from the pole vault manufacturing company, Styrelsen för Teknisk Utveckling (STU) and also IUC, and I started working with these "scientific" pole vault simulations part time (but during daily working hours) in the beginning of 1989. It was stimulating work, but the money in the project soon ran out and I ended up with a lot of interesting simulation results, managed to write a report to the companies that financed the project as I was obliged to, but I didn't have time or money to sum up the work in scientific papers.

About that time (1990) I got married, and we bought an old farmhouse outside of Skellefteå that we started renovating. I also started working a little in our forest in my spare time, so there was little time to do scientific work. We also had a son in September 1990 who unfortunately stopped breathing and died two months old. Eventually I managed to sum up my work with pole-vault simulations and the PhD courses mainly in my spare time. Finally, in 1995 I could finish the work with a licentiate thesis consisting of two papers published in the *Journal of Biomechanics*. Among other things that complicated life slightly during this period (especially during 1994) was that I had a serious accident in April 1994 that nearly killed me. I fell off a rocky precipice near home when my neighbour and I were setting up a nesting box for a kestrel (*tornfalk* in Swedish) and I cracked my upper vertebra, broke my jaw into four pieces and lost most of my upper teeth. Luckily enough, I received no permanent injuries—I only got an involuntary diet treatment for 7 weeks. Also, we had a second son in November 1994. To sum it up, it was a great relief to be finished with and put aside the scientific career in 1995, being a Licentiate of Technology. Now I could devote my daily time to consultant work and my free time to my leisure work and family and not to writing scientific papers. To work with a licentiate thesis that sometimes interferes with your gainful employment, and not to feel that your employer fully encourages it, that is not a fruitful situation. My advice is that such work should be avoided. By the way, the kestrel hasn't used our nesting box (yet).

Anyway, in about 1991 the marketing work for the supercomputer had successively come to an end, since interest in using the supercomputer in the way that was expected was limited (to say the least). Instead, I came to do regular consulting commissions for companies due to the interest that came out of our marketing efforts. One of the customers of my consulting services was my former employer Stal-Laval. The consulting work was exciting and challenging, and things went on pretty well. By 1995 the consulting business had become very successful both financially (for my employer) and technically.

At that point I felt it was time to change employers, and I went on to another consulting company in Skellefteå, this time on a strictly commercial basis. I worked with this consulting company until 2002 and did various consulting tasks leading a group of engineers mainly doing FEM calculations for Swedish companies. We had great success during the good years 1995–2001 but during 2001–2002 we (and I think also the rest of Sweden) got caught in a stock market recession, and my work for this company came to an end.

Living and working in Skellefteå of course led to connections to wood and wood research via LTU and the Division of Wood Science and Technology in Skellefteå and via Träteknik (the Swedish Research Institute for Wood) in Skellefteå. From about 1995 I was teaching solid mechanics in the autumns at LTU, and I also did consultant work on the strength of wood bridges and other wood components for Träteknik. The commissions were challenging and interesting, and these contacts eventually led to my employment at LTU in Skellefteå from 2002.

When my consulting employment came to an end in 2002 I had to search for another job. I didn't want to go into consulting again, and I would have preferred to work again for a large industrial company, but did not want to move from Skellefteå. Such jobs did not exist here at that time. However, I was also interested in an academic job, and I managed to get a job at LTU in Skellefteå, since they needed me mainly for teaching solid mechanics to engineering students. At first, I worked mainly with teaching, but soon I started to do FEM simulations on compression-wood boards together with Jan Nyström and Michael Öhman. It felt then and still feels very nice to be "back in serious business" doing some real scientific work and being able to dig deep into something. Compared to my scientific research work, mainly in my spare time, during the years 1990–1995, it felt like heaven or paradise doing research work on paid work time and with colleagues that are doing the same thing and with encouraging advisors. From the simulations came first a paper on a method to compute fibre directions from CT images (paper 1 in this thesis). It ended up with me being a PhD student, and eventually the rest of the papers in this thesis were developed.

Well, that's it, and now finally I must thank my supervisor Professor Anders Grönlund, who let me do this work and managed all the financing, mainly from Formas (the Swedish Research Council for Environment, Agricultural Sciences and Spatial Planning), and of course all of my colleagues for the pleasant, friendly and stimulating environment at LTU Skellefteå. Also thanks to my family Berith, Samuel and Sandra who in their own ways have contributed to this thesis.

Skellefteå in August 2006

Mats Ekevad

"Philosophy is written in this grand book—I mean the universe—which stands continually open to our gaze, but it cannot be understood unless one first learns to comprehend the language in which it is written. It is written in the language of mathematics, and its characters are triangles, circles, and other geometric figures, without which it is humanly impossible to understand a single word of it; without these, one is wandering about in a dark labyrinth "

Galileo Galilei (1623)

List of papers

This doctoral thesis is based on work reported in the following four papers:

1. Ekevad, M. (2004). Method to compute fiber directions in wood from computed tomography images. *J Wood Sci* 50:41–46.
2. Ekevad, M. (2005). Twist of wood studs: dependence on spiral grain gradient. *J Wood Sci*, 51:455-461.
3. Danvind, J. & Ekevad, M. (2006). Local water vapour diffusion coefficient when drying Norway spruce sapwood. *J Wood Sci* 52:195-201.
4. Ekevad, M., Salin, J.-G., Grundberg, S., Nyström, J., Grönlund, A. (2006). Modelling of adequate pretwist for obtaining straight timber. Accepted for publication in *Wood Material Science and Engineering*.

Specification of the author's (Mats Ekevad) contribution to papers with several authors:

3. Dr. Danvind made the CT scanning and evaluated the diffusion and mass transfer coefficients according to method two. The author made the evaluation of the diffusion and mass transfer coefficients according to method one, made the FEM simulations and assisted in the CT experiments.
4. Dr. Salin made the laboratory experiments, Dr. Nyström and Dr. Grundberg made the industrial tests, Professor Grönlund wrote a part of the text, the author made the FEM simulations.

Also included in the last appendix is the licentiate thesis from 1995 “On the Mechanics of Pole Vaulting” which includes two papers:

1. Ekevad, M. & Lundberg, B. 1997. Influence of pole length and stiffness on the energy conversion in pole vaulting. *J. Biomechanics* 30: 259-264.
2. Ekevad, M. & Lundberg, B. 1995. Simulation of smart pole vaulting. *J. Biomechanics* 28:1079-1090.

Contents

Abstract.....	i
Sammanfattning.....	iii
Acknowledgement.....	v
Preface.....	vii
List of papers.....	xi
Contents.....	xiii
1 Notations.....	1
1.1 Abbreviations	
1.2 General notations	
1.3 Units	
1.4 Stress notations	
1.5 Strain notations	
1.6 Temperature and MC notations	
1.7 Thermal expansion notations	
1.8 Moisture expansion notations	
1.9 Elasticity notations	
1.10 Plasticity notations	
1.11 FEM notations	
2 Introduction.....	7
2.1 Computer modelling	
2.2 Wood distortions	
2.3 Objective and limitations	
2.4 Outline of the thesis	
3 Theory.....	13
3.1 The inner structure of wood	
3.2 Qualities and defects of wood	
3.3 Wood as an orthotropic material	
3.4 Moisture content, temperature, shrinkage and fibre saturation point	
3.5 The drying process	
3.6 FEM for wooden components	
3.7 Validation and measurements	
3.8 Diffusion, elasticity, plasticity, creep and mechanosorption	
3.9 Linear elastic-plastic constitutive equations for orthotropic materials	
3.9.1 Linear elastic behaviour for a one-dimensional (1D) case	
3.9.2 Linear elastic behaviour for a three-dimensional (3D) case	
3.9.3 Yield limits for a linear elastic 3D case	
3.9.4 Behaviour after yield for a linear elastic-ideally plastic material, 3D case	

	3.9.5 Behaviour after yield for a strain hardening linear elastic-plastic material, 3D case	
	3.9.6 Linear elastic-plastic behaviour for a 3D case	
	3.9.7 Use of constitutive equations in FEM program	
	3.9.8 Iterative procedure for the calculation of λ	
4 Results.....		41
	4.1 Paper 1: Method to compute fiber directions from computed tomography images	
	4.2 Paper 2: Twist of wood studs: dependence on spiral grain gradient	
	4.3 Paper 3: Local water vapour diffusion coefficient when drying Norway spruce sapwood	
	4.4 Paper 4: Modelling of adequate pretwist for obtaining straight timber	
5 Discussion.....		53
6 References.....		59
Appendices		

Paper 1: Ekevad, M. (2004). Method to compute fiber directions in wood from computed tomography images. *J. Wood Sci.* 50:41–46.

Paper 2: Ekevad, M. (2005). Twist of wood studs: dependence on spiral grain gradient. *J. Wood Sci.* 51:455–461.

Paper 3: Danvind, J. & Ekevad, M. 2006. Local water vapour diffusion coefficient when drying Norway spruce sapwood. *J. Wood Sci.* 52:195–201.

Paper 4: Ekevad, M., Salin, J.-G., Grundberg, S., Nyström, J., Grönlund, A. 2006. Modelling of adequate pretwist for obtaining straight timber. Accepted for publication in *Wood Material Science and Engineering*.

Ekevad, M. 1995. *On the Mechanics of Pole Vaulting*. Licentiate thesis. Uppsala University, Division of Solid Mechanics, Department of Technology.

1 Notations

1.1 Abbreviations

CT	computed tomography
EMC	equilibrium moisture content
Eq.	equation
FEM	finite element method
Fig.	figure
FSP	fibre saturation point
MC	moisture content
1-D	one-dimensional
2-D	two-dimensional
3-D	three-dimensional

1.2 General notations

A symbol without overbar is a scalar value; a symbol with one overbar (or denoted by a bold lowercase symbol) is a vector; and a symbol with double overbars (or a bold uppercase symbol) is a matrix. Superindex T on a vector or matrix means that the vector or matrix is transposed. Symbols separated by commas inside parentheses mean “function of”; e.g., $E = E(T, u)$ means that E is a function of T and u . Differentials of a function are denoted by a d before the function; e.g., dE . Partial derivatives are denoted by parentheses

with the fixed variables as subindices; e.g., $\left(\frac{\partial \varepsilon}{\partial \sigma}\right)_{T,u}$ means the partial derivative of strain

ε with respect to stress σ when temperature T and moisture content u are kept constant (but sometimes the subindices are omitted in order to increase readability). Subindices 1, 2, 3, 4, 5, 6 in stress or strain vectors are equal to subindices 1, 2, 3, 12, 13, 23, respectively, and denote the same components (3 normal and 3 shear components). $diag(x, y, z)$ means a 3 by 3 diagonal matrix with x , y and z on the diagonal.

The deplorable use of the same symbol for different quantities or of different symbols for the same quantity is unfortunately not completely avoided in this thesis. This is due to the fact that the papers in the appendices and also cited papers are not completely consistent when it comes to the use of symbols. However, symbols that can be misunderstood are always explained in the text close to the symbol and the risk for misunderstanding is thus minimal. Below is a list of symbols and explanations taken from papers 1 to 4.

g	: mass flux
C	: a constant
D	: diffusion coefficient (paper 3), a constant (paper 2)
l	: length
r	: radius
r_m	: mean radius for the section
s	: relative shrinkage
x, y, z	: coordinates

- ΔW : ratio of change of mass of moisture to the mass of dry wood
 α_t, α_l : moisture expansion coefficients in tangential and fiber direction (paper 2) but α is also used as the thermal expansion coefficient, see section 1.7 below
 β : moisture expansion coefficient (see section 1.8 below), mass transfer coefficient (paper 3)
 φ, ρ : twist angle in paper 2 and 4, respectively
 ρ_p : pretwist angle
 ρ_0 : dry density
 θ, Θ : spiral grain angle in paper 2 and 4, respectively
 θ_m : spiral grain angle, mean value for the section

1.3 Units

SI units are used unless otherwise stated.

1.4 Stress notations

Stress, stress vector:

$$\sigma, \bar{\sigma} = (\sigma_1 \quad \sigma_2 \quad \sigma_3 \quad \tau_{12} \quad \tau_{13} \quad \tau_{23})^T = (\sigma_1 \quad \sigma_2 \quad \sigma_3 \quad \sigma_4 \quad \sigma_5 \quad \sigma_6)^T$$

Normal stress: $\sigma, \sigma_1, \sigma_2, \sigma_3$

Shear stress: $\tau, \tau_{12}, \tau_{13}, \tau_{23}, \sigma_4, \sigma_5, \sigma_6$

Yield stress: $\sigma_s, \sigma_{1s}, \sigma_{2s}, \sigma_{3s}, \sigma_{4s}, \sigma_{5s}, \sigma_{6s}, \tau_{12s}, \tau_{13s}, \tau_{23s}$

Yield stress in tension: $\sigma_{sd}, \sigma_{1sd}, \sigma_{2sd}, \dots$

Absolute value of yield stress in compression: $\sigma_{sc}, \sigma_{1sc}, \sigma_{2sc}, \dots$

Virgin yield stress in tension: σ_{sd}^0

Virgin yield stress vector in tension (for a material with equal yield stresses in 1-D

compression and tension tests): $\bar{\sigma}_{sd}^0 = (\sigma_{1sd}^0 \quad \sigma_{2sd}^0 \quad \sigma_{3sd}^0 \quad \sigma_{4sd}^0 \quad \sigma_{5sd}^0 \quad \sigma_{6sd}^0)^T$

Virgin yield stress vector (if the yield stresses in 1-D compression and tension tests differ for normal stress components):

$$\bar{\sigma}_{sdc}^0 = (\sigma_{1sd}^0 \quad \sigma_{1sc}^0 \quad \sigma_{2sd}^0 \quad \sigma_{2sc}^0 \quad \sigma_{3sd}^0 \quad \sigma_{3sc}^0 \quad \tau_{12s}^0 \quad \tau_{13s}^0 \quad \tau_{23s}^0)^T$$

Yield stress vector (for a material with equal yield stresses in 1-D compression and

tension tests): $\bar{\sigma}_s = (\sigma_{1s} \quad \sigma_{2s} \quad \sigma_{3s} \quad \tau_{12s} \quad \tau_{13s} \quad \tau_{23s})^T$

Yield stress vector if the yield stresses differ (for normal stress components) in tension

and compression: $\bar{\sigma}_s = (\sigma_{1sd} \quad \sigma_{1sc} \quad \sigma_{2sd} \quad \sigma_{2sc} \quad \sigma_{3sd} \quad \sigma_{3sc} \quad \tau_{12s} \quad \tau_{13s} \quad \tau_{23s})^T$

Effective stress: σ_e

Effective stress (for 3-D orthotropic materials): σ_{es}^a

1.5 Strain notations

Strain, strain vector: $\varepsilon, \bar{\varepsilon} = (\varepsilon_1 \quad \varepsilon_2 \quad \varepsilon_3 \quad \gamma_{12} \quad \gamma_{13} \quad \gamma_{23})^T = (\varepsilon_1 \quad \varepsilon_2 \quad \varepsilon_3 \quad \varepsilon_4 \quad \varepsilon_5 \quad \varepsilon_6)^T$

Normal strain: $\varepsilon, \varepsilon_1, \varepsilon_2, \varepsilon_3$

Shear strain: $\varepsilon_4, \varepsilon_5, \varepsilon_6$

Plastic strain: ε^P

Effective plastic strain: ε_e^P

Plastic work: W^P

1.6 Temperature and MC notations

Temperature: T

Initial (= start) temperature: T_0

Reference temperature: T_{ref}

Moisture content as water mass/dry wood mass: u

EMC for the surrounding air: u_∞

1.7 Thermal expansion notations

Thermal expansion coefficient: α

(True) thermal expansion coefficient at zero stress: α_0

Mean thermal expansion coefficient at zero stress between T_0 and T : $\alpha_{0m}(T, T_0, u)$

Mean thermal expansion coefficient at zero stress between T_{ref} and T : $\alpha_{0m}^{ref}(T, T_{ref}, u)$

Thermal expansion coefficient vector: $\bar{\alpha} = (\alpha_1 \ \alpha_2 \ \alpha_3 \ \alpha_4 \ \alpha_5 \ \alpha_6)^T$ where the subindices refers to the three normal and three shear directions.

(True) thermal expansion coefficient vector at zero stress:

$$\bar{\alpha}_0 = (\alpha_1^0 \ \alpha_2^0 \ \alpha_3^0 \ 0 \ 0 \ 0)^T$$

Mean thermal expansion coefficient vector at zero stress between T_0 and T :

$$\bar{\alpha}_{0m} = (\alpha_1^{0m} \ \alpha_2^{0m} \ \alpha_3^{0m} \ 0 \ 0 \ 0)^T$$

1.8 Moisture expansion notations

Moisture expansion coefficient: β

(True) moisture expansion coefficient at zero stress: β_0

Mean moisture expansion coefficient at zero stress between u_0 and u : $\beta_{0m}(T, u, u_0)$

Mean moisture expansion coefficient at zero stress between u_{ref} and u : $\beta_{0m}^{ref}(T, u, u_{ref})$

Moisture expansion coefficient vector: $\bar{\beta} = (\beta_1 \ \beta_2 \ \beta_3 \ \beta_4 \ \beta_5 \ \beta_6)^T$ where the subindices refer to the three normal and three shear directions.

(True) moisture expansion coefficient vector at zero stress:

$$\bar{\beta}_0 = (\beta_1^0 \ \beta_2^0 \ \beta_3^0 \ 0 \ 0 \ 0)^T$$

Mean moisture expansion coefficient vector at zero stress:

$$\bar{\beta}_{0m} = (\beta_1^{0m} \ \beta_2^{0m} \ \beta_3^{0m} \ 0 \ 0 \ 0)^T$$

1.9 Elasticity notations

Diagonal matrices expressing the relative rate of change of the elastic modulus with respect to temperature or MC, respectively: $\overline{\overline{M}}_T, \overline{\overline{M}}_u$

Elastic modulus: E, E_1, E_2, E_3

Shear modulus: $G, G_{12}, G_{13}, G_{23}$

Poisson's ratios: $\nu_{12}, \nu_{21}, \nu_{13}, \nu_{31}, \nu_{23}, \nu_{32}$ where $\nu_{ij}/E_i = \nu_{ji}/E_j$ for $i, j = 1, 2, 3$.

The flexibility matrix: $\overline{\overline{F}} = \overline{\overline{C}}^{-1} = \left(\frac{\partial \overline{\overline{\varepsilon}}}{\partial \overline{\overline{\sigma}}} \right)_{T,u}$

The stiffness matrix: $\overline{\overline{C}} = \overline{\overline{F}}^{-1} = \left(\frac{\partial \overline{\overline{\sigma}}}{\partial \overline{\overline{\varepsilon}}} \right)_{T,u}$

Elastic modulus vector: $\overline{\overline{E}} = (E_1 \ E_2 \ E_3 \ G_{12} \ G_{13} \ G_{23})^T$

Elastic modulus vector (if the yield stresses for normal components differ in compression and tension): $\overline{\overline{E}}_{dc} = (E_1 \ E_1 \ E_2 \ E_2 \ E_3 \ E_3 \ G_{12} \ G_{13} \ G_{23})^T$

1.10 Plasticity notations

Yield function: $f = 1$ when yielding occurs, $= 0$ unloaded.

Coefficients in Tsai-Wu yield function: f_i and f_{ij} for $i, j = 1, 2, 3, \dots, 6$ and $f_{ij} = f_{ji}$.

Coefficients in Hill's yield function: F, G, H, L, M, N

Plastic, or hardening modulus: H

Ratio between plastic and elastic modulus: h

Positive constant: λ

Ratio between yield stress in compression (absolute value) and in tension: ψ

1.11 FEM notations

Node displacement vector: $\overline{\overline{\delta}}$

Outer or applied load vector: $\overline{\overline{p}}$

Inner nodal force vector: $\overline{\overline{q}}$

Correction (to displacement) vector: $\overline{\overline{c}}$

Superindex, but no subindex, e.g., $\overline{\overline{q}}^j, \overline{\overline{\delta}}^j$, means exact variable or vector value at load

increment j . Subindex and superindex, e.g., $\overline{\overline{\delta}}_i^j$, means approximate variable or vector value at iteration i and at load increment j . No index at all on a variable or vector means exact value at total, full load.

Force vector function: $\overline{\overline{F}}$

Unbalance load vector: $-\overline{\overline{F}}$

Jacobian matrix or tangent stiffness matrix at load increment j and iteration i : $\left(\frac{\partial \overline{\overline{F}}_i^j}{\partial \overline{\overline{\delta}}} \right)$

Elastoplastic stiffness matrix at load increment j and iteration i : $\overline{\overline{C}}^{EP} = \left(\frac{\partial \overline{\sigma}}{\partial \overline{\varepsilon}} \right)_{\delta_i^j}$

Positive constant at iteration i : λ_i

2 Introduction

This thesis contains a main text part followed by five appendices. The appendices are four papers in chronological order and a licentiate thesis (which itself contains two papers: Ekevad & Lundberg 1995; Ekevad & Lundberg 1997). The function of the main text is to describe the background and comprehensive objective that was the guideline for the research work that resulted in the papers. A further purpose is to link together, summarize and draw conclusions in the best possible way based on what is described in the papers. Finally, the main text shows deductions and explains things about wood and simulations that are not presented in detail in the papers.

2.1 Computer modelling

Computer modelling of events or processes is often done with commercial computer programs as a basis, but with the addition of specially written subroutines for the process in question. Commercial computer programs suitable for simulation of dynamic and quasistatic events in that way are, for example, Matlab (Anon. 2001) and ABAQUS (Anon. 2003). The general principle in performing computer simulations with the purpose of optimizing a process that is being simulated is to first do a calibration in which the results from the computer model are tuned to agree with the experimental results for the same ordinary load case by adjusting one or several coefficients in the model. This calibration procedure may be done for several load cases and with several adjustable coefficients in the model. If after this calibration the model produces results that agree, within the desired range of accuracy, with the corresponding experimental results for one or several load cases, then the model may be accepted. Then, as a second step, the simulation model is used to perform simulations in which the results of process changes are tried out with the purpose of finding the process changes that optimize the total output in the desired way. Often, considerable effort must be put into the first calibration part, since it is possible that the simulation model must be changed or refined several times in order to obtain the desired accuracy. The advantage of using computer models is that the effort to perform lots of simulations in the second, optimizing part is fast and cheap compared to trying out the effects of process changes in reality. If the final, optimized process is very different from the calibrated test cases, then there may be a concern that the results of the simulations may be inaccurate. If such a concern exists, then experiments must be performed in order to check the accuracy of the results.

The finite element method (FEM) is a general mathematical method for solving partial differential equations, and it is frequently used in performing computer simulations. Descriptions of FEM are given by, for example, ABAQUS Theory Manual (Anon 1998), Bathe (1982), Cook (2001) and Zienkiewicz & Taylor (2000). FEM is used in mechanical engineering as a numerical method for computer simulation of the deformation of deformable bodies by loading. FEM has been used commercially since the 1970s in the manufacturing industry, mainly for strength and deformation analyses of parts or structures. FEM in general is a method whereby the structure in question is divided into many small elements of elementary shape, e.g., tetrahedral or hexagonal elements. An elementary function (e.g., a linear or a quadratic function) with unknown coefficients is assumed to describe the sought variable (e.g., the displacements) within each element. By

minimizing a suitable functional (e.g., the potential energy of the structure) with respect to the unknown coefficients in the sought variable functions, a solution can be found. It can be shown that this solution approaches the exact solution when the number of elements goes to infinity.

FEM can be used both for modelling the MC in wood material during the drying process (Fig. 1) and the following deformations resulting from shrinkage due to a decrease of MC. Normally, these two processes are simulated in separate simulations with the MC output of the first simulation going into the second simulation. The drying and deformation simulations are dynamic; i.e., they are simulations in time. However, the deformation simulation is only quasistatic, since it is so slow that it has negligible inertia effects. FEM may also be used for simulation of the pole-vaulting process. Simulations of pole-vaulting are dynamic simulations in which inertia has a large effect.

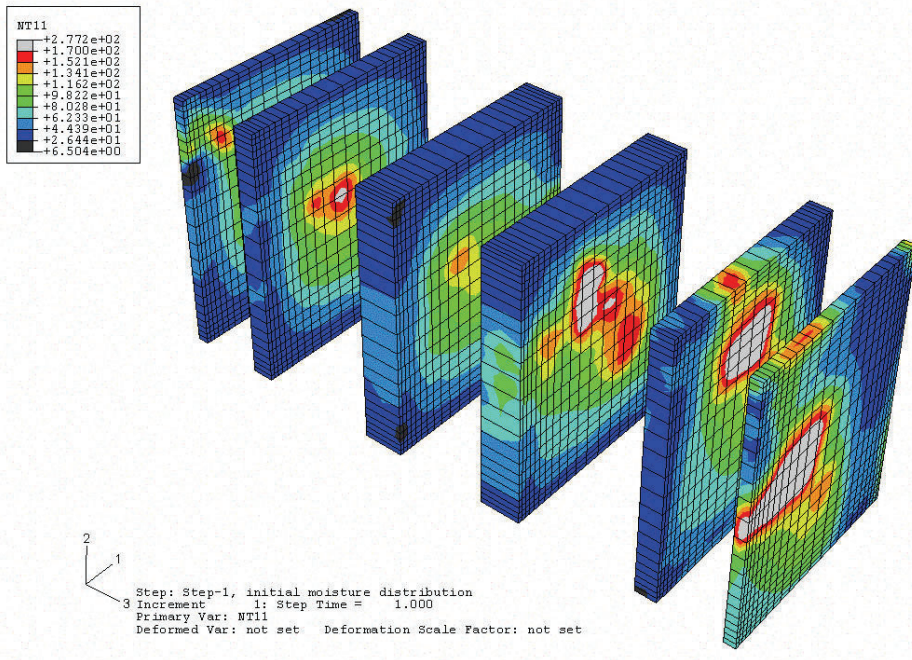


Fig. 1. Example of output from an FEM simulation of the drying process. Drying of a rectangular, solid wood piece, shown here as cut up in slices in order to show the results inside the solid volume. Results shown are MC expressed as mass of water per volume (kg/m^3).

2.2 Wood distortions

An important disadvantage with wood is that wood deforms during drying. Warp of dried wood boards is a reason for quality degrade, and thus income loss, in the production of boards. Due to this negative property, wood products have lost market share in

applications where wood traditionally has been the natural choice of material (Johansson et al. 1994; Eastin et al. 2001). Deformation of wood due to variations in air humidity may also be a problem for wood products during their life cycle. The deformations may cause cracks, malfunctions or other types of problems.

“The six major types of warp are bow, crook, twist, oval, diamond and cup,” (Wood Handbook 1999) and many scientists have studied warp and investigated which parameters have influenced the magnitude of warp when MC changes (Danborg 1994; Woxblom 1999; Forsberg 1999). In this thesis, only twist is studied, because it is believed to be one of the worst kinds of defects. Twist is mainly influenced by the magnitude of spiral grain and the distance from the pith (Booker 2005; Forsberg 1999; Forsberg & Warensjö 2001; Gjerdrum, Säll & Storö 2002; Harris 1989; Johansson, Perstorper, Kliger & Johansson 2001; Johansson & Kliger 2002; Nyström 2000; Nyström & Grundberg 2002; Nyström 2002; Nyström 2003; Sepulveda 2003; Skatter & Kucera 1998; Stevens & Johnston 1960; Säll 2002; Woxblom 1999), but also by the gradient of the spiral grain angle (paper 2; Forsberg 1999). Spiral grain occurs naturally in trees (Säll 2002), and the normal pattern in the northern hemisphere is that the spiral is left-handed in young wood, with a change to right handed in mature wood (Skatter & Kucera 1998). Some trees, however, seem to stay left-handed and just increase the left-handed spiral with age. Boards sawn from these trees have a very great tendency to twist (Nyström 2002).

Spiral grain on logs and boards can be measured with the aid of the tracheid effect. The tracheid effect utilizes the light-conducting properties of the softwood tracheids to measure the direction of spiral grain. A small laser point is projected onto the wood surface. The light transmitted in the wood and scattered back forms an elliptic shape extended in the direction of the fibres. The ellipse of light is registered with a camera, and the orientation of the ellipse’s major axis corresponds to the fibre direction (Nyström 2003).

Bow and crook are influenced by differences in the longitudinal shrinkage in different parts of a piece of wood. The differences in longitudinal shrinkage depend mainly on the distribution and magnitude of compression wood and juvenile wood (Johansson & Kliger 2002).

Control and understanding of how drying distortions evolve are essential in order to reduce distortions and thus increase the quality of sawn timber. Changes in the manufacturing process for wood products may overcome or reduce some of the problems with twist. Simulation techniques are tools that help to understand and control the factors that affect drying distortions. Computer simulations of twist can be used to study the influence of changes in the manufacturing process and thus lead to knowledge that is hard to obtain in any other way. As a byproduct, knowledge of how to model wood behaviour is not only valuable when it comes to modelling wood-drying distortions; it is also valuable when it comes to modelling wood products exposed to all other sorts of loads.

2.3 Objective and limitations

The objective of this work, with focus on wood-drying distortions, was to develop methods and simulation models for wood-drying deformations (mainly twist). A part of this objective was also to present results that showed the validity of the simulation models, to increase understanding of the causes of twist and to present results from simulations that point out manufacturing process changes that would reduce twist distortions. Local variations of material characteristics were to be included as much as possible, and methods to measure these local variations were to be used or developed.

The main limitations of this work were believed to be that only twist was considered, that the log model had no knots and that the only wood species that was considered was Norway spruce (*Picea abies*). Also, the material model for wood was limited to an elastic-plastic model. The material coefficients that were used in this model were taken or estimated from several different literature sources, and the level of accuracy may be low for some coefficients.

2.4 Outline of the thesis

The unique ingredients of this doctoral thesis are the results of the efforts to model local material variations in wood by using CT techniques (paper 1, paper 3), the derivation of the influence on twist of the spiral grain gradient on the twist of wood studs (paper 2) and the derivation of an elastic-ideally plastic material model for wood and the results that this model gives (paper 4). The simulations of the drying deformations are done in two steps by first using a drying-simulation model and then secondly a deformation-simulation model. The connection between these two steps and the papers in this thesis is shown in Fig. 2.

The licentiate thesis in Appendix 5 describes the simulation models that were developed to simulate pole-vaulting. The objective of this work was to develop methods and simulation models for pole-vaulting, to present results that showed the validity of the simulation models, to present results of vaulting heights that were possible to reach and to optimize the pole with respect to vaulting height. All of this was mainly done in order to develop a pole-design method and pole-design tool so that the pole designer could design better poles. Two models were developed. The first was a model with a passive, point-mass vaulter. This model was used to calculate the influence of pole length and stiffness on the vault height for a given vaulter. The second model had an active and “smart” vaulter in the sense that he tried to control his muscle torques in order to achieve the highest possible vault. In modelling pole-vaulting there was a need to model the material behaviour of the pole, but also for the second model to model how the human muscle torques acted on the pole and vaulter. The unique ingredients in the licentiate thesis (Appendix 5) were the optimization of the pole length and stiffness for a given vaulter (Ekevad & Lundberg 1997) and the simulation model and the results for a model of a pole and a “smart” vaulter (Ekevad & Lundberg 1995) (see Fig. 2).

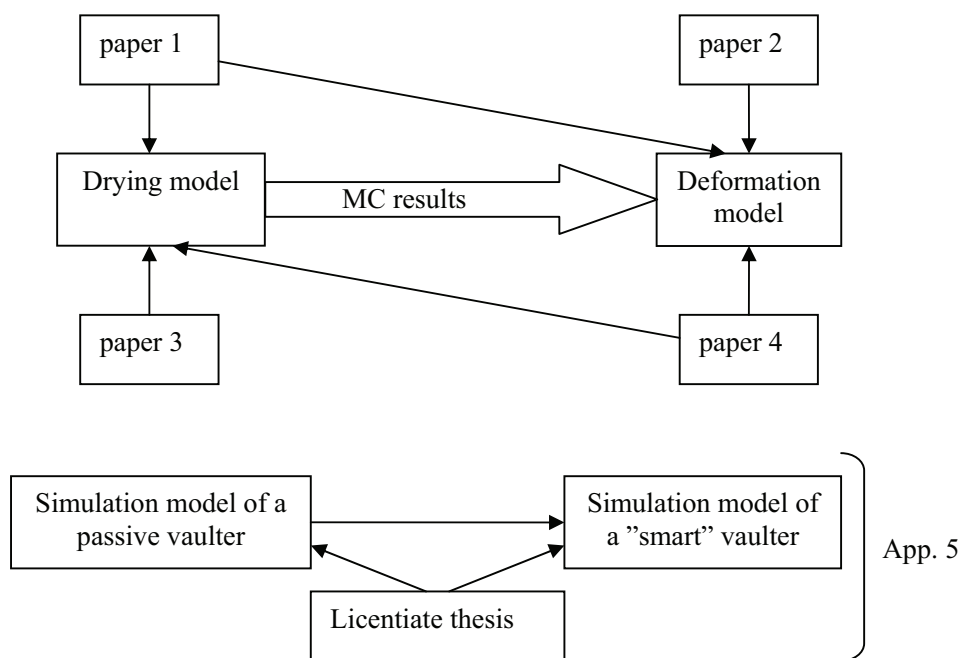


Fig. 2. Outline of the relationship between the papers and the simulation models.

What links together the wood-drying simulations and the pole vault simulations are that they are both simulations of dynamic or quasistatic events and that they are done using FEM, ABAQUS and user-written subroutines. However, there are both similarities and differences between the two kinds of simulations. The materials used in the dynamic and quasistatic events, glass-fibre for pole-vaulting and wood for wood-drying simulations, are both orthotropic fibre materials, but they are described with different material models in the simulations. The material description is purely elastic in the pole-vault simulations, but is elastic-plastic in the wood-drying simulations. Most of the user subroutines were written for the material description in the case of the wood-drying simulations, but mainly written for the description of the control of muscle torque of the vaulter in the pole-vault simulations. Inertia effects are important, and the deformations of the pole and vaulter are large, in the relatively fast event of pole-vaulting. But inertia is not very important, and the deformations are small, in the relatively slow process of wood drying. However, perhaps the most important difference between the two types of simulations is that glass-fibre material is manufactured, and variations in material properties achieved during manufacturing are controlled and limited. In contrast to this, wood is a biological material, and every tree and every board is different. Sorting logs or boards in groups with similar characteristics may limit variations within groups to some extent, but still the material properties vary considerably between individual boards. Thus material properties of wood found in handbooks are always mean values, and one must bear in mind that an individual piece of wood may have deviant properties.

3 Theory

This theory section contains basic explanations and definitions of wood mechanics, wood drying, computer FEM simulations, material modelling and the linear elastic-plastic orthotropic material theory that was used in paper 4. The description of wood is made with special reference to softwoods and especially Norway spruce (*Picea abies*), because it is the material that is treated in this thesis. This means that the description is not valid in all respects for other species, especially hardwoods.

3.1 *The inner structure of wood*

Information about this subject may be found in Wood Handbook (Anon. 1999), Dinwoodie (2000), Gibson & Ashby (1988) and Johansson (2002). The description here is simplified and is focused on wood behaviour from a mechanical point of view and for use in the simulation models of wood-drying deformations.

A tree grows in diameter and height periodically in annual cycles, and the wood material in a tree is thus characterized by a cylindrical geometry with growth rings. The stem has a small taper, since the tree is thinner (and thus younger) at the top than at the root. A tree grows horizontally (i.e., in diameter) because a new growth ring is added to the old ones every growth season. The only exception to this is the leading shoot, which grows both in diameter and vertically upwards to enable the tree to grow in height.

Within a single growth ring there is a first, less dense part called earlywood that grows in springtime and early summer. Then there is a second, denser part called latewood that grows during the late summer. There is no growth during the autumn and winter. The first 20 to 30 growth rings close to the pith are called juvenile wood (Thörnqvist 1990) and have lower strength and higher shrinkage in the fibre direction than the rest of the growth rings. The outer and younger part of the stem fulfils the function of storage and conduction of water and nutrients and is called sapwood. The inner and older part (closer to the pith) of a mature tree stem no longer fulfils these tasks and is called heartwood. The growth of a tree only takes place outside of the outermost growth ring, through cell division in the cambium, just beneath the inner bark.

The flow of water upwards in the tree takes place in the sapwood, and a downward flow of nutrients takes place in the inner bark. In microscopic detail, the main part of the wood material consists of slender, approximately vertically aligned fibres (or cells or tracheids) that are a kind of hollow “pipes” about 1.7–3.7 mm long and 0.02–0.04 mm thick (Fengel & Wegener 1984) (see Fig. 3). The hollow spaces in the fibres are called lumen and in sapwood are normally filled with water to be transported upwards from the root to the top of the tree. The fibres have pit openings at the ends, but also in the walls that make a flow between fibres possible. The solid material in the cell walls has a density of about 1500 kg/m³, and since dry wood has a density of about 400 kg/m³ we conclude that about 70% of the volume of a piece of dry wood is hollow space and about 30% is solid cell walls. There are also other kinds of cells, such as ray tracheids, ray parenchyma and epithelial cells, oriented in the radial direction in the wood material, but they are not nearly as

numerous as the vertical fibres in softwoods. Wood material without knots or defects of any kind is called clearwood.

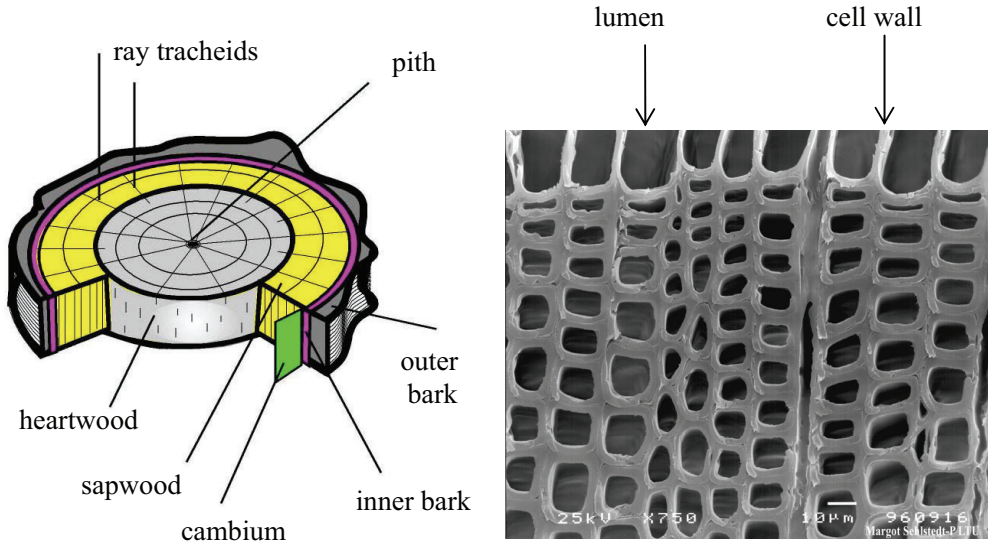


Fig. 3. To the left a cross-section of a tree stem. To the right an enlargement showing a crosscut through the fibres (cells) with the hollow space (lumen) and the cell walls.

3.2 Qualities and defects of wood

The properties of a wood sample are determined by the qualities and defects of the tree from which the sample is taken. A quality characteristic for a tree may be a defect for a wood sample. Knots and branches are essential for a living tree and are thus positive qualities, but they may be defects in sawn timber because strength and deformation properties deteriorate (Foley 2001, 2003; Saarman 1986; Shigo 1988; Xu 2002). However, from a visual point of view, knots may increase the beauty and thus the quality of wood (Buchanan 1998). Knots affect the properties of the wood material in the vicinity of the knots because the fibres close to the knot are directed either into the knot (going out into the tree branch) or are directed around the knot and further upwards in the tree (Kramer 2002; Kramer & Borkowski 2004). The density of the wood and growth ring distance in the vicinity of knots are affected by knots. There is often compression wood on the lower side of a knot, since there are compressive stresses there due to the weight of the branch. Knots may be completely or partially live or dead and firmly or loosely connected to the surrounding wood material. Knots may contain cracks (especially after drying), and they affect the visual impression and the deformation and strength properties of the wood.

Compression wood may be formed in certain volumes of a living tree due to compressive stresses during growth (Nyström & Hagman 1999; Öhman 2001; Öhman & Nyström

2002). Compression wood adds compressive stresses that make the fibres expand in the fibre direction. The quality of compression wood for a living tree is that it makes the tree return to a vertical height increase even if the wind or the ground has caused the tree to lean. Compression wood also helps the branches stay horizontal and not deform too much under load. However, for sawn timber, compression wood is a defect since it is hard, brittle and harder to saw, shrinks more in the fibre direction and is harder to put a nail through, than ordinary wood. There is a tall story that says that in the old days skis were best made out of compression wood, but the truth of that is unknown.

Top breakages of the leading shoot because of frost, snow load or moose eating is quite common in Sweden. The tree repairs the damage by using a nearby branch as the next leading shoot, and the result is eventually crooked pith, which affects the fibre direction near the damage and thus the strength of the wood material.

3.3 Wood as an orthotropic material

Definitions of orthotropic materials are given by Lai, Rubin & Krempl (1996) and Malvern (1969).

For each point in an orthotropic material there are three orthogonal normal directions that define symmetry planes in the material, and there are different properties in each orthotropic direction. Wood may be treated as an orthotropic material, with the three orthogonal directions being the radial \mathbf{r} , the tangential $\boldsymbol{\varphi}$ and the fibre direction \mathbf{z} (bold symbols denote vectors). The orthogonal directions vary locally from point to point, since the fibre direction varies due to knots and other fibre disturbances.

One possibility to measure these directions is to use computed tomography (CT) images (see Lindgren 1992) and to measure the orthogonal directions directly (and nondestructively) as discussed in paper 1 or by the method presented by Sepulveda, Oja & Grönlund (2002). The CT-direction method presented in paper 1 measures locally varying directions throughout the volume of the wood piece based on density variations. However, local variations of fibre directions around knots cannot be detected with the available resolution. Another more approximate and simpler approach is to use a combination of theory and measurements. First we measure or calculate the pith line position (as a curve or a straight line), the taper angle φ_c (as a constant or a function of axial position) and the spiral grain angle θ (as a function of radius). Then the local coordinate system $\mathbf{r}\text{-}\boldsymbol{\varphi}\text{-}\mathbf{z}$ is defined according to Fig. 4 by at first drawing a line AB from, and perpendicular to, the pith line, to the point in question. Then the coordinate system is placed with its origin in the point in question, the radial direction in the direction of AB, the fibre direction parallel to the pith line and the tangential direction so that $\mathbf{r}\text{-}\boldsymbol{\varphi}\text{-}\mathbf{z}$ forms a right-handed coordinate system. Finally, the coordinate system $\mathbf{r}\text{-}\boldsymbol{\varphi}\text{-}\mathbf{z}$ is rotated first at the angle φ_c around $\boldsymbol{\varphi}$ in order to allow for a taper and then followed by a rotation θ around \mathbf{r} in order to allow a spiral grain angle (positive if right-handed). This method gives the mean or general fibre directions in a tree or log, but does not take knots and other fibre disturbances into account.

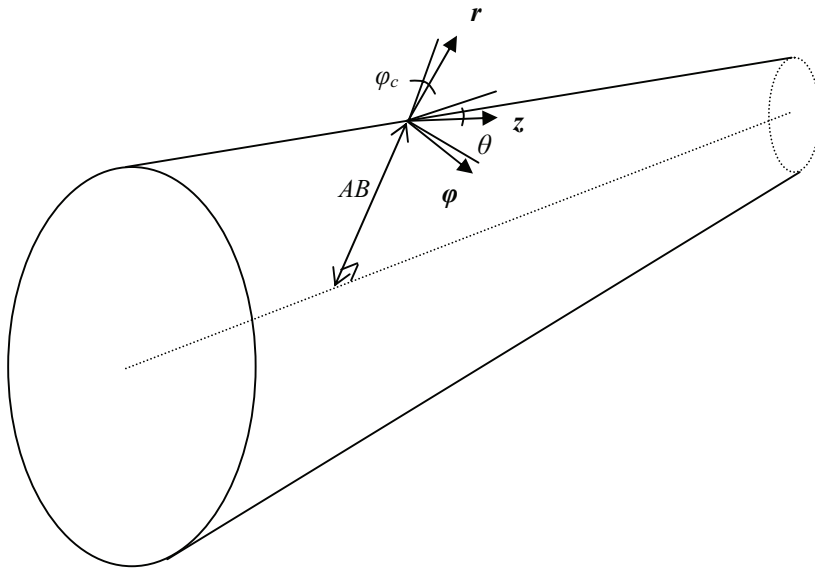


Fig. 4. Model for local orthotropic directions r - ϕ - z in wood. Taper angle φ_c and spiral grain angle θ . Line AB from pith, and perpendicular to pith, to point in question.

3.4 Moisture content, temperature, shrinkage and fibre saturation point

Wood is a hygroscopic material that normally contains water. The cell walls are hygroscopic and may bind water, and the hollow spaces in the cells (lumina) may be filled with water. The moisture content (MC) $u = m_w/m_0$, where m_w is the mass of water and m_0 is the mass of dry wood, describes the amount of water that the wood contains. In the green, living condition, the cell walls are saturated with water, and the cavities (lumina) are partially or totally filled with free water. Green heartwood holds less water than green sapwood, but u in green condition varies considerably depending on species, on type of wood (heartwood or sapwood) and on season of the year. Usually for Norway spruce (*Picea abies*), u in green condition is about 40% for heartwood and about 150% for sapwood (Sehlstedt-Persson 2005). If green wood material is exposed to surrounding air, the surface, and eventually also the inside of the wood piece, dries. Wood in contact with air strives to achieve equilibrium with the surrounding air, and this is expressed by the sorption isotherm curve that shows (for a given temperature) the equilibrium (i.e., long-term) MC (EMC) in wood as a function of the relative humidity in the surrounding air.

All mechanical material properties of wood are more or less dependent on MC (below FSP) and temperature (Green, Evans, Logan & Nelson 1999; Kretschmann 1996; Siimes 1967). The stiffness and strength of wood increase with decreasing MC and decrease with increasing temperature.

Wood shrinks when MC falls below FSP, and shrinkage is often assumed to be proportional to the fall of MC below FSP (Wood Handbook 1999). The proportionality coefficient is the moisture expansion coefficient. Shrinkage is highest in the tangential ϕ direction, about half this value in the radial r direction and very small (practically zero) in the fibre direction z (except for compression and juvenile wood).

3.5 The drying process

When exposed to air, the surface dries first, and free water from the inside of the wood piece is rapidly transported to the surface by capillary forces. When the MC eventually has reached the fibre saturation point (FSP), all or most of the free water has evaporated, and water transport from the inside towards the surface now changes to a slower mechanism. Transport of water now takes place as bound water diffusion in the cell walls and as moisture diffusion via humid air in the lumina. FSP is about 25%–30% at room temperature and is the point where the cells walls are saturated with water, but the hollow space (lumen) is empty of free water. Sawmills dry the wood according to the customers' wishes, normally to an MC of 8%–18%.

The goal of sawmills is to produce sufficiently dry, stress-free, crack-free and straight boards in the shortest possible time. During drying, shrinkage in combination with spiral grain, knots, compression wood and other defects will lead to distortions such as twist, crook and bow. Convective air-drying of wood is often done in kilns at elevated temperatures in order to shorten the drying time, but the wood material also becomes more flexible and less brittle at higher temperatures. Raising the temperature means we get more plastic deformations, which reduces distortions, compared to drying at room temperature. However, shorter drying times will also mean larger MC gradients and thus higher stresses during drying. This increases the risk of getting more cracks. The restraints on deformation during drying are an important parameter of the drying process. Measurement and modelling of the drying process have been done by Awadalla, El-Dib, Mohamad, Reuss & Hussein (2004); Danvind (2002); Danvind & Morén (2004); Hunter (2001); Kontenta (2003); Morén (1993); Ormarsson (1999); Salin (2002); Wiberg (2001) and Wiberg & Morén (1999), among others. Studies of the diffusion and mass-transfer processes and evaluation techniques for them have been reported by Cai & Avramidis (1997); Fatullayev (2001); Hukka (1999); Hukka & Oksanen (1999); Koc, Houska & Stok (2003); Liu, Simpson & Verrill (2001); Liu & Simpson (1999); Pang (1996); Peralta & Bangi (2003); Plumb, Spolek & Olmstead (1985); Rosenkilde & Arfvidsson (1997); Salin (1996, 1997, 2002); Simpson & Liu (1997); Söderström & Salin (1993); Time (2002); Wadsö (1993) and others.

The uneven shrinkage in the r - ϕ - z directions of the wood material during drying results in stresses that can be great enough to produce permanent, plastic deformations, even cracks. MC gradients in the boards and restraints on deformation during drying also contribute to the stress field. After drying, internal, self-equilibrating stresses may remain in the boards. They may be the result of growth stresses during the tree's life that already existed before and after sawing, or they may be the result of remaining MC gradients in the boards after

drying. They may also appear as a result of uneven shrinkage during drying or be the result of a combination of all these causes (Tronstad 2005; Mackay & Rumball 1971; Mackay 1973; Northway 1981; Salin, Esping & Hajek 2005; Salin 2005; Visser & Vermaas 1988).

3.6 FEM for wooden components

Examples of the use of FEM for wooden components are given by Holmberg (1998); Ormarsson (1999); Ormarsson, Dahlblom & Peterson (2000) and Serrano (2000). Simulations using FEM on wooden components involve some special considerations when it comes to modelling the material behaviour as compared to FEM modelling dealing with components made of manufactured materials such as metallic materials such as steel or nonmetallic materials such as plastic. FEM and continuum mechanics are in general based on the condition that the material within a solid body (a continuum) is continuous, i.e., homogeneous (i.e., there are no holes within the body). Manufactured materials are normally considered homogeneous, but also uniform, and their properties are often standardized. Uniformity means that the material properties do not vary within the body in question (unless the state of the material varies). A standardized material has well-defined properties that are not allowed to vary much, and variations of properties outside of a small, allowed span lead to rejection of the material. Efficient production of parts or structures, especially mass production, is facilitated by the use of materials that are uniform and standardized.

Wood and other biological materials are, on the contrary, materials with widely varying properties. Sources of variation between wood pieces can be, for example, variations in knot size, density and amount of compression wood. There are also large variations within a wood piece—each wood piece is an individual, and wood is basically not a uniform, homogeneous or standardized material. The wood manufacturer (i.e., the sawmill) may sort the boards into different quality classes by visual inspection by, looking at the outer surfaces or by measuring the deflection of the boards under a specified load. In this way a certain kind of uniformity and standardization is achieved, but only in terms of one or a few global, mean properties of the boards such as bending stiffness or number and size of knots. No uniformity is today achieved on a smaller scale level, i.e., within the boards.

3.7 Validation and measurements

Simulations based on different model assumptions are not very useful if they don't correlate with the true behaviour. When studying local three-dimensional (3-D) characteristics and behaviour such as fibre direction and MC in reality, a sophisticated measuring technique is needed. At LTU Skellefteå there has been a medical X-ray Computed Tomography (CT) scanner (Somatom AR.T.) installed since the middle of the 1990s. Many research projects have used this equipment over the years. This tool has proven to be very useful in development and validation of simulation models (paper 1 and paper 3). The CT measurements give 3-D density information as a function of time, e.g., during drying of a wood piece.

3.8 Diffusion, elasticity, plasticity, creep and mechanosorption

Real material behaviour is often complex and hard to describe in mathematical terms, especially if the dependence of stress, temperature and MC is to be included. It is advantageous to use the simplest and most well-established material models as possible, such as diffusion, elastic, plastic or creep models, when modelling material behaviour. Diffusion, elasticity, plasticity and creep are classical, well-defined phenomena that are theoretically deducible or explainable from a micromechanical point of view. Also, they give results that agree with experimental results for many types of materials, e.g., manufactured materials such as metals and plastics. However, another approach is to use a material model that makes simulation results agree with experimental results and not to focus on whether the material model can be explained from a micromechanical point of view. Instead, the material model may be seen as a mathematical construct whose purpose is to create good simulation results.

Elasticity is described in general terms by Timoshenko (1970). Elastic materials deform under load, but return to their unloaded configuration after removal of the load. Elastic deformations in metals are due to small movements of atoms in the crystal structure due to loading and the return of these atoms to their original positions after unloading. Elastic deformations in wood are in the same way due to movements of wood polymers due to loading and the return of these wood polymers to their original positions after unloading

Plastic deformations are deformations that are irreversible; i.e., the deformations are permanent and do not disappear. Irreversible deformations make it possible to reduce or even eliminate the distortions of a stud or board. Modelling the irreversible material behaviour in a realistic way is essential for valid simulations of wood-drying deformations. General plasticity theory and strength theory are discussed by DeTeresa & Larsen (2003); Han & Reddy (1999); Hill (1948); Khan & Huang (1995); Lubliner (1990); Oller, Car & Lubliner (2003); Sonnen, Laval & Seifert (2003) and Tsai & Wu (1971). Wood plasticity is discussed by Babeshko & Shevchenko (2005); Clouston & Lam (2001, 2002); Hanhijärvi & Mackenzie-Helnwein (2003); Hammoum & Audebert (1999); Kharouf, McClure & Smith (2003); Mackenzie-Helnwein & Hanhijärvi (2003); Mackenzie-Helnwein, Eberhardsteiner & Mang (2003, 2005); Moses & Prion (2004); Thomas (1983) and Hu (2005). Plastic materials also deform due to loading, but they stay deformed after removal of the load. Plasticity in metals is due to the movements of dislocations and the resulting permanent rearrangement of atoms in the crystal structure. Plasticity in wood does not have to do with dislocation movements, but is instead due to other permanent rearrangements of material (Mackenzie-Helnwein, Eberhardsteiner & Mang 2003) that reveal themselves by a nonlinear stress-strain curve after exceeding a yield stress and by permanent deformation after unloading.

Materials that creep will also deform under load and stay deformed after removal of the load, but the difference between plastic and creep deformation has to do with time. Creep is a time-dependent phenomenon that results in an increasing deformation with time, whereas plasticity is not time dependent; i.e., the deformation, if any, is immediate. Elastic deformations will appear no matter how small the load is, but a load that exceeds a

certain yield limit is necessary for plastic deformations to be of importance. Creep deformations are normally only of significance for load cases with high temperatures or long duration of loads, or both.

Mechanosorption is a phenomenon that occurs in wood (and other sorptive materials) due to stress in combination with a change in MC. The result of mechanosorption is an added strain increment. Some experiments indicate that the added strain increment is always positive (i.e., in the same direction as the strain due to the stress), no matter the sign of the MC increment. Experimental results, possible explanations and models for mechanosorption are discussed in papers by Armstrong & Christensen (1961); Grossmann (1976); Hanhijärvi (2000); Hoffmeyer & Davidson (1989); Houska & Koc (2000); Hunt (1999); Kowalski & Musielak (1999); Muszynski, Shaler & Davids (2005); Mårtensson & Svensson (1997); Navi, Pittet & Plummer (2002); Ranta-Maunus (1990); Salin (1992); Svensson & Mårtensson (2002) and Svensson & Toratti (2002). The added strain increment terms in the theoretical mechanosorption models mentioned here are mostly proportional to stress times the increment of MC or the absolute value of the increment of MC. However, an “ordinary” term of such kind also appears in the incremental form of elastic strain-stress equations due to the moisture dependence and temperature dependence of the material coefficients (see the deductions in later theory sections of this thesis, pp. 21 ff., and especially the last two terms of Eq. (10) and (29)). Rosenfield & Averbach (1956) describe the appearance and effects of this ordinary term, which they call a stress-dependent expansion coefficient. Some papers describe mechanosorption via an added strain-increment term due to mechanosorption, but no ordinary term that indicates that the ordinary term is included in the mechanosorption term. Other papers include both the ordinary term and an added term due to mechanosorption. At any rate, what seems to be clear is that experiments reveal that stress in combination with MC changes lead to unexpected and permanent additions of strains and that the elastic material model with an ordinary strain increment term is not capable of explaining that. Unfortunately, no physical explanation with a derivation of a mechanosorptive strain increment term from a theoretical and micromechanical point of view seems to exist. Without such a theoretical derivation, any addition of a term is just the addition of an experimental correction term that takes care of deviations between experiments and the elastic-plastic and creep terms. Such correction terms are a type of “curve-fitting terms” that do not explain the mechanosorption phenomenon; they just improve the correlation between theory and experiment in a certain range. Thus it may be concluded that mechanosorption seems to be a phenomenon whose effects on strain may be modelled in several ways, but for which a wholly clear explanation is still lacking.

Drying behaviour was simulated with a diffusion model (paper 3, paper 4). This model is believed to be appropriate if the MC is lower than FSP and capillary transport is not dominating. Above FSP the diffusion model is not as good as below FSP, since capillary water transport dominates. However, since the focus of this work was on the regime below FSP, the shortcomings of the diffusion model above FSP were accepted, and the diffusion model was used for the regime above FSP as well. The motivation was that there was no shrinkage that contributed to deformations and stresses above FSP. The

diffusion coefficient was allowed to be dependent on MC, temperature and distance from surface. Above FSP a high diffusion coefficient was used to simulate capillary water transport.

The material modelling in the deformation model was done with elastic (paper 2) and elastic-plastic (paper 4) material models. The use of an elastic model was obvious, since wood is generally classified as elastic. The use of the plastic model was due to the necessity of including in paper 4 an ingredient that can give permanent deformations. Plasticity is believed to be important especially at the high temperatures used in kiln drying of wood. Creep and mechanosorption models were not included.

3.9 Linear elastic-plastic constitutive equations for orthotropic materials

In paper 2, wood was treated as a linear elastic orthotropic material and in paper 4, wood was treated as a linear elastic- ideally plastic orthotropic material with a Tsai-Wu yield function. The material coefficients were dependent on temperature T and moisture content u , and strains were small. In the following, derivations of the constitutive equations for linear elastic and linear elastic-plastic orthotropic materials are shown. The derivations are made step by step in a pedagogic way, starting with the simplest 1-D linear elastic case and ending with the most complicated 3-D orthotropic linear elastic-ideally plastic case used in paper 4.

3.9.1 Linear elastic behaviour for a one-dimensional (1-D) case

Strain ε is a state function of stress σ , temperature T and moisture content (MC) u ,

$$\varepsilon = \varepsilon(\sigma, T, u). \quad (1)$$

(Note that a superindex e on strain, normally designating elastic strain, is skipped here in for the sake of clarity, since no plastic or other type of strain is involved so far). Thus, there are 3 independent state parameters that can be chosen arbitrarily among the 4 candidates ε , σ , T and u . Any 3 state parameters describe fully the state or the condition of a point in the material, and the fourth state parameter is given by the state function (1). The existence of a state function (1) means that the material state at a certain moment in time does not depend on the previous history of the state parameters for the point. In other words, the loading path to reach the state in question is not important, but instead, the state only depends on the instantaneous value of 3 independent state parameters at that moment in time. Such a material (i.e., a material that consists of such points) behaves elastically.

The strain ε in a point in an elastic material returns to its initial (start) value after a loading scheme is applied to it (and thus the configuration of the whole of a body in question consisting of such elastic points), provided that σ , T and u returns to their initial values at the end of the load scheme. The load scheme may consist of arbitrary variations of σ , T and u , but the loading history does not influence the final state, which is equal to the initial state.

The constitutive equations for an elastic, path-independent material can be written in a total form, i.e., with a state function as in (1). This total form of the constitutive equations may also be transformed into a differential form, as will be shown below. On the other hand, as we will see below for an elastic-plastic material, the constitutive equations for a non-elastic, path-dependent material cannot be written in a total form, i.e., with a state function as in (1). Only a differential form of the equations is possible, and the final state must be calculated via an integration of the differential form of the equations.

Time is not involved in any way in the behaviour of an elastic material. The load scheme is a sequence of variations of the parameters σ , T and u one after the other. Time is not needed as a parameter in any equation. However, it is often fruitful to think of time as a parameter to keep track of the chain of events in a load scheme, and to use time as a parameter to register in the order in which changes in loading take place. For the elastic-plastic material described below, too, time is not involved. Contrary to many textbooks, the use of time derivatives dt and rate descriptions such as $\dot{\varepsilon}$, $\dot{\sigma}$ and \dot{u} has been avoided in the text below due to the fact that time is not involved in the material behaviour, and also because it is believed that the clarity of the descriptions of the theory increases if rates of variables are not introduced when not necessary. Instead, differentials are used here. Since time is not involved, creep is not included in the material behaviour.

Since ε is a state function, there is a perfect differential

$$d\varepsilon = \left(\frac{\partial \varepsilon}{\partial \sigma} \right)_{T,u} d\sigma + \left(\frac{\partial \varepsilon}{\partial T} \right)_{\sigma,u} dT + \left(\frac{\partial \varepsilon}{\partial u} \right)_{\sigma,T} du. \quad (2)$$

Measurements on a real piece of wood of the relation between a small change of strain $d\varepsilon$ and the corresponding small change of stress $d\sigma$ when keeping T and u constant reveal that $d\varepsilon/d\sigma$ is approximately constant within a certain range $-\sigma_s < \sigma < \sigma_s$, where σ_s is the yield stress. Thus we may define $E = E(T, u)$ to be the elastic modulus (not a function of σ) within that range. and we define the flexibility

$$\left(\frac{\partial \varepsilon}{\partial \sigma} \right)_{T,u} = \frac{1}{E(T, u)}. \quad (3)$$

This means that in addition to the elasticity assumption, we have now added the linearity assumption and defined a linear elastic material. We also define

$$\left(\frac{\partial \varepsilon}{\partial T} \right)_{\sigma,u} = \alpha(\sigma, T, u) \quad \text{and} \quad \left(\frac{\partial \varepsilon}{\partial u} \right)_{\sigma,T} = \beta(\sigma, T, u) \quad (4a, 4b)$$

to be the thermal expansion coefficient and the moisture expansion coefficient, respectively. Note that these two coefficients α and β depend on σ and are not the usual expansion coefficients that are normally measured and tabulated in handbooks (see

Rosenfield & Averbach (1956) for information about stress-dependent expansion coefficients). However, since E does not depend on σ , we may achieve an expression for the dependence of α and β on σ as follows: the order of differentiation is immaterial when differentiating two times, which means that

$$\frac{\partial}{\partial \sigma} \left(\frac{\partial \varepsilon}{\partial T} \right) = \frac{\partial \alpha}{\partial \sigma} = \frac{\partial}{\partial T} \left(\frac{\partial \varepsilon}{\partial \sigma} \right) = \frac{\partial}{\partial T} \left(\frac{1}{E} \right) = -\frac{1}{E^2} \frac{\partial E}{\partial T}. \quad (5)$$

Since E is not a function of σ , we may integrate (5) to give

$$\alpha(\sigma, T, u) = \alpha_0(T, u) - \frac{\sigma}{E^2} \frac{\partial E}{\partial T}(T, u), \quad (6)$$

where $\alpha_0(T, u)$ is the (true) thermal expansion coefficient at zero stress. In the same way we have

$$\frac{\partial}{\partial \sigma} \left(\frac{\partial \varepsilon}{\partial u} \right) = \frac{\partial \beta}{\partial \sigma} = \frac{\partial}{\partial u} \left(\frac{\partial \varepsilon}{\partial \sigma} \right) = \frac{\partial}{\partial u} \left(\frac{1}{E} \right) = -\frac{1}{E^2} \frac{\partial E}{\partial u}. \quad (7)$$

Since E is not a function of σ we may integrate (7) to give

$$\beta(\sigma, T, u) = \beta_0(T, u) - \frac{\sigma}{E^2} \frac{\partial E}{\partial u}(T, u), \quad (8)$$

where $\beta_0(T, u)$ is the (true) moisture expansion coefficient at zero stress. α_0 and β_0 may be taken from experiments as

$$\left(\frac{\partial \varepsilon}{\partial T} \right)_{\sigma=0, u} = \alpha_0(T, u) \quad \text{and} \quad \left(\frac{\partial \varepsilon}{\partial u} \right)_{\sigma=0, T} = \beta_0(T, u). \quad (9a, 9b)$$

These two coefficients α_0 and β_0 do not depend on σ . The results (6) and (8) together with (2) give an incremental form of the linear elastic constitutive behaviour of the material:

$$d\varepsilon = \frac{d\sigma}{E} + \alpha_0 dT + \beta_0 du - \frac{\sigma}{E^2} \left(\frac{\partial E}{\partial T} dT + \frac{\partial E}{\partial u} du \right). \quad (10)$$

The expression inside the parentheses is equal to the differential dE , i.e., the change of the elastic modulus during the increment. The last term is proportional to stress and MC change. Kowalski & Musielak (1999) call such a term “mechanosorptive” and point out that such terms exist when “one assumes the material coefficients to be moisture dependent.” Since we are dealing with an elastic, path-independent material, we may get

the total form of the linear elastic constitutive behaviour of the material as follows: we integrate between an initial (starting) state (with index 0) and a final state (with no index)

$$\int d\varepsilon = \int \frac{d\sigma}{E} + \int \alpha_0 dT + \int \beta_0 du - \int \frac{\sigma}{E^2} \left(\frac{\partial E}{\partial T} dT + \frac{\partial E}{\partial u} du \right) = \int d \left(\frac{\sigma}{E} \right) + \int \alpha_0 dT + \int \beta_0 du,$$

which gives

$$\varepsilon - \varepsilon_0 = \frac{\sigma}{E} - \frac{\sigma_0}{E_0} + \alpha_{0m}(T - T_0) + \beta_{0m}(u - u_0), \quad (11)$$

where

$$\alpha_{0m}(T, T_0, u) = \frac{1}{(T - T_0)} \int_{T_0}^T \alpha_0(T, u) dT \quad (12)$$

is the mean thermal expansion coefficient at zero stress between T_0 and T . In the same way

$$\beta_{0m}(T, u, u_0) = \frac{1}{(u - u_0)} \int_{u_0}^u \beta_0(T, u) du \quad (13)$$

is the mean moisture expansion coefficient at zero stress between u_0 and u . It is these mean expansion coefficients that are normally measured and tabulated in handbooks. Often, mean values of measured expansion coefficients at zero stress are presented as mean values between a reference value (temperature or MC) and a tabulated value. If the reference state does not agree with the initial state, then the following expressions are used:

$$\alpha_{0m}(T, T_0, u) = \frac{1}{(T - T_0)} \int_{T_0}^T \alpha_0(T, u) dT = \frac{1}{(T - T_0)} \left(\int_{T_{ref}}^T \alpha_0(T, u) dT - \int_{T_{ref}}^{T_0} \alpha_0(T, u) dT \right) = \frac{(T - T_{ref})}{(T - T_0)} \alpha_{0m}^{ref}(T, T_{ref}, u) - \frac{(T_0 - T_{ref})}{(T - T_0)} \alpha_{0m}^{ref}(T_0, T_{ref}, u) \quad (14)$$

and

$$\beta_{0m}(T, u, u_0) = \frac{1}{(u - u_0)} \int_{u_0}^u \beta_0(T, u) du = \frac{1}{(u - u_0)} \left(\int_{u_{ref}}^u \beta_0(T, u) du - \int_{u_{ref}}^{u_0} \beta_0(T, u) du \right) = \frac{(u - u_{ref})}{(u - u_0)} \beta_{0m}^{ref}(T, u, u_{ref}) - \frac{(u_0 - u_{ref})}{(u - u_0)} \beta_{0m}^{ref}(T, u_0, u_{ref}), \quad (15)$$

where $\alpha_{0m}^{ref}(T, T_{ref}, u)$ and $\beta_{0m}^{ref}(T, u, u_{ref})$ are the mean thermal expansion coefficient at zero stress between T and T_{ref} at moisture content u and the mean moisture expansion

coefficient at zero stress between u and u_{ref} at temperature T , respectively. If (14) and (15) are inserted into (11) we get

$$\begin{aligned} \varepsilon - \varepsilon_0 = & \frac{\sigma}{E} - \frac{\sigma_0}{E_0} + (T - T_{ref})\alpha_{0m}^{ref}(T, T_{ref}, u) - (T_0 - T_{ref})\alpha_{0m}^{ref}(T_0, T_{ref}, u) + \\ & (u - u_{ref})\beta_{0m}^{ref}(T, u, u_{ref}) - (u_0 - u_{ref})\beta_{0m}^{ref}(T, u_0, u_{ref}). \end{aligned} \quad (16)$$

In order to use the incremental form of the linear elastic constitutive behaviour (10), we may sometimes need to calculate the (true) values of the temperature and moisture expansion coefficients at zero stress from the corresponding values of the mean expansion coefficients at zero stress. In that case, (12) gives

$$\alpha_0(T, u) = \left(\frac{\partial \alpha_{0m}}{\partial T} \right)_{T, T_0, u} (T - T_0) + \alpha_{0m}(T, T_0, u) \quad (17)$$

and (13) gives

$$\beta_0(T, u) = \left(\frac{\partial \beta_{0m}}{\partial u} \right)_{T, u, u_0} (u - u_0) + \beta_{0m}(T, u, u_0). \quad (18)$$

Normally, it is the mean values of the expansion coefficients that are measured and tabulated in handbooks, but transformations between mean values for different reference values and between (true) values and mean values are possible using (12)–(18). However, in order to increase the clarity of the description in the following text, we assume α_{0m} and β_{0m} to be constants and set $\alpha_0 = \alpha_{0m}$ and $\beta_0 = \beta_{0m}$. Then (11) is the total form of the linear elastic constitutive behaviour, and (10) is the incremental form.

3.9.2 Linear elastic behaviour for a three-dimensional (3-D) case

The strain vector $\bar{\varepsilon} = \bar{\varepsilon}(\bar{\sigma}, T, u)$ is a state function of the stress vector $\bar{\sigma}$, the temperature T and the MC u , and we get the perfect differential vector

$$d\bar{\varepsilon} = \left(\frac{\partial \bar{\varepsilon}}{\partial \bar{\sigma}} \right)_{T, u} d\bar{\sigma} + \left(\frac{\partial \bar{\varepsilon}}{\partial T} \right)_{\bar{\sigma}, u} dT + \left(\frac{\partial \bar{\varepsilon}}{\partial u} \right)_{\bar{\sigma}, T} du. \quad (19)$$

Experiments measuring the relation between stress and strain components with T and u kept constant ($dT = du = 0$) reveal that the elastic flexibility matrix (symmetric) may be expressed as

$$\bar{\bar{F}} = \bar{\bar{F}}(T, u) = \left(\frac{\partial \bar{\varepsilon}}{\partial \bar{\sigma}} \right)_{T, u} = \begin{bmatrix} 1/E_1 & -v_{21}/E_2 & -v_{31}/E_3 & 0 & 0 & 0 \\ -v_{12}/E_1 & 1/E_2 & -v_{32}/E_3 & 0 & 0 & 0 \\ -v_{13}/E_1 & -v_{23}/E_2 & 1/E_3 & 0 & 0 & 0 \\ 0 & 0 & 0 & 1/G_{12} & 0 & 0 \\ 0 & 0 & 0 & 0 & 1/G_{13} & 0 \\ 0 & 0 & 0 & 0 & 0 & 1/G_{23} \end{bmatrix}. \quad (20)$$

We assume linear elasticity by setting the Poisson's ratios v_{ij} as constants and the elastic modules E_i and G_{ij} as functions of T and u , but not $\bar{\sigma}$, at least within a range where $\bar{\sigma}$ is "below yield" (we will return to the limits for this linear elastic range later). The thermal expansion coefficient vector is

$$\left(\frac{\partial \bar{\varepsilon}}{\partial T} \right)_{\bar{\sigma}, u} = \bar{\alpha}(\bar{\sigma}, T, u) = (\alpha_1 \quad \alpha_2 \quad \alpha_3 \quad \alpha_4 \quad \alpha_5 \quad \alpha_6)^T, \quad (21)$$

and the moisture expansion coefficient vector is

$$\left(\frac{\partial \bar{\varepsilon}}{\partial u} \right)_{\bar{\sigma}, T} = \bar{\beta}(\bar{\sigma}, T, u) = (\beta_1 \quad \beta_2 \quad \beta_3 \quad \beta_4 \quad \beta_5 \quad \beta_6)^T, \quad (22)$$

where the elements of the vectors are functions of $\bar{\sigma}$, T and u (note that there are no zero elements in these vectors). Now, since $\bar{\bar{F}}$ is not a function of $\bar{\sigma}$, then we may express the $\bar{\sigma}$ dependence of $\bar{\alpha}$ and $\bar{\beta}$ as follows: the order of differentiation when differentiating two times is immaterial, which means that

$$\frac{\partial}{\partial \bar{\sigma}} \left(\frac{\partial \bar{\varepsilon}}{\partial T} \right) = \frac{\partial \bar{\alpha}}{\partial \bar{\sigma}} = \frac{\partial}{\partial T} \left(\frac{\partial \bar{\varepsilon}}{\partial \bar{\sigma}} \right) = \frac{\partial \bar{\bar{F}}}{\partial T} = -\bar{\bar{F}} \bar{\bar{M}}_T \quad (23)$$

$$\text{where } \bar{\bar{M}}_T = \text{diag} \left(\begin{array}{c} \left(\frac{\partial E_1}{\partial T} \right) \\ E_1 \end{array}, \begin{array}{c} \left(\frac{\partial E_2}{\partial T} \right) \\ E_2 \end{array}, \begin{array}{c} \left(\frac{\partial E_3}{\partial T} \right) \\ E_3 \end{array}, \begin{array}{c} \left(\frac{\partial G_{12}}{\partial T} \right) \\ G_{12} \end{array}, \begin{array}{c} \left(\frac{\partial G_{13}}{\partial T} \right) \\ G_{13} \end{array}, \begin{array}{c} \left(\frac{\partial G_{23}}{\partial T} \right) \\ G_{23} \end{array} \right), \quad (24)$$

i.e., a diagonal matrix with the elements shown in (24) on the diagonal. Since $\overline{\overline{F}}$ and $\overline{\overline{M}}_T$ are functions of T and u and not functions of $\overline{\sigma}$, we may integrate (23), and after some manipulation we get

$$\overline{\alpha}(\sigma, T, u) = \overline{\alpha}_0(T, u) - \overline{\overline{F}} \overline{\overline{M}}_T \overline{\sigma} \quad (25)$$

where $\overline{\alpha}_0(T, u) = (\alpha_1^0 \quad \alpha_2^0 \quad \alpha_3^0 \quad 0 \quad 0 \quad 0)^T$ is the (true) thermal expansion coefficient vector at zero stress. In the same way for $\overline{\beta}$ we get

$$\frac{\partial}{\partial \overline{\sigma}} \left(\frac{\partial \overline{\varepsilon}}{\partial u} \right) = \frac{\partial \overline{\beta}}{\partial \overline{\sigma}} = \frac{\partial}{\partial u} \left(\frac{\partial \overline{\varepsilon}}{\partial \overline{\sigma}} \right) = \frac{\partial \overline{F}}{\partial u} = -\overline{\overline{M}}_u \quad (26)$$

where

$$\overline{\overline{M}}_u = \text{diag} \left(\frac{\left(\frac{\partial E_1}{\partial u} \right)}{E_1} \quad \frac{\left(\frac{\partial E_2}{\partial u} \right)}{E_2} \quad \frac{\left(\frac{\partial E_3}{\partial u} \right)}{E_3} \quad \frac{\left(\frac{\partial G_{12}}{\partial u} \right)}{G_{12}} \quad \frac{\left(\frac{\partial G_{13}}{\partial u} \right)}{G_{13}} \quad \frac{\left(\frac{\partial G_{23}}{\partial u} \right)}{G_{23}} \right), \quad (27)$$

i.e., a diagonal matrix with the elements shown in (27) on the diagonal and zeroes elsewhere. Since $\overline{\overline{F}}$ and $\overline{\overline{M}}_u$ are functions of T and u and not functions of $\overline{\sigma}$, we may integrate (26) and get

$$\overline{\beta}(\sigma, T, u) = \overline{\beta}_0(T, u) - \overline{\overline{F}} \overline{\overline{M}}_u \overline{\sigma} \quad (28)$$

where $\overline{\beta}_0(T, u) = (\beta_1^0 \quad \beta_2^0 \quad \beta_3^0 \quad 0 \quad 0 \quad 0)^T$ is the (true) moisture expansion coefficient vector at zero stress. Now, (19) with (20), (25) and (28) gives the incremental form of the linear elastic constitutive relation

$$d\overline{\varepsilon} = \overline{\overline{F}} d\overline{\sigma} + \overline{\alpha}_0 dT + \overline{\beta}_0 du - \overline{\overline{F}} \left(\overline{\overline{M}}_T \overline{\sigma} dT + \overline{\overline{M}}_u \overline{\sigma} du \right), \quad (29)$$

to be compared with the 1-D relation (10). Eq. (29) may be integrated between an initial state (with index 0) and a final state (with no index) as follows:

$$\begin{aligned} \int d\overline{\varepsilon} &= \int \overline{\overline{F}} d\overline{\sigma} + \int \overline{\alpha}_0 dT + \int \overline{\beta}_0 du - \int \overline{\overline{F}} \left(\overline{\overline{M}}_T \overline{\sigma} dT + \overline{\overline{M}}_u \overline{\sigma} du \right) = \\ &= \int d\left(\overline{\overline{F}} \overline{\sigma} \right) + \int \overline{\alpha}_0 dT + \int \overline{\beta}_0 du = \int \left(\overline{\overline{F}} d\overline{\sigma} + d\overline{\overline{F}} \overline{\sigma} \right) + \int \overline{\alpha}_0 dT + \int \overline{\beta}_0 du \end{aligned} \quad (30)$$

which gives the total form of the linear elastic constitutive relation

$$\bar{\varepsilon} - \bar{\varepsilon}_0 = \bar{F} \bar{\sigma} - \bar{F}_0 \bar{\sigma}_0 + \bar{\alpha}_{0m} (T - T_0) + \bar{\beta}_{0m} (u - u_0) \quad (31)$$

where

$$\bar{\alpha}_{0m}(T, T_0, u) = \frac{1}{(T - T_0)} \int_{T_0}^T \bar{\alpha}_0(T, u) dT \quad (32)$$

is the mean thermal expansion coefficient vector at zero stress between T_0 and T . In the same way,

$$\bar{\beta}_{0m}(T, u, u_0) = \frac{1}{(u - u_0)} \int_{u_0}^u \bar{\beta}_0(T, u) du \quad (33)$$

is the mean moisture expansion coefficient vector at zero stress between u_0 and u . If there is a need for a change of reference values or a need to transform between (true) values and mean values for the expansion coefficients, then the same discussion is valid in this 3-D case as for the 1-D case above; i.e., similar equations as (12)–(18), but for the 3-D case, must be used. However, in the following text we assume $\bar{\alpha}_{0m}$ and $\bar{\beta}_{0m}$ to be constant vectors and just call them $\bar{\alpha}_{0m} = \bar{\alpha}_0$ and $\bar{\beta}_{0m} = \bar{\beta}_0$ and use (31) as the total form of the linear elastic constitutive behaviour and (29) as the incremental form.

A simplified form of the constitutive equations can be used when the thermal expansion is assumed to be negligible in comparison to the moisture expansion, but \bar{F} still depends on both T and u . In that case, $\bar{\alpha}_{0m} = \bar{\alpha}_0 = \bar{0}$ and we get

$$d\bar{\varepsilon} = \bar{F} d\bar{\sigma} + \bar{\beta}_0 du - \bar{F} \left(\bar{M}_T \bar{\sigma} dT + \bar{M}_u \bar{\sigma} du \right) \quad (34)$$

as the incremental form of the constitutive equation and

$$\bar{\varepsilon} - \bar{\varepsilon}_0 = \bar{F} \bar{\sigma} - \bar{F}_0 \bar{\sigma}_0 + \bar{\beta}_{0m} (u - u_0) \quad (35)$$

as the total form. These two constitutive equations were used in paper 2 and are used in what follows for the elastic part of the behaviour of the elastic-plastic material. The following theory for elastic-plastic materials was used in paper 4.

3.9.3 Yield limits for a linear elastic 3-D case

A yield limit for 3-D orthotropic materials is assumed to be in the form of a yield function $f = f(\bar{\sigma}, a, b, c, \dots)$ which is = 0 when $\bar{\sigma} = \bar{0}$ and which is = 1 at the yield limit. a, b, c, \dots are a set of coefficients that are evaluated from the experimental yield limits measured with various combinations of stress components. Hill's yield condition (Hill 1948) assumes an orthotropic material that has equal absolute values of the yield limit in 1-D tension and compression; i.e., the yield condition is symmetric for each of the stress

components. It is also assumed that addition of a hydrostatic stress condition will not alter the value of the yield function f , i.e., an assumption that the plastic deformation is incompressible. These assumptions result in

$$f = \sqrt{F(\sigma_{22} - \sigma_{33})^2 + G(\sigma_{33} - \sigma_{11})^2 + H(\sigma_{11} - \sigma_{22})^2 + 2L\tau_{23}^2 + 2M\tau_{31}^2 + 2N\tau_{12}^2}. \quad (36)$$

The root sign is optional, which means that another yield function without the root sign might be used instead and give the same yield limit. A disadvantage with the root sign is that f is undefined if the value under the root sign becomes negative. The 6 coefficients F , G , H , L , M and N are evaluated most easily using 1-D test results for the 6 stress components separately. Hill's yield function is of the polynomial type because the expression under the root sign contains a polynomial of the stress components, which contains no constant term and only some linear and second-order terms due to the assumptions of symmetry and insensitivity to hydrostatic stress.

A general, second-order polynomial function, often called the Tsai-Wu yield function (Tsai & Wu 1971), using all linear and second-order terms is

$$f = f_i\sigma_i + f_{ij}\sigma_i\sigma_j. \text{ (summation on } i \text{ and } j) \quad i, j = 1, 2, 3, 4, 5, 6 \quad (37)$$

This yield function was used in paper 4. Here the denotation is such that $\sigma_4, \sigma_5, \sigma_6$ are the shear stresses $\tau_{12}, \tau_{13}, \tau_{23}$, respectively. f_i and $f_{ij} = f_{ji}$ are coefficients, and this polynomial contains a total of 6 linear and 21 second-order independent terms. From this general equation a number of special cases may be deduced for different kinds of materials. Some or many of the coefficients may be set to zero due to assumptions of, for example, symmetry of yield in tension and compression or other types of restrictions. The remaining coefficients must be experimentally determined by performing 1-D tests, but possibly also by performing 2-D and 3-D tests. A special form of this polynomial function is used in our case (paper 4). It is achieved if we assume symmetry with respect to the sign of the shear-stress components, but no symmetry for the normal-stress components. In that case, all coefficients that have one index equal to 4, 5 or 6 are zero, and we get a total of 12 (3 linear, 6 quadratic and 3 mixed second-order) nonzero terms in (37). With 1-D yield limits (3 shear-stress yield limits, 3 normal-stress yield limits in tension and 3 normal-stress yield limits in compression) we may evaluate 9 material coefficients. They are

$$f_i = -\frac{(\sigma_{isd} - |\sigma_{isc}|)}{\sigma_{isd}|\sigma_{isc}|}, \quad f_{ii} = \frac{1}{\sigma_{isd}|\sigma_{isc}|}, \quad i = 1, 2, 3 \quad (38)$$

and

$$f_{ii} = \frac{1}{\sigma_{is}^2}, \quad i = 4, 5, 6 \quad (39)$$

where σ_{isd} is the yield limit in tension for 1-D loading of stress component i , σ_{isc} is the yield limit in compression for the i :th component of stress and σ_{is} is the yield limit in both tension and compression for 1-D loading of stress components i . The remaining 3 coefficients are f_{12} , f_{13} and f_{23} , which describe the coupling effect between stress components σ_1 , σ_2 and σ_3 with reference to the yield limit. If there is a lack of experimental data, then they may be set to zero, as was the case in paper 4. The ratio

$$\psi = \frac{|\sigma_{isc}|}{\sigma_{isd}} \leq 1, \quad i = 1, 2, 3 \text{ is assumed to be constant.}$$

A simple polynomial form of the yield function is achieved if symmetry is assumed for all stress components, which makes all linear and mixed ($i \neq j$) terms disappear; i.e., $f_i = 0$ for all i and $f_{ij} = 0$ for all $i \neq j$, and we get

$$f = \left(\frac{\sigma_1}{\sigma_{1s}} \right)^2 + \left(\frac{\sigma_2}{\sigma_{2s}} \right)^2 + \left(\frac{\sigma_3}{\sigma_{3s}} \right)^2 + \left(\frac{\sigma_4}{\sigma_{4s}} \right)^2 + \left(\frac{\sigma_5}{\sigma_{5s}} \right)^2 + \left(\frac{\sigma_6}{\sigma_{6s}} \right)^2 \quad (40)$$

where the 6 coefficients have been evaluated, and the six yield stresses are put into the yield function.

3.9.4 Behaviour after yield for a linear elastic-ideally plastic material, 3-D case

Often, it is advantageous to think of $\bar{\sigma}$ as a vector in 6-D space and f as a yield surface in that space, which limits the size of $\bar{\sigma}$ to be within the yield surface (see for example, Lubliner (1990)). The limit for the size of $\bar{\sigma}$ depends on which direction in space $\bar{\sigma}$ has. Yield surfaces in general may be visualized as some kind of distorted “balloons”, “cylinders” or “curtains” that surround the origin of coordinates of a 6-D coordinate system. A yield surface may be closed (i.e., the “balloon” case) but may also be open (i.e., the “cylinder” or “curtain” case) in certain directions in space. The Hill yield surface is open in the directions of an addition of a pure hydrostatic stress, since the yield condition is independent of hydrostatic pressure (or tension). The modified yield surface is a closed ellipsoid in 6-D space with its principal axes along the directions of the individual stress components. The state is elastic as long as $\bar{\sigma}$ is within the yield surface, but eventually, when $\bar{\sigma}$ in a loading scheme touches the surface, then the elastic state is at its limit and yielding may begin or may not begin, depending on what happens in the next loading increment. Since $\bar{\sigma}$ is not allowed to penetrate the yield surface and go into the space on the outside of the yield surface, then we realize that some stress increments are impossible. The only allowable stress increments are those increments that will be such that $\bar{\sigma}$ will decrease and re-enter the elastic space or such that $\bar{\sigma}$ will remain on the yield surface during the increment. If the next increment $d\bar{\sigma}$ is such that the differential

$df = \left(\frac{df}{d\sigma} \right) d\sigma < 0$, then the material point is unloaded elastically into an elastic state. If

the next increment $d\bar{\sigma}$ is such that the differential $df = \left(\frac{df}{d\sigma}\right)d\sigma = 0$, then the next increment is elastic-plastic, and the material point will exhibit a plastic strain increment; i.e., plastic flow will occur. If the next increment $d\bar{\sigma}$ is such that $df > 0$, this will lead to an impossible stress state, since $f > 1$ is not allowed, and thus this $d\bar{\sigma}$ is impossible. This requirement puts restrictions on $d\bar{\sigma}$ and on the plastic strain increment. For an elastic-ideally plastic material, the yield surface is constant and permanently fixed in 6-D space (except for movements due to dependence on T and u). As an example of an impossible loading condition $df > 0$ for an elastic-ideally plastic material, we may think of a situation in 1-D an attempt is made to increase the load in a 1-D tension test when the test piece is already loaded to the yield limit. Clearly, this is an impossible kind of loading, since you can't increase the load on a structure that is already bearing its ultimate load.

3.9.5 Behaviour after yield for a strain hardening linear elastic-plastic material, 3-D case

If the material is linear elastic-plastic and strain-hardening, then the yield surface may move and expand in 6-D space due to plastic flow, and in this case there is no difficulty applying an arbitrary $d\bar{\sigma}$, since the yield surface may move with $d\bar{\sigma}$ or expand in a way such that $\bar{\sigma}$ will still lie on the yield surface at the end of the load increment. Strain hardening can be introduced by assuming that the yield limits that are used to determine the coefficients in the yield function dependent on one or several strain-hardening parameters, such as the effective (or accumulated) plastic strain (Bathe 1982).

In a 1-D monotonic loading case of an isotropic material, the yield limit in tension

depends on the plastic strain, $\sigma_{sd} = \sigma_{sd}^0 + \frac{hE}{(1-h)}\varepsilon^p$ where σ_{sd}^0 is the virgin yield stress, $H = hE$ is the plastic modulus, E is the elastic modulus, h is the ratio between the plastic and elastic modulus and ε^p is the plastic strain (see Fig. 5). For a 3-D situation with an isotropic material, we may define an effective plastic strain.

$$\varepsilon_e^p = \int d\varepsilon_e^p \quad \text{where} \quad d\varepsilon_e^p = \sqrt{\frac{2}{3} d\bar{\varepsilon}^{pT} d\bar{\varepsilon}^p} \quad (41)$$

is the effective plastic strain increment and $d\bar{\varepsilon}^p$ is the plastic strain increment. With these definitions, the plastic work increment during a plastic increment is

$$dW^p = \bar{\sigma}^T d\bar{\varepsilon}^p = \sigma_e d\varepsilon_e^p \quad (42)$$

where σ_e is the effective stress according to von Mises. This definition of the effective plastic strain and its increment is also used below for the orthotropic case. As will be shown below, this procedure will lead to a definition of an effective stress for the orthotropic case.

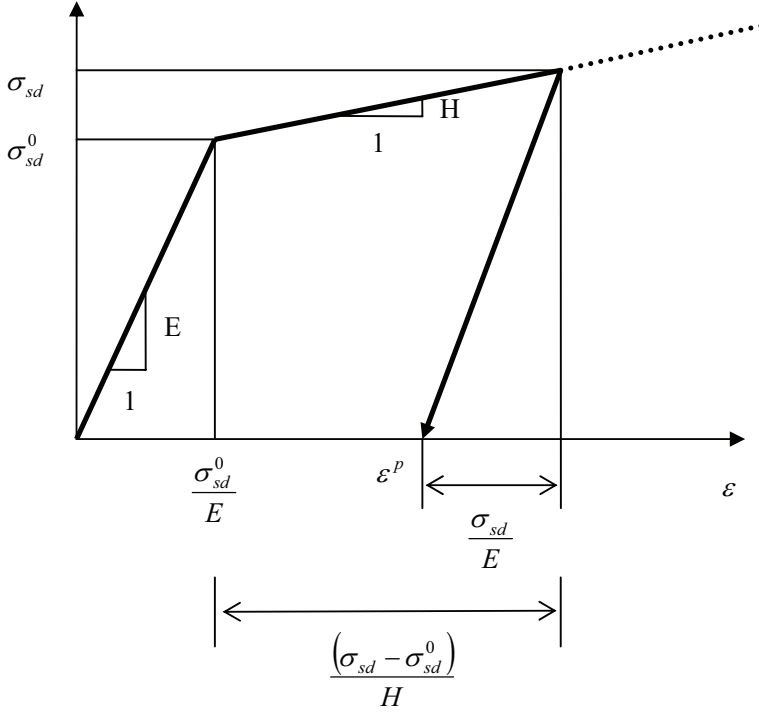


Fig. 5. Stress-strain curve for 1-D loading and unloading of a linear elastic-plastic strain-hardening isotropic material.

For orthotropic materials with equal yield stresses in 1-D compression and tension and equal ratio between the plastic modulus and the elastic modulus for all stress components, we assume a yield stress vector

$$\bar{\sigma}_{sd} = \bar{\sigma}_{sd}^0 + \frac{h}{(1-h)} \bar{E} \varepsilon_e^p \quad (43)$$

where $\bar{E} = (E_1 \ E_2 \ E_3 \ G_{12} \ G_{13} \ G_{23})^T$ is a vector containing the elastic and shear moduli, $\bar{\sigma}_{sd}^0$ is the virgin yield stress vector and h is the ratio between the plastic modulus and the elastic modulus. This defines a sort of orthotropic hardening in which the yield surface expands in all directions (but not equally much in all directions) due to a plastic strain increment at one particular point on the surface. If there are different 1-D yield stresses in compression and tension for the normal stress components, but not for the shear stress components, then

$$\bar{\sigma}_{sdc} = \bar{\sigma}_{sdc}^0 + \frac{h}{(1-h)} \bar{E}_{dc} \varepsilon_e^p \quad (44)$$

where $\bar{E}_{dc} = (E_1 \ E_1 \ E_2 \ E_2 \ E_3 \ E_3 \ G_{12} \ G_{13} \ G_{23})^T$ is a vector containing the elastic and shear moduli and

$\left(\bar{\sigma}_{sdc}^0\right) = (\sigma_{1sd} \ \sigma_{1sc} \ \sigma_{2sd} \ \sigma_{2sc} \ \sigma_{3sd} \ \sigma_{3sc} \ \tau_{12s} \ \tau_{13s} \ \tau_{23s})^T$ is the virgin yield stress vector.

There exists no unambiguous, effective stress measure or effective yield-stress measure for 3-D orthotropic materials. However, we may define an effective yield-stress measure (scalar value) by assuming the same effective plastic strain increment definition as above (41) and by calculating an effective yield stress related to the effective plastic strain increment as

$$\sigma_{es}^a = \frac{dW^p}{d\bar{\varepsilon}_e^p} = \frac{\bar{\sigma}^T d\bar{\varepsilon}^p}{\sqrt{\frac{2}{3} d\bar{\varepsilon}^{pT} d\bar{\varepsilon}^p}}. \quad (45)$$

3.9.6 Linear elastic-plastic behaviour for a 3-D case

Plastic behaviour is path dependent, and there exists no state function to describe the strain as a function of some state parameters. Thus the constitutive equations must be stated in incremental form. At first we separate the total strain increment into elastic and plastic strain increment,

$$d\bar{\varepsilon} = d\bar{\varepsilon}^e + d\bar{\varepsilon}^p, \quad (46)$$

and use (34) for the calculation of $d\bar{\varepsilon}^e$ (note that from now on we use a superindex e on strain to designate elastic strain, a superindex p on strain to designate plastic strain and no superindex to designate total strain). Then $d\bar{\varepsilon}^p$ may be deduced from some experimental observations (“postulates”) about the plastic behaviour. A usual assumption in plasticity theory is that increments of plastic strain are directed perpendicular to the yield surface at the point where the stress vector touches the yield surface and that the yield surface is convex. Both assumptions are due to (Drucker’s) energy postulates (Lubliner 1990; Khan & Huang 1999). If we adopt those postulates we get

$$d\bar{\varepsilon}^p = \lambda \frac{\partial f}{\partial \sigma} \quad (47)$$

where λ is a positive constant that can be determined by using the fact that $df = 0$ during a plastic strain increment.

The yield function f is a function of $\bar{\sigma}$ and the yield stress vector $\bar{\sigma}_{sdc}$. For a strain hardening material, $\bar{\sigma}_{sdc}$ is a function of ε_e^p and quantities that are functions of T and u , and we get $f = f(\bar{\sigma}, \bar{\sigma}_{sdc}(\varepsilon_e^p, T, u)) = f(\bar{\sigma}, \varepsilon_e^p, T, u)$. Then $df = 0$ gives

$$df = \left(\frac{\partial f}{\partial \bar{\sigma}} \right)^T d\bar{\sigma} + \left(\frac{\partial f}{\partial \varepsilon_e^p} \right) d\varepsilon_e^p + \left(\frac{\partial f}{\partial T} \right) dT + \left(\frac{\partial f}{\partial u} \right) du = 0. \quad (48)$$

Now, multiplying (34) with \bar{C} and using (46) and (47) we get

$$d\bar{\sigma} = \bar{C}(d\varepsilon - \lambda \frac{\partial f}{\partial \bar{\sigma}}) + (\bar{M}_u \bar{\sigma} - \bar{C}\beta_0) du + \bar{M}_T \bar{\sigma} dT \quad (49)$$

where $\bar{C} = \bar{F}^{-1}$ is the elastic stiffness matrix. We also have

$$\frac{\partial f}{\partial \varepsilon_e^p} = \left(\frac{\partial f}{\partial \bar{\sigma}_s} \right)^T \left(\frac{\partial \bar{\sigma}_s}{\partial \varepsilon_e^p} \right). \quad (50)$$

The notation $\bar{\sigma}_s$ stands for either $\bar{\sigma}_{sd}$ or $\bar{\sigma}_{sdc}$, depending on which yield function is used, either a yield function with equal or one with differing yield stresses in tension and compression. $\left(\frac{\partial f}{\partial \bar{\sigma}_s} \right)$ can be calculated from the actual yield function, and for the Hill yield function (36) we get for a normal component

$$\frac{\partial f}{\partial \sigma_{1s}} = \frac{(-\sigma_1^2 + \sigma_1(\sigma_2 + \sigma_3) - \sigma_2\sigma_3)}{\sigma_{1s}^3} \quad (51)$$

and for a shear component

$$\frac{\partial f}{\partial \tau_{12s}} = -\frac{\tau_{12}^2}{\tau_{12s}^3}. \quad (52)$$

The other components are achieved by permuting indices. For the Tsai-Wu yield function (37–39) we get

$$\frac{\partial f}{\partial \sigma_{1sd}} = -\frac{1}{2} \frac{\sigma_1}{\sigma_{1sd}^2} \left(1 + \frac{1}{\psi} \frac{\sigma_1}{\sigma_{1sd}} \right) \quad \text{and} \quad \frac{\partial f}{\partial \sigma_{1sc}} = \frac{1}{2\psi^2} \frac{\sigma_1}{\sigma_{1sd}^2} \left(1 - \frac{\sigma_1}{\sigma_{1sd}} \right). \quad (53, 54)$$

The shear-stress components are the same as in (52). All other components are achieved by permuting indices. For the modified yield function we get for all components

$$\frac{\partial f}{\partial \sigma_{1s}} = -\frac{\sigma_1^2}{\sigma_{1s}^3}, \quad (55)$$

and the rest of the components are obtained by permuting indices. From (43–44) we get $\frac{\partial \bar{\sigma}_{sd}}{\partial \varepsilon_e^p} = \frac{h}{1-h} \bar{E}$ or $\frac{\partial \bar{\sigma}_{sdc}}{\partial \varepsilon_e^p} = \frac{h}{1-h} \bar{E}_{dc}$, depending on which yield function is used, and from (41) and (47) we get

$$d\varepsilon_e^p = \sqrt{\frac{2}{3} d\varepsilon^{-pT} d\varepsilon^{-p}} = \sqrt{\frac{2}{3}} \lambda \left| \frac{\partial f}{\partial \sigma} \right|. \quad (56)$$

The third and fourth term of (48) are

$$\frac{\partial f}{\partial T} = \frac{\partial f}{\partial \sigma_s} \frac{\partial \bar{\sigma}_s}{\partial T} = \frac{\partial f}{\partial \sigma_s} \left(\frac{\partial \bar{\sigma}_s^0}{\partial T} + \frac{h}{1-h} \varepsilon_e^p \frac{\partial \bar{E}}{\partial T} \right) \quad (57)$$

and

$$\frac{\partial f}{\partial u} = \frac{\partial f}{\partial \sigma_s} \frac{\partial \bar{\sigma}_s}{\partial u} = \frac{\partial f}{\partial \sigma_s} \left(\frac{\partial \bar{\sigma}_s^0}{\partial u} + \frac{h}{1-h} \varepsilon_e^p \frac{\partial \bar{E}}{\partial u} \right). \quad (58)$$

If the results (49–58) are put into (48) and the equation is solved for λ , we get

$$\lambda = \frac{\left(\frac{\partial f}{\partial \sigma} \right)^T \left(\bar{C} d\varepsilon - \bar{C} \beta_0 du + \bar{M}_T \bar{\sigma} dT + \bar{M}_u \bar{\sigma} du \right) + \left(\frac{\partial f}{\partial \sigma_s} \right)^T \left(\frac{\partial \bar{\sigma}_s^0}{\partial T} + \frac{h}{1-h} \varepsilon_e^p \frac{\partial \bar{E}}{\partial T} + \frac{\partial \bar{\sigma}_s^0}{\partial u} + \frac{h}{1-h} \varepsilon_e^p \frac{\partial \bar{E}}{\partial u} \right)}{\left(\frac{\partial f}{\partial \sigma} \right)^T \bar{C} \left(\frac{\partial f}{\partial \sigma} \right) - h \sqrt{\frac{2}{3}} \left| \frac{\partial f}{\partial \sigma} \right| \left(\frac{\partial f}{\partial \sigma_s} \right)^T \bar{E}} \quad (59)$$

This value of λ may be put into (49), and this defines the incremental constitutive equation for a linear elastic-plastic material as $d\bar{\sigma} = d\bar{\sigma}(d\varepsilon, \bar{\sigma}, T, u)$. However, as we will show below, there is also an alternative, iterative technique to calculate the value of λ and this alternative technique was used in paper 4.

3.9.7 Use of constitutive equations in FEM program

Here is a description of how the constitutive equations derived above are used in the ABAQUS FEM programme. In a nonlinear finite-element program we have on the global structural level the equation

$$\bar{q} = \bar{p} \tag{60}$$

to solve, where \bar{q} is the nodal force vector that is due to the element stresses, also called the inner nodal force vector, and \bar{p} is the (known) vector of applied nodal forces, also called the outer nodal force vector (Bathe 1982; ABAQUS User Manual 2003). Eq. (60) expresses the sought equilibrium between outer applied forces and inner forces due to stresses in the structure. The inner nodal force vector is a nonlinear function of the displacements $\bar{q} = \bar{q}(\bar{\delta})$. Here, $\bar{\delta}$ is the sought vector of unknown node displacements. We use an incremental technique to solve this nonlinear equation, which means that we load the structure gradually in small load increments such that the final load is \bar{p} . Now, in order to create an iterative solution scheme, we reason as follows: Suppose that the true solution $\bar{\delta}^{j-1}$ at load increment $j - 1$ is known; i.e., $\bar{q}(\bar{\delta}^{j-1}) = \bar{p}^{j-1}$. At the next load increment j we must solve the nonlinear system of equations $\bar{q}(\bar{\delta}^j) = \bar{p}^j$ to get the unknown true solution $\bar{\delta}^j$. We calculate an approximation to this true solution by using an iterative Newton-Rhapson method wherein we assume that we know an approximate solution $\bar{\delta}_i^j$ at iteration i at load increment j . The true solution is $\bar{\delta}^j = \bar{\delta}_i^j + \bar{c}^j$ where \bar{c}^j is the unknown (small and exact) correction vector that will give us the true solution $\bar{\delta}^j$. From (60) we have

$$\bar{q}(\bar{\delta}_i^j + \bar{c}^j) - \bar{p}^j = \bar{0}. \tag{61}$$

Eq. (61) may be rewritten as a vector function (a force vector function)

$$\bar{F} = \bar{F}(\bar{\delta}_i^j + \bar{c}^j) = \bar{0}, \tag{62}$$

and this function may be expanded as a Taylor series

$$\bar{F}(\bar{\delta}_i^j) + \left(\frac{\partial \bar{F}_i^j}{\partial \bar{\delta}} \right) \bar{c}^j + \dots = \bar{0}. \tag{63}$$

Excluding the higher order terms we get approximately

$$\left(\frac{\partial \bar{F}_i^j}{\partial \bar{\delta}} \right) \bar{c}_i^j = -\bar{F}(\bar{\delta}_i^j), \tag{64}$$

i.e., a linear system of equations to be solved for an approximate correction vector \bar{c}_i^j at iteration i . Then the next (better) approximate solution is $\bar{\delta}_{i+1}^j = \bar{\delta}_i^j + \bar{c}_i^j$. In that way (64) is solved over and over again in an iterative way until the corrections are small enough. As an initial solution in the first iteration of a load increment, we may use the final solution for the previous load increments, i.e., $\bar{\delta}_1^j = \bar{\delta}_{n^{j-1}}^{j-1}$, where n^{j-1} is the number of iterations performed in the previous load increment $j - 1$. As an initial solution in the first iteration in the first load increment, we may use the zero vector. If the solution does not converge after a reasonable number of iterations, then the current load increment may be decreased and the solution can be restarted in the hope of getting convergence for a smaller load increment. An example of the use of a Newton-Rhapson method for a 1-D example is shown in Fig. 6.

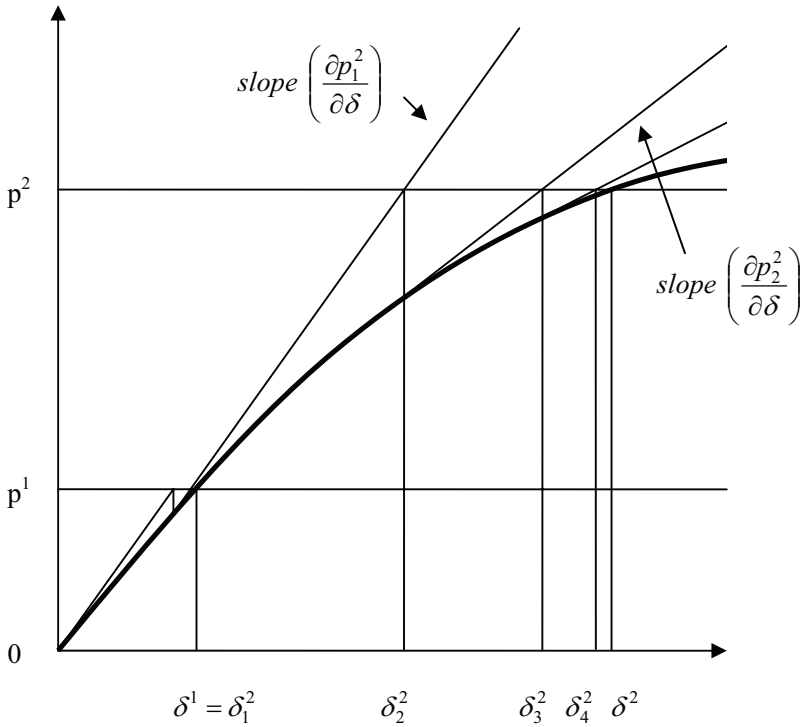


Fig. 6. Newton-Rhapson method used to solve a 1-D equation. Bold line is the unknown sought function $p(\delta)$. Two increments of load p are shown with the solutions δ^1 and δ^2 .

Looking at (64) and the definition of \bar{F} in (61–62) we see that the right hand side of (64) is the unbalance load vector

$$-\bar{F}(\delta_i^j) = \bar{p}^j - \bar{q}_i^j, \quad (65)$$

which expresses the unbalance in equilibrium that is to be reduced to zero. The left hand side is the Jacobian matrix $\left(\frac{\partial \bar{F}_i^j}{\partial \bar{\delta}} \right)$, also called the tangent stiffness matrix, times the

approximate correction vector \bar{c}_i^j . In order to save time and computational effort, it is possible to use a Jacobian matrix that is not the exact one or to choose not to update the Jacobian matrix in every iteration i , but instead to update the Jacobian only at the start of each load increment or after a fixed number of iterations. In that case the convergence may be slower, but still the right solution is found eventually (if the solution converges). Looking at the effects on the constitutive equations of the description above we see that

from the approximate displacement vector $\bar{\delta}_i^j$ we will be able to calculate a corresponding total strain vector with the ordinary displacement to strain equations used in FEM programs. Now, the increment in the total strain vector is the current total strain vector minus the total strain vector in the last but one load increment, and with this total strain increment vector we may use (49) to calculate the corresponding stress increment vector and thus the stress vector. From the stress vector, the corresponding inner nodal force vector may be calculated, which is \bar{q}_i^j in (65). The Jacobian matrix $\left(\frac{\partial \bar{F}_i^j}{\partial \bar{\delta}} \right)$ is the

change of the unbalance load vector with respect to the change of the nodal displacements. The Jacobian matrix can be calculated from the elastoplastic stiffness matrix $\bar{C}^{EP} = \left(\frac{\partial \bar{\sigma}}{\partial \bar{\varepsilon}} \right)_{\bar{\delta}_i^j}$, which is derived from (49) and (59), by putting $du = dT = 0$, as

$$\bar{C}^{EP} = \left(\frac{\partial \bar{\sigma}}{\partial \bar{\varepsilon}} \right)_{\bar{\delta}_i^j} = \bar{C} - \frac{\bar{C} \frac{\partial f}{\partial \bar{\sigma}} \left(\frac{\partial f}{\partial \bar{\sigma}} \right)^T \bar{C}}{\left(\frac{\partial f}{\partial \bar{\sigma}} \right)^T \bar{C} \left(\frac{\partial f}{\partial \bar{\sigma}} \right) - h \sqrt{\frac{2}{3}} \frac{\partial f}{\partial \bar{\sigma}} \left(\frac{\partial f}{\partial \bar{\sigma}_s} \right)^T \bar{E}}. \quad (66)$$

Now, in that way we see that the main FEM equation to solve is (64), and the constitutive equations that are involved are (66) in order to calculate the Jacobian matrix and (49) together with (59) in order to calculate the stress increment $d\bar{\sigma}$ that will arise from a given total strain increment $d\bar{\varepsilon}$.

3.9.8 Iterative procedure for the calculation of λ

Instead of using (59) to calculate λ , we may use an iterative technique. Assume that the state of the material at a certain load increment is calculated. The stress vector is on the yield surface, and we assume that there is going to be plastic flow in the next load increment. In the iterative FEM procedure shown above, we then go on by testing a given strain increment and seek to find out what the resulting stress increment and λ value will be. The solution is the λ value that will make $f = 1$ at the end of the increment. Thus we

may write that $f = f(\lambda) = 1$ is the equation to solve. This equation may be solved numerically with any numerical equation-solving method, e.g., the Newton-Raphson method as described above. In this case we get, at iteration i ,

$$\lambda_{i+1} = \lambda_i - \frac{f(\lambda_i) - 1}{\left(\frac{df}{d\lambda}\right)}. \quad (67)$$

The derivative in the denominator can be calculated numerically by using the two f values that are closest to one. As starting values for the λ iterations we may use any two λ values.

4 Results

4.1 Paper 1: Method to compute fibre directions from computed tomography images

Knowledge of local fibre directions is essential for modelling wood strength and stiffness. The radial, tangential and fibre directions are the orthotropic directions in a point, and they determine in which direction stiffness is high and in which direction stiffness is low. In wood, the fibre direction is the direction of highest stiffness and strength, and the tangential direction is the direction of lowest stiffness and strength. Since the orthotropic directions vary from point to point in a tree and thus also in a board, a nondestructive method to measure orthotropic directions locally at every point in a wood piece is desirable.

A simple and traditional method of measuring fibre direction is by measuring the spiral grain angle by scratching the surface of a log or a board with a needle and measuring the angle between the scratch mark and the pith line (Harris 1989). In a more modern method, a laser light in principle does the same thing as the needle (Nyström 2000) and gives a measure of the spiral grain angle. A theoretical and approximate way of calculating fibre directions is to assume a cylindrical or conical log shape and to calculate the orthotropic directions (see section 3.3) by using the pith line position, the conical angle and the spiral grain angle. However, this method requires several measurements on several radii in order to get the fibre directions throughout the volume of the body, and to attain that we will have to cut up the wood piece, and thus the method becomes a destructive method.

CT is a nondestructive way to measure density inside a wood volume. The resolution in our case was about 0.5 mm in the radial-tangential plane and about 2 mm in the axial direction. Sepulveda, Oja & Grönlund (2002) measured spiral grain angles by using CT images projected on a single radius. They recognized streaks of deviant densities in these images and measured the angle between these streaks and the pith direction and concluded that this was a method to measure spiral grain angle.

Paper 1 describes the theory and test results of another related method to measure the radial, tangential and fibre direction directly, automatically, nondestructively and locally in points inside a wood piece. The method produces the directions from a set of 2-D CT images of a wood piece taken at different axial positions. The method is based on the fact that a spherical body (e.g., a solid ball) with constant density has no preferred directions when it comes to rotational inertia. In other words, such a ball will spin equally easy whatever spin axis we give it. In theoretical terms, this sphere has the same principal moments of inertia around all possible rotation axes through the centre of gravity (the midpoint of the sphere), and there are no unique principal directions. However, if we introduce a streak of material with deviant density through such a ball, then we will get a unique principal direction along the streak of deviant density and a corresponding unique principal moment of inertia with respect to rotation around this principal axis. Thus a calculation of the principal moments of inertia with corresponding principal directions will reveal if there are streaks of density in the sphere and, if so, the directions of these

streaks. Principal moments of inertia and corresponding principal directions (i.e., the principal values) are basic properties of a solid body and easy to calculate.

Thus, for each point in the wood piece, an imaginable sphere was placed and the principal values for this sphere were calculated (see Fig. 7). If the result was that one principal value was unique compared to the other two or all three were unique compared to each other, then one or three streaks of deviant densities existed and had directions along the principal directions, respectively. However, there were things to consider in this process, viz., to determine the radius of the sphere and to decide exactly how much two principal values had to differ in order for them to be considered unique. Also, in practice, there was a question of whether we may get very fluctuating directions from neighbouring spheres that would indicate that the directions of the deviant density streaks did not coincide with the orthotropic directions.

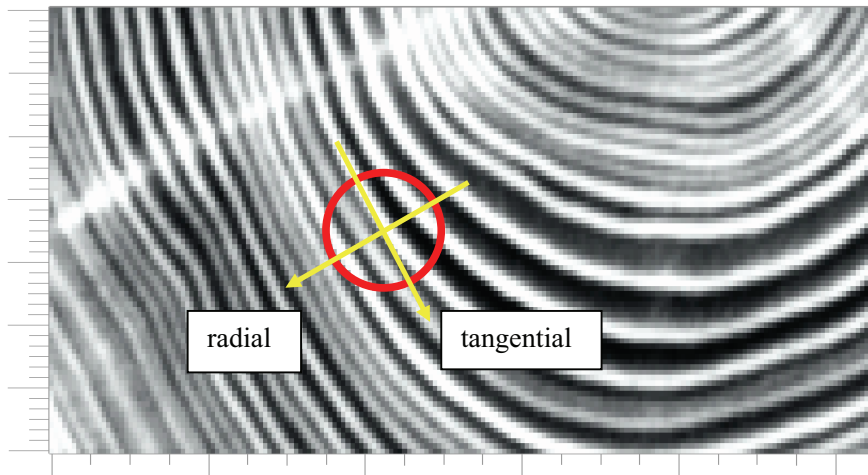


Fig. 7. CT image showing the densities for a section with normal direction approximately in the fibre direction. The circle is a section through the calculation sphere, and the radial and tangential principal directions of inertia are shown with arrows. The third, axial eigenvector points out of the figure in the fibre direction.

Tests of the method were performed on three wood samples. Spiral-grain angles were calculated from the measured orthogonal directions and compared with measured spiral-grain angles with the tracheid-effect method (Nyström 2002). The comparisons showed that there was considerable spread in the output from the method, but that the mean values from a volume in the wood sample agreed with results of the tracheid-effect method. Fig. 8 shows the results for one of these wood samples.

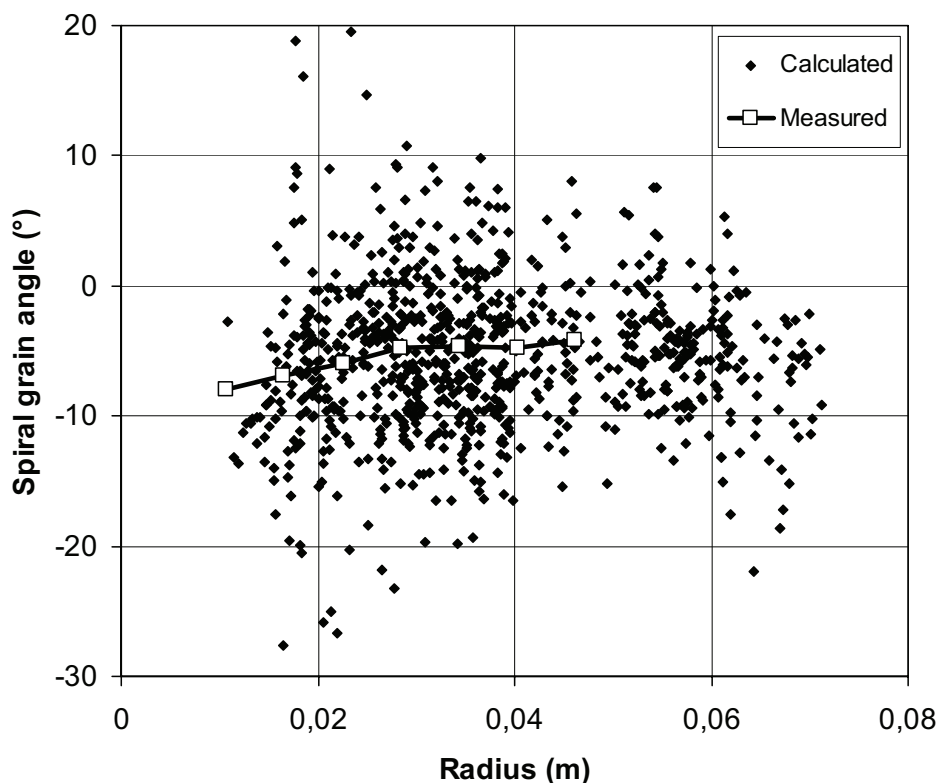


Fig. 8. Calculated spiral grain angle as a function of radius (i.e., distance from pith) for individual spheres compared to values measured with the tracheid-effect method for a dried wood sample made of Norway spruce (*Picea abies*).

The reason for the spread was probably that the method registered deviant density streaks and only indirectly the orthotropic directions. The deviant density streaks may point in various directions, and certainly not in the orthotropic directions, for all calculation spheres, but the results indicate that they point in the orthotropic directions in a mean sense.

The method is valuable for measuring local orthotropic directions in a nondestructive way for dried wood. The drawbacks or limitations with the method as it stands today are the large spread and the fact that the method was only tested on a few dried wood samples. The possibilities or potentials in the future are that the method can be developed and further improved in order to reduce spread and that it may be possible to use the method on green wood as well. This method or variants on it could be used with input data obtained with other methods than CT.

4.2 Paper 2: Twist of wood studs: dependence on spiral-grain gradient

Twist distortion is caused by spiral grain in combination with shrinkage during drying. A formula developed during the late 50s for a thin-walled wooden cylindrical shell (Stevens & Johnston 1960) gives the twist angle φ as a function of the length l and radius r of the cylindrical wood shell, the relative shrinkage s across the grain and the spiral-grain angle θ .

$$\varphi = \frac{l}{r} \frac{2s\theta}{(1+s)}.$$

However, ordinary wood boards do not consist of cylindrical wood shells; they have only parts of growth rings within their cross-sections. A board sawn from the outer parts of a log may have rather flat growth rings with large radii, and the cross-section may only consist of small parts of such growth rings. The growth ring parts that are within a board cross-section may be more or less upright, lying or diagonally situated. This means that Stevens & Johnston's formula can not accurately predict the twist of an ordinary board. It has been used for boards in spite of that, since no other formula for twist of wooden boards has existed before, and since Stevens & Johnston's formula in many cases gives at least an approximate result.

My own early FEM simulations of twist deformation revealed that for a board with a linear relationship between the spiral-grain angle and the radius, for a specific sawing pattern, we had the phenomenon that a board section with left-handed spiral grain throughout the cross-section might twist to the right. This was surprising at first, but I also soon found that there were other FEM results that showed the same tendency (Ormarsson 1999). This phenomenon was in contradiction to Stevens & Johnston's formula, but there seemed to be no explanation of the phenomenon in the literature. In order to explain it, theoretical analyses and corresponding FEM analyses of the twist of a cylindrical shell, a cylinder with and without an axial cut and a thin strip, all made of wood, were performed. The theoretical analyses showed that the twist of a wooden board consisted of two contributions that could be expressed as two terms in a formula:

$$\varphi = -l\Delta w(\alpha_t - \alpha_l) \left(C \frac{2\theta_m}{r_m} + D \left(\frac{d\theta}{dr} \right)_0 \right).$$

In this formula, Δw (< 0 for drying) is the ratio of the change of mass of the moisture to the mass of the dry wood, but only the moisture mass change below FSP is considered. α_t and α_l denote tangential and longitudinal shrinkage coefficients, respectively, and they are defined as relative length change per change in moisture ratio Δw . θ_m is the spiral-grain angle, and r_m is the radius in the middle of the board cross-section. $\left(\frac{d\theta}{dr} \right)_0$ is the gradient of the spiral-grain angle (assumed to be constant in the whole of the log cross-section) and

C and D are two undetermined constants that are positive and of the order of magnitude 1. The formula was explained as follows: at first there is the effect of shrinkage of wooden cylinders or shells in nearly the same way as in Stevens & Johnston's original formula, which results in the first term. The difference compared to Stevens & Johnston's original formula is that the wood cylinders or shells (i.e., the growth rings) are not full or may have axial cuts. Therefore, the first term is about equal to Stevens & Johnston's original formula multiplied with a reduction factor C . Secondly, there is the effect of shrinkage of flat growth rings when there is a spiral-grain gradient in the radial direction. This effect gives a second term that is new and counteracts the first term for an ordinary board (i.e., a board with mean properties), because the second term is proportional to the radial gradient of the spiral-grain angle. A Norway spruce (*Picea abies*) log from Scandinavia normally has a spiral-grain angle that starts left-handed (negative) at the pith, but turns right-handed (positive) with age (Säll 2002). This means that the radial gradient is normally positive in the whole of a log and thus also in a board sawn from a log. The sum of the two terms makes up the total twist of a board, and in this way there is the possibility that a board with a left-handed (negative) spiral-grain throughout the cross-section might twist to the right due to the influence of the second term if the spiral-grain gradient is positive and sufficiently high. The first term dominates for boards that are sawn close to the pith, and the importance of the second term increases with distance to pith.

Linear FEM analyses confirmed that the results of the new formula were accurate and that the constants C and D were 1.05 and 0.48, respectively. However, comparisons with measurements by Trätekt (Anon. 2003) gave C and D as 0.37 and 0.74, respectively. The discrepancy between linear FEM results and Trätekt results showed that nonlinear effects are important for drying wood in practice and that linear FEM analysis is not very accurate. Other measurements that confirm the existence of a second term have also been done (Forsberg & Warensjö 2001) for boards of Norway spruce (*Picea abies*). These measurements showed that among the tested correlations, the correlation was highest for twist versus both gradient of spiral-grain angle and spiral-grain angle. The correlation was lower for twist versus spiral-grain angle alone.

A quick and simple formula for the calculation of twist is useful, since an FEM analysis, which is an alternative, is often time consuming and complicated. An example of use of the formula could be to predict twist after drying for individual boards sawn from a log using measurements of the spiral-grain angle on the outside of the logs or measurements on the sides of the boards. Measurements with the tracheid-effect method (Nyström 2002) can easily and automatically be made on two sides at several points on moving boards. Since different measurement points lie at different distances from pith, it is possible to calculate a value for the gradient of the spiral-grain angle. These measurements and calculations of twist could be done at full production speed.

The formula also gives a way of understanding why twist occurs, what the mechanisms are that give rise to twist. In that way we increase understanding of what the influencing variables are and which variables are most important to change if twist is to be reduced.

4.3 Paper 3: Local water vapour diffusion coefficient when drying Norway spruce sapwood.

The first step in simulating wood-drying deformations is to use a drying model to simulate the drying process (Figs. 1 and 2). A simulation of the drying process for a board gives as output the MC as a function of position and time in the board. The MC can afterwards be used as input to another simulation that gives stresses, strains and deformations in the board as a function of position and time.

Especially the drying sequence below FSP is important for the drying distortions, because shrinkage of wood takes place below FSP. A diffusion model was used here for moisture transport simulations, but required diffusion and mass-transfer coefficients as input, D and β , respectively. In paper 3, CT measurements of MC were made during drying of a sample of Norway spruce (*Picea abies*) sapwood. The diffusion coefficient D and mass-transfer coefficient β were calculated from the experimental MCs, first with a simpler 1-D method and then with a more complex 2-D method. In 1-D, a modified Fick's first law was used for diffusion, and it was stated as

$$g = -D \frac{du}{dx} \quad (68)$$

where $g = g(x, t)$ was the mass flux in the positive x direction per area unit, at position x at time t , $u = u(x, t)$ was the MC at x and t . Mass conservation and Eq. (68) gave

$$\dot{u} = \frac{1}{\rho_0} \frac{d}{dx} \left(D \frac{du}{dx} \right), \quad (69)$$

which was a modified Fick's second law. The general boundary conditions to be used with Eq. 68 and 69 were specified values of u (essential conditions) or g (natural conditions) or $g = \beta(u - u_\infty)$ (convective conditions or mixed conditions) on all or parts of the boundaries. $\rho_0 = \rho_0(x)$ was the dry density of the wood sample, and u_∞ was the EMC for wood in contact with the surrounding air. In 2-D, corresponding diffusion equations were used.

The diffusion coefficient D describes the amount of water that is transported per MC gradient, and the mass-transfer coefficient β describes the amount of water that is transported through a surface per difference in EMC between air and wood surface. In the capillary phase above FSP, there is no shrinkage, and the MC distribution is thus of no importance for the deformations and stresses unless for the influence it has on the MC distribution below FSP, which will eventually follow after the capillary phase. The diffusion model was used here also above FSP as an approximation with a very high moisture diffusion coefficient.

The results for the diffusion coefficient showed at first that use of MC expressed as mass of water divided by mass of dry wood as potential was better than using MC expressed as

concentration (mass of water per volume). The reason for this was that the dry density ρ_0 was not constant, but a function of position x , and because of that the concentration may vary with x , but still not give rise to a mass flux. The result of the comparison between the 1-D and 2-D method was that the diffusion coefficients from the 1-D and 2-D evaluations were nearly equal, but the 2-D method gave less spread. It was also shown that the diffusion coefficients were functions of both MC and depth, i.e., distance to surface when the distance to the surface was less than about 8 mm (Fig. 9).

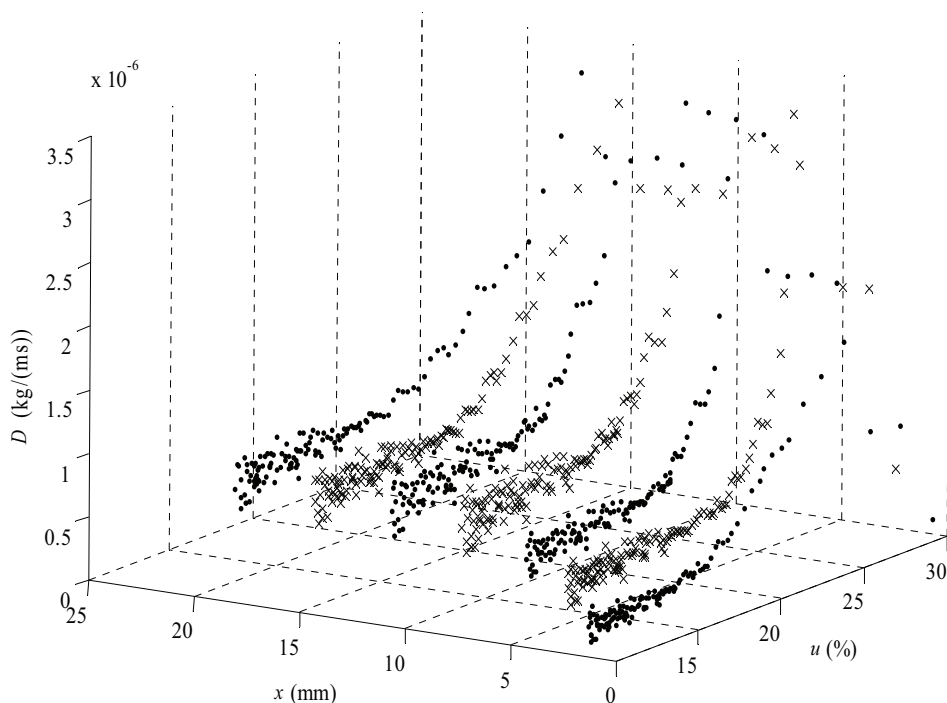


Fig. 9. Measured values of the diffusion coefficient D as a function of depth, i.e., distance to surface, and MC. Evaluated with the 2-D method on a sample of Norway spruce (*Picea abies*).

The dependence of u on D has long been recognized by others, but the influence of depth was new. Some significant change in the way moisture transport takes place near the surface as compared to distant from the surface was indicated by the dependence on depth. The probable or possible causes of this depth dependence may be surface stresses, time dependence or the influence of a dry shell, which has been detected close to the surface (Salin 2002; Wiberg 2001).

The mass-transfer coefficient β was calculated in a number of ways with different assumptions about how to calculate the surface MC (Fig. 10). Surface MC cannot be measured; instead, MC values a bit from the surface were used to calculate or extrapolate

a surface MC. There are different possible ways to do this calculation, and the results of these extrapolations differ.

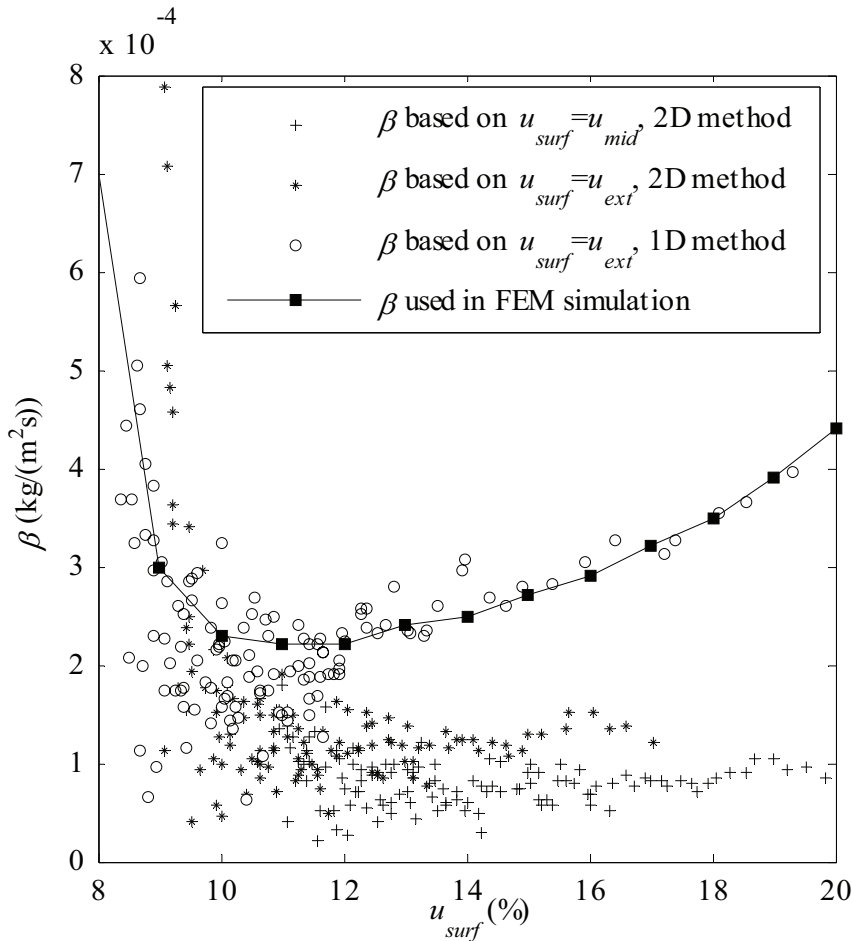


Fig. 10. Measured values of mass-transfer coefficient β as a function of surface MC. Evaluated with 1-D and 2-D methods on a sample of Norway spruce (*Picea abies*). Since surface MC was not measured directly, different alternatives for the extrapolation of measured values to obtain a surface MC are shown. Also shown is the curve that was used in the FEM simulations.

Finally, the evaluated diffusion and mass-transfer coefficients were used in FEM simulations of the original wood-drying experiments, and the MC results from FEM and CT were compared. The comparison showed satisfactory agreement, which indicated that the evaluation methods for D and β worked satisfactory. However, the evaluation was sensitive to errors when MC was measured as a function of time. The spread in D and β increased when MC decreased.

4.4 Paper 4: Modelling of adequate pretwist for obtaining straight timber

Wooden studs warp mainly due to spiral grain, knots and juvenile and compression wood in combination with shrinkage during the drying process. The most unwanted kind of warp is often twist, which is due to spiral grain in combination with shrinkage. A problem for sawmills in Scandinavia is that lack of straightness of wooden studs has resulted in the replacement of wooden studs by steel studs in many applications. In paper 4, FEM simulations were performed in which the twist of boards after drying was the output. The boards were dried with or without restraints and with or without pretwist during drying. The results from FEM and laboratory experiments with the corresponding conditions were first made to agree by adjusting material coefficients in the FEM simulations. Secondly, FEM simulations using the adjusted material coefficients were performed in order to compare twist results after drying with results from an industrial test for boards dried with or without restraint.

The first experiments (Salin et al. 2005; Salin 2005) were performed in the laboratory, where boards were dried without restraints, with fixed restraints or with a pretwisted, fixed position in the opposite direction to the expected twist direction after drying. The results showed that it was possible to counteract the expected twist, totally or to a large extent, with an adequate pretwist in the opposite direction during drying. This was obviously due to a non-elastic, permanent kind of deformation that appeared during drying in a fixed position. A regression analysis of an experiment with 18 centre boards (2X log) fixed during drying with various amounts of pretwist gave as result the twist after drying

$$\rho = 0.510 \cdot \Theta + 0.812 \cdot \rho_p. \quad (70)$$

ρ_p was the pretwist used ($^{\circ}/m$, positive if right-handed) and Θ was the spiral grain angle measured on the board sap side. Fig. 11 indicates the degree of explanation ($R^2 = 0.89$) of Eq. (70) for the 18 boards.

Spiral grain can be measured on the surface of logs or boards automatically during production (Nyström & Grundberg 2002). It is in that way possible to sort out specific logs or boards with respect to the spiral-grain angle. An industrial test (Nyström 2002) showed the relationship between twist after drying, spiral-grain angle on the log surface and layer number in the drying stack. The layer number reflects the fact that the higher the layer number, the higher the load on the board during drying due to the weight of the boards above the board in question. The load on the board affects the degree of restraint on the board such that layer one, on top of the drying stack, has zero load and is thus free and without restraint. A board with a high layer number, for example, 20 or higher, has a high load and is approximately fixed during drying. The results showed that there was a relationship between the variables: twist after drying, spiral grain angle on the log surface and layer number in the drying stack.

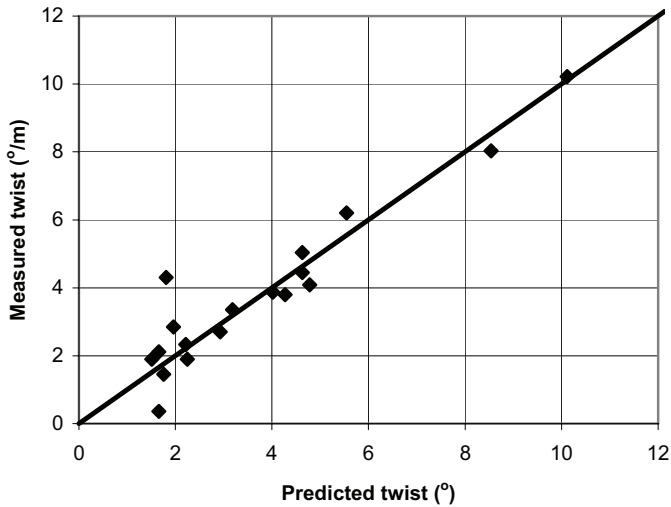


Fig. 11. Measured twist after drying as a function of the predicted twist according to $\rho = 0.510 \cdot \Theta + 0.812 \cdot \rho_p$ [Eq. (70)] for 18 boards of Norway spruce (*Picea abies*) dried with various amounts of pretwist. Line is equal measured and predicted twist.

First, FEM simulations corresponding to the laboratory experiments for 47 x 100 mm boards were performed. The simulations were divided into two steps: first a drying step and second a deformation step using the MC values from the first step as input. A diffusion model was used in the first step, in which the diffusion and mass-transfer coefficients were taken from earlier experiments (paper 3). The second deformation step used an elastic-plastic material model with material coefficients that were dependent on MC and temperature to simulate the material behaviour of the wood (see section 3.9). Permanent deformations were possible due to plastic, permanent strains due to high stresses. The elastic material coefficients were all taken from literature or were estimated based on data in the literature. However, the yield stresses were undetermined at start, but then tried out or determined in a way such that the results from the FEM simulations and the laboratory experiments agreed as much as possible. Fig. 12 shows a comparison between the final FEM results and Eq. (70), which represents the results from the laboratory experiments.

As the second step, FEM simulations corresponding to the industrial test for 38 x 125 mm and 50 x 150 mm boards were performed for fixed restraints and for freely drying boards using the yield stresses that were set in the simulations of the laboratory experiments. The validity of the simulation model could be tested in this way. The results from the FEM simulations and the industrial test results are compared in Fig. 13. There is a discrepancy in level such that the FEM results are higher, but the slopes of the curves agree.

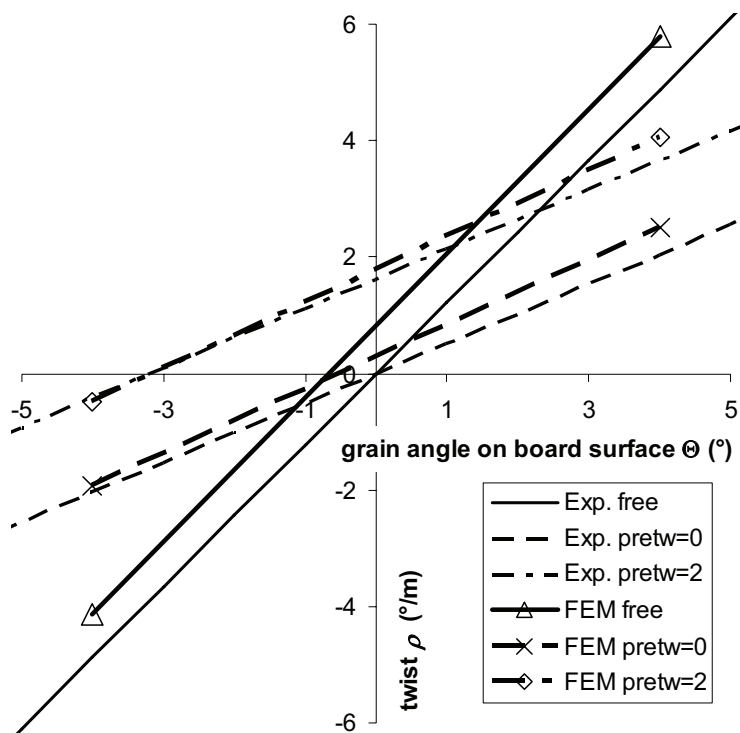


Fig. 12. Twist after drying as a function of spiral-grain angle and amount of pretwist for boards of Norway spruce (*Picea abies*). Experimentally determined and FEM results are shown.

The conclusions were that the simulation model gave a realistic output of permanent deformations, stresses and strains after drying for industrial conditions with no pretwist. Probably this was valid also for the pretwist condition, but that ability was not tested. The discrepancies that occurred between FEM simulation results and industrial test results were probably due to natural spread in the wood material or biased measurements or other uncertainties. Differences between the laboratory experiments and the industrial tests with regard to drying schemes and end restraints could also have influenced the comparison between FEM simulation results and industrial test results. Yield stresses for wood were obtained as a byproduct, but the appropriateness of the yield stresses was uncertain, since no source of corresponding experimentally determined yield stresses was known.

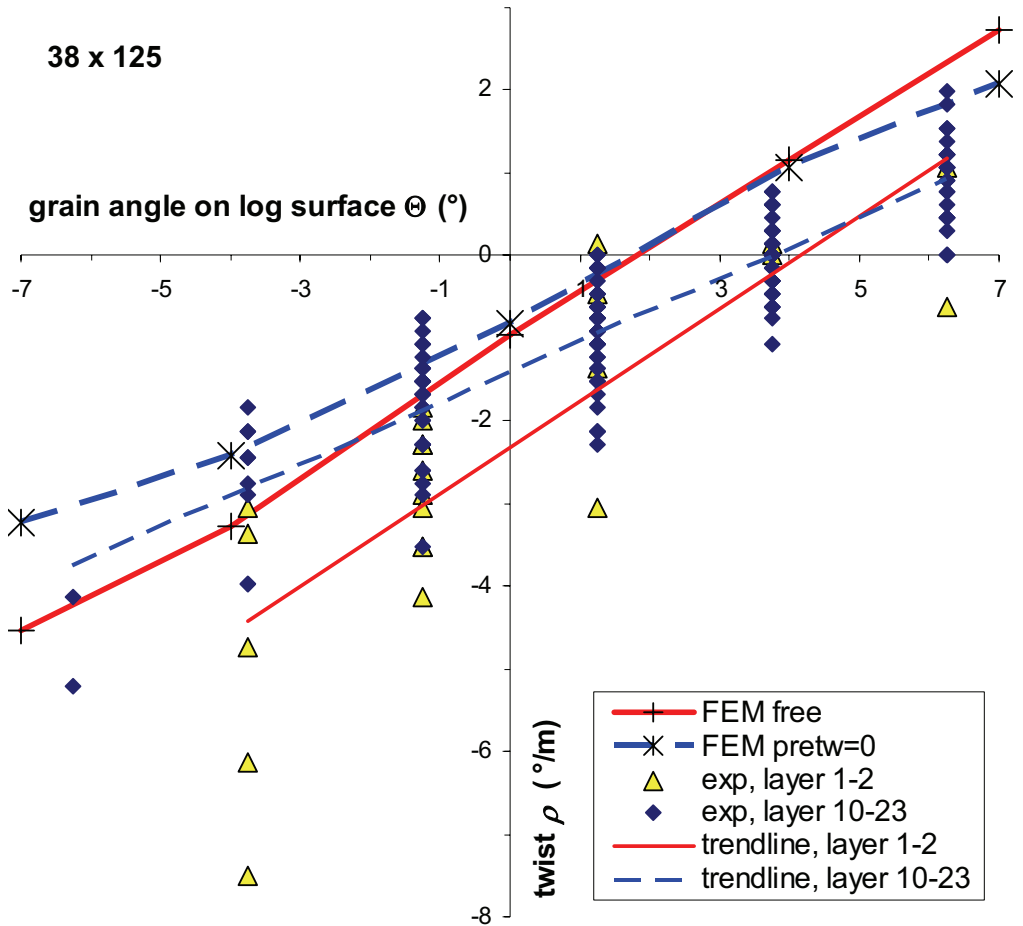


Fig. 13. Twist after drying as a function of spiral-grain angle on log surface for free and fixed boards of Norway spruce (*Picea abies*). From industrial test on 38- x 125-mm boards. Industrial test results and FEM results are shown.

5 Discussion

Practical use of research results for industrial purposes is often the goal of research today, and the procedure for accomplishing that here is described by Fig. 14 in very general terms. The procedure that takes place is a sequence that starts with an observation of the behaviour of wood in some respect, here twisted boards after drying. Then measurements in the laboratory confirm the behaviour, and as the third step the theoretical simulation takes place. From theory and simulations we get knowledge of how to control the behaviour by changing process parameters (here, pretwist during drying), and finally, an industrial implementation may be started. The industrial implementation often consists of measuring some parameters, in this case spiral grain angle, for example, and by controlling the process from that information. Papers 1 and 2 belong to the laboratory measurement phase, paper 3 to the simulation and theory phase and paper 4 to the industrial verification phase of this procedure.

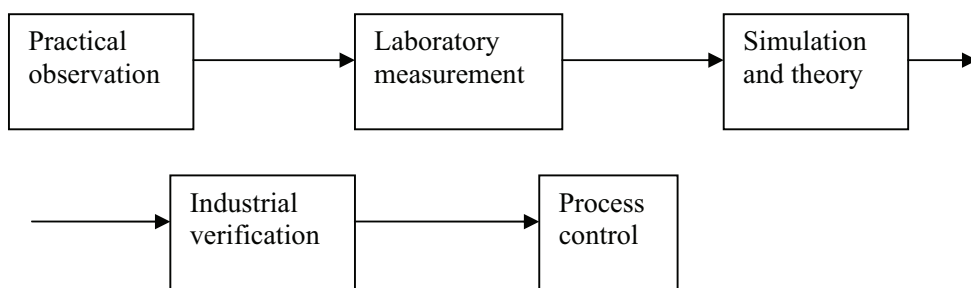


Fig. 14. Practical use of simulation results

The results in papers 2, 3 and 4 have shown that it is possible to realistically simulate wood-drying behaviour by using a FEM simulation technique. The limitations of the simulation model were believed to be the simplified log model and the uncertain material coefficients. Use of measured local fibre directions with the method presented in paper 1 would probably produce a more realistic simulation model. However, this method has not been used yet. For the pole-vaulting simulations, the simulation results have shown that realistic behaviour of a pole and a vaulter in a pole vault can also be simulated in a realistic way. In this case, the limitations lie mainly in the description of the human behaviour and the interaction between vaulter and pole. A FEM simulation is in general a powerful tool and has no limitations when it comes to modelling physical events, provided that a formulation of the problem in mathematical terms is possible.

Material modelling is a complicated issue when it comes to modelling wood behaviour. A homogenous material is a material that is solid with no holes in it but wood is not homogeneous on a microscopic scale. The reason for this is that there are small holes (lumina) within the material that can be filled with air or water or a mixture of air and water. However, the holes are so small that the wood material can often be approximated as homogeneous for a simulation of a piece that contains a large number of cells. The condition for this is that the scale of each lumen has to be much smaller than the scale of

the analyzed structure and the scale of the variation of the load and the results. However, there are cases, e.g., simulations of cutting of wood with a sharp edge, where the loaded part of the body is so small that the cell structure probably influences the results. In such cases, the wood material cannot be regarded as a homogeneous material, and the wood material must be modelled as consisting of only the cell walls. As a consequence, each cell with its cell walls and lumen must be modelled.

Besides from homogeneity there is also a question of whether there is uniformity. Uniformity for a material means that the material has constant properties in the whole of the volume in question. If we assume homogeneity for the wood material, there are many possibilities when it comes to the uniformity, but two extremes can be mentioned. The first, simplest and perhaps least accurate approach, is to model the material as uniform, which means that we use the mean material properties for the whole of the wood material in question. The mean properties are taken from measurements on several, relatively large, real pieces of wood. This will mean that the result of the simulation is valid for a hypothetical wood piece that happens to consist of uniform material with these mean properties. Hopefully, the simulation result will also agree with the mean value of the experimental result for a sufficiently large group of individual wood pieces. The other extreme possibility, which is much trickier, but more accurate, is to model the material as nonuniform. This means that we use the local properties for an individual wood part, and we model the material with varying material properties; i.e., the material properties are described as varying in the volume of the material. In this way the results will be valid for this individual only, and the result is in general not valid as a mean value for a group of wood pieces (unless the individual piece happens to be a “mean” wood piece). As a possibility in between those extremes there is the possibility to model some material properties as uniform and some as varying, e.g., by modelling the stiffness properties as uniform and by modelling the spiral-grain angle as varying with distance from pith.

With regard to modelling varying material properties, there is also a question of what scale of variations is appropriate. Is it appropriate to disregard the variation between growth rings and only model a larger scale variation with, for example, distance from pith? Or is it necessary to model the variation between growth rings or to go to an even smaller scale and model the variation of material properties within each wood cell or fibre? The most extreme method is perhaps to model each cell with its cell walls containing several different layers and to take into account the hollow space inside the cell (lumen). The drawback of going into such extreme detail is that the material properties are hard to determine or measure in small detail and that the FEM model will take a long time to solve, even for a very small model. The answer to the question of what is the best is, of course, that it depends on what you are aiming at, since the output will vary with the same scale as the input data varies. The goal is a model that will yield simulation results that agree with experimental results measured with the resolution that you decide is sufficient.

The wood-modelling problem may be viewed as taking place in a two-dimensional (2-D) model space (Fig. 15). At point A we model the geometry of the wood material as

homogeneous, and we use a local description of material properties; for example, variations of material coefficients between earlywood and latewood in growth rings can be taken into account. At point B we also model the geometry of the wood material as homogeneous, but we use global mean material properties throughout the wood piece. Thus point B is the simpler of the two models A and B. At point C we make a detailed geometrical model of the individual cells in the wood piece and also use a local description of material properties. Thus point C is the most detailed of the models. At point D we make a detailed geometrical model of the individual cells in the wood piece, but we use global mean material properties throughout the wood piece. The closer we get to the origin in Fig. 15, the more accurate is the solution, but the more costly is the simulation. The exact solution for the simulation lies in the origin in Fig. 15, but to reach this point is impossible, since the cost increases with decreasing distance from the origin. The closer we get to the origin, the more refined and detailed experimental results are needed in order to calibrate the model.

In the simulations in this thesis, all wood material models have a large geometrical scale; i.e., we consider the wood material to be continuous, and we do not model individual fibres or cells. For the computer simulation models in this thesis (papers 3 and 4), variation of diffusion coefficient with distance from surface and variation of spiral-grain angle with radius are considered, but other properties are considered to be uniform; i.e., the models can be placed somewhere between A and B in Fig. 15.

There are limitations regarding material models due to the mathematical difficulty in formulating the behaviour of the material coefficients in the state space involved in a simple and efficient way. In simulations of the drying process in wood, the state space of the material coefficients is the space that is spanned by T and u if the material coefficients are assumed to be functions of T and u . Thus the state space is in this case 2-D. The experimental numerical determination of the material coefficients is tedious if the dimension of the state space is two. Extensive testing of the material behaviour or use of other people's experimental data is needed. Often, assumptions or even guesses about material behaviour for the states that are not exactly known or tested need to be made. Thus, compared to other materials such as metals, which have a state space that is 1-D (only T is involved), wood is more difficult to work with. There is also the question of whether there may exist any additional state parameters for wood that would explain the material behaviour, such as the mechanosorptive behaviour, in a better way. This would mean that if the number of state parameters is increased from two to three or more that the amount of testing needed to fully try out the whole state space of the wood material would increase tremendously. On the other hand, a more complex material model could probably better explain unexpected behaviour of wood compared to simpler material models with fewer state parameters.

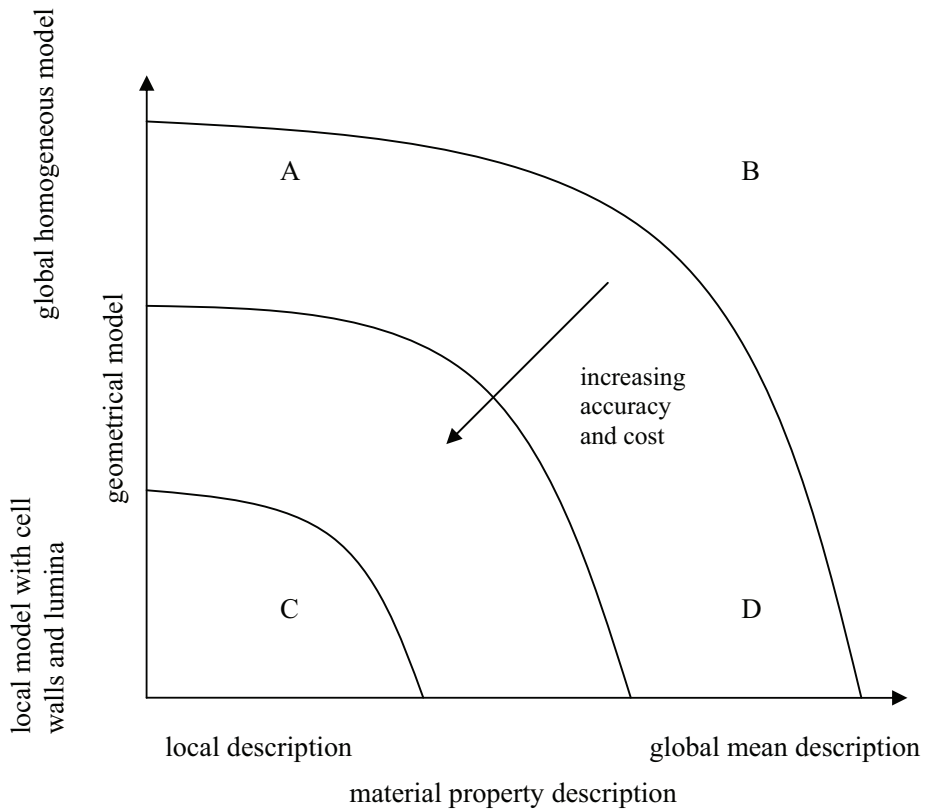


Fig. 15. Two-dimensional description of the material-modelling possibilities for wood. The curved lines represent equivalent accuracy and cost.

The pole-vaulting simulations did not suffer from the same limitations in material modelling as the simulations of wood-drying distortions. The pole material was modelled as elastic, and there was a zero-dimensional state space, since no variation of temperature took place. This means that the determination of the material coefficients was much easier than in the wood-drying simulations. However, the model used for the pole vault simulations suffered, instead, from limitations in the model of the interaction between the human vaulter and the pole. The algorithm that specifies the behaviour of the vaulter in the licentiate thesis was rather crude compared to the real behaviour, which we must assume to be more complex, advanced and intelligent.

The work described in this thesis has shown that FEM is a powerful and useful tool for simulations of wood behaviour due to inner and outer loads. Simulations of this kind are of utmost importance for understanding the mechanisms that give rise to different kinds of wood behaviour. Also the simulations are important for developing new types of improved process control methods in the wood manufacturing industry and for improving design methods for wood structures.

Future work in the subject of wood-drying distortion simulations is needed in order to improve the usefulness of the model. The elastic-plastic material model used in paper 4 worked well and showed that it could be an alternative for modelling drying behaviour of wood alongside other possible models, such as elastic-mechanosorptive models. The log model works well for twist deformations, but if other types of warp are to be simulated, then the introduction of a knot model is believed to be necessary. This knot model would better model the fibre-direction changes around knots that influence crook, for example. Also an increased use of locally varying material coefficients to model juvenile and compression wood, for example, and more use of locally varying fibre directions would be necessary. In addition, measurements of elastic and elastic-plastic material coefficients as function of MC and temperature would improve the validity of the simulation model.

6 References

- Anon. 1999. *Wood Handbook-Wood as an engineering material*. Forest Products Laboratory. US Department of Agriculture.
- Anon. 2001. *Matlab Version 6.1.0.450 release 12.1*. The MathWorks Inc., 3 Apple Hill Drive Natick, MA 01760-2098, USA.
- Anon. 1998. *ABAQUS Theory Manual Version 5.8*. ABAQUS Inc. 1080 Main Street, Pawtucket, USA.
- Anon. 2003. *ABAQUS Users Manual Version 6.4*. ABAQUS Inc. 1080 Main Street, Pawtucket, USA.
- Anon. 2003. *Kontenta 0312045*. Results from Träteknik (the Swedish Institute for Wood Technology Research). In Swedish.
- Anon. 2005. *Effect of top loading on the deformation of sawn timber during kiln drying*. Tronstad, S., ed. Report No. 59. Norsk Treteknisk Institutt, Oslo.
- Armstrong, L. D. and Christensen, G. N. 1961. Influence of moisture changes on deformation of wood under stress. *Nature* 191, 1961:869–870.
- Awadalla, H. S. F., El-Dib, A. F., Mohamad, M. A., Reuss, M. and Hussein, H. M. S. 2004. Mathematical modelling and experimental verification of wood drying process. *Energ. Convers. Manage.* 45:197–207.
- Babeshko, M. E. and Shevchenko, Y. N. 2005. Plastic incompressibility of anisotropic materials. *Int. Appl. Mech.* 41(3):256–263.
- Bathe, K. J. 1982. *Finite element procedures in engineering analysis*. New Jersey: Prentice-Hall Inc.
- Booker, R. M. 2005. Geometric model to predict twist in unrestrained boards. *Wood Sci. Technol.* 39:269–289.
- Buchanan, J. W. 1998. Simulating wood using a voxel approach. *Comput. Graph. Forum* 17(3):105–112.
- Cai, L. and Avramidis, S. 1997. A study on the separation of diffusion and surface emission coefficients in wood. *Dry. Technol.* 15(5):1457–1473.
- Clouston, P. L. and Lam, F. 2001. Computational modelling of strand-based composites. *J. Eng. Mech.* 127(8):844–851.

Clouston, P. L. and Lam, F. 2002. A stochastic plasticity approach to strength modelling of strand-based wood composites. *Compos. Sci. Techno.* 62:1381–1395.

Cook, R. D. 2001. *Concepts and Applications of Finite Element Analysis*. New York: J. Wiley & Sons.

Danborg, F. 1994. Drying properties and visual grading of juvenile wood from fast grown picea-abies and picea-sitchensis. *Scand. J. Forest Res.* 9(1):91–98.

Danvind, J. 2002. *Measuring strain and moisture content in a cross-section of drying wood using Digital Speckle Photography and Computerised X-ray Tomography*. 13th International Symposium on Nondestructive Testing of Wood. 19–21 August, Berkley, California, USA.

Danvind, J. and Morén, T. 2004. *Using X-ray CT-scanning for moisture and displacement measurements in knots and their surroundings*. EU COST 15 Wood Drying Conference Proceedings, April 22–23, Athens, Greece.

Danvind, J. and Ekevad, M. 2006. Local water vapour diffusion coefficient when drying Norway spruce sapwood. *J. Wood Sci* 52:195–201.

DeTeresa, S. J. and Larsen, G. J. 2003. Reduction in the number of independent parameters for the Tsai-Wu tensor polynomial theory of strength for composite materials. *J. Compos. Mater.* 37(19):1769–1785.

Dinwoodie, J. M. 2000. *Timber, its nature and behavior*. London: E & FN Spon.

Eastin, I. L.; Shook, S. R.; Fleishman, S. J. 2001. Material substitution in the U.S. residential construction industry, 1994 versus 1998. *Forest Prod. J.* 51(8) (September):30–37.

Ekevad, M. and Lundberg, B. 1995. Simulation of smart pole vaulting. *J. Biomechanics* 28:1079–1090.

Ekevad, M. and Lundberg, B. 1997. Influence of pole length and stiffness on the energy conversion in pole vaulting. *J. Biomech.* 30:259–264.

Ekevad, M. 2004. Method to compute fiber directions in wood from computed tomography images. *J Wood Sci* 50:41–46.

Ekevad, M. 2005. Twist of wood studs: dependence on spiral grain gradient. *J. Wood Sci.* 51(5) (October):455–461.

Ekevad, M., Salin, J.-G., Grundberg, S., Nyström, J. and Grönlund, A. 2006. Modelling of adequate pretwist for obtaining straight timber. Accepted for publication in *Wood Material Science and Engineering*.

Fatullayev, A. 2001. Determination of unknown coefficient in nonlinear diffusion equation. *Nonlinear Anal.-Theor.* 44(3):337–344.

Fengel, D. and Wegener, G. 1984. *Wood: chemistry, ultrastructure, reactions*. Berlin: de Gruyter.

Foley, C. 2001. A three-dimensional paradigm of fiber orientation in timber. *Wood Sci. Technol.* 35:453–465.

Foley, C. 2003. *Modelling the effects of knots in structural timber*. Doctoral Thesis, Lund Institute of Technology, Report TVBK-1027.

Forsberg, D. 1999. *Warp, in particular twist, of sawn wood of Norway spruce (Picea abies)*. Thesis, Swedish University of Agricultural Sciences, Department of Forest Management and Products, Box 7060, S-750 07 Uppsala, Sweden. Acta Universitatis Agriculturae Sueciae - Silvestria 1999 No. 119.

Forsberg, D. and Warensjö, M. 2001. Grain angle variation: a major determinant of twist in sawn *Picea Abies* (L.) Karst. *Scand. J. Forest Res.* 16:269–277.

Gibson, L. F. and Ashby, M. F. 1988. *Cellular solids-structure and properties*. Oxford, New York: Pergamon Press.

Gjerdrum, P., Säll, H. and Storö, H. M. 2002. Spiral grain in Norway spruce: constant change rate in grain angle in Scandinavian sawlogs. *Forestry* 75:163–170.

Green, D. W., Evans, J. W., Logan, J. D. and Nelson, W.J. 1999. Adjusting modulus of elasticity of lumber for changes in temperature. *Forest Prod. J.* 49(10):82–94.

Grossman, P. U. A. 1976. Requirements for a model that exhibits mechano-sorptive behaviour. *Wood Sci. Technol.* 10:163–168.

Hanhijärvi, A. 2000. Deformation properties of Finnish spruce and pine wood in tangential and radial directions in association to high temperature drying. Part IV. Modelling. *Holz Roh Werk.* 58:211–216.

Hanhijärvi, A. and Mackenzie-Helnwein, P. 2003. Computational analysis of quality reduction during drying of lumber due to irrecoverable deformation. I: Orthotropic visco-elastic-mechanosorptive-plastic material model for the transverse plane of wood. *J. Engrg. Mech.* 129(9):996–1005.

- Hammoum, F. and Audebert, P. 1999. Modeling and simulation of (visco)-plastic behaviour of wood under moisture change. *Mech. Res. Commun.* 26(2):203–208.
- Han, W. and Reddy, B. D. 1999. *Plasticity: mathematical theory and numerical analysis*. Berlin: Springer-Verlag.
- Harris, J. M. 1989. *Spiral grain and Wave Phenomena in Wood Formation*. Berlin: Springer-Verlag.
- Hill, R. 1948. *The mathematical theory of plasticity*. Oxford: Clarendon Press.
- Hoffmeyer, P. and Davidson, R. W. 1989. Mechano-sorptive creep mechanism of wood in compression and bending. *Wood Sci. Technol.* 23(3):215–227.
- Holmberg, S. 1998. *A numerical and experimental study of initial defibration of wood*. Doctoral Thesis. Lund University, Division of Structural Mechanics, Report TVSM-1010.
- Houska, M. and Koc, P. 2000. Sorptive stress estimation: an important key to the mechano-sorptive effect in wood. *Mech. of Time-Depend. Mater.* 4:81–98.
- Hu, W. 2005. An orthotropic yield criterion in a 3-D general stress state. *Int. J. Plasticity* 21:1771–1796.
- Hukka, A. 1999. The Effective Diffusion Coefficient and Mass Transfer Coefficient of Nordic Softwoods as Calculated from Direct Drying Experiments. *Holzforschung* 53:534–540.
- Hukka, A. and Oksanen, O. 1999. Convective mass transfer coefficient at wooden surface in jet drying of veneer. *Holzforschung* 53:204–208.
- Hunt, D. G. 1999. A unified approach to creep of wood. *P. Roy. Soc. Lond. A. Mat.* 455:4077–4095.
- Hunter, A. J. 2001. An analytic model for air drying of impermeable wood. *Wood Sci. Technol.* 34:481–492.
- Johansson, G., Kliger, R., and Perstorper, M. 1994. Quality of structural timber-product specification system required by end-users. *Holz Roh Werk.* 52(1):42–48.
- Johansson, M., Perstorper, M., Kliger, R. and Johansson, G. 2001. Distorsion of Norway spruce timber Part 2. Modelling twist. *Holz Roh Werk.* 59(3) (June):155–162.
- Johansson, M. 2002. *Moisture induced distortions in Norway spruce timber-experiment and models*. Doctoral Thesis, Chalmers University of Technology, Dep. of Structural Engineering Steel and Timber Structures.

Johansson, M. and Kliger, R. 2002. Influence of material characteristics on warp in Norway spruce studs. *Wood Fiber Sci.* 34(2) (April):325–336.

Khan, A. S. and Huang, S. 1995. *Continuum theory of plasticity*. New York: John Wiley & Sons.

Kharouf, N., McClure, G. and Smith, I. 2003. Elasto-plastic modelling of wood bolted connections. *Comput. Struct.* 81:747–754.

Koc, P., Houska, M. and Stok, B. 2003. Computer aided identification of the moisture transport parameters in spruce wood. *Holzforschung* 57:533–538.

Kowalski, S. J. and Musielak, G. 1999. Deformations and stresses in dried wood. *Transport Porous Med.* 34:239–248.

Kramer, E. M. 2002. A mathematical model of pattern formation in the vascular cambium of trees. *J. Theor. Biol.* 216:147–158.

Kramer, E. M. and Borkowski, M. H. 2004. Wood grain patterns at branch junctions: modeling and implications. *Trees* 18:493–500.

Kretschmann, D. E. 1996. Modeling moisture content-mechanical property relationships for clear southern pine. *Wood Fiber Sci.* 28(3)320–337.

Lai, W. M., Rubin, D. and Krempf, E. 1996. *Introduction to continuum mechanics*. Woburn, MA: Butterworth-Heinemann Ltd.

Lindgren, O. 1992. *Medical CT-scanners for Non-Destructive Wood Density and MC Measurements*. Doctoral Thesis, Luleå University of Technology, Thesis No. 1992:111D.

Liu, J. Y., Simpson, W. T. and Verrill, S. P. 2001. An inverse moisture diffusion algorithm for the determination of diffusion coefficient. *Dry. Technol.* 19(8):1555–1568.

Liu, J. Y. and Simpson, W. T. 1999. Two-stage moisture diffusion in wood with constant transport coefficients. *Dry. Technol.* 17(1 & 2):257–299.

Lubliner, J. 1990. *Plasticity theory*. New York: Macmillan.

Mackay, J. F. G. and Rumball, B. L. 1971. Drying of distortion prone juvenile core radiata pine for house studs. *Aust. Timb. J.* 37(6):43–57.

Mackay, J. F. G. 1972. The influence of drying conditions and other factors on twist and torque in *Pinus Radiata* studs. *Wood Fiber Sci.* 4(4):264–271.

- Mackenzie-Helnwein, P., Eberhardsteiner, J. and Mang, H. A. 2003. A multi-surface plasticity model for clear wood and its application to the finite element analysis of structural details. *Comput. Mech.* 31:204–218.
- Mackenzie-Helnwein, P., Eberhardsteiner, J. and Mang, H. A. 2005. Rate-independent mechanical behaviour of biaxially stressed wood: Experimental observations and constitutive modelling as an orthotropic two-surface elasto-plastic material. *Holzforschung* 59:311–321.
- Mackenzie-Helnwein, P. and Hanhijärvi, A. 2003. Computational analysis of quality reduction during drying of lumber due to irrecoverable deformation. II: Algorithmic aspects and practical application. *J. Eng. Mech.* 129(9):1006–1016.
- Malvern, L. E. 1969. *Introduction to the mechanics of a continuous medium*. New Jersey: Prentice-Hall Inc.
- Morén, T. 1993. *Creep, Deformation and Moisture Redistribution During Air Convective Wood Drying and Conditioning*. Doctoral Thesis, Department of Wood Technology, Luleå University of Technology 1993:116D.
- Moses, D. M. and Prion, H. G. L. 2004. Stress and failure analysis of wood composites: a new model. *Compos. Part B-Eng.* 35:251–261.
- Muszynski, L., Lagana, R., Shaler, S. M. and Davids, W. 2005. Comments on the experimental methodology for determination of the hygro-mechanical properties of wood. *Holzforschung* 59:232–239.
- Mårtensson, A. and Svensson, S. 1997. Stress-strain relationship of drying wood. Part 1: Development of a constitutive model. *Holzforschung* 51:472–478.
- Navi, P., Pittet, V. and Plummer, C. J. G. 2002. Transient moisture effects on wood creep. *Wood Sci. Technol.* 36:447–462.
- Northway, R. 1981. *Restraint forces needed to hold radiate pine heart-in studs straight during high-temperature drying*. 20th Forest Products Research Conference, CSIRO, Melbourne.
- Nyström, J. and Hagman, O. 1999. Real-time spectral classification of compression wood in *Picea abies*. *J. Wood Sci.* 45(1):30–37.
- Nyström, J. 2000. Automatic measurement of fiber orientation in softwoods by using the tracheid effect. In *Proceedings of the Fourth International Conference on Image Processing and Scanning of Wood*. 21–23 August, 2000. Mountain Lake, Virginia, USA. Kline, D. E. and Abbott, A. L., eds.

Nyström, J. and Grundberg, S. 2002. *Real-time, noncontact measurement of spiral grain on debarked sawlogs*. Paper presented at The 13th International Symposium on Nondestructive Testing of Wood. 19–21 August 2002. University of California, Berkely Campus, California, USA. Also in Doctoral Thesis 2002:37 Luleå University of Technology.

Nyström, J. 2002. *Automatic measurement of compression wood and spiral grain for the prediction of distortion in sawn wood products*. Doctoral Thesis 2002:37. Luleå University of Technology.

Nyström, J. 2003. Automatic measurement of fiber orientation in softwoods by using the tracheid effect. *Comput. Electron. Agr.* 41(1–3) (December):91–99.

Oller, S., Car, E. and Lubliner, J. 2003. Definition of a general implicit orthotropic yield criterion. *Comput. Methods Appl. Mech. Engrg.* 192:895–912.

Ormarsson, S. 1999. *Numerical analysis of moisture-related distortions in sawn timber*. Doctoral Thesis, Chalmers University of Technology, Dep. of Structural Mechanics.

Ormarsson, S., Dahlblom, O. and Petersson, H. 2000. Numerical study of the shape stability of sawn timber subjected to moisture variation. Part 3: Influence of annual ring orientation. *Wood Sci. Technol.* 34(3) (Oct.):207–219.

Pang, S. 1996. External heat and mass transfer coefficients for kiln drying of timber. *Dry. Technol.* 14(3 & 4):859–871.

Peralta, P. N. and Bangi, A. P. 2003. A nonlinear regression technique for calculating the average diffusion coefficient of wood during drying. *Wood Fiber Sci.* 35(3):401–408.

Plumb, O. A., Spolek, G. A. and Olmstead, B. A. 1985. Heat and mass transfer in wood during drying. *Int. J. Heat Mass Tran.* 28(9):1669–1678.

Ranta-Maunus, A. 1990. Impact of mechano-sorptive creep to the long-term strength of timber. *Holz Roh Werk.* 48:67–71.

Rosenfield, A. R. and Averbach, B. L. 1956. Effect of stress on the expansion coefficient. *J. Appl Phys.* 27(2):154–156.

Rosenkilde, A. and Arfvidsson, J. 1997. Measurement and Evaluation of Moisture Transport Coefficients during Drying of Wood. *Holzforschung* 51:372–380.

Saarman, E. 1986. *Fiberstörningar i trä, neutralisering av hållfasthetsnedsättning, litteraturstudie*. KTH Träteknologi, Rapport 35.

- Salin, J.-G. 1992. Numerical prediction of checking during timber drying and a new mechano-sorptive creep model. *Holz Roh Werk.* 50:195–200.
- Salin, J.-G. 1996. Mass transfer from wooden surfaces and internal moisture non-equilibrium. *Dry. Technol.* 14(10):2213–2224.
- Salin, J.-G. 1997. Letter to the editor. *Dry. Technol.* 15(10):2621–2624.
- Salin, J.-G. 2002. *Theoretical analysis of mass transfer from wooden surfaces.* 13th international drying symposium, Aug. 27–30, Beijing, China.
- Salin, J.-G., Esping, B. and Hajek, B. 2005. *Drying and re-conditioning of pre-twisted boards. Laboratory and Industrial tests.* SP Report 2005:14. Swedish Natinal Testing and Research Institute, Borås, Sweden.
- Salin, J.-G. 2005. Drying of boards, prone to twist, in a pre-twisted position. *Proceedings of the 9th IUFRO wood drying conference.* Nanjing, China, August 21–26:253–258.
- Sehlstedt-Persson, M. 2005. *Properties of Solid Wood.* Licentiate Thesis 2005:70. Luleå University of Technology. Division of Wood Science and Technology.
- Sepulveda, P., Oja, J. and Grönlund, A. 2002. Predicting spiral grain by computed tomography of Norway Spruce. *J. Wood Sci.* 48:479–483.
- Sepulveda, P. 2003. *Non-destructive measurement of spiral grain with computed X-rays in laboratory and in industry.* Doctoral Thesis, Luleå University of Technology, Division of Wood Technology, Skellefteå, Sweden.
- Serrano, E. 2000. *Adhesive joints in timber engineering-modeling and testing of fracture properties.* Doctoral Thesis. Lund University, Department of Mechanics and Materials, ISRN LUTVDG/TVSM—00/1012—SE(1-173), ISBN 91-7874-095-9, ISSN 0281-6679.
- Shigo, A. L. 1988. *A new tree biology: facts, photos, and philosophies on trees and their problems and proper care.* 2nd ed. Durham: Shigo and Trees Assoc.
- Siimes, F. E. 1967. *The effect of specific gravity, moisture content, temperature and heating time on the tension and compression strength and elasticity properties perpendicular to the grain of Finnish pine, spruce and birch wood and the significance of these factors on the checking of timber at kiln drying.* Publication 84, The State Institute for Technical Research, Helsinki, Finland.
- Simpson, W. T. and Liu, J. Y. 1997. An optimization technique to determine red oak surface and internal moisture transfer coefficients during drying. *Wood Fiber Sci.* 29(4):312–318.

- Skatter, S. and Kucera, B. 1998. The cause of the prevalent directions of the spiral grain patterns in conifers. *Trees-Struct. Funct.* 12(5):265–273.
- Sonnen, M. , Laval, C. and Seifert, A. 2003. *New ways in analytical calculation of laminates and composite structures*. Composites 2003, October 2, 2003, Anaheim, California, USA.
- Stevens, W. C. and Johnston, D. D. 1960. Distortion caused by spiralled grain. *Timber Tech.* 68:217–218.
- Svensson, S. and Mårtensson, A. 2002. Simulation of drying stresses in wood. Part II. Convective air drying of sawn timber. *Holz Roh Werk.* 60:72–80.
- Svensson, S. and Toratti, T. 2002. Mechanical response of wood perpendicular to grain when subjected to changes of humidity. *Wood Sci. Technol.* 36:145–156.
- Säll, H. 2002. *Spiral grain in Norway spruce*. Doctoral Thesis, Växjö University 22.
- Söderström, O. and Salin, J.-G. 1993. On determination of surface emission factors in wood drying. *Holzforschung* 47:391–397.
- Time, B. 2002. Studies on hygroscopic moisture transport in Norway spruce (*Picea abies*). Part 2: Modelling of transient moisture transport and hysteresis in wood. *Holz Roh Werk.* 60:405–410.
- Thomas, H. R. 1983. Numerical analysis of drying induced stresses in timber: an orthotropic model. *Mech. Mater.* 2:249–263.
- Thörnqvist, T. 1990. *Juvenile wood in coniferous trees*. The Swedish University of Agricultural Sciences. Report No 10.
- Timoshenko, S. P. and Goodier, J. N. 1970. *Theory of elasticity*. 3rd ed. New York: McGraw-Hill.
- Tsai, S. W. and Wu, E. M. 1971. A general theory of strength for anisotropic materials. *J. Compos. Mater.* 5:58–80.
- Visser, J. J. and Vermaas, H. F. 1988. Steaming under restraint to remove twist in previously dried *Pinus radiata* boards. *Holzforschung* 42(1):59–63.
- Wadsö, L. 1993. Surface mass transfer coefficients for wood. *Dry. Technol.* 11(6):1227–1249.

Wiberg, P. and Morén, T. 1999. New Information on Sapwood Drying: CT-Scanning Profiles of Moisture Content during Drying. *Proc. of the first Wood Drying Workshop in COST ACTION E15*, Edinburgh.

Wiberg, P. 2001. *X-ray CT-scanning of wood during drying*. Doctoral Thesis, Luleå University of Technology, Thesis No.2001:10.

Woxblom, L. 1999. *Warp of sawn timber of Norway Spruce in Relation to End-user Requirements*. Doctoral Thesis, Swedish University of Agricultural Sciences.

Xu, P. 2002. Estimating the influence of knots on the local longitudinal stiffness in radiate pine structural timber. *Wood Sci. Technol.* 36:501–509.

Zienkiewicz, O. C. and Taylor, R. L. 2000. *Finite Element Method*. 5th ed. vol. 1 - *The Basis*. Elsevier.

Zienkiewicz, O. C. and Taylor R. L. 2000. *Finite Element Method* 5th ed. vol. 2 - *Solid Mechanics*. Elsevier.

Öhman, M. 2001. *The Measurement of Compression Wood and Other Features and the Prediction of Their Impact on Wood Products*. Doctoral Thesis 2001:42. Luleå University of Technology.

Öhman, M. and Nyström, J. 2002. Measurement of green plank shape for prediction and elimination of compression wood. *Scand. J. Forest Res.* 17(4):377–384.

Appendices

Paper 1

Mats Ekevad

Method to compute fiber directions in wood from computed tomography images

Received: July 26, 2002 / Accepted: February 10, 2003

Abstract This paper describes a new method, called the CT-direction method, in which the fiber directions in wood in three-dimensional space are calculated from the pixel information on a series of two-dimensional computed tomography images. Local fiber directions are calculated from the principal directions of inertia of measurement spheres distributed throughout the body of the wood object. The calculated fiber directions are probably due to density streaks in the material, such as fiber bundles, which are directed in the fiber direction, and not the density of individual fibers, which are too small to be detected. The fiber directions vary locally, and density streaks from knots, growth rings, and compression wood influence the results, which adds spread to the results. The fiber directions are presented as spiral grain angles and conical angles and are compared with spiral grain angles measured with the tracheid-effect method. The comparisons show that the CT-direction method is a nondestructive way to measure fiber directions locally and in the interior of the body of a piece of wood.

Key words Wood · Fiber direction · Spiral grain · Computed tomography · FEM

Introduction

Computed tomographic (CT) images of the interior of a piece of wood are often easy to understand, as the example in Fig. 1 shows. The pith position, growth rings, knots, areas with compression wood, and juvenile wood can be visually observed as characteristic patterns, streaks, points, lines, or areas in the image. A CT image is a matrix of discrete density values, called pixel values, viewed as a two-

dimensional (2-D) contour plot. The CT scanning process produces a three-dimensional (3-D) description of the density as a series of images with the wood object being translated a bit between each image. The geometric resolution of the image is the pixel size (i.e., the size of the volume for which each discrete density value stands). The pixel values for the series of 2-D images are stored on data files and can be handled with computer programs.

The pith position and the tangential and radial directions of the growth rings can be determined visually from a 2-D CT image of a section perpendicular to the pith direction. However, the fiber directions, which are approximately along the pith direction, are not directly visible. The CT-direction method described in this paper calculates local fiber directions in the body of a wood object from the information in a series of 2-D CT images.

One use for the local fiber directions is for finite element (FE) calculations on wood, for which an orthotropic material model is used. Knowledge of the orthotropic stiffnesses (i.e., the elastic moduli) in the material is required as well as the orthotropic directions themselves (i.e., radial, tangential, and fiber directions). The CT-direction method suggests a new way to achieve local, orthotropic directions for wood to be used for FE calculations. If such local data are used in FE calculations, realistic simulations of drying deformations of real planks are possible; and local crooks, twists, and bows can be simulated.

No other methods to detect 3-D fiber directions automatically in a computer program from CT images are known to the author, although Sepulveda¹ manually measured the spiral grain angle from CT images of a log by creating images on concentric surfaces and recognizing patterns in the images. Investigations of other phenomena in the 3-D interior of wood by CT have also been reported. Bhandarkar et al.² used CT to detect internal log defects and to determine how they are directed. Illman and Dowd³ used 3-D microtomography to obtain spatial information and characterize the structural integrity of wood. Values for the spiral grain angle and older, traditional methods for measuring the spiral grain angle have been reported by Harris.⁴

M. Ekevad (✉)
Division of Wood Technology, Skellefteå Campus, Luleå University
of Technology, Skeria 3, S-931 87 Skellefteå, Sweden
Tel. +46-910-585377; Fax +46-910-585399
e-mail: mats.ekevad@tt.luth.se

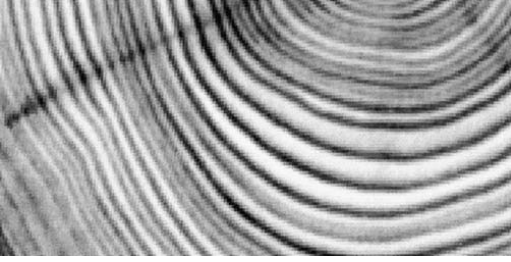


Fig. 1. Two dimensional computed tomography (2-D CT) image of a section through a piece of wood. The densities are in the range of 235 kg/m³ (white areas) to 557 kg/m³ (black areas). Plank E, section 22

Theory

Principal directions

The radial, tangential, and fiber directions are calculated from the principal moments of inertia and the principal directions of fictitious, small (4–15 mm diameter) “measurement bodies” (spheres) that are distributed throughout the inside of the body of the piece of wood. The theory is as follows: The mass center position X_{cg} , Y_{cg} , Z_{cg} of a specific body is

$$X_{cg} = \frac{\int X\rho dV}{\int \rho dV}, \quad Y_{cg} = \frac{\int Y\rho dV}{\int \rho dV}, \quad Z_{cg} = \frac{\int Z\rho dV}{\int \rho dV} \quad (1)$$

where ρ is the density, V is the volume of the body, and X - Y - Z is an arbitrarily placed Cartesian coordinate system. The integrations are performed numerically with the density distribution known at discrete points and interpolated values in between. The mass distribution of the body is described by the moment of inertia tensor

$$\bar{I} = \begin{bmatrix} I_{xx} & -I_{xy} & -I_{xz} \\ -I_{xy} & I_{yy} & -I_{yz} \\ -I_{xz} & -I_{yz} & I_{zz} \end{bmatrix} \quad (2)$$

where

$$\begin{aligned} I_{xx} &= \int_V (y^2 + z^2)\rho dV, & I_{yy} &= \int_V xy\rho dV, & I_{zz} &= \int_V xz\rho dV, \\ I_{yy} &= \int_V (x^2 + z^2)\rho dV, & I_{yz} &= \int_V yz\rho dV, & I_{zz} &= \int_V (x^2 + y^2)\rho dV \end{aligned} \quad (3)$$

and x - y - z is a Cartesian coordinate system that has its origin in the mass center of the body. The principal directions (eigenvectors) and principal values (eigenvalues) for \bar{I} are calculated as the solutions of the eigenvalue problem

$$(\bar{I} - \bar{\lambda}\bar{E})\bar{P} = \bar{0} \quad (4)$$

where $\bar{\lambda}$ is a diagonal matrix containing the three principal values on the diagonal, \bar{E} is the identity matrix, and \bar{P} is a matrix with the three principal directions as column vectors. The principal values are the principal moments of inertia, and the principal directions are the principal directions of inertia.

The three principal moments of inertia are, in general, unequal for a spherical body with an arbitrarily varying mass distribution; as a result, the three principal directions are unique and orthogonal. There are interesting special cases, however, such as the double and triple eigenvalue problem. For a spherical body the geometry in itself does not prefer any direction; consequently, a spherical body with constant density has arbitrarily directed principal directions, and all three principal moments of inertia are equal. In this case we have a triple eigenvalue problem, and the column vectors in \bar{P} are three arbitrary but orthogonal directions.

In the case of two principal moments of inertia being equal we have a double eigenvalue problem, and the principal directions belonging to the double eigenvalues are arbitrarily directed in a specific plane. Thus, \bar{P} contains two arbitrary but orthogonal vectors in the specific plane and one unique column vector normal to the specific plane. Two special cases for wood exemplify the double eigenvalue problems: For a spherical body containing a plane slice or layer of material with a density different from the rest of the body, such as a growth ring layer, the unique principal direction lies in the direction normal to the layer, and the other two directions lie arbitrarily in the plane of the layer. For a spherical body containing a small straight cylinder of material with a density different from the rest of the body, such as a fiber bundle, one principal direction lies in the direction of the small cylinder, and the other two directions lie arbitrarily directed in the plane perpendicular to the first principal direction.

The question of whether a principal direction is unique is, in practice, treated in the following way. The ratios between the eigenvalue in question and the two other eigenvalues are formed; if they differ from 1 by more than ϵ , the eigenvalue in question is unique. The ϵ value is a nondimensional limit defined by the user.

The primary cause of unique principal directions in wood is the growth rings (i.e., density variations in the radial direction). A growth ring is approximately a conical layer in the material that consists of an inner sublayer of earlywood with low density and an outer sublayer of latewood with high density. Growth rings from consecutive years appear in a piece of wood as a series of concentric conical layers. An eigenvalue calculation for a sphere containing such layered material results in three eigenvectors approximately in the radial, tangential, and axial directions of the cone and three corresponding eigenvalues. The tangential and axial eigenvalues may be equal or nearly equal, which indicates that the unique direction is the radial direction and that all vectors lying in the plane spanned by the tangential and axial eigenvectors are eigenvectors. However, if streaks of material with a density different from that of the surrounding material exist and point in the fiber

direction, the axial eigenvector is unique and points in the fiber direction.

There is a need for a statistical averaging procedure when calculating fiber directions because not only fiber bundles influence the density distribution; knots, compression wood, ray cells, and noncircular or markedly curved growth rings affect the calculated directions. Results for individual spheres vary, and it is necessary to take an average over a number of spheres to obtain meaningful results. The pixel size also influences the results and sets a limit for how small the material streaks which are possible to detect may be. The sphere size sets a limit for how large the material streaks (also possible to detect) may be.

For FE purposes it is, in addition to knowing the orthotropic stiffnesses, necessary to know the local material directions; the pith position and spiral grain angle are not interesting in themselves. However, it is interesting to calculate traditional measures such as the spiral grain angle to compare results from the CT-direction method with the results of other methods.

Calculation of fiber angles

The series of 2-D CT images are put in an X - Y - Z Cartesian coordinate system. The X - Y coordinate plane is parallel to the image planes, and Z is the axial coordinate, directed perpendicular to the image planes, approximately along the pith direction. At first the pith positions for all sections are either determined by visual inspection of the images or are calculated by an other method. Here the pith positions are calculated automatically by a method suggested by Ekevad (to be published). The succession of pith positions is a curve in 3-D space, called the pith curve. Approximate radial, tangential, and axial directions are calculated for each sphere from the pith position and the position of the sphere center.

Eigenvectors for all spheres are calculated and sorted in the order radial, tangential, and axial eigenvectors by comparing the eigenvectors with the approximate radial, tangential, and axial directions. The axial eigenvector is assumed to point in the fiber direction and is called $\bar{\psi}$.

The spiral grain angle β and the conical angle φ are calculated by projecting $\bar{\psi}$ on two planes. The first is the tangential plane to the growth ring cone through the point in question, and the second is the pith plane, which is spanned by the pith direction vector \bar{m} and the radius vector \bar{r} , (Fig. 2). The calculations for a sphere with its center point position vector $\bar{x} = (X_{cg}, Y_{cg}, Z_{cg})^T$ are as follows, where \bar{x}_0 is the pith position vector for the section which is closest to the sphere's center point, and \bar{m} is the pith direction vector (directed from the pith position in the current section to the pith position in the next section). The radial vector

$$\bar{r} = \bar{x} - \bar{x}_0 - \left[\bar{m} \cdot (\bar{x} - \bar{x}_0) \right] \bar{m} \quad (5)$$

is the shortest possible vector from the pith curve to the sphere center. The pith plane spanned by \bar{r} and \bar{m} has the normal vector

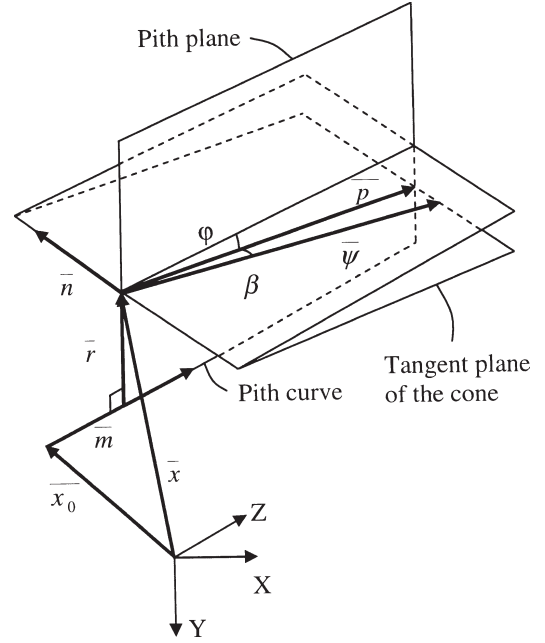


Fig. 2. Geometry in three-dimensional space. The spiral grain angle β and the conical angle φ for a sphere with center point position vector \bar{x} . The pith position vector is \bar{x}_0 , and the pith direction vector is \bar{m} . The radius vector is \bar{r} , and \bar{n} is the normal vector of the pith plane. The eigenvector in the fiber direction is $\bar{\psi}$, and its projection on the pith plane is \bar{p}

$$\bar{n} = \frac{\bar{r} \times \bar{m}}{|\bar{r} \times \bar{m}|} \quad (6)$$

and

$$\bar{p} = \bar{n} \times (\bar{\psi} \times \bar{n}) \quad (7)$$

is the projection of the eigenvector in the fiber direction $\bar{\psi}$ on the pith plane. The conical angle φ where

$$|\varphi| = \arccos(\bar{p} \cdot \bar{m}) \quad (8)$$

is the angle between \bar{m} and \bar{p} . The sign of φ is defined to be positive if

$$\bar{r} \cdot \bar{p} < 0 \quad (9)$$

which means a decreasing growth ring radius with increasing axial coordinate, and negative otherwise. Normally, φ is positive if the positive axial coordinate direction is from the root to the top of the tree. The tangent plane of the cone in the actual point \bar{x} is spanned by \bar{p} and $\bar{\psi}$. The spiral grain angle β , where

$$|\beta| = \arccos(\bar{\psi} \cdot \bar{p}) \quad (10)$$

is the angle between $\bar{\psi}$ and \bar{p} . The sign of β is positive if

$$\bar{\psi} \cdot \bar{n} < 0 \quad (11)$$

which means that a positive twist is right-handed, as in a right-hand threaded screw. Normally, β is negative in the wood objects treated here (i.e., left-handed spiral grain).

Materials, methods, results

The CT images of two planks of Norway spruce (*Picea abies*) from northern Sweden, designated planks D and E with cross sections measuring 85×40 mm and lengths 350 mm were analyzed according to the above procedure. The planks were free from knots in the areas treated but achieved a twist deformation of about 4 degrees/m during the drying process, which indicates that the spiral grain angles were rather large. The distances between the CT images were 2 mm, and the centers of the spheres were evenly distributed over each image area with 1 mm distance between adjacent sphere centers for both planks. The fiber directions β and φ were calculated and are shown in Figs. 3–6 for one axial position in plank D and two axial positions in plank E. Spheres with centers in three to five images were used to calculate the fiber directions for each axial position. Unique eigenvectors in the fiber direction were ensured by setting ε at 0.005 for plank D and at 0.004 for plank E, values that have been used to give low spread in the final results. Sphere diameters were 7 mm for plank D and 4 mm for plank E; the pixel size was 0.4466 mm; and the distances between growth rings were in the range of 1.5–5.0 mm.

The results for β are presented in two alternative ways for plank D in Fig. 3 and for the two axial positions for plank E in Figs. 5 and 6. The first way to present the results is as all but a few of the individual β -values for all the spheres which fulfil the condition for uniqueness of the eigenvector (a few β -values are outside the limits of the diagrams and are not shown). The second way to present the results is as statistical measures for groups of β -values. Here mean-, mid-, lower quartile- and upper quartile-values for β are shown for all spheres which lie in groups with radii 0–10, 10–20 mm and so on. The φ value is shown in Fig. 4 for plank D and only as individual values for each sphere. The angles φ and β are presented as functions of the radius to the pith (i.e., the distance from the sphere center of gravity to the pith).

Measured values of the angle β with the method developed by Nyström⁵ are shown in Figs. 3, 5, and 6 for comparison. These values are measured at a single point on the plank upper side for each radius. The chosen points for measurement are “good” points; that is, no knots or other phenomena are visible near the points.

Discussion

Figures 3, 5, and 6 show the variation in spiral grain angles between the individual spheres in the three test cases. There is significant spread in the results for individual spheres,

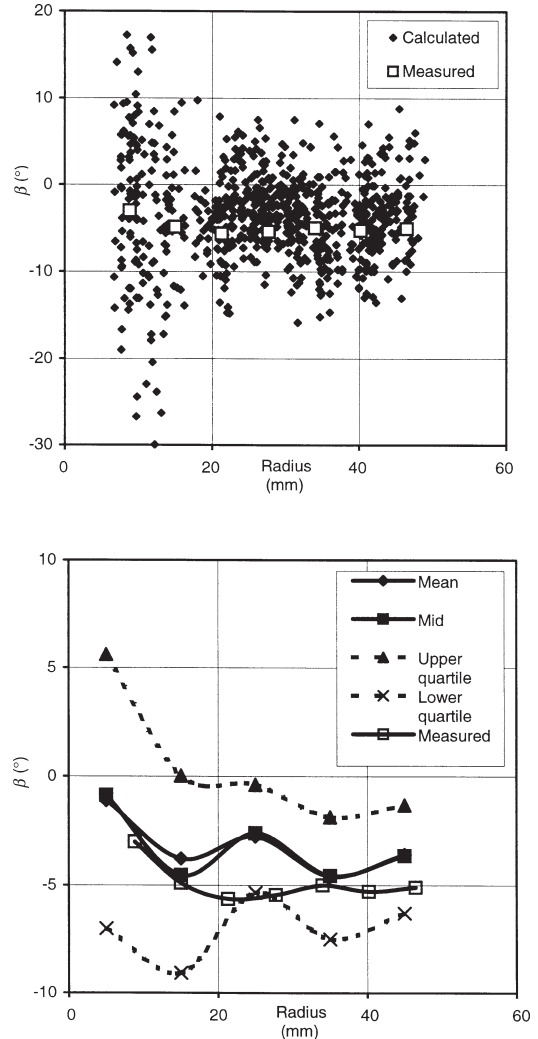


Fig. 3. Calculated spiral grain angle β for the spheres in sections 3–7 in plank D as a function of the radius from the pith. The factor ε is 0.005, which gives 792 unique angles from a total of 9990 spheres. Spiral grain angle β was measured by the tracheid-effect method by Nyström.⁵ The mean, mid, lower quartile, and upper quartile values for the data were collected from five groups with radii of 0–10, 10–20, 20–30, 30–40, and 40–50 mm

and a possible explanation is as follows: The CT-direction method detects directions in the density distribution in the piece of wood, directions that are due to systematic density variations. The pixel size used here is not small enough to capture density variations between individual fibers; it probably captures density variations due to bundles of fibers and other density streaks that follow the fiber direction. However, the density variations, which reveal the fiber directions, are not particularly significant compared to

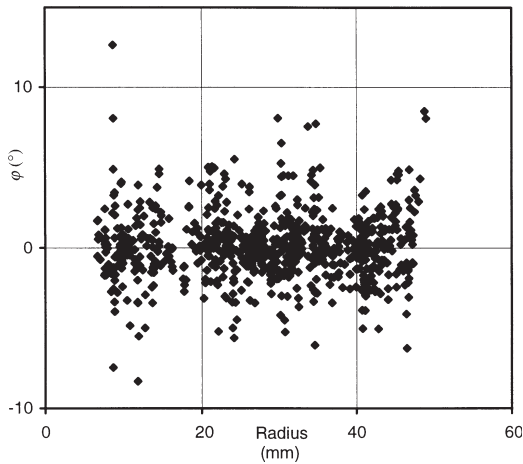


Fig. 4. Conical angle φ for the same spheres as in Fig. 3 as a function of the radius from the pith

other causes of density variations, such as knots, growth rings, and compression wood. Therefore, the calculations of spiral grain angles and conical angles have a significant spread, and statistical treatment of the results from many individual spheres is needed.

The mean and mid values in Figs. 3, 5, and 6 agree well with the results from the tracheid-effect method of Nyström.⁵ The spiral grain angles are rather large (about 5 degrees left-handed), as would be expected from the large twists of the planks that occur during the drying process. The conical angle φ is about 0 degrees/m (Fig. 4), a value that seems reasonable for the short (<10 cm) axial lengths studied, although no other data are available for comparison.

It is found, in general, that the spread decreases if spheres from more than one image are combined because the increased number of spheres gives a more reliable statistical evaluation. However, the spreads are increased if more than about three to five images are grouped together which indicate that the fiber directions (or the possibility of detecting fiber directions), vary in the axial direction of the planks. Also, certain images give more spread than others: compare Figs. 3 and 6, which indicate that certain sections of the planks contain fewer or smaller fiber bundles, which are more difficult to detect than those in other sections. The spread is generally larger for small radii than for large radii (Figs. 3, 5). Part of that spread is due to the fact that small errors in the pith position or in the fiber angles influence the calculation of spiral grain angles for small radii more than for large radii.

The figures describe the angles β and φ as functions of the radial coordinates, as they are usually described. Generally, however, there are also variations in the tangential direction, in the axial direction, and around knots, which cause part of the spreads in the figures.

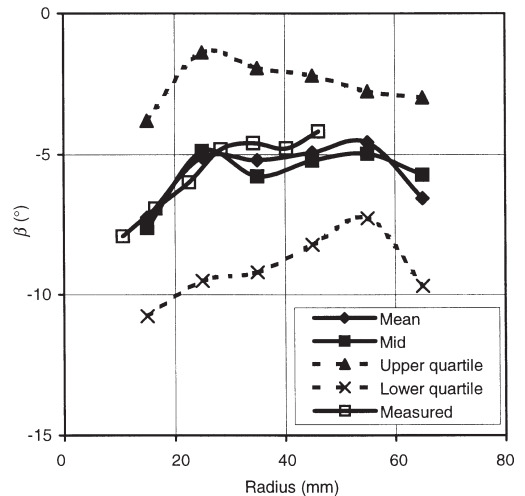
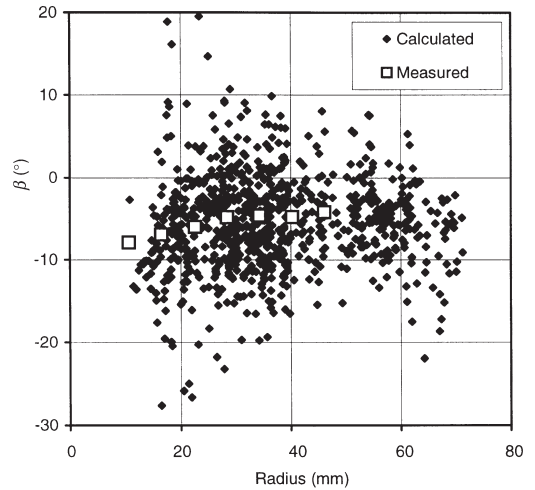


Fig. 5. Calculated spiral grain angle β for the spheres in sections 10–12 in plank E as a function of the radius from the pith. The factor ε is 0.004, which gives 858 unique angles from a total of 8160 spheres. Spiral grain angle β was measured by the tracheid-effect method by Nyström.⁵ The mean, mid, lower quartile, and upper quartile values for the data were collected from six groups with radii of 10–20, 20–30, 30–40, 40–50, 50–60, and 60–70 mm

The sphere size and the pixel size determine the size of the density streaks, which are possible to detect. Decreased sizes make it possible to detect smaller density streaks. The sphere sizes used here, 4 and 7 mm, were used to give as small a spread as possible, and they worked about equally well for planks D and E. The pixel size used was as small as possible with the available CT scanner.

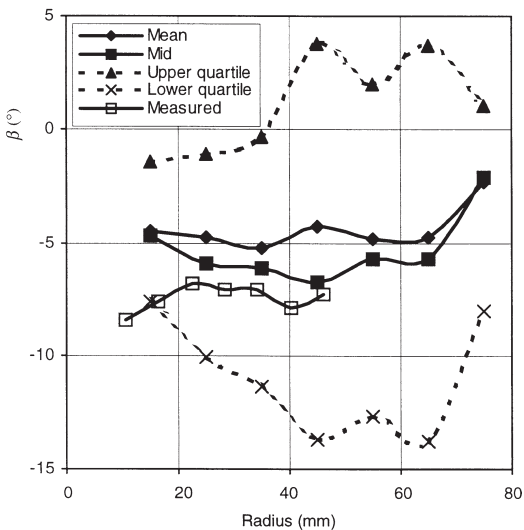
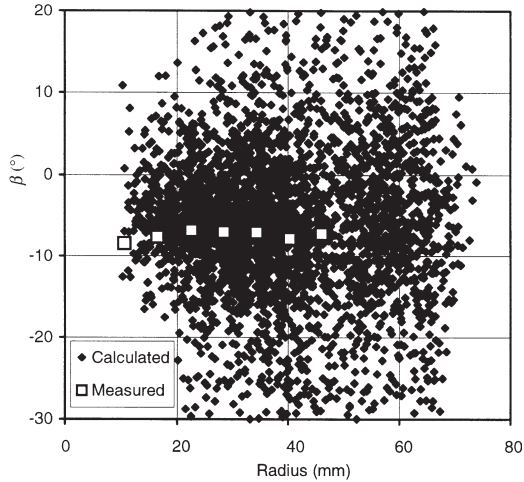


Fig. 6. Calculated spiral grain angle β for the spheres in sections 20–24 in plank E as a function of the radius from the pith. The factor ϵ is 0.004, which gives 2414 unique angles from a total of 13600 spheres. Spiral grain angle β was measured by the tracheid-effect method by Nyström.⁵ The mean, mid, lower quartile, and upper quartile values for the data were collected from seven groups with radii of 10–20, 20–30, 30–40, 40–50, 50–60, 60–70, and 70–80 mm

Conclusions

The results presented in this paper show that the axial eigenvector, if it is unique, points in the fiber direction in an average sense. Thus, the CT-direction method works and can be used to detect local fiber directions for various purposes (e.g., for FE calculations). It is also possible to use the method to obtain 3-D density data, which are measured with methods other than CT. Further work, such as investigations of the influence of the pixel size of the tomograph, could improve the CT-direction method.

Acknowledgment I thank Formas (the Swedish Research Council for Environment, Agricultural Sciences and Spatial Planning) for their support.

References

1. Sepulveda P (2000) Non-destructive measurement of spiral grain with computed tomography. Licentiate thesis, Luleå University of Technology, Division of Wood Technology, Skellefteå, Sweden
2. Bhandarkar SM, Faust TD, Tang M (1999) Catalog: a system for detection and rendering of internal log defects using computer tomography. *Machine Vis Applications* 11:171–190. Springer-Verlag, Berlin Heidelberg
3. Illman B, Dowd B (1999) High-resolution microtomography for density and spatial information about wood structures. In: *Proceedings of SPIE – The International Society for Optical Engineering*, v3772: *Proceedings of the 1999 developments in X-ray tomography II*, Denver, pp 198–204
4. Harris JM (1989) *Spiral grain and wave phenomena in wood formation*. Springer-Verlag, Berlin Heidelberg
5. Nyström J (2000) Automatic measurement of fiber orientation in softwoods by using the tracheid effect. In: Kline DE, Abbott AL (eds) *Proceedings of the fourth international conference on image processing and scanning of wood*, Mountain Lake, VA

The publication of this article was made possible by an Emachus Research Fund. The author is grateful for the fund.

Paper 2

Mats Ekevad

Twist of wood studs: dependence on spiral grain gradient

Received: April 5, 2004 / Accepted: September 8, 2004

Abstract Distortions due to moisture changes during drying or in service are a major problem for construction timber. Twist, caused mainly by the cylindrical geometry, the orthotropic nature of the wood material, and the tendency of the wood fibers to grow in a spiral around the stem, is often regarded as the most detrimental distortion of sawn timber. There is a need for a basic mechanical understanding of how the twist distortion arises and also a need for a simple formula to predict the amount of twist distortion. In this article such a formula is proposed, and theory and experimental data that indicate the validity of the formula are shown. The first term in the formula is a modification of a traditional expression which is proportional to the mean value of the spiral grain angle in the cross section in question. The second term in the formula is new and is proportional to the gradient of the spiral grain angle, and this term normally counteracts the first term so that a stud with a left-handed spiral grain might achieve a right-handed twist. Linear elastic finite element method (FEM) results and comparisons with experimental data show that the formula works well and that linear FEM calculations exaggerate the twist, which is probably partly due to nonlinear effects. The formula could be used to predict the twist of sawn timber from measured spiral grain angles on the log surface.

Key words Wood · Spiral grain · Grain angle · Twist · FEM

Introduction

The goal of the sawmill industry is to produce straight sawn timber to be used as building material. Thus, distortions due to moisture changes during drying and during service are a

major problem for construction timber. Distortion is divided into crook, bow, cup, and twist, although twist is often regarded as the most detrimental distortion. The causes of distortions are mainly the cylindrical geometry caused by the growth rings and the orthotropic nature of the wood material, i.e., varying shrinkage and elasticity in the radial, tangential, and longitudinal directions. Twist is mainly caused by the tendency of the wood fibers to grow in a spiral around the stem, which causes the sawn and dried timber to twist. Knots and other kinds of local fiber variations also influence distortion to a great degree.

Spiral grain angle can be measured in studs and in logs with older manual methods¹ or automatically² or by computerized means.³ Measurements of spiral grain angle and its correlation to twist angle and other parameters, such as distance from pith, log diameter, compression wood, and growth conditions, have been made by many researchers. Sawn timber in general is a material with varying properties due to circumstances such as the different growth conditions of individual trees, and statistical methods must be used in order to handle the large spread in the measured data. Nyström² has measured twist angle and spiral grain angle on log surfaces and found a strong correlation. Forsberg and Warensjö⁴ have found that the spiral grain angle on a log surface and the slope of the spiral grain angle curve are strongly correlated to twist angle. Säll⁵ and Johansson et al.⁶ have measured twist and spiral grain angle in different ways and found correlation. Older experimental results are described by, among others, Forsberg and Warensjö.⁴ Ormarsson et al.⁷ have calculated twist distortions for sawn timber using finite element methods (FEM).

Even though FE calculations can give detailed information about drying distortions such as the twist of sawn timber, there is a need for a basic mechanical understanding of the cause of twist distortion, and, preferably, a simple formula to make rapid calculations and predict twist distortions. Until now, the formula

$$\varphi = \frac{l}{r} \frac{2s\theta}{(1+s)} \quad (1)$$

M. Ekevad (✉)
Division of Wood Technology, Skellefteå Campus, Luleå University
of Technology, Skeria 3, S-931 87 Skellefteå, Sweden
Tel. +46-910-585377; Fax +46-910-585399
e-mail: mats.ekevad@ltu.se

derived in the late 1950s by Stevens and Johnston⁸ has often been used to calculate twist distortions. The formula is valid for the twist angle φ of a thin-walled cylinder of wood with the center axis along the pith axis, length l , radius r , thickness t , where $t \ll r$, spiral grain angle θ , and the relative shrinkage s across the grain. In spite of the formula's validity only for thin cylinders of wood, it is also often used for the prediction of all sorts of twist in sawn timber. In these cases the distance from the pith to some point in the cross section in question, e.g., the middle point, is used as the "mean" radius r in the formula.

In this article, the shortcomings of using Eq. 1 for calculating theoretical twist angles for sawn timber are discussed, and a new formula is proposed where the spiral grain angle and the gradient of the spiral grain angle with respect to the radius and the distance to pith are included. A physical explanation and motivation for the terms in the formula are given, as are FE calculations and measurements which justify the modified formula.

Theory

Twist of a thin-walled cylinder

A thin-walled cylinder (cf. a single growth ring) is considered (see Fig. 1). The length is l , the radius is r , the spiral grain angle is θ (>0 for right-handed spiral grain), and the shrinkage coefficients are α_t in the cross-fiber direction and α_l in the fiber direction. The wall thickness is negligible compared to the radius, and the shrinkage coefficients are defined as relative length change per change in moisture ratio Δw . Δw (<0 for drying) is the ratio of the change of mass of the moisture to the mass of the dry wood, but only the moisture mass change below the fiber saturation point is considered. A fibre coordinate system r - t - l is defined for a point on the cylinder surface in the radial, tangential, and

fiber directions and a cylinder coordinate system x - y - z is defined along the radial, tangential, and axial directions. Presuming we have no stresses, the normal strains due to Δw are $\epsilon_r = \alpha_t \Delta w$ and $\epsilon_l = \alpha_l \Delta w$. After a rotation θ in the t - l plane, by using Mohr's strain circle, we get

$$\epsilon_y = \alpha_t \Delta w, \epsilon_z = \alpha_l \Delta w, \gamma_{yz} = -2\Delta w(\alpha_t - \alpha_l)\theta, \tag{2}$$

where it is assumed that θ is small. The strains ϵ_y and ϵ_z represent changes in circumference and length of the cylinder, respectively, and the shear strain γ_{yz} leads to a twist of the cylinder. From the elementary theory of torsion of circular shafts (e.g., see Timoshenko and Goodier⁹) we have the kinematic relation

$$\gamma_{yz} l = \varphi r \tag{3}$$

where φ is the twist angle of the cylinder (>0 for right-handed twist). Eliminating γ_{yz} with Eqs. 2 and 3 we get

$$\varphi = -\frac{l}{r} 2\Delta w(\alpha_t - \alpha_l)\theta \tag{4}$$

which is essentially the same formula as that of Stevens and Johnston⁸ if $-\Delta w\alpha_t$ is replaced with s and α_l is set to zero. Because $\alpha_t > \alpha_l$, drying ($\Delta w < 0$) will give φ the same sign as θ , i.e., a right-handed spiral grain will result in a right-handed twist and vice versa. The twist distortion appears without stresses.

Twist of a circular, thick, solid cylinder

Here we disregard radial shrinkage and approximate a solid cylinder with outer radius r_y as a set of concentric thin-walled cylinders with varying radii coupled in parallel via end torques. Each thin-walled cylinder has the same shear modulus and is able to twist due to the end torques. The spiral grain angle is considered a function of the radius, $\theta = \theta(r)$. We use the condition that the angle of twist is equal and that the resulting torque is zero from all the thin-walled cylinders and we get the twist angle

$$\varphi = -\frac{l}{r_y^4} 8\Delta w(\alpha_t - \alpha_l) \int_0^{r_y} \theta r^2 dr. \tag{5}$$

If θ is constant and not a function of the radius, then using Eq. 5 we find that Eq. 4 can be used for a solid cylinder if $r = r_m = 3r_y/4$ is used as a "mean" radius in Eq. 4. If $\theta(r)$ is a linear function

$$\theta(r) = \theta_0 + \left(\frac{d\theta}{dr}\right)_0 r \tag{6}$$

where $\left(\frac{d\theta}{dr}\right)_0$ is the (constant) gradient of the spiral grain angle function, then using Eq. 6 in Eq. 5 we conclude that Eq. 4 gives the same result as Eq. 5 if "mean" values $r = r_m = 3r_y/4$ and $\theta = \theta_m = \theta(3r_y/4)$ is used in Eq. 4. In this case the resulting twist distortion creates self-equilibrating shear

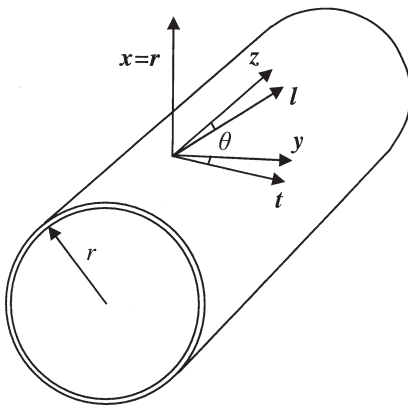


Fig. 1. Thin-walled cylinder with radius r , length l , and spiral grain angle θ

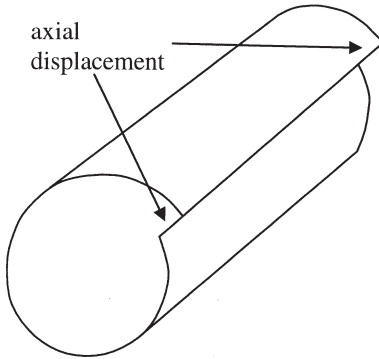


Fig. 2. Warp of a thin-walled cylinder with an axial cut exposed to a shear strain γ_{yz}

stresses in the cylinder, but the twist angle is not dependent on the size of the shear modulus.

Twist of thin-walled and solid cylinders with axial cuts

In both of the two cases treated above, the cross sections of the twisted bodies will not warp; i.e., they will remain plane due to the cylindrical symmetry. However, when timber is sawn, the growth rings are cut and the cross sections of the sawn timber will consist of only parts of growth rings. Thus, there is no cylindrical symmetry, and the cross sections may warp; i.e., the cross sections do not remain plane. As an example we may think of a thin-walled cylinder with an axial cut. If the cylinder surface exhibits a shear strain γ_{yz} , then the cut axial adjacent edges may move axially relative to each other (i.e., the cross section warps) and form what is called a screw dislocation instead of receiving a twist distortion (see Fig. 2). In practice, a thin-walled cylinder with an axial cut will receive a combination of twist and warp, and thus the twist angle is reduced compared with the twist angle of an uncut cylinder. Likewise, a solid cylinder with an axial cut from the outside to the pith will also have cross sections which will warp, and the twist angle will be less than the twist angle for an uncut solid cylinder. In practice we may multiply Eq. 4 with a constant factor C , $0 < C < 1$ in order for it to be valid also for a thin-walled or solid cylinder with an axial cut

$$\varphi = -C \frac{l}{r_m} 2\Delta w (\alpha_t - \alpha_l) \theta_m. \tag{7}$$

Twist of a thin strip

The twist of a thin strip is interesting to study as a simple extreme case, because sawn timber with cross sections lying near the outside of thick logs will have rather flat growth rings. Here the thin strip is interpreted as a part of the

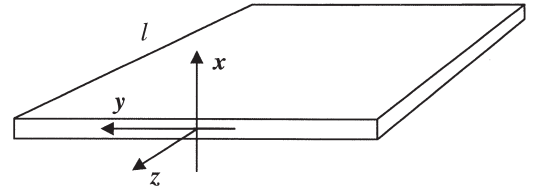


Fig. 3. Thin strip to be twisted around z -axis

surface of a thin-walled cylinder with a very large radius. The twist of a thin strip loaded with torques at the ends is treated in elementary solid mechanics textbooks (e.g., see Timoshenko and Goodier⁹), but instead, here we treat a variant of the elementary problem where the twist angle φ of the strip as a function of the shear strain γ_{yz} due to shrinkage is sought. We study the strip in a Cartesian coordinate system x - y - z , where x is pointing in the radial direction, y in the tangential direction, and z in the axial direction of the strip (see Fig. 3). The strip is thin in the x -direction, and thus the shear strains $\gamma_{xy} = \gamma_{xz} = 0$, and the only nonvanishing shear strain is γ_{yz} . Therefore, γ_{yz} from Eq. 2 and a linear θ variation from Eq. 6 give

$$\gamma_{yz}(x) = -2\Delta w (\alpha_t - \alpha_l) \left(\theta_0 + \left(\frac{d\theta}{dx} \right)_0 x \right) = \gamma_0 + \left(\frac{d\gamma_{yz}}{dx} \right)_0 x. \tag{8}$$

We now divide the influence on the twist angle φ from γ_{yz} into two separate parts, namely, first the influence of the

first term γ_0 and the influence of the second term $\left(\frac{d\gamma_{yz}}{dx} \right)_0 x$.

We then realise at first that the constant part γ_0 will not affect the twist, because the strip is able to get a simple shear deformation in the y - z plane due to γ_0 . However, when it comes to the influence of the second term, which is proportional to x , such a simple shear deformation is not possible. Instead, the result is a twist angle φ which we show as follows. Twist deformation of the thin strip gives displacements

$$u_x = -\frac{\varphi}{l} yz, u_y = \frac{\varphi}{l} xz, u_z = \frac{\varphi}{l} \psi(x, y) \tag{9}$$

according to Saint-Venant's theory of torsion.⁹ u_x , u_y , and u_z are displacements in the x , y , and z directions, respectively; ψ is the warping function, and l is the length of the strip. The displacement/strain relations give zero normal strains, but the shear strains become

$$\gamma_{xy} = 0, \gamma_{yz} = \frac{\varphi}{l} \left(\frac{d\psi}{dy} + x \right), \gamma_{xz} = \frac{\varphi}{l} \left(\frac{d\psi}{dx} - y \right). \tag{10}$$

Since $\gamma_{xz} = 0$ is a condition due to the thinness of the thin strip, Eq. 10 gives the solution $\psi = xy$. This solution also fulfils Laplace's equation $\Delta\psi = 0$, which is a necessary requirement in torsion theory. Now Eq. 10 with $\psi = xy$ gives

$$\gamma_{yz} = 2x \frac{\varphi}{l}, \tag{11}$$

which is the relation between shear strain and twist we seek. Equation 11 with γ_{yz} from the second term of Eq. 8 finally gives the twist angle

$$\varphi = -l\Delta w(\alpha_t - \alpha_b) \left(\frac{d\theta}{dx} \right)_0. \tag{12}$$

Thus, the twist of a thin strip is not dependent on the constant part of $\theta(x)$ but instead is proportional to the gradient of θ . Because $\alpha_t > \alpha_b$, drying ($\Delta w < 0$) will give φ the same sign as $\left(\frac{d\theta}{dx} \right)_0$; i.e., a positive spiral grain gradient (θ increases with increasing radius) will give a positive φ and vice versa. The sum of influences on φ of Eqs. 12 and 4 contains two terms which can act opposite to each other, as is the case for Norway spruce. Norway spruce normally has a left-handed spiral grain ($\theta_0 < 0$) at the pith which linearly changes toward a right-handed spiral grain at the log surface ($\left(\frac{d\theta}{dx} \right)_0 > 0$).^{2,5}

Twist of studs with arbitrary cross sections

A dimensional analysis of the twist angle of a stud with a specified cross section $b \times h$ cut from a log at different distances r_m from the pith (see Fig. 4) is done under the following assumptions: θ is a linear function (see Eq. 6) which here is characterised by a value θ_m in the middle of the cross section, and the constant gradient $\left(\frac{d\theta}{dr} \right)_0$. φ is proportional to $-\Delta w(\alpha_t - \alpha_b)l$ and is a function of θ_m , $\left(\frac{d\theta}{dr} \right)_0$, r_m , and the cross section width b and height h . Then $\varphi/[-\Delta w(\alpha_t - \alpha_b)l]$ is a function of θ_m , $\left(\frac{d\theta}{dr} \right)_0$, r_m , b , and h .

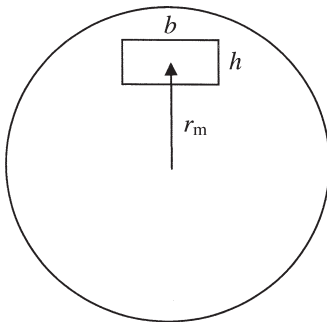


Fig. 4. Place of cross section of stud in log

According to standard theory of dimensional analysis, $\varphi r_m/[-\Delta w(\alpha_t - \alpha_b)l]$ must then be a function of the four dimensionless variables θ_m , $\left(\frac{d\theta}{dr} \right)_0 r_m$, b/h , and b/r_m . Rewriting and expanding φ as a series according to Taylor's formula, retaining only the linear, first-order terms and using the condition that $\varphi = 0$ if $\theta_m = \left(\frac{d\theta}{dr} \right)_0 = 0$ gives as the only option the first-order approximation

$$\varphi = -l\Delta w(\alpha_t - \alpha_b) \left(C \frac{2\theta_m}{r_m} + D \left(\frac{d\theta}{dr} \right)_0 \right) \tag{13}$$

where C and D are undetermined constants. The reason for choosing $2C$ and not C as a constant is in order to keep similarity with Eqs. 4 and 7. Now, in view of the discussion of the case of the twist of a thin-walled cylinder and the twist of a thin strip, the two terms in Eq. 13 can be physically explained as follows: realistic studs have cross sections that consist of more or less complete growth rings, growth-ring half rings, or parts of growth rings that are quite flat. The twist angle can be approximated as a sum of contributions from both the effect of spiral grain of growth ring cylinders according to Eqs. 4 and 7 and the effect of the spiral grain gradient of flat growth rings according to Eq. 12. The C and D constants determine the contribution of each term, and we expect them to be of the order of magnitude +1. The second term explains the perhaps surprising result from FE calculations that Eq. 4 does not explain, namely, that a stud with a cross section where the middle point and also all other points in the cross section have a left-handed spiral grain can still exhibit a right-handed twist after drying.

With Eq. 6 we can substitute θ_m for θ_0 in Eq. 13 and get

$$\varphi = -l\Delta w(\alpha_t - \alpha_b) \left(C \frac{2\theta_0}{r_m} + (2C + D) \left(\frac{d\theta}{dr} \right)_0 \right). \tag{14}$$

Solving for the cross section radius r_{m0} which will give twist angle $\varphi = 0$, gives

$$r_{m0} = - \frac{2C}{(2C + D)} \frac{\theta_0}{\left(\frac{d\theta}{dr} \right)_0}. \tag{15}$$

If the r value where $\theta = 0$ is notated as $r_{\theta 0}$, then from Eq. 15 we get

$$r_{m0} = \frac{2C}{(2C + D)} r_{\theta 0}. \tag{16}$$

Equation 16 shows that if $r_{m0} = r_{\theta 0}$, then $D = 0$ and no gradient term exists. If $r_{m0} \neq r_{\theta 0}$ then the gradient term exists and $D \neq 0$. This fact can be used to experimentally prove the existence of the second term; i.e., that $D \neq 0$. There is no influence from the cross section dimensions b and h in the first-order approximation according to Eq. 13, but such an influence will exist if a second-order analysis is made.

Table 1. Orthotropic material constants

	Direction		
	Radial (<i>r</i>)	Tangential (<i>t</i>)	Fiber (<i>l</i>)
Elastic modulus E_r, E_t, E_l (MPa)	400	220	9700
Shear modulus G_{rt}, G_{rl}, G_{tl} (MPa)	25	400	250
Poisson's ratio $\nu_{rq}, \nu_{rz}, \nu_{qz}$	0.55	0.0124	0.0136
Moisture expansion coefficients $\alpha_r, \alpha_t, \alpha_l$	0.19	0.35	0.0045

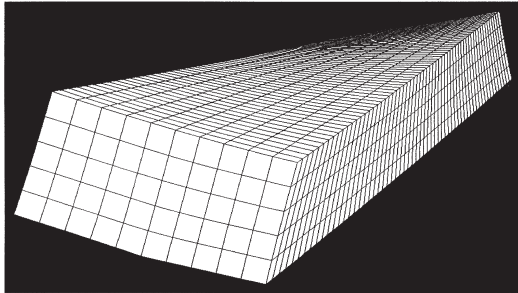


Fig. 5. Finite element method (FEM) calculated deformed shape of 50 × 100-mm stud with $r_m = 25$ mm, $\theta_m = -3^\circ$, $l = 3$ m, $\left(\frac{d\theta}{dr}\right)_0 = 0$, $\Delta w = -0.11$, $\alpha_r - \alpha_t = 0.345$. The deformation is exaggerated by a factor 2

Materials, methods, and results

FEM calculations were made using ABAQUS¹⁰ with a cylindrical, linear elastic orthotropic material model for 50 × 100-mm cross sections. The FEM model has 50 × 10 × 50 parabolic elements and the boundary conditions only restrict rigid-body movements. The elastic, orthotropic material data (see Table 1), are valid for Norway spruce and taken from Ormarsson et al.⁷ A typical deformed stud is shown in Fig. 5.

Twist angles when drying studs are calculated with FEM for different values of θ_m , $\left(\frac{d\theta}{dr}\right)_0$, and r_m . The FEM results for $r_m = 25$ mm and $r_m = 50$ mm are shown in Fig. 6a and 6b as the influence of $\left(\frac{d\theta}{dr}\right)_0$ on φ for constant θ_m and the influence of θ_m on φ for constant $\left(\frac{d\theta}{dr}\right)_0$, respectively. The linear behaviour shown in Fig. 6a and 6b agrees with the predicted linear behaviour of Eq. 13 and an evaluation of C and D by fitting Eq. 13 to the FEM results for varying r_m values gives the C and D values shown in Fig. 7. $C = 0.48$ and $D = 1.05$ are chosen here as the C and D values that make Eq. 13 agree with linear FEM.

Twist angles φ for studs have been measured¹¹ and correlated to the spiral grain angle measured on the stud surface

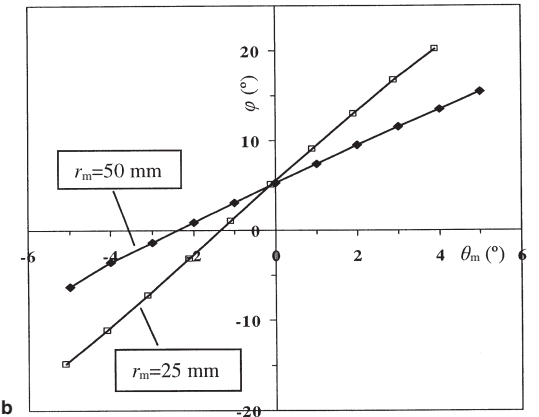
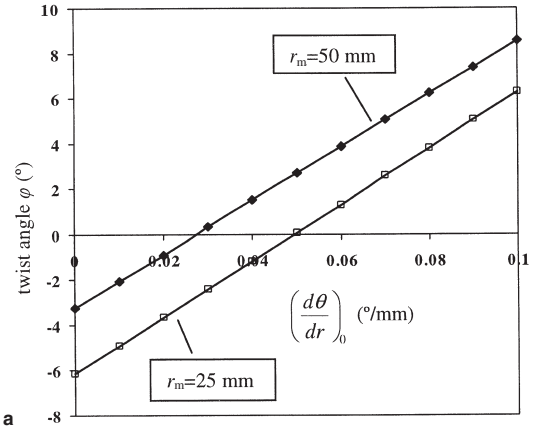


Fig. 6. a Twist angle φ as a function of $\left(\frac{d\theta}{dr}\right)_0$ for $\theta_m = -1.5^\circ$. b Twist angle φ as a function of θ_m for $\left(\frac{d\theta}{dr}\right)_0 = 0.044^\circ/\text{mm}$. Calculated with FEM for $r_m = 25$ mm and 50 mm for a 50 × 100-mm cross section with $l = 3$ m, $\Delta w = -0.11$ and $\alpha_r - \alpha_t = 0.345$

θ_{stud} . The result is $\varphi = 1.23 \theta_{\text{stud}}$ for 50 × 100-mm cross sections with $r_m = 25$ mm, $\Delta w = -0.1$, $l = 1$ m, and $\alpha_r - \alpha_t = 0.345$. This result corresponds to Eq. 13 with $C = 0.37$ and $D = 0.74$.

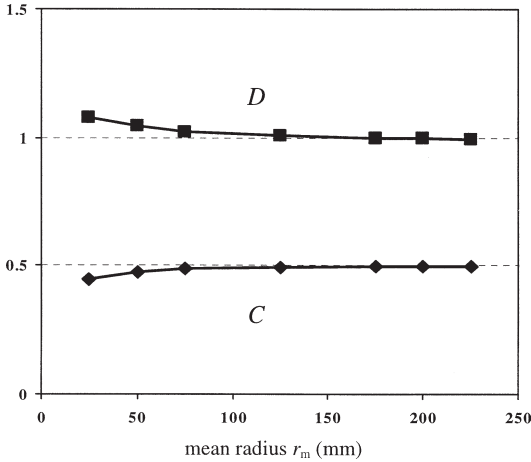


Fig. 7. *C* and *D* constants for varying radii r_m evaluated from FEM calculations on 50×100 -mm cross sections with $\theta_0 = -3^\circ$ and $\left(\frac{d\theta}{dr}\right)_0 = 0$ and $0.03^\circ/\text{mm}$, respectively. $l = 3\text{ m}$, $\Delta w = -0.11$, $\alpha_i - \alpha_j = 0.345$

Figure 8 shows the influence of each of the two terms of Eq. 13 on φ for the two sets of *C* and *D* constants mentioned above, namely, $C = 0.48$ and $D = 1.05$ from linear FEM and $C = 0.37$ and $D = 0.74$ from Trättek¹¹ measurements. Equation 1 is also shown in Fig. 8.

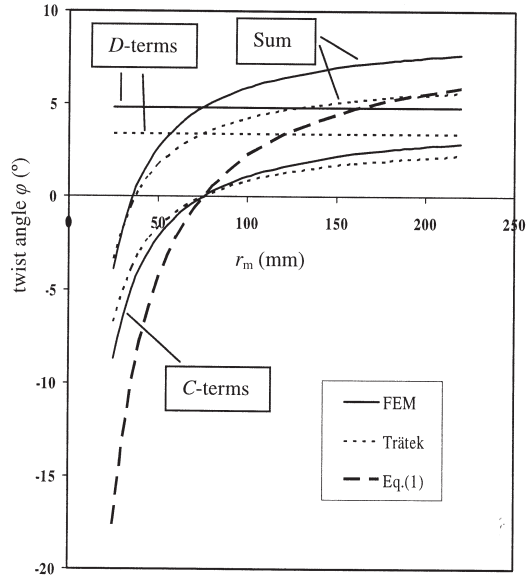


Fig. 8. Twist angle φ according to Eq. 13 shown as divided in the *C* term and the *D* term and the sum of the terms and according to Eq. 1. Linear FEM has $C = 0.48$ and $D = 1.05$ and the Trättek¹¹ measurement

has $C = 0.37$ and $D = 0.74$. $\theta_0 = -3.3^\circ$, $\left(\frac{d\theta}{dr}\right)_0 = 0.044^\circ/\text{mm}$, $l = 3.0\text{ m}$, $\Delta w = -0.10$, and $\alpha_i - \alpha_j = 0.345$

Discussion

Figure 7 shows that the *C* and *D* values are reasonably constant, and therefore Eq. 13 has good accuracy compared with the FEM calculations for r_m values in the interval of

25 to 225 mm. The linear relation between $\left(\frac{d\theta}{dr}\right)_0$ and φ for constant r_m and θ_m shown in Fig. 6a indicates the validity of Eq. 13 and the influence of the second term in Eq. 13. In the same way, Fig. 6b shows the linear relation between φ and θ_m for constant $\left(\frac{d\theta}{dr}\right)_0$ and r_m , which shows the influence of the first term of Eq. 13. The FEM results confirm that a cross section with negative θ values in all material points all over the cross section may achieve a positive twist if the gradient $\left(\frac{d\theta}{dr}\right)_0$ is positive enough.

Comparison with the experimental results obtained at Trättek¹¹ (see Fig. 8 and Table 2) show that Eq. 13 overestimates the twist if the *C* and *D* values which conform to linear elastic FEM calculations are used. If the *C* and *D* values are chosen to make Eq. 13 fit to the Trättek¹¹ experi-

Table 2. Evaluated *C* and *D* factors

Method	<i>C</i>	<i>D</i>
From linear FEM	0.48	1.05
From experiments by Trättek ¹¹	0.37	0.74

mental results, then we get lower *C* and *D* values. The reason for the overestimation of twist in the FEM calculations may be the linear elastic assumption in the FEM calculations, which excludes plastic and creep effects. In practice, this reduces the drying deformations and makes the FEM calculation exaggerate the twist. Also, Δw is not constant in practice, as is assumed in the FEM calculations, but instead can vary over the cross section. Thus, Eq. 13 with $C = 0.48$ and $D = 1.05$ gives an upper limit for the twist angle φ , which can possibly be reached for a stud with no constraints during drying and exposed to a very slow low-temperature drying course of events with small creep or plastic effects. Figure 8 shows the relationship between the *C* term and the *D* term in Eq. 13 and that the *D* term is larger than the *C* term for $r_m > 35\text{ mm}$. Also Fig. 8 shows that Eq. 1 overestimates φ for small r_m values. This behavior was also observed by Säll⁵ and Johansson et al.⁶

Equation 13 with *C* and *D* values adjusted to fit the situation in question, whether it is an experimental or a

theoretical situation, could be a good choice for calculating the twist angle φ for a stud, knowing the spiral grain angle θ at an arbitrary point in the log cross section, e.g., a point on the log surface or a point on the stud surface. One practical use of the formula is to predict the twist a certain stud will achieve after drying with the aid of measured θ angles on the log surfaces, e.g., in a sawmill.

Acknowledgment The author expresses his gratitude to Formas (the Swedish Research Council for Environment, Agricultural Sciences, and Spatial Planning) for their support.

References

1. Harris JM (1989) *Spiral grain and wave phenomena in wood formation*. Springer, Berlin Heidelberg New York
2. Nyström J (2003) Automatic measurement of fiber orientation in softwoods by using the tracheid effect. *Comput Electr Agric* 41: 91–99
3. Ekevad M (2004) Method to compute fiber directions in wood from computed tomography images. *J Wood Sci* 50:41–46
4. Forsberg D, Waresjö M (2001) Grain angle variation: a major determinant of twist in sawn *Picea abies* (L.) Karst. *Scand J Forest Res* 16:269–277
5. Säll H (2002) *Spiral grain in Norway spruce*. Doctoral Thesis, Växjö University 22 (2002). Wood design and Technology
6. Johansson M, Perstorper M, Kliger R, Johansson G (2001) Distortion of Norway spruce timber. Part 2. Modelling twist. *Holz Roh Werkst* 59:155–162
7. Ormarsson S, Dahlblom O, Petersson H (2000) Numerical study of the shape stability of sawn timber subjected to moisture variation. Part 3: influence of annual ring orientation. *Wood Sci Technol* 34:207–219
8. Stevens WC, Johnston DD (1960) Distortion caused by spiralled grain. *Timber Technol* 68:217–218
9. Timoshenko SP, Goodier JN (1970) *Theory of elasticity*, 3rd edn. McGraw-Hill, Tokyo, pp 291–338
10. Anon. (2003) ABAQUS users manual version 6.4. ABAQUS Inc. Pawtucket, USA
11. Anon. (2003) Kontenta 0312045 Results from Träteck (the Swedish Institute for Wood Technology Research, Box 5609, 11786 Stockholm)(in Swedish)

The publication of this article was made possible by an Emachu Research Fund. The author is grateful for the fund.

Paper 3

Jonas Danvind · Mats Ekevad

Local water vapor diffusion coefficient when drying Norway spruce sapwood

Received: April 19, 2005 / Accepted: July 20, 2005

Abstract In this article, a one-dimensional and a two-dimensional approach to the evaluation of local diffusion coefficients for Norway spruce sapwood from measured moisture content (MC) values are presented. A studied wood sample was dried from the initial green condition to about 15% mean MC, but here only the diffusive part of the drying process between approximately 25% and 15% mean MC was treated. Measured local MC values were based on nondestructive X-ray computed tomography data. Finite element calculations were performed with two alternative diffusion coefficients to test the appropriateness of the diffusion coefficients that were evaluated from the measured MC values. The evaluated diffusion coefficients show interesting dependence on MC and distance from the evaporation surface. The advantage of using the methods presented is that the diffusion coefficient is calculated on a local level without having to define a function for the diffusion coefficient's dependency on other parameters.

Key words Wood · FEM · Drying · Diffusion coefficient · Computed tomography

Introduction

When physically describing the drying behavior of wood, the drying process can be divided into the capillary part and the diffusion part. In the capillary part, the moisture content

(mass of water/mass of dry wood; MC) is high and there is free water present in the voids of the wood fibers. When the MC is lower and there is moisture only bound in the cell walls of the fibers, then the moisture flux is driven by diffusion. Internal stresses are induced in the diffusion part of the drying process due to anisotropic shrinkage, which may cause checking and drying distortions that reduce the quality of the timber. Large MC gradients during the diffusive process give a fast drying process but cause large stresses. It is of importance to understand the drying behavior of wood in order to avoid quality degradation due to drying. One way to do this is through simulation.

Simulations of the wood drying process using three-dimensional (3D) finite element method (FEM) can provide detailed and realistic information about the local MC, local stress, and global deformation history. 3D FEM calculations require, among other material data, diffusion coefficients that are valid locally throughout the material. The objective of this work is to determine local diffusion coefficients using nondestructive measurements and numerical methods.

Alternative approaches to the evaluation of local diffusion coefficients for Norway spruce sapwood are presented based on experiment. A clearwood sample (Fig. 1) was dried from the initial green condition to about 15% mean MC (mean value for the wood sample in question), but here only the diffusive part of the drying process between approximately 25% and 15% mean MC was treated. The measured local MC values were based on nondestructive X-ray computed tomography (CT) data.

Several authors (Hukka,¹ Hukka and Oksanen,² Liu et al.,³ Rosenkilde and Arfvidsson⁴) have found that the diffusion coefficient for a certain wood sample is not constant, but is dependent on MC in addition to the dependence on temperature. The diffusion coefficients obtained are global mean values for a wood sample of a certain size.

The CT method used here to measure local interior two-dimensional (2D) densities and MCs of the wood sample is described by Lindgren,⁵ Danvind and Moren,⁶ and Wiberg.⁷ The advantage of using the methods presented in this article is that the diffusion coefficient is calculated on a local level

J. Danvind · M. Ekevad (✉)
Division of Wood Technology, Skellefteå Campus, Luleå University of Technology, Skeria 3, Skellefteå SE-931 87, Sweden
Tel. +46-910-585300; Fax +46-910-585399
e-mail: mats.ekevad@ltu.se

J. Danvind
Valutec AB, Skellefteå SE-931 27, Sweden

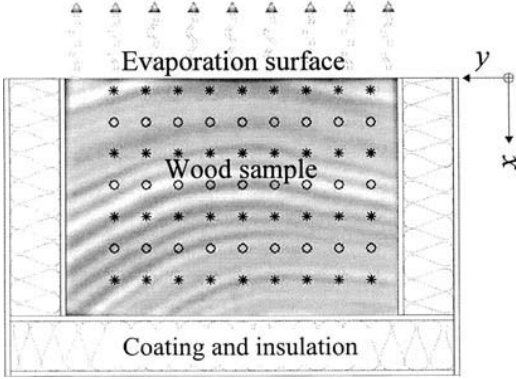


Fig. 1. Wood sample. Asterisks and circles denote center points of cells

without having to define a function for the diffusion coefficient's dependencies on other parameters such as MC. The possibility of using CT data to determine local properties in wood other than moisture properties, such as spiral grain angles, is demonstrated by Ekevad⁸ and Sepulveda et al.⁹

Theory

Isothermal conditions are considered, and a Cartesian coordinate system and a referential (Lagrangian) viewpoint are adopted in order to deal with the shrinkage of the material. Thus, the coordinates x , y , and z denote the coordinates of a material point in the green condition, and all lengths, areas, and volumes are values in this green state and remain constant during the drying process. In the first approach to determining the diffusion coefficient D , the moisture flux is assumed to be one dimensional (1D) in the radial direction (x) and a modified Fick's first law is stated as

$$g = -D \frac{du}{dx}. \quad (1)$$

where $g = g(x, t)$ is the mass flux in the positive x direction per unit area at position x at time t , $u = u(x, t)$ is the MC at x and t . u is used as the driving potential in the modified Fick's first law (Eq. 1) instead of using the moisture concentration $w = u \rho_0$, where $\rho_0 = \rho_0(x)$ is the basic density of wood (dry mass of wood per green volume). It was found experimentally that u is a better way to express the amount of moisture in our case where ρ_0 varied in space (Fig. 2). This was confirmed in our experiments, because it was found that a gradient $dw/dx \neq 0$ could exist without creating a mass flux, due to local variations of ρ_0 . In that case, $dw/dx \neq 0$ due to a gradient $d\rho_0/dx \neq 0$ but $du/dx = 0$. Physically it can be reasoned that u is a better measure of MC than w when it comes to bound water diffusion because water molecules

are attracted to wood molecules and not to a specific volume. Mass conservation and Eq. 1 give

$$\dot{u} = \frac{1}{\rho_0} \frac{d}{dx} \left(D \frac{du}{dx} \right) \quad (2)$$

which is a modified Fick's second law. The general boundary conditions to be used with Eqs. 1 and 2 are specified values of u (essential conditions) or g (natural conditions) or

$$g = \beta(u - u_\infty) \quad (3)$$

(convective conditions or mixed conditions) on all or parts of the boundaries. Here the convective condition is used for the evaporation surface and the natural condition $g = 0$ for all the other surfaces. The initial condition is $u = u_0(x, t_0)$ at the starting time t_0 . β is the mass transfer coefficient for the moisture vaporization into the surrounding air on the boundary surface, and u_∞ is the equilibrium MC for wood under ambient air conditions.

The equations for 2D mass flux in the x and y directions are a modified Fick's first law for an orthotropic material,

$$\mathbf{g} = (g_x, g_y)^T = -\mathbf{D} \text{grad}(u) = -\mathbf{D} \left(\frac{\partial u}{\partial x}, \frac{\partial u}{\partial y} \right)^T \quad (4)$$

where

$$\mathbf{D} = \begin{bmatrix} D_{xx} & D_{xy} \\ D_{yx} & D_{yy} \end{bmatrix} \quad (5)$$

is the symmetric diffusion coefficient matrix. Here it is assumed that radial and tangential directions coincide with the x and y directions, respectively (Fig. 1). Mass conservation and Eq. 4 give

$$\dot{u} = \frac{1}{\rho_0} \text{div}[\mathbf{D} \text{grad}(u)] \quad (6)$$

or expanded

$$\rho_0 \frac{\partial u}{\partial t} = \frac{\partial}{\partial x} \left(D_{xx} \frac{\partial u}{\partial x} + D_{xy} \frac{\partial u}{\partial y} \right) + \frac{\partial}{\partial y} \left(D_{yx} \frac{\partial u}{\partial x} + D_{yy} \frac{\partial u}{\partial y} \right) \quad (7)$$

which is a modified Fick's second law. The boundary conditions are specified values of u or \mathbf{g} or convective conditions (Eq. 3). The initial condition is $u = u_0(x, y, t_0)$.

Materials and methods

A wood sample made of clear sapwood of Norway spruce (*Picea abies*) with the green dimensions of 31, 42, and 205 mm in the x (radial), y (tangential), and z (longitudinal) directions, respectively, was dried in this study. Five surfaces of the sample were coated using polyurethane glue (Cascol 1809, Casco) and aluminum foil (Fig. 1). The coated

surfaces were also thermally insulated using Styrofoam. Three temperature sensors were placed within the sample at 1, 11, and 21 mm depths from the surface, but in different positions in the longitudinal direction. One additional sensor was placed on the surface. During drying, the humidity, temperature, and speed of the circulating air were approximately constant at 43% relative humidity, 50°C, and 4 m/s, respectively. A Siemens Somatom AR.T. X-ray CT scanner was used to capture a density image in the tangential–radial plane of the interior at a constant longitudinal position every 10 min during drying.

Evaluation of D from the CT data, 1D method

$u(x, t)$ values for small volumes ($0.14 \times 0.14 \times 5 \text{ mm}^3$) in 3D space (voxel values) were measured with CT (see Danvind and Morén⁶ for a description of the method). In order to reduce spread and increase accuracy, mean MCs $u(x_i, t_i)$ for seven discrete volumes along the x axis with center positions at $x_i = 2.0, 5.9, 9.8, 13.7, 17.6, 21.6,$ and 25.5 mm for $i = 1$ to 7 were evaluated. A value of u at $x_8 = 29.2 \text{ mm}$ was set equal to the value of u at $x = x_7$, $x_0 = 0$ was the surface position, and $x_9 = 31.0 \text{ mm}$ denoted the inner, insulated boundary. u values were measured at discrete time points, t_k , between $t_0 = 0 \text{ h}$ and $t_{200} = 100 \text{ h}$ with a time step of 0.5 h, except between $t = 83 \text{ h}$ and $t = 95 \text{ h}$ and between $t = 42.5 \text{ h}$ and $t = 44 \text{ h}$ due to malfunction of the equipment. Denoting d/dx with a prime, using mass conservation and a central difference scheme we get the mass flux gradient,

$$g_i^{\prime k} = -\rho_0 u_i^{\prime k} = -\rho_0 \frac{(u_i^{k+1} - u_i^{k-1})}{(t_{k+1} - t_{k-1})} \quad (8)$$

where the subindex i denotes the position $x_i = 2.0, 5.9 \dots 29.2 \text{ mm}$ for $i = 1$ to 8 and superindex k denotes the time step $t_k = 0, 0.5, 1.0 \dots \text{ h}$ for $k = 1$ to 199. Integration of Eq. 8 gives the surface mass flux

$$g_{\text{surf}}^k = g(0, t_k) = -\int_0^l g' dx = -\sum_{i=1}^8 g_i^{\prime k} \Delta x_i \quad (9)$$

where $\Delta x_i = x_{i+1} - x_i$ is the length in the x direction of the volume associated with each value u_i . The mass flux at position i is

$$g_i^k = g(x_i, t_k) = g_{\text{surf}}^k + \int_0^x g' dx = g_{\text{surf}}^k + \sum_{j=1}^i g_j^{\prime k} \Delta x_j \quad (10)$$

where Δx_j is the length in the x direction of each of the volumes that has x coordinates lower than x_i . Now Eq. 1 with a central difference scheme gives

$$D_i^k = -\frac{g_i^k}{u_i^{\prime k}} = -\frac{g_i^k (x_{i+1} - x_{i-1})}{(u_{i+1}^k - u_{i-1}^k)} \quad (11)$$

The mass transfer coefficient β is evaluated from Eq. 3 as

$$\beta^k = \frac{g_{\text{surf}}^k}{(u_{\text{surf}}^k - u_{\infty}^k)} \quad (12)$$

where u_{surf}^k is evaluated by a parabolic extrapolation to the surface using the three u_i values that are closest to the evaporation surface.

Evaluation of D from the CT data, 2D method

Mean $u(x, y, t)$ values for cells, $4.1 \times 4.1 \times 5 \text{ mm}^3$, in 3D space are evaluated from the CT data. The total mass flux, g_{surf}^k , transferred from the sample at time $t = t^k$ is calculated by using the total mass decrease, the time step $\Delta t^k = t^{k+1} - t^{k-1}$ and the area of the convective surface, A_{surf} . The mass flux is

$$g_{\text{surf}}^k = \frac{\sum_{i=1}^M \sum_{j=1}^N (m_{i,j}^{k+1} - m_{i,j}^{k-1})}{\Delta t^k \cdot A_{\text{surf}}} \quad (13)$$

where subindices i and j denote the positions in the x and y directions, respectively. $M = 7$ and $N = 9$ are the number of cells in the x and y directions, respectively (Fig. 1), and m is mass.

The mass transfer coefficient, β^k , at time $t = t^k$ is calculated as

$$\beta^k = \frac{g_{\text{surf}}^k A_{\text{surf}}}{\sum_{j=1}^N (u_{\infty}^k - u_{\text{surf},j}^k) A_{\text{surf},j}} \quad (14)$$

where $u_{\text{surf},j}^k$ is the MC at time $t = t^k$ for the surface of a cell adjacent to the evaporation surface with $y = y_j$. $u_{\text{surf},j}^k$ is linearly extrapolated from the MCs of the two cells next to the surface. $A_{\text{surf},j}$ is the evaporation surface area of the cell at $y = y_j$. The modified Fick's first law of diffusion (Eq. 4) is used for the mass flux of the interior cell's boundary surfaces. In the first iteration of an iterative scheme, the coupling term, D_{xy} , in Eq. 5, is set equal to zero. For a cell on the evaporation surface at position $(i, j) = (\text{surf}, j)$, surface mass transfer is assumed to govern the mass flux, which is calculated using β^k from Eq. 14. The modified Fick's second law (Eq. 7) is used for mass balances in cells, and the spatial derivatives of D are assumed to be zero in a cell. Based on these assumptions, Eq. 7 can be stated in numerical form as:

$$\begin{aligned} \rho_0 \frac{u_{ij}^{k+1} - u_{ij}^{k-1}}{t^{k+1} - t^{k-1}} &= \frac{1}{\Delta x} \left[D_{x,j-0.5,j}^k \cdot \frac{u_{i-1,j}^k - u_{i,j}^k}{x_{i-1,j} - x_{i,j}} - D_{x,j+0.5,j}^k \cdot \frac{u_{i,j}^k - u_{i+1,j}^k}{x_{i,j} - x_{i+1,j}} \right] \\ &+ \frac{1}{\Delta y} \left[D_{y,i,j-0.5}^k \cdot \frac{u_{i,j-1}^k - u_{i,j}^k}{y_{i,j-1} - y_{i,j}} - D_{y,i,j+0.5}^k \cdot \frac{u_{i,j}^k - u_{i,j+1}^k}{y_{i,j} - y_{i,j+1}} \right] \\ &= \left[\begin{array}{l} x_{i-1,j} - x_{i,j} = x_{i,j} - x_{i+1,j} = \Delta x; \\ y_{i,j-1} - y_{i,j} = y_{i,j} - y_{i,j+1} = \Delta y; \\ D_{x,j-0.5,j}^k = D_{x,j+0.5,j}^k = D_{x,j,j}^k; \\ D_{y,i,j-0.5}^k = D_{y,i,j+0.5}^k = D_{y,i,j}^k \end{array} \right] = D_{x,j,j}^k \cdot \frac{1}{\Delta x^2} \\ &\cdot [u_{i-1,j}^k - 2u_{i,j}^k + u_{i+1,j}^k] + D_{y,i,j}^k \cdot \frac{1}{\Delta y^2} \cdot [u_{i,j-1}^k - 2u_{i,j}^k + u_{i,j+1}^k] \end{aligned} \quad (15)$$

In Eq. 15 it is assumed that all elements have the same size, Δx , and Δy . From the CT experiments, all parameters except $D_{x,i,j}$ and $D_{y,i,j}$ can be achieved for each cell of 30×30 voxels in the CT image. Hence, there is one equation (Eq. 15) and two unknowns for each cell; thus, the equation system for all elements is underdetermined. By setting $D_{x,i,j}$ and $D_{y,i,j}$ equal in adjacent cells, in this case 2×6 cells (8.1×24.3 mm), the number of unknowns for the equation system is reduced, and thereby an overestimated system is achieved which is solved in a least-squares sense using standard Matlab¹⁰ routines. By moving the position of the 2×6 cells and repeating the calculation procedure 12 times, once for each movement of the cells, 12 sets of $D_{x,i,j}$ and $D_{y,i,j}$ are achieved in each cell. The median values of the 12 solution sets are then taken as estimated solutions of $D_{x,i,j}$ and $D_{y,i,j}$ in each cell.

In a second iteration using $u_{i,j}$, $D_{x,i,j}$, and $D_{y,i,j}$, the mass fluxes, $g_{x,i,j}$ and $g_{y,i,j}$, are calculated using a numerical form of Eq. 4. $g_{x,i,j}$ and $g_{y,i,j}$ are used to recalculate the diffusion coefficients, including the coupling term, D_{xy} . This procedure gives two equations and three unknowns, D_{xx} , D_{yy} , and D_{xy} , per cell; i.e., when setting up a matrix system of equations for all cells, an underdetermined system is obtained. This time the number of unknowns is reduced by setting D_{xx} , D_{yy} , and D_{xy} constant in 2×2 cells and by solving the overdetermined system in a least-squares sense. As before, by moving the position of the 2×2 cells and by solving the system four times, four sets of diffusion coefficients per cell are achieved in each cell, and the median values are chosen as solutions. Using the coupled diffusion coefficients, local mass fluxes can be derived, and the procedure of deriving diffusion coefficients can be iterated until values stabilized. Here, only the first and second iterations have been done. In this study, the diffusion in the radial direction (x) was to be studied. Therefore, diffusion coefficients in the horizontal direction (y) of the CT image are not presented.

FEM calculation

ABAQUS¹¹ was used with a 3D isothermal and isotropic diffusion model as a solver of the diffusion equation (Eq. 6). As boundary conditions, we had zero mass flux on five surfaces and convection on the evaporation surface (Fig. 1). The initial condition $u(x, t_0)$ at $t_0 = 30.1$ h was taken from the measured data. Based on experimental findings shown below, two alternatives for D were used. As the first alternative $D = D(u)$ was adapted, and as a second alternative $D = D(u, x)$ was used. The measured values of $\beta(u)$ were used during the FEM calculations.

Results

All results shown in this article relate to the diffusion part of the total drying process and hence use a time scale that starts at time 30.1 h. The temperature differences between three internal positions in the test sample and in the air

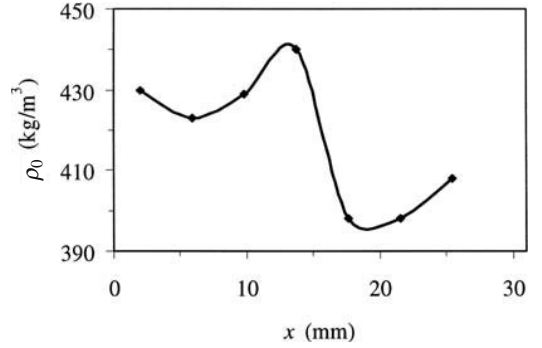


Fig. 2. Measured basic density $\rho_0(x)$

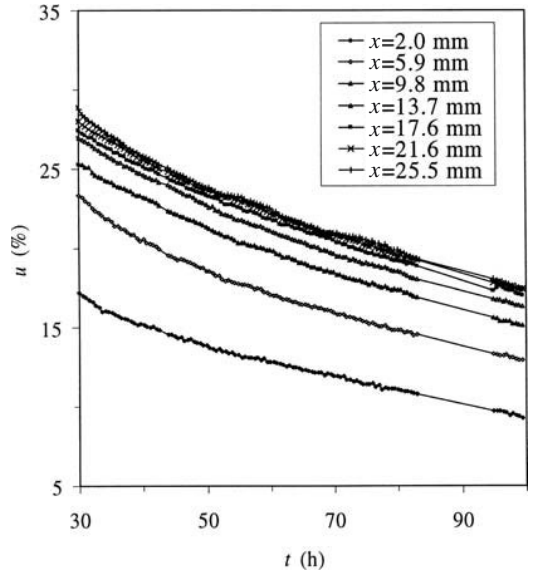
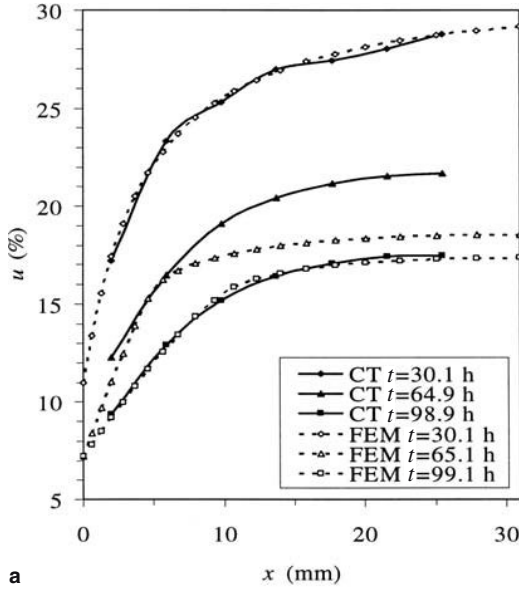
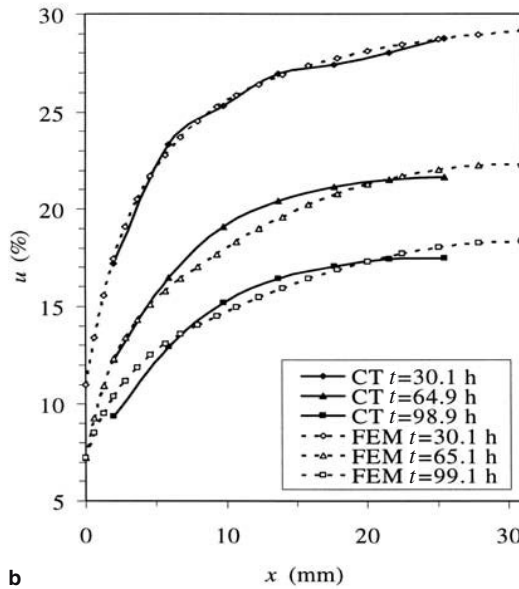


Fig. 3. Measured moisture content $u(t)$ for different x values in consecutive order from the lowest curve with the lowest x value

were $< 0.8^\circ\text{C}$ during the test. $\rho_0(x)$ is shown in Fig. 2, $u(t)$ for different x values is shown in Fig. 3, and $u(x)$ for different times in Fig. 4. $D(u)$ for the 1D method is shown in Fig. 5 for $x \leq 13.7$ mm and $\beta(u)$ is shown in Fig. 6. For the 2D method, $D(u)$ is shown in Fig. 7 and $\beta(u)$ in Fig. 6. The objective in the FEM calculations was to find D values that gave $u(x)$ good correlation to the experimental result at the final time $t = 99$ h. The agreement between experiment and calculation was then checked at an intermediate time $t = 65$ h. The FEM simulation using the first alternative $D = D(u)$ according to Fig. 8a gives an agreement with the CT measurements according to Fig. 4a. The second alternative $D = D(u, x)$ according to Fig. 8b has an agreement according to Fig. 4b.

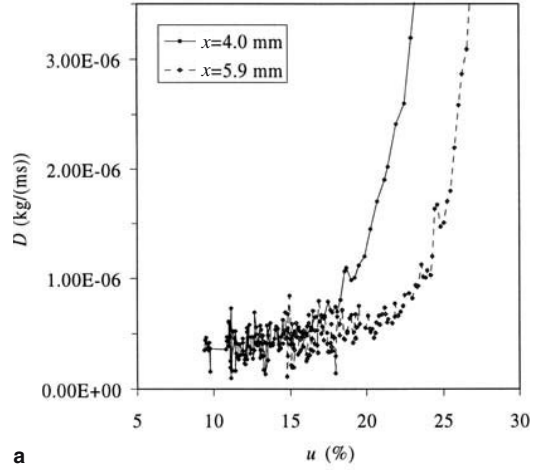


a

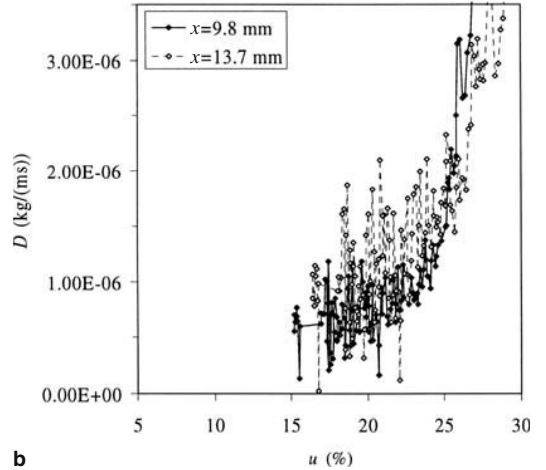


b

Fig. 4a,b. Moisture content $u(x)$ at different times t measured with computed tomography and calculated with finite element method (FEM). **a** FEM approach $D = D(u)$. **b** FEM approach $D = D(u, x)$



a



b

Fig. 5a,b. $D(u)$ evaluated with the one-dimensional (1D) method for different x values. **a** $x = 4.0$ and 5.9 mm. **b** $x = 9.8$ and 13.7 mm

The initial conditions u_0 at $t_0 = 30.1$ h for the FEM simulations are the same for both alternatives.

Discussion

For the 1D method, D shows a rather clear dependence on u and x as is seen from Fig. 5. The curves for $x = 5.9, 9.8,$ and 13.7 mm agree well (Fig. 5) but the curve for $x = 4.0$ mm is translated to the left and downward compared with the other curves. The curve for $x = 17.6$ mm (not shown) agrees quite well with the curves for $x = 5.9, 9.8,$ and 13.7 mm, but shows more spread. The curves for $x = 21.6$ and 25.5 mm

(not shown) show even more spread, but they seem to agree with the curves for $x = 5.9, 9.8, 13.7,$ and 17.6 mm. Thus, there is a unique curve for $x = 4.0$ mm, and all of the rest of the curves at the other x values seem to agree reasonably well. The reason for the large spread of D for large x values is probably the decreasing MC gradient and the decreasing mass flux with depth (x), which make the numerical errors large (Eq. 11). The overall conclusion is that the diffusion coefficient is a function of MC and depth, $D = D(u, x)$. The dependence on u is especially large in the interval where $16\% < u < 30\%$, while for $u < 16\%$, D seems rather constant.

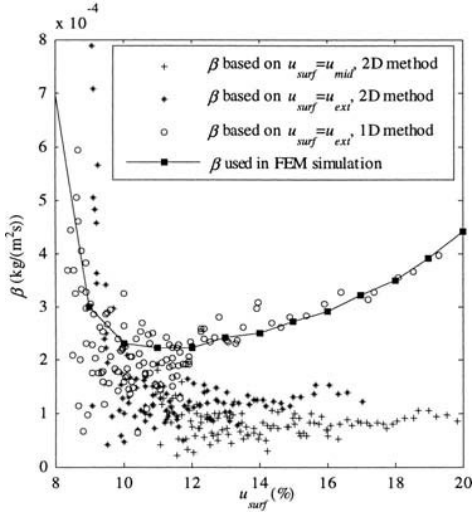
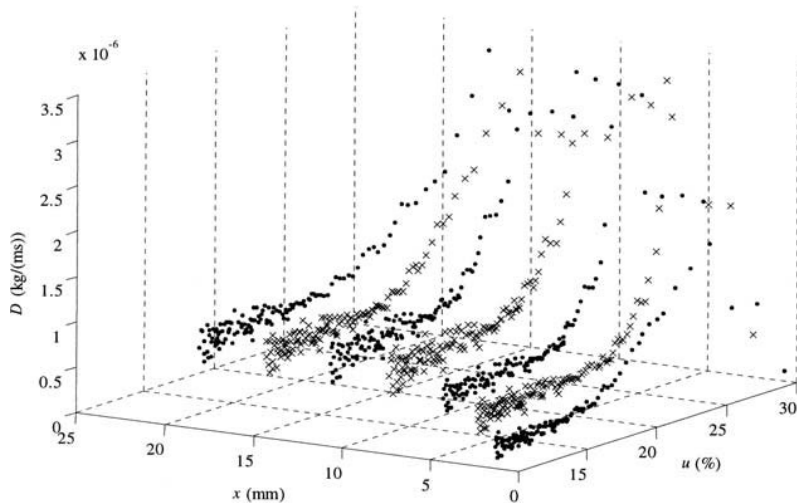


Fig. 6. $\beta(u)$ evaluated with the 1D and 2D methods with alternative surface moisture contents. u_{ext} , linear extrapolation from two adjacent u values or parabolic extrapolation from three adjacent u values; u_{mid} , mean value of the surface cell; i.e., $u_{\text{mid}} = u(x_{i+1}, t)$

Fig. 7. Diffusion coefficient $D(u, x)$ evaluated with the 2D method. $x = 2.0, 5.9, 9.8, 13.7, 17.6, 21.6, 25.5$ mm shown as alternating series of dots and crosses



The dependence on the distance from surface x is only significant when $x < 5$ mm, i.e., near the surface. β shows more spread at lower mean MC due to smaller $u_{\text{surf}} - u_{\infty}$ than at higher mean MC (Fig. 6).

For the 2D method, only D_x values are presented. This is due to large spread in D_y , probably caused by the one-directional drying resulting in almost constant values of u in the y direction, which strongly influenced the derivation of D_y, D_x values (Fig. 7) are similar to the results from the 1D method, but the results have less spread. A reason for the lower spread is probably the calculation method in which the median values of several solution sets are taken as D . β values for the 2D method are lower than for the 1D method (Fig. 6). This is due to the different choices of u_{surf} .

When trying to reproduce the original, measured $u(x)$ values at $t = 99.1$ h with the FEM calculation, the second alternative with $D = D(u, x)$ is best (Fig. 4b). This shows the validity of the experimentally derived D values and the dependence of D on distance to the evaporation surface. The first alternative with $D = D(u)$ gave good correlation at $t = 99.1$ h but poor correlation at $t = 65.1$ h (Fig. 4a).

In Fig. 8b, evaluations of D from Hukka¹ and Rosenkilde and Arfvidson² are compared with our values used for FEM calculations. Their values and ours agree quite well, at least for $u < 15\%$. The discrepancy in D for $u > 20\%$ between our values and theirs could be due to differences in wood material (Hukka¹ used Norway spruce heartwood and Rosenkilde and Arfvidson² used Scots pine sapwood) and differences in evaluation methods. Hukka¹ assumed that $D(u)$ is an exponential function and Rosenkilde and Arfvidson² used another type of curve-fitting method. The rate of the mean MC for a wood sample is essentially controlled by β and not D when u is high, and vice versa. However, an appropriate $D(u)$ description is important for realistic local $u(x)$ values.

The dependence on depth can be a dependence not on depth itself but via some other parameter (not measured

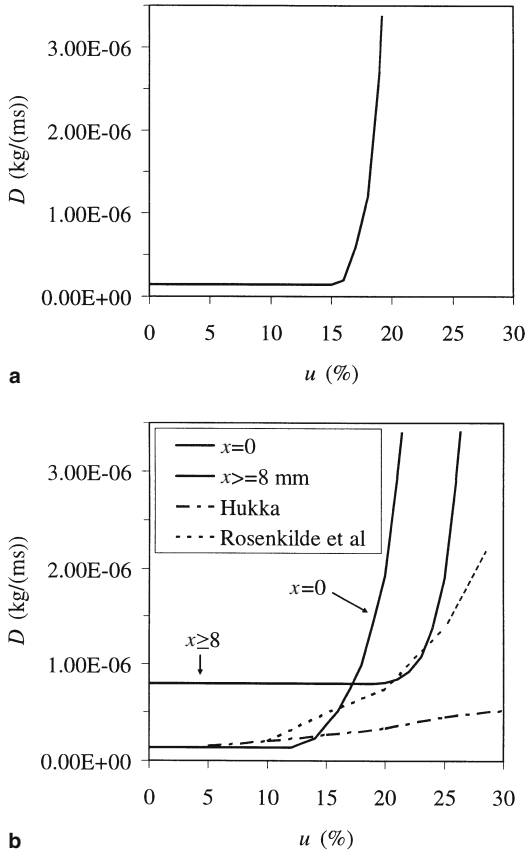


Fig. 8. **a** $D(u)$ used in the first approach of FEM calculations. **b** $D(u, x)$ used in the second approach of FEM calculations. Linear interpolation of D for $0 < x < 8$ mm using the curves for $x = 0$ and $x = 8$ mm. Comparison values of Hukka's values are for Norway spruce heartwood, those of Rosenkilde and Arfvidsson's are for Scots pine sapwood

here), which itself is a function of depth. Such a parameter is stress, because there are probably large stresses near the surface. Also, \dot{u} is a function of depth because the material near the surface has a faster changing moisture situation than the material far away from the surface.

Another possible reason for the behavior of D near the surface could be the position of the evaporation front during drying. Wiberg⁷ and Rosenkilde and Arfvidsson⁴ show how the evaporation front recedes into the material in the capillary regime of drying, creating a dry "shell" near the surface. This dry shell probably exists also in the beginning of the diffusion regime. The dry shell may have caused $u_{i=1,j}$ to have lower values than they would have had if the dry

shell had not existed. Hence, one can propose to include a dry shell formulation in future evaluations of D , as suggested by Salin.¹²

The calculations of D are sensitive to measurement errors of ρ_0 , u , t , and x values, because derivatives of u in space and time are estimated by numerical schemes (Eqs. 8–11 and Eqs. 13–15). An error estimate of u based on the spread of the graph of $\dot{u}(t)$ calculated with a central difference approximation (Eq. 8) was made. The assumption was that $u(t)$ is a normally distributed stochastic variable and that t values are exact, which results in an estimated standard deviation of u of the order of 0.04% when u is approximately 20%. This standard deviation of u is considered low in comparison with earlier values (see Danvind¹³). It is believed that this spread in measured u values is the main cause of spread in D . The spread in D increases when u decreases.

Acknowledgments The authors express their gratitude to Valutec AB, Formas (the Swedish Research Council for Environment, Agricultural Sciences and Spatial Planning), Vinnova (the Swedish Agency for Innovation Systems) through the Skewood programme, and to Kempestiftelsen for their support.

References

- Hukka A (1999) The effective diffusion coefficient and mass transfer coefficient of Nordic softwoods as calculated from direct drying experiments. *Holzforschung* 53:534–540
- Hukka A, Oksanen O (1999) Convective mass transfer coefficient at wooden surface in jet drying of Veener. *Holzforschung* 53:204–208
- Liu JY, Simpson WT, Verrill SP (2001) An inverse moisture diffusion algorithm for the determination of diffusion coefficient. *Dry Technol* 19:1555–1568
- Rosenkilde A, Arfvidsson J (1997) Measurement and evaluation of moisture transport coefficients during drying of wood. *Holzforschung* 51:372–380
- Lindgren O (1992) Medical CT-scanners for non-destructive wood density and MC measurements. Doctoral Thesis, Luleå University of Technology, Thesis No. 1992:111D
- Danvind J, Morén T (2004) Using X-ray CT-scanning for moisture and displacement measurements in knots and their surroundings. EU COST 15 Wood Drying Conference Proceedings, April 22–23, Athens, Greece
- Wiberg P (2001) X-ray CT-scanning of wood during drying. Doctoral Thesis, Luleå University of Technology, Thesis No. 2001:10
- Ekevad M (2004) Method to compute fiber directions in wood from computed tomography images. *J Wood Sci* 50:41–46
- Sepulveda P, Oja J, Grönlund A (2002) Predicting spiral grain by computed tomography of Norway spruce. *J Wood Sci* 48:479–483
- Anon (2001) Matlab version 6.1.0.450 release 12.1. The MathWorks, Natick, MA
- Anon (2003) ABAQUS users manual version 6.4. ABAQUS, Pawtucket, RI
- Salin JG (2002) Theoretical analysis of mass transfer from wooden surfaces. Proceedings of 13th International Drying Symposium, 27–30 August, Beijing, China
- Danvind J (2002) Measuring strain and moisture content in a cross-section of drying wood using digital speckle photography and computerised X-ray tomography. Proceedings of 13th International Symposium on Nondestructive Testing of Wood. 19–21 August, Berkeley, CA, USA

Paper 4

Modelling of adequate pretwist for obtaining straight timber

Mats Ekevad¹, Jarl-Gunnar Salin², Stig Grundberg³, Jan Nyström¹, Anders Grönlund¹

¹: Division of Wood Science and Technology, Luleå University of Technology,
SE-931 87 Skellefteå, Sweden

²: SP Wood Technology, Box 5609, SE-114 86 Stockholm, Sweden

³: SP Wood Technology, Skeria 2, SE-931 77 Skellefteå, Sweden

Abstract:

Wood in general and wooden studs in particular are often distorted due to uneven shrinkage during the drying process in the sawmill. Twist is often the most detrimental of all types of distortion, and it is caused by spiral grain in combination with variations in moisture content. For sawmills, the objective is to produce dried, straight boards, and one method of dealing with boards with excessive spiral grain is to sort them out and then dry them in a pretwisted position in order to obtain straight boards after drying.

A model using the finite element (FE) method for the simulation of drying twist distortions was first calibrated against laboratory experiments in which boards were dried with and without restraints and pretwists. Secondly, after the calibration, the FE results were compared to industrial test results for boards that were dried without restraints or with restraints with zero pretwist, i.e., straight restraints. The FE model used an elastic-ideally plastic material model in order to obtain permanent deformations. The calibration was to set the yield stresses so that there was a good match between FE results and results from the laboratory experiments. The comparison between the industrial test results and the FE results showed that the FE model is capable of realistic simulations of drying boards with and without restraints and presumably also pretwists.

Keywords: Distortion, Drying, Elastic, FEM, Plastic, Pretwist, Simulation, Spiral grain, Straight, Studs, Timber, Twist, Warp, Wood, Yield

1. INTRODUCTION

One important disadvantage of wood is that wood can distort. The result of this negative property is that wood products have lost market shares in applications where wood traditionally has been the natural choice of material. Steel studs have replaced wood in many applications mainly due to lack of straightness of the wooden studs (Johansson et al. 1994; Eastin et al. 2001).

Many scientists have studied wood distortions and the parameters that influence the magnitude of the distortion arising when moisture content (MC) changes (Danborg 1994; Woxblom 1999; Perstorper 1994). Three common modes of distortion are twist, bow and crook. Twist is mainly influenced by the magnitude of spiral grain and the distance from the pith (Johansson et al. 2001), but also by the gradient of the spiral grain angle (Ekevad 2005). Bow and crook are influenced by differences in the longitudinal shrinkage in different parts of a piece of wood and by growth stresses. The differences in longitudinal shrinkage depend mainly on the distribution and magnitude of compression wood and juvenile wood (Johansson & Klieger 2002). The juvenile wood content in a board can be controlled by proper selection of sawing pattern, i.e., by controlling where in the cross-section a board is sawn. Compression wood in logs is today mainly estimated by visual inspection of the end surfaces of the logs but can also to some extent be predicted with aid of the longitudinal shape of the logs (Öhman 2001).

Spiral grain occurs naturally more or less in all trees. Instead of running parallel to the pith, the grain runs spirally around the trunk like a helix. Since wood is an orthotropic material with higher shrinkage perpendicular to than parallel with the grain, the tree will twist when dried, and a board cut from the same tree will also twist (Säll 2002). The normal pattern on the northern hemisphere is that the spiral is left-handed in young wood, with a change to right handed in mature wood (Skatter & Kucera 1998). Some trees, however, seem to stay left-handed and just increase the left-handed spiral with age. Boards sawn from these trees have a very large tendency to twist (Nyström 2002). Spiral grain angles on logs and boards can be measured with aid of the tracheid effect. The tracheid effect utilizes the light-conducting properties of the softwood tracheids to measure the spiral grain angle. A small laser point is projected onto the wood surface. The light transmitted in the wood and scattered back forms an elliptic shape extended in the direction of the fibres. The ellipse of light is registered with a camera, and the orientation of the ellipse's major axis corresponds to the fibre direction (Nyström 2002).

Twist of boards with spiral grain occurs during MC changes and is most evident during the drying process. How the drying process is performed is therefore crucial for the final result. One way to decrease the twist problem is to pretwist the drying stacks in the opposite direction of the normal twist direction. This method has been in practise in New Zealand and Australia for many years in the drying of *Pinus radiata* (Northway 1981; Visser & Vermaas 1988). However, they have not reported how great the pretwist should be for different grain orientations in the sawn board and how different process parameters affect the result. For Norway spruce (*Picea abies* (L.) Karst.), reports of results from pretwisting experiments have recently been published by Salin et al. (2005) and Salin (2005).

Simulations of the drying of wood and of drying distortions of wood have been performed with finite element (FE) simulation methods or other methods by many scientists (Thomas 1983; Pang 1996; Mårtensson & Svensson 1997; Ormarsson 1999; Hammoun & Audebert 1999). However, it seems that no simulation of the adequate amount of pretwist that is needed in order to produce straight boards has been done. Thus, the objective of this work was to determine the magnitude of pretwist (depending on size of spiral grain angle) that was needed to keep boards straight after drying and to do this by using a (FE) simulation model. The FE results were to be compared with experimental results from the laboratory and from an industrial test in order to ensure the validity of the FE results.

2. MATERIAL AND METHODS

Laboratory experiments

The experiments (Salin et al. 2005) were performed in a laboratory dryer in which up to 4 boards can be dried in a twisted position. A few boards free to move can be dried at the same time. The twisted boards were fastened in a specially designed steel frame, which was inserted and locked into the dryer (see Fig. 1). The boards had to be about 1.5 m in length, and both ends were fastened by bolts in holders so that the effective twisted length was 1.37 m. The holder in one end was fixed and the other could be turned around an axis (in the board direction) and fixed in the position wanted. The torsional moment needed to twist the board into that position could also be measured. The drying schedules used in the experiments were quite normal, with a gradually increasing wet-bulb depression. However, the drying schedule was based on “constant dry bulb, decreasing wet-bulb temperature” and not on “constant wet bulb, increasing dry bulb-temperature”, which is more common in Scandinavian practice.

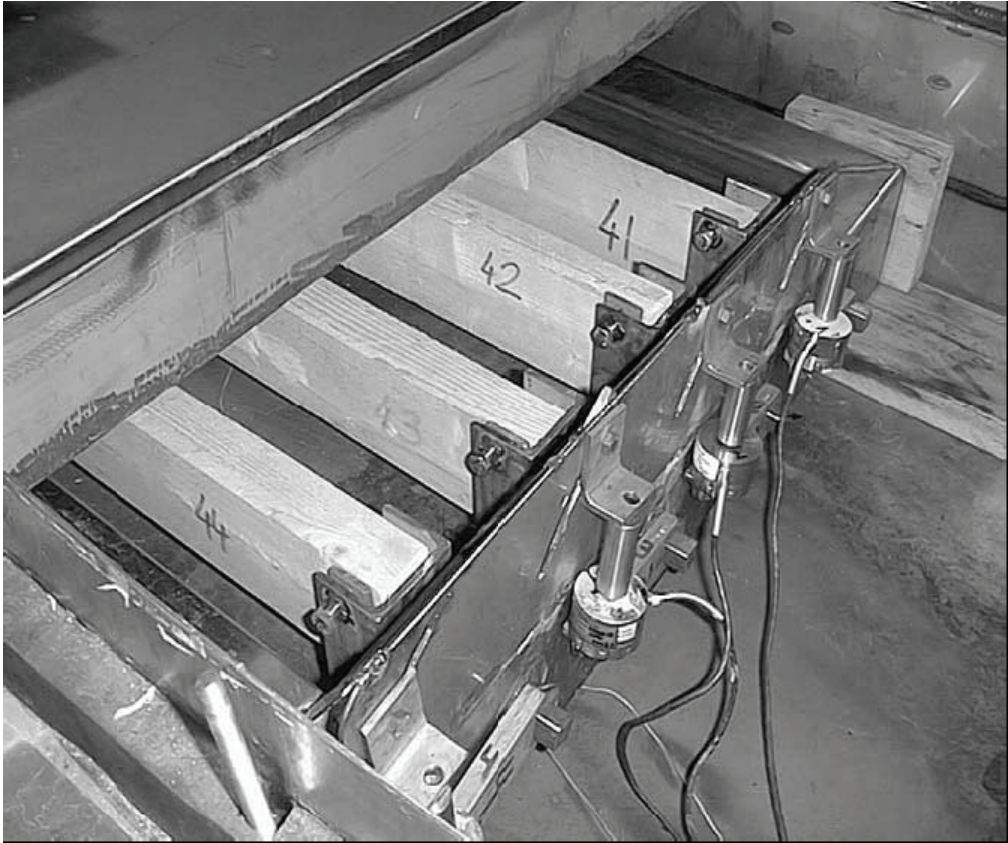


Fig. 1. The picture shows the ends of four boards fastened in a specially designed steel frame. The frame with the boards is inserted and locked into the dryer.

In a first step, 16 Norway spruce (*Picea abies* (L.) Karst.) boards with dimensions 47 x 100 mm and a length of about 1.5 m were dried completely free to twist and move. The boards were not from the same tree or the same log. Mean characteristic properties were measured for each board, namely spiral grain angle (by the scratching method on the sap side of the board), final MC, density, distance from the pith and twist both before and after drying. In the next step, a series of drying experiments with pretwisted boards was performed in the drier described above. In this step, 18 Norway spruce (*Picea abies* (L.) Karst.) boards with the same dimensions as the previous boards were dried. For each board the same mean characteristic properties as in the first step were measured, but in addition, the pretwist angle was also recorded.

Industrial test

The industrial test (Nyström 2002) was carried out at a sawmill in northern Sweden that was sawing Norway spruce (*Picea abies* (L.) Karst.) at the time. The spiral grain angle Θ (positive if right-handed) was measured on the log surface with a matrix camera utilizing the tracheid effect (Nyström & Grundberg 2002). All boards included in this study were square sawn and curve sawn. A total of 843 boards from the main yield were divided into six spiral grain classes according to the value of the spiral grain angle of the log to which they belonged. Each class was represented by the mid value of the interval as approximation of the spiral grain angle. The boards were also later measured manually for twist. The square-sawing pattern made the main yield touch the pith with one side. Thus the distance from pith was approximately constant for all boards with the same dimensions. The spiral grain angle classes of the 470 selected boards that were taken out to be included in this study (out of the total of 843 boards from the main yield) are described by Table 1. The reason for using only 470 selected boards was that the measured spiral grain angle for all produced boards followed a normal distribution, so the number of produced boards in the middle spiral grain classes was much higher than the number of produced boards in the extreme spiral grain classes. Therefore, only a randomly sampled partial set of the middle spiral grain classes was included in this study in order to get a more level number of boards in each spiral grain class. The distribution in Table 1 is thus not a true representation of the entire population.

Spiral grain interval (°)	$\Theta < -5^\circ$	$-5^\circ < \Theta < -2.5^\circ$	$-2.5^\circ < \Theta < 0^\circ$	$0^\circ < \Theta < 2.5^\circ$	$2.5^\circ < \Theta < 5^\circ$	$5^\circ < \Theta$	Sum for all angles
Mid value (°)	-6.25°	-3.75°	-1.25°	1.25°	3.75°	6.25°	
38x125 mm	2	20	60	79	82	31	274
50x150 mm	13	25	69	11	42	36	196
Sum for both dimensions	15	45	129	90	124	67	Total: 470

Table 1. Number of boards for different dimensions and spiral grain angle classes.

The sawn boards were dried in normal production at the sawmill. The boards were placed side by side in layers with stickers in between every layer. A number of layers with stickers in between were placed on top of each other in a drying stack. Four drying stacks were then placed on top of each other and placed in the kiln. All stacks of measured boards were placed as the top stacks in the kiln and thus without load on the top layers. Each stack comprised 23 or 20 layers of boards for thicknesses 38 or 50 mm respectively. The layers were numbered from the top to the bottom so that the top layer number was 1, and this was the layer in which all the boards could move freely. The load on every consecutive layer increased with increasing layer number due to the weight of the boards and stickers above the layer in question. All dimensions were dried to an MC of 18 % with a drying schedule with a dry-bulb temperature of 75°C and a wet-bulb temperature of 60°C at the end of the drying phase (corresponding to an equilibrium MC of 6.4 %).

Twist was manually measured after drying by laying each board on two parallel supports 3 m apart. The size of the twist was defined as the distance from the support to the fourth edge of the board while the three first edges were in contact with the support. To avoid the effects of cupping, all boards were measured with the sapwood side (concave) towards the support. Positive and negative twists were defined as in Fig. 2. The angular twist was calculated from these measurements.

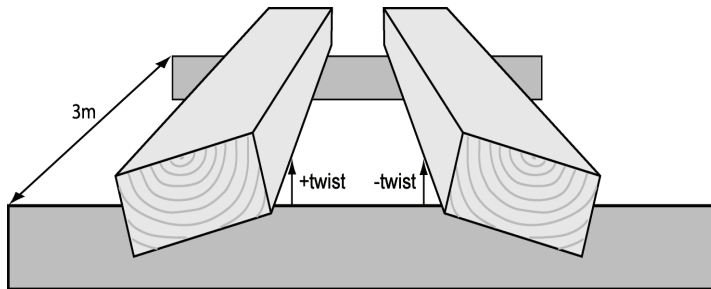


Fig. 2. Manual twist measurements where right-handed twist was defined as positive and left-handed twist as negative and measured over 3 m length.

Finite element analysis

In a first step, the drying process was simulated using a three-dimensional FE diffusion model with the MC u (mass of water/mass of dry wood) as the driving potential. A convective boundary condition was used where the boundary mass flow was $g = \beta_M (u_x - u_{EMC})$, where β_M was the mass transfer coefficient and u_{EMC} was the equilibrium MC of wood in the

surrounding air. $u_x = \min(u, u_{fsp})$ where u was MC on the boundary surface and u_{fsp} was the fibre saturation point. The boards were all assumed to have an initial MC of 80 % and an initial temperature of 20°C. Fig. 3 shows the values of u_{EMC} and (dry) temperature T of the surrounding air used to simulate the complete drying schedule for both the laboratory experiments and the industrial test. It was the normal drying schedule at the sawmill where the industrial test was performed. The drying schedule shown in Fig. 3 was used for all boards with thickness 47 and 50 mm, but was shortened 10 h for boards with thickness 38 mm.

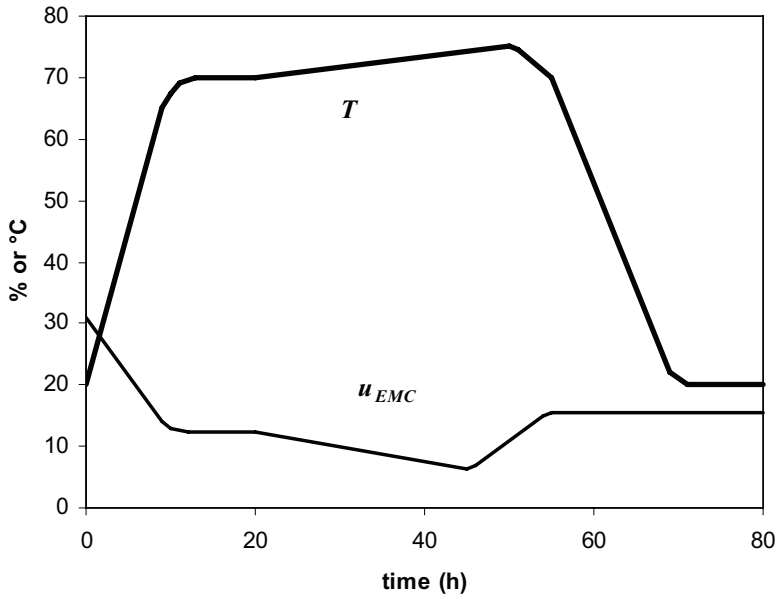


Fig. 3. Dry temperature T and equilibrium MC u_{EMC} of the surrounding air as a function of time. Input to the convective boundary condition of the diffusion model and used to simulate the drying schedule for boards with thicknesses 47 and 50 mm.

The diffusion coefficient and the mass transfer coefficient were taken from experiments (Danvind & Ekevad 2005) valid for Norway spruce (*Picea abies* (L.) Karst.), and the temperature was assumed to be uniform and equal to the dry temperature throughout the whole of the boards. The temperature dependence of the diffusion coefficient was an Arrhenius equation taken from Wiberg & Morén (1999), but the mass transfer coefficient was assumed not to depend on temperature. The commercial FE programme ABAQUS (Anon. 2004) was used together with user subroutines in order to model

wood as an orthotropic material. The orthotropic axes were modelled in a cylindrical coordinate system modified to take into account the spiral grain angle Θ to get appropriate radial, tangential and longitudinal directions as in Ormarsson (1999). The results from the first step were the distribution of u in the body as a function of time.

Then, in a second step, the stresses, strains and displacements (as functions of time) were calculated using the previously calculated distribution of u as input. In order to achieve permanent plastic deformations, an elastic-ideally plastic material description was introduced (Lubliner 1990; Clouston & Lam 2001; Mackenzie-Helnwein et al. 2005). A polynomial yield function (Tsai & Wu 1971; Deteresa & Larsen 2003) was used to calculate the yield limit and the direction of the plastic strain increments. Of the available 27 material coefficients in the yield function, a total of 9 material coefficients were set to be nonzero. These 9 material coefficients were calculated from the tension- and compression-yield stresses for one-dimensional (1D) normal loading in the three orthogonal directions and the shear yield stresses for 1D shear loading in the three shear directions. Since true yield stresses were not known, at first, 1D ultimate stresses in tension and shear were taken partly from strength values in Siimes (1967) and partly estimated from data in Wood Handbook (Anon. 1999) (see appendix). The three ultimate stresses in compression were set to half the value of the corresponding value in tension, based on observations of the relation between the ultimate stress limits in tension and compression (Wood Handbook 1999; Mackenzie-Helnwein et al. 2005). The material coefficients were functions of MC and temperature. Then, these ultimate stresses were multiplied by a factor S , $0 < S < 1$, and S was varied in order to give FE results that were as close to the laboratory results as possible. In this way, S was iterated and found to be 0.20, and the same $S = 0.20$ was used for all FE simulations that were intended to resemble the industrial test. The boundary conditions in the second step were fixed displacements at the ends (due to stickers) for the cases with specified pretwist or completely free displacements for freely drying boards. The remaining twist of the boards after drying, cooling to room temperature and removal of the stickers was taken as the result from the second step.

One of the most important input parameters when it came to twist calculations was the spiral grain angle Θ and its dependence on distance from pith. Here Θ was assumed to be a linear function of the radius varying from a constant value of -3.3° (i.e., left-handed 3.3°) at the pith (Nyström & Grundberg 2002) to the value in question either measured on the board surface (in the laboratory experiments) or the log surface (in the industrial test). This assumption made the gradient of Θ vary with the measured values

of Θ . Both Θ itself and the gradient of Θ influence twist (Stevens & Johnston 1960; Ekevad 2005).

The functions that were used for the moisture and temperature dependence in the elastic-ideally plastic material formulation and the fiber saturation point are shown in the appendix. Also shown are all numerical values of the coefficients that were used in the material equations described above.

3. RESULTS

Laboratory experiments

A regression analysis for the boards that were free to move during drying showed a significant relationship between Θ and twist after drying. No correlation to the final MC (shrinkage) and the distance from the pith was found. The correlation found may be expressed as

$$\rho = 1.220 \cdot \Theta \quad (1)$$

where ρ was the twist angle ($^{\circ}/\text{m}$, positive if right-handed) and the coefficient of determination was $R^2 = 0.81$. The result is also presented in Fig. 4. Eq. 1 predicts the amount of twist for boards located at the top of the kiln stack when no top loading is applied.

For the 18 boards that were dried with various amounts of pretwist, only the pretwist angle and Θ were found to significantly influence twist after drying. As above, no correlation with final MC or the distance from the pith was found. The drying schedule used was the same as for the free boards described above. The correlation found was

$$\rho = 0.510 \cdot \Theta + 0.812 \cdot \rho_p \quad (2)$$

where ρ_p was the pretwist used ($^{\circ}/\text{m}$, positive if right-handed) with $R^2 = 0.89$. ρ_p was kept constant for each board during the drying process. The results are illustrated by Fig. 5, which compares measured twist and predicted twist (Eq.2) after drying.

Finite element simulations of laboratory experiments

Fig. 6 shows the results for the FE simulations of the laboratory experiments for freely drying boards and pretwisted boards with $\rho_p = 0^{\circ}/\text{m}$ and $\rho_p = 2^{\circ}/\text{m}$ for the factor $S = 0.20$ compared to the laboratory results according to Eq. 2. A higher value of S than 0.20 will not give the difference in slope between free and pretwisted boards that is evident from the laboratory experiments.

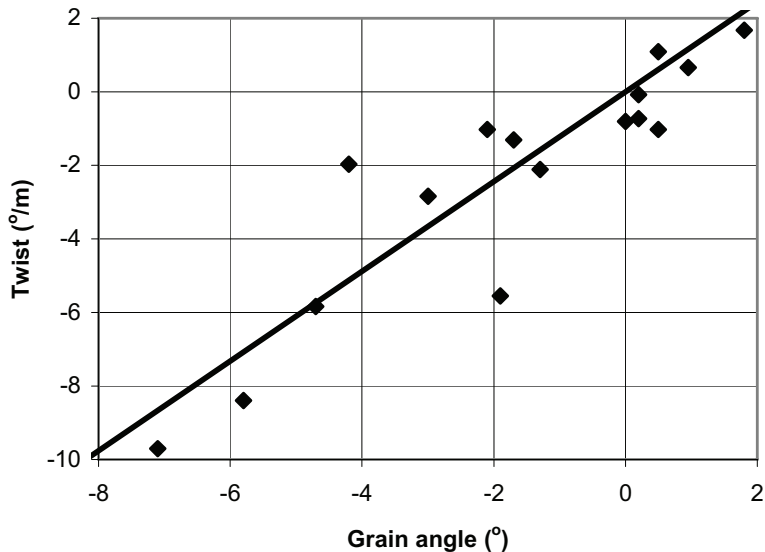


Fig. 4. Twist after drying as a function of the spiral grain angle Θ for boards that are free to move. Dots are measured twist, and the line is predicted twist calculated as $\rho = 1.220 \cdot \Theta$, (Eq. 1).

Industrial test and corresponding FE results

Figs. 7 and 8 show industrial test results and corresponding FE results for boards with dimensions 38 x 125 mm and 50 x 150 mm respectively. The industrial test results are shown as individual board results and trend lines. One symbol and trend line are used for layer 1 and 2 together and another symbol and trend line are used for layers 10 and higher. Test results for layers 1 and 2 together correspond approximately to FE results for freely drying boards, and test results for layers 10 and higher together correspond approximately to FE results for boards with pretwist equal to zero. The trend lines for the test results are lines fitted through the median twist values of all boards in each spiral grain angle interval.

For 38 x 125 mm boards in Fig. 7, the curve for the FE results for freely drying boards is above the trend line for the test results for layers 1 and 2. Also, the curve for the FE results for pretwist = 0 lies above the test results for layers 10 and higher. The slopes of the FE result curves agree with the slopes of the corresponding trend lines for the test results.

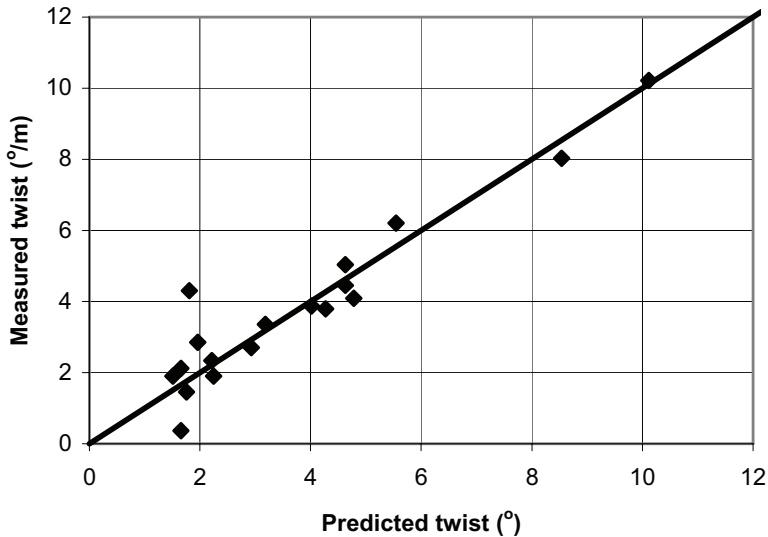


Fig. 5. Measured twist after drying as a function of predicted twist after drying for 18 boards which were dried with various amounts of pretwist ρ_p . Predicted twist ρ was calculated as $\rho = 0.510 \cdot \Theta + 0.812 \cdot \rho_p$, (Eq.2), where Θ was spiral grain angle. Dots are measured twist, and the line is equal measured and predicted twist.

For 50 x 150 mm boards in Fig. 8, the FE results for freely drying boards and the FE results for boards with pretwist = 0 approximately agree with the trend lines for the corresponding test results in the left half of the diagram, i.e., for left-handed spiral grain angles on the log surfaces. On the right side, i.e., for right-handed spiral grain angles on the log surfaces, the FE results are above the corresponding trend lines for the test results. The slopes of the FE result curves are higher than the slopes of the corresponding trend lines for the test results.

4. DISCUSSION

Laboratory experiments

The reason for the lack of correlation of the twist after drying to the final MC and the distance from the pith was presumed to be the small variation in these variables and the limited number of boards. Eq. 2 shows quite clearly that it was possible to “deform” a board by a pretwist operation, so that it became much straighter than a board that was free to move during drying.

This applies to the situation shortly after the drying process; i.e., long-term behaviour has to be investigated separately.

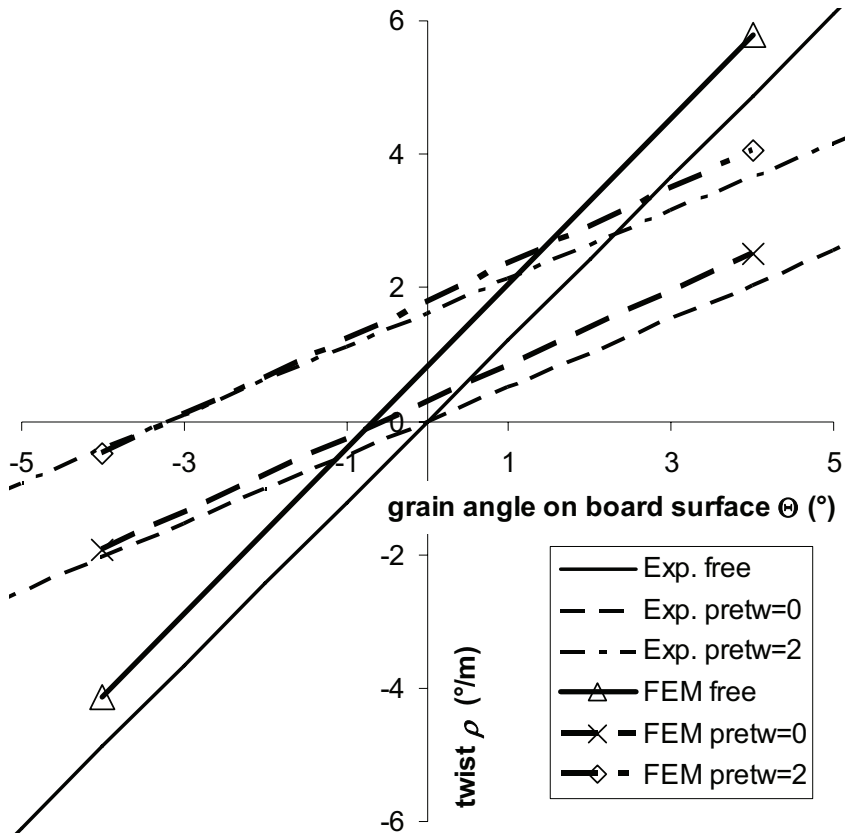


Fig. 6. Experimental results according to $\rho = 0.510 \cdot \Theta + 0.812 \cdot \rho_p$, (Eq. 2), for 47 x 100 mm boards which are free or pretwisted 0°/m or 2°/m during drying and corresponding FE results for $S = 0.20$.

Finite element simulations of laboratory experiments

The value $S = 0.20$ was found to give the best agreement between simulation and laboratory results. This may be regarded as a low value; i.e., it predicts low yield stresses, at least at room temperature, compared to the ultimate stresses. However, the dominant part of the drying process takes place at a high temperature (70°C to 75°C), and the value $S = 0.20$ was therefore believed to best predict yield stresses at this high temperature. S was assumed to be constant in this paper, even though in reality S may depend on temperature and MC. The largest discrepancy between FE results and

experimental results appears for the freely dried boards in which the FE twist results are larger than the experimental results; i.e., the FE method (FEM) gives more right-handed twist than the laboratory experiments for the same spiral grain angle.

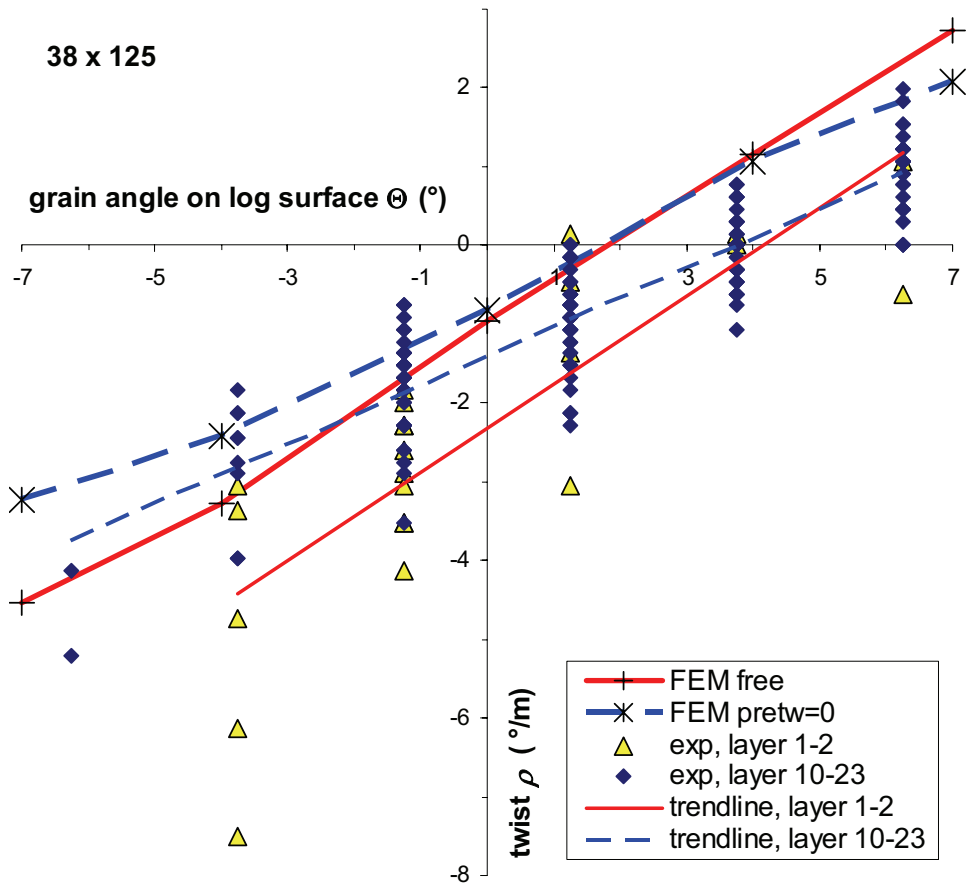


Fig. 7. Results from industrial test and corresponding FE results for 38 x 125 mm boards. Linear trend lines fitted through experimental median points.

Industrial test and corresponding FE results

The FE results agree well with the test results, bearing in mind the spread of the test results for individual boards. In detail, there is a tendency towards higher FE twist results than the test results, especially for right-handed (positive) spiral grain angles on the log surfaces. It is believed that most of the discrepancies between FE results and measurements that are shown in this paper are caused by the assumptions about the distribution of the spiral

grain angle, the assumptions regarding the yield stresses and also possible bias error in the industrial measurement of the spiral grain angle. However, other discrepancies may also be of influence, namely that the drying in the laboratory experiments took place on all four sides of the boards whereas in the industrial test drying took place on only two sides due to the side-by-side placement of the boards in the drying stack. Also, the restraints at the ends of the boards in the laboratory experiments and in the simulations are not similar to the restraints in the industrial test.

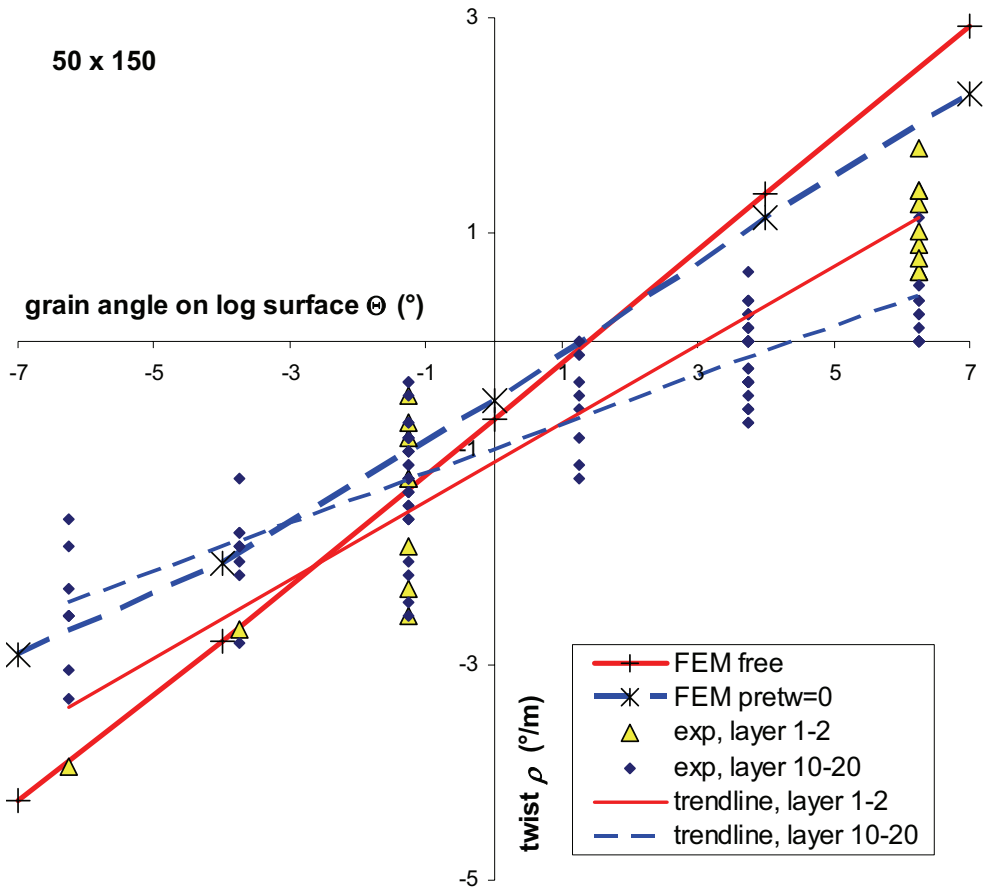


Fig. 8. Results from industrial test and corresponding FE results for 50 x 150 mm boards. Linear trend lines fitted through experimental median points.

This is because the end of a board in a drying stack in the industrial test may be placed a bit from the nearest sticker and thus a bit of the board near the end may be free. Also, in the industrial test there are several (at the most eleven) stickers along the length of a board. The drying scheme used in the

laboratory experiments and in the industrial test is not in detail the same, and especially the cooling phase may be different and may not be the one shown in Fig. 3. This is due to the fact that the drying scheme in Fig. 3 is an estimate of the desired values of the conditions as a function of time, and not the actual values. The final MC may also differ between the boards in the simulation and in the industrial test. The measurements of the spiral grain angle in the industrial test were done on the outer log surfaces, and the relevant spiral grain angles are in the board cross-sections, which are near the pith. This means that the relevant spiral grain angles in the board cross-sections and the value of the gradients of the spiral grain angles are sensitive to the assumption of the spiral grain angle value at the pith (-3.3°) and the assumption of a linearly varying spiral grain angle. Values of the yield stresses for Norway spruce (*Picea abies* (L.) Karst.) as a function of temperature and MC are not known, and the values found here from the calibration between the FE results and the laboratory experiment results depend on the assumption of a constant ratio between yield stresses and ultimate stresses even if the temperature and MC change, and that may not be an appropriate assumption. The industrial test was performed at full production speed, and there is a possibility that the spiral grain angles may have a bias error. Such a bias error would move the experimental points in Figs. 7 and 8 sideways, and that could explain part of the discrepancy between FE results and the industrial test results. Further tests of the FE model and more experiments are necessary in order to further increase the accuracy of the model and its predictions.

As a by-product, the calibration of the model gives as output the yield stresses for wood. However, it is unclear whether these yield stresses are realistic as yield stresses for wood or if they are only a means of curve-fitting this model to the experimental data. Thus, a detailed knowledge of reliable yield stresses for wood as a function of relevant temperatures and MCs is necessary in order to further investigate this issue, and that information is to a great degree lacking today. Also lacking is an explanation of what the causes of plasticization of wood are. Permanent deformations are only caused by permanent rearrangement of material, and it is important to discover the mechanisms of that rearrangement. The appropriateness of the elastic-ideally plastic model compared to other models such as mechanosorptive material models or combined elastic-plastic-mechanosorptive material models is unknown, and such an investigation would be beneficial.

Conclusions

The results show that realistic and permanent twist deformations can be achieved with this elastic-ideally plastic material model for industrial cases with pretwist = zero and for freely drying boards with no restraints. The model is presumably also capable of predicting the outcome for industrial cases with pretwists differing from zero, as was shown in the laboratory experiments, but no industrial confirmation of that capability was done.

5. ACKNOWLEDGEMENT

The authors express their gratitude to Formas (the Swedish Research Council for Environment, Agricultural Sciences and Spatial Planning), the European Commission through the STRAIGHT project (QLK5-2001-00276) and Swedish sawmills.

6. REFERENCES

Anon. (1999). *Wood Handbook-Wood as an engineering material*. Forest Products Laboratory. US Department of Agriculture.

Anon. (2004). *ABAQUS Users manual*. ABAQUS, Inc., RI, USA.
www.abaqus.com.

Clouston, P. L. and Lam, F. (2001). Computational modelling of strand-based composites. *Journal of Engineering Mechanics*, 127(8), 844–851.

Danborg, F. (1994). Drying properties and visual grading of juvenile wood from fast grown picea-abies and picea-sitchensis. *Scandinavian Journal of Forest Research*, 9(1), 91–98.

Danvind, J. and Ekevad, M. (2006). Local water vapour diffusion coefficient when drying Norway spruce sapwood. *Journal of Wood Science*, 52(3), 195–201.

DeTeresa, S. J. and Larsen, G. J. (2003). Reduction of the number of independent parameters for the Tsai-Wu tensor polynomial theory of strength for composite materials. *Journal of Composite Materials*, 37(19), 1769–1785.

Eastin, I. L., Shook, S. R. and Fleishman, S. J. (2001). Material substitution in the U.S. residential construction industry, 1994 versus 1998. *Forest Products Journal*, 51(8), 30–37.

Ekevad, M. (2005). Twist of wood studs: dependence on spiral grain gradient, *Journal of Wood Science*, 51(5), 455–461.

Hammoum, F. and Audebert, P. (1999). Modeling and simulation of (visco)-plastic behaviour of wood under moisture change. *Mechanics Research Communications*, 26(2), 203–208.

Johansson, G., Kligler, R. and Perstorper, M. (1994). Quality of structural timber-product specification system required by end-users. *Holz als Roh- und Werkstoff*, 52(1), 42–48.

Johansson, M., Perstorper, M., Kliger, R. and Johansson, G. (2001). Distortion of Norway spruce timber Part 2. Modelling twist. *Holz als Roh- und Werkstoff*, 59(3), 155–162.

Johansson, M. and Kliger, R. (2002). Influence of material characteristics on warp in Norway spruce studs. *Wood and Fiber Science*, 34(2), 325–336.

Lubliner, J. (1990). *Plasticity theory*. New York: Macmillan Publishing. ISBN 0-02-372161-8.

Mackenzie-Helnwein P., Eberhardsteiner, J. and Mang, A. (2005). Rate-independent mechanical behaviour of biaxially stressed wood: Experimental observations and constitutive modeling as an orthotropic two-surface elasto-plastic material. *Holzforschung*, 59, 311–321.

Mårtensson, A. and Svensson, S. (1997). Stress-strain relationship of drying wood. Part 1: Development of a constitutive model. *Holzforschung*, 51, 472–478.

Northway, R. (1981). Restraint forces needed to hold radiata pine heart-in studs straight during high temperature drying. *20th Forest Products Research Conference*, CSIRO, Melbourne, Nov. 1981.

Nyström, J. (2002). *Automatic measurement of compression wood and spiral grain for the prediction of distortion in sawn wood products*. Doctoral Thesis 2002:37. Luleå University of Technology.

Nyström, J. and Grundberg, S. (2002). Real-time, noncontact measurement of spiral grain on debarked sawlogs. Paper presented at *The 13th International Symposium on Nondestructive Testing of Wood*. 19–21 August 2002. University of California, Berkely Campus, California, USA. Also in Doctoral Thesis 2002:37 Luleå University of Technology.

Ormarsson, S. (1999). *Numerical analysis of moisture-related distortions in sawn timber*. Doctoral Thesis 1531. Chalmers University of Technology.

Pang, S. (1996). External heat and mass transfer coefficients for kiln drying of timber. *Drying Technology*, 14(3&4), 859–871.

Perstorper, M. (1994) *Quality of structural timber. End-user requirements and performance control*. Chalmers Tekniska Hogskola, Doktorsavhandlingar, n 998.

Salin, J.-G., Esping, B. and Hajek, B. (2005). *Drying and re-conditioning of pre-twisted boards. Laboratory and industrial tests*. Report on WP 2.4 and WP 2.7 of the STRAIGHT project. SP Report 2005:14.

Salin, J.-G. (2005). Drying of boards, prone to twist, in a pre-twisted position. *Proceedings of the 9th International IUFRO wood drying conference*, Nanjing, China, 21-26 August 2005 (pp. 253–258).

Siimes, F. E. (1967). *The effect of specific gravity, moisture content, temperature and heating time on the tension and compression strength and elasticity properties perpendicular to the grain of Finnish pine, spruce and birch wood and the significance of these factors on the checking of timber at kiln drying*. Publication 84, The state institute for technical research, Helsinki, Finland.

Skatter, S. and Kucera, B. (1998). The cause of the prevalent directions of the spiral grain patterns in conifers. *Trees: Structure and Function*, 12(5), 265–273.

Stevens, W. C. and Johnston, D. D. (1960). Distortion caused by spiralled grain. *Timber Technology*, 68, 217–218.

Säll, H. (2002). *Spiral grain in Norway spruce*. Doctoral Thesis, no. 22/2002. Växjö University.

Thomas, H. R. (1983). Numerical analysis of drying induced stresses in timber: an orthotropic model. *Mechanics of Materials*, 2, 249–263.

Tsai, S. W. and Wu, E. M. (1971). A general theory of strength for anisotropic materials. *Journal of Composite Materials*, 5, 58–80.

Visser, J. J. and Vermaas, H. F. (1988). Steaming under restraint to remove twist in previously dried *Pinus radiata* boards. *Holzforschung*, 42(1), 59–63.

Wiberg, P. and Morén, T. (1999). New Information on Sapwood Drying: CT-Scanning Profiles of Moisture Content during Drying, *Proceedings of the first Wood Drying Workshop in COST ACTION E15*, Edinburgh.

Woxblom, L. (1999). *Warp of sawn timber of Norway spruce in Relation to End-user Requirements*. Doctoral Thesis. Swedish University of Agricultural Sciences.

Öhman, M. (2001). *The Measurement of Compression Wood and Other Features and the Prediction of Their Impact on Wood Products*. Doctoral Thesis 2001:42. Luleå University of Technology.

9. APPENDIX

Material coefficients used in the FE simulations

Indices 1, 2 and 3 stand for radial, tangential and fibre directions respectively. Indices 1 to 6 on stress, strain and elastic modulus components indicate normal directions 1, 2 and 3 and shear directions 12, 13 and 23 respectively.

Elastic material coefficients at $T = 20^\circ\text{C}$ and $u = 20\%$ in MPa were set as (estimated from data in *Wood Handbook* (1999)): $E_1 = 424.8$, $E_2 = 249.4$, $E_3 = 11390$, $E_4 = G_{12} = 34.17$, $E_5 = G_{13} = 729.0$, $E_6 = G_{23} = 694.8$. The variations with T and u for all E and G components were brought about via the linear functions f_i and g_{Ei} , as $E_i(T, u) = E_i(T = 20^\circ\text{C}, u = 20\%) \cdot f_i(T) \cdot g_{Ei}(u)$ for $i = 1, 2, \dots, 6$. The gradients of the linear functions f_i were for $i = 3$

$$\frac{\partial f_3}{\partial T} = -0.00233 \frac{1}{^\circ\text{C}} \text{ and for the other components } (i = 1, 2, 4, 5, 6),$$

$$\frac{\partial f_i}{\partial T} = -0.011 \frac{1}{^\circ\text{C}}. \text{ The gradients of the linear functions } g_{Ei} \text{ were for } u < (u_{\text{fsp}} -$$

$$0.04) \text{ and } i = 3 \quad \frac{\partial g_{E3}}{\partial u} = -0.7344 \text{ and for}$$

$$u < (u_{\text{fsp}} - 0.04) \text{ and } i = 1, 2, 4, 5, 6 \quad \frac{\partial g_{Ei}}{\partial u} = -4.67. \text{ The gradients of the linear}$$

functions g_{Ei} were zero for all components, i.e. $g_{Ei} = g_{Ei}(u = u_{\text{fsp}} - 0.04)$ for $u > (u_{\text{fsp}} - 0.04)$. The fibre saturation point was set as $u_{\text{fsp}} = 0.3298 - 0.001 \cdot T$ (T in $^\circ\text{C}$). Poissons ratios were set as constants, $\nu_{12} = 0.418$, $\nu_{13} = 0.00707$, $\nu_{23} = 0.00521$. Symmetry gave for $i, j = 1, 2, 3$ that $\nu_{ij}/E_i = \nu_{ji}/E_j$. Constant moisture expansion coefficients were set as $\beta_1 = 0.1367$, $\beta_2 = 0.2267$, $\beta_3 = 0$ for $u < u_{\text{fsp}}$. For $u > u_{\text{fsp}}$ there was no moisture expansion.

1D ultimate stresses at $T = 20^\circ\text{C}$ and $u = 20\%$ in MPa were set as (estimated from *Wood Handbook* (1999) and Siimes (1967)): $\sigma_{1u} = 4.6$, $\sigma_{2u} = 4.6$, $\sigma_{3u} = 60.$, $\tau_{12u} = 1.66$, $\tau_{13u} = 7.2$, $\tau_{23u} = 7.2$.

Variations with T and u were brought about via the linear functions f_i (the same functions as shown above) and $g_{\sigma i}$ for all σ and τ components, $\sigma_i(T, u) = \sigma_i(T = 20^\circ\text{C}, u = 20\%) \cdot f_i(T) \cdot g_{\sigma i}(u)$ where the gradients

$$\text{for } u < (u_{\text{fsp}} - 0.04) \text{ and } i = 3 \text{ were } \frac{\partial g_{\sigma 3}}{\partial u} = -2.917 \text{ and for } u < (u_{\text{fsp}} - 0.04) \text{ and}$$

$$i = 1, 2, 4, 5, 6 \text{ were } \frac{\partial g_{\sigma i}}{\partial u} = -4.67. \text{ For } u > (u_{\text{fsp}} - 0.04) \text{ then the gradients of } g_{\sigma i}$$

were zero, i.e. $g_{\sigma i} = g_{\sigma i}(u = u_{\text{fsp}} - 0.04)$ for all components.

1D yield stresses in tension and shear were obtained from the 1D ultimate stresses shown above as $\sigma_{isd} = S\sigma_{iu}$ for $i = 1, 2, \dots, 6$. $0 < S < 1$ was the yield stress factor. 1D yield stresses in compression for the normal stress components were assumed to be $\sigma_{isc} = \sigma_{isd}/2$ for $i = 1, 2, 3$.

Appendix 5

ON THE MECHANICS OF POLE VAULTING

by

Mats Ekevad

Licentiate thesis

*Division of Solid Mechanics, Department of Technology, Uppsala University,
S-751 21 Uppsala, Sweden*

UPPSALA UNIVERSITY 1995

This licentiate thesis comprises the following papers:

- I. M. EKEVAD and B. LUNDBERG, Influence of pole length and stiffness on the energy conversion in pole vaulting. Submitted for publication (1995).
- II. M. EKEVAD and B. LUNDBERG, Simulation of "smart" pole vaulting. *J. Biomechanics*, Vol. 28, No. 9, pp. 1079-1090, 1995.

Abstract

Pole vaulting is simulated for a passive and an active vaulter using two different finite element models.

In the simulation of a passive vaulter in Paper I, a vaulter represented by a point mass at the end of a pole is used. The pole is modelled with twenty beam elements. Simulations with a given vaulter show that there exists an optimum combination of pole length and stiffness which gives the vaulter the maximum vault height. In this optimum pole vault, the increase of the potential energy of the vaulter is 0.87 times the initial kinetic energy of the vaulter and the pole.

In the simulation of an active vaulter in Paper II, a vaulter represented by seven beam elements linked together by pin joints is used. The pole is modelled with twenty beam elements. Limited muscle torques at the vaulter joints control the vaulter movements. A control strategy such that the vaulter strives to carry through a prescribed sequence of motions, corresponding to a given style, is used for the control of the muscle torques. Simulations with different pole lengths for a given vaulter show that there exists an optimum pole length which gives the vaulter the maximum vault height. In this optimum pole vault, the increase of the potential energy of the vaulter is 1.27 times the initial kinetic energy of the vaulter and the pole. The simulation model can also be used to judge the importance of vaulter strength or to optimize the vaulting style.

1. Introduction

Pole vaulting is a sports discipline where a sportsman uses a pole to lift his body as high as possible in order to pass a bar. The influence of the pole on the heights that can be reached is great as can be understood from the historical development of the pole vault world record in conjunction with the introduction of new pole designs and materials. See Section 2 below for a historical review of pole vaulting. The introductions of new and better pole materials have led to changes in pole designs and vaulting styles and these changes have led to new pole vault world records. It is generally not possible to separate from each other the effects on the world record of the developments of vaulting style, training methods, pole materials and pole design, as all these factors are interdependent.

As it has been in the past, the development of pole vaulting in the future will be dependent on the development of pole design. Traditionally, new pole designs have been developed by trial and error. By testing different pole designs and pole materials, and by altering vaulting styles to suit these new poles, new successful pole designs have evolved.

The research work described in Papers I and II is an attempt to increase the understanding of the mechanics of the pole vault and to create an efficient computer tool for pole vault simulations. An increased theoretical understanding of the mechanics of the pole vault helps in the process of finding new pole designs, and a computerized simulation tool helps to evaluate new pole designs. It is believed that this research work can result in an increase of the speed with which new, successful pole designs can be developed. Also, there is a possibility to simulate and evaluate changes in vaulting style and vaulter strength.

Several authors have studied or simulated the pole vaulting process. Dillman and Nelson (1968) determined experimentally kinetic and potential energies for a pole vaulter during a vault. Hubbard (1980) made computer simulations with an elastica pole and a three-segment vaulter controlled by internal muscle torques and studied the effect of the initial velocity of the vaulter. Walker and Kirmser (1982) used a one-segment pendulum vaulter to study the effect of pole stiffness. McGinnis (1984) made finite element simulations with different pole stiffnesses for a vaulter with a fixed scheme of motions. Jayasuriya, Hubbard and Hovorat (1984) used optimal-aim control to derive muscular controls for a simulation of a pole vault. Braff and Dapena (1985) used a ten-segment vaulter and an elastica pole to simulate pole vaulting with different pole stiffnesses. However, no one seems to have made a parameter optimization with a passive vaulter model as described in Paper I or made simulations with an active and "smart" vaulter capable of vaulting well with different poles as described in Paper II.

In Paper I a passive vaulter represented by a point mass at the top of a pole

is used in a finite element computer simulation. The variables of the problem are non-dimensionalized and a performance figure of the vault is defined. Effects on the performance figure of variations of pole length and pole stiffness for a given vaulter are studied. It is shown that an optimum combination of pole length and stiffness exists for a given vaulter.

In Paper II a method for simulation of pole vaulting with an active, "smart" vaulter is described. A standard finite element programme together with an algorithm for the definition of the "smart" control of the vaulter's movements, is used. The vaulter model has five independent segments and the simulated vaulter uses his limited muscle torques to move according to a prescribed vaulting scheme (simulating a given vaulting style) as fast as is necessary to be finished with the movement scheme when the pole is standing vertically over the pole box.

In Section 2, the history of pole vaulting is shortly reviewed. Simulations of pole vaulting with a passive and an active vaulter are the subject of Papers I and II, respectively. The methods and some results from these papers are presented in Sections 3 and 4, respectively. Finally, in Section 5 conclusions from the simulations are made.

2. History of pole vaulting

The history of modern pole vaulting is described by Ganslen (1973), and a short review of this description with emphasis on the development of poles is made here. Pole vaulting is a very old sports game, but in 1889 the rule was stated that the lower hand is not allowed to be moved above the upper hand. The popular technique of pole climbing was ruled out, and the history of modern pole vaulting started. The history of pole vault world records between 1903 and 1994 is shown in Fig. 1, with data from Ganslen (1973), Bra Böckers Lexikon (1989) and *Idrottsboken årets idrott* (1990-1994). Wooden poles were used in the beginning, but the idea of using bamboo poles can be traced back to 1879. However, bamboo poles did not become popular until after 1900, and the bamboo era was at its peak in the 1930s before World War II. Some vaulters continued to use bamboo poles into the early 1950s. The aluminium pole appeared on the market in the 1930s but did not become successful. It was light but very stiff. In the 1940s the steel pole entered the market and in 1948 the first fibreglass poles became available. The fibreglass poles have dominated the market since the late 1950s, and the steep increase in world records since then is mainly due to the development of the fibreglass poles and the corresponding vaulting styles. Other technical developments, which have influenced the world records during the period shown in Fig. 1, are the introduction of the pole box (about 1910), the synthetic runways (in the 1970s) and softer landing areas.

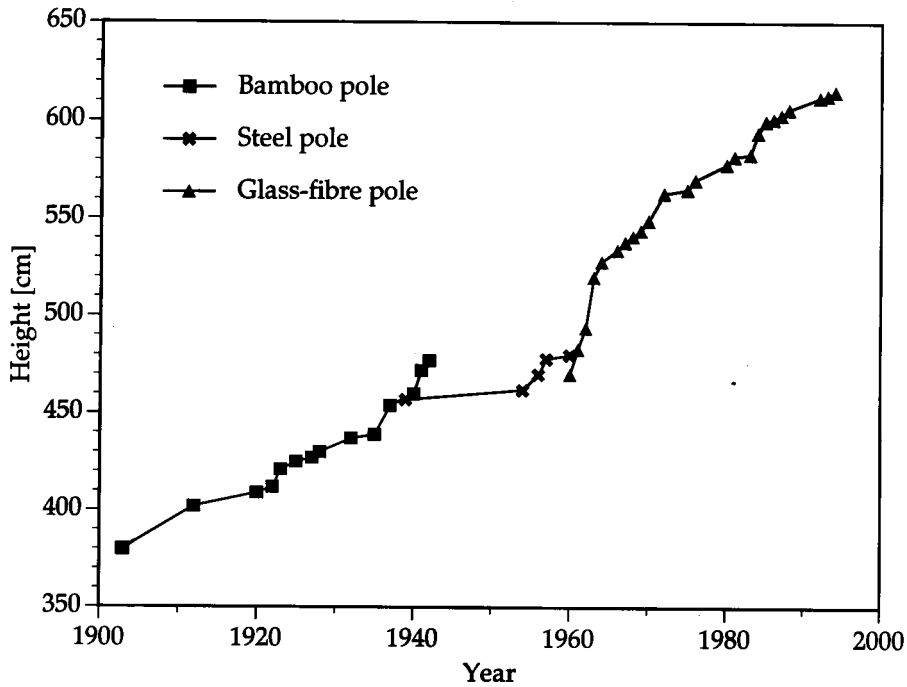


Fig. 1. The history of pole vault world records between 1903 and 1994 with different poles.

3. Simulation of pole vaulting with a passive vaulter

A simple impact process representing a pole vault is shown in Fig. 2. The pole is represented by an oblique, slightly curved beam and the vaulter is represented by a point mass attached to the top end of the pole. The pole and the vaulter have an initial velocity and at time zero the bottom end of the pole impacts a rigid support. The path of the vaulter is studied as time progresses and the maximum height of the vaulter is determined. Gravity influences the two-dimensional process. The purpose with the process is a transformation of kinetic energy of the vaulter and the pole to potential energy of the vaulter.

The performance figure of the pole vault is defined as the ratio of the potential energy of the vaulter to the initial kinetic energy of the vaulter and the pole, i.e.,

$$\eta = \frac{Mg(Y_M - H)}{(M + mL)V^2/2} \quad (1)$$

where M is the mass of the vaulter, g is the acceleration of gravity, Y_M is the maximum vertical height of the vaulter, H is the grip height, m is the

mass per unit length of the pole and V is the initial velocity of the vaulter and the pole.

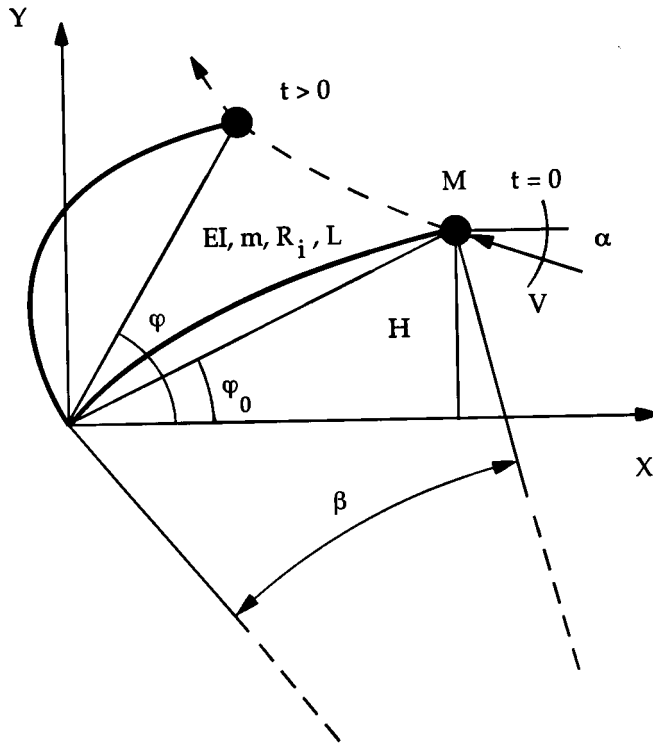


Fig. 2. Point mass on a beam with initial curvature impacting a stiff support.

Simulations of the pole vault are carried out in the finite-element programme ABAQUS and the performance figure is calculated as a function of dimensionless variables. The dimensionless variables involved in the pole vault are

$$\begin{aligned} h = H/L, \quad \beta = L/R, \quad r_i = R_i/L, \quad \nu, \quad \alpha, \\ v = V/(gL)^{1/2}, \quad \mu = M/mL, \quad \kappa = EI/mgL^3, \end{aligned} \quad (2)$$

where h is the dimensionless vaulter grip height, L is the pole length, β is the pole prebend angle, R is the constant radius of curvature of the prebent pole, r_i is the dimensionless pole radius of inertia, R_i is the pole radius of inertia, ν is Poissons ratio, α is the take-off angle, v is the dimensionless vaulter initial velocity, μ is the dimensionless vaulter mass and κ is the dimensionless pole stiffness. The quantity EI is the bending stiffness of the

pole. Variations of the pole length are carried out by defining dimensionless variables with index 0 based on a fixed pole length L_0 for variables h , r_1 , v , μ , and κ and by defining a dimensionless pole length $\lambda=L/L_0$.

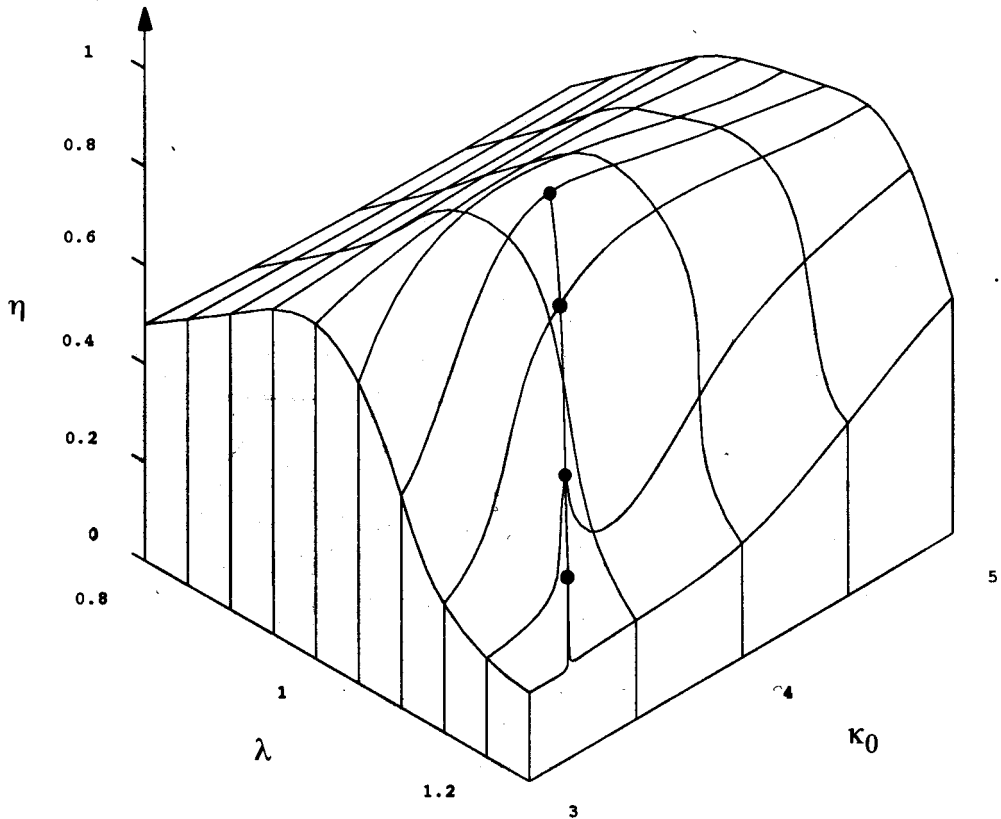


Fig. 3. Performance figure η versus dimensionless pole stiffness κ_0 and dimensionless pole length λ for the passive vaulter with a flexible pole with $3 \leq \kappa_0 \leq 5$ and $0.8 \leq \lambda \leq 1.25$. The curve on the surface shows where the angle-to-ground at the top position φ_M is 90° .

The performance figure η as a function of dimensionless pole length λ and dimensionless pole stiffness κ_0 is shown in Fig. 3 for a given vaulter with a mass M of 75 kg, a grip height H of 2.25 m, a take-off velocity V of 8.5 m/s and a take-off angle α of 20° . Also, the vaulter have a reference pole with a length L_0 of 5.0 m, a prebend angle β of 0.40, a pole mass per unit length m of 0.60 kg/m, a radius of inertia R_1 of 15 mm, and a Poisson's ratio ν of 0.25. These are realistic values for an elite pole vaulter and an appropriate pole. The acceleration of gravity g is taken to be 10 m/s². The corresponding

dimensionless variables are: $\mu_0=25$, $v_0=1.2$, $h_0=0.45$ and $r_{i0}=0.0030$. The performance figure has a global maximum of 0.87 for $\lambda=1.1$ (corresponding to a pole length of 5.5 m) and $\kappa_0=3.7$. In Fig. 4 the trajectory for this "optimum" pole vault is shown.

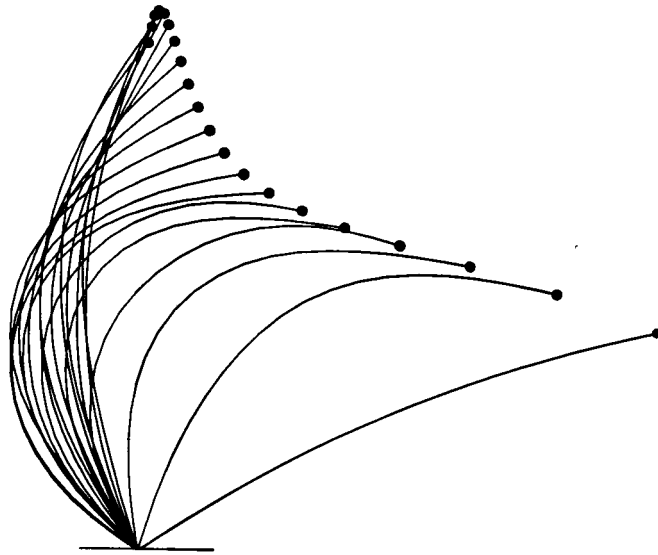


Fig. 4. Deformed configuration of the pole and position of the passive vaulter at different times. Pole with optimal combination of length and stiffness, $\lambda=1.1$ and $\kappa_0=3.7$.

4. Simulation of pole vaulting with an active vaulter

The two-dimensional finite element model of the pole vault is shown in Fig. 5. The pole is modeled with twenty beam elements and the vaulter with seven such elements linked together by pin joints. Muscle torques at the vaulter joints control the angles between each vaulter segment, see Fig. 6. The muscle torques are limited to realistic values for an elite pole vaulter.

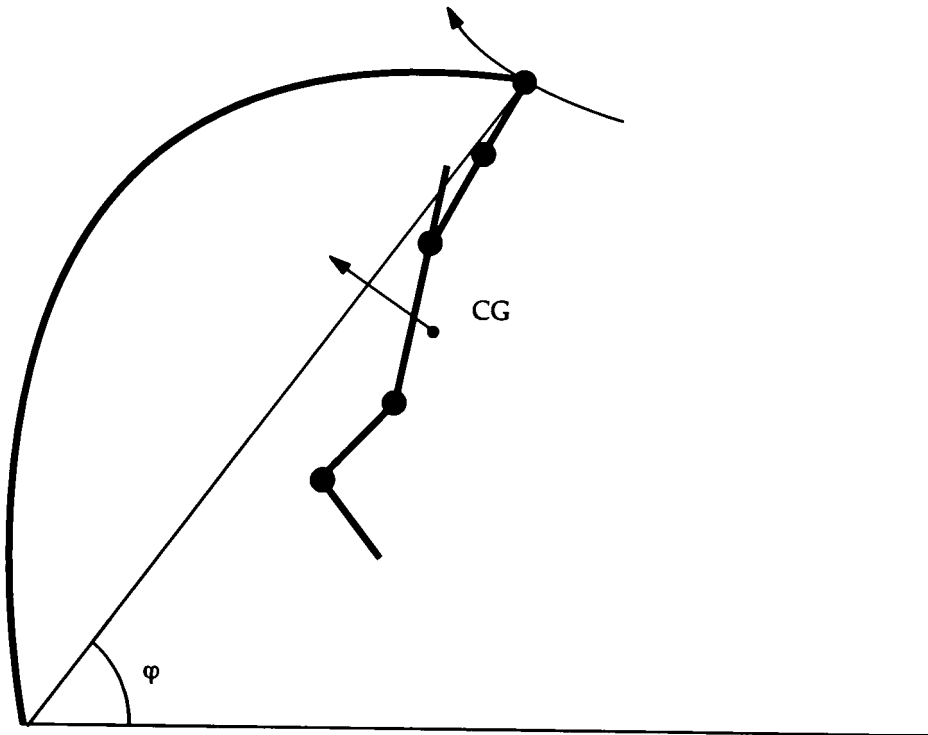
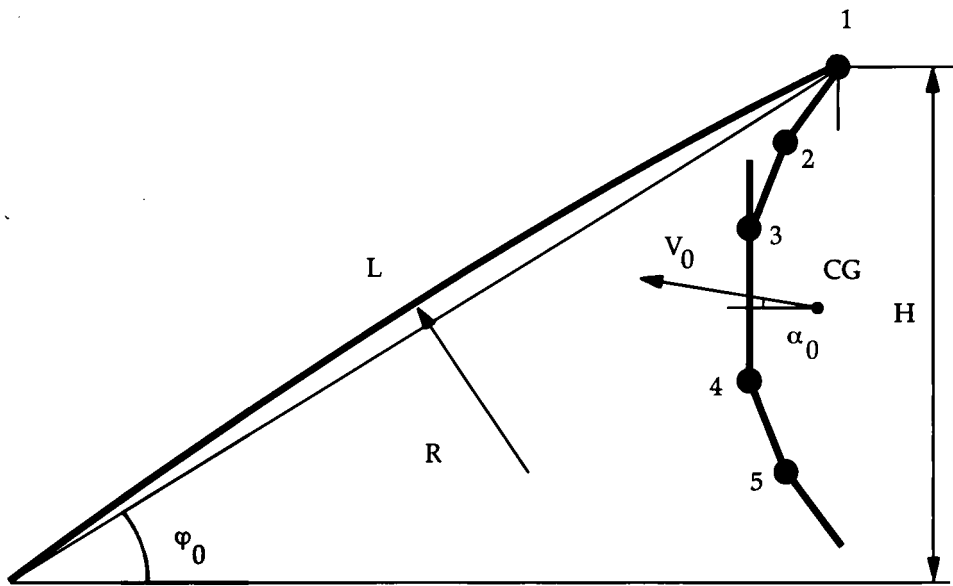


Fig. 5. (a) Pole and active vaulter in initial configuration when the last foot of the vaulter leaves ground. The leg shown is in an intermediate position between the real legs. CG denotes the center of gravity of the vaulter and R is the radius of curvature of the initially circular pole. (b) Pole and active vaulter at time t.

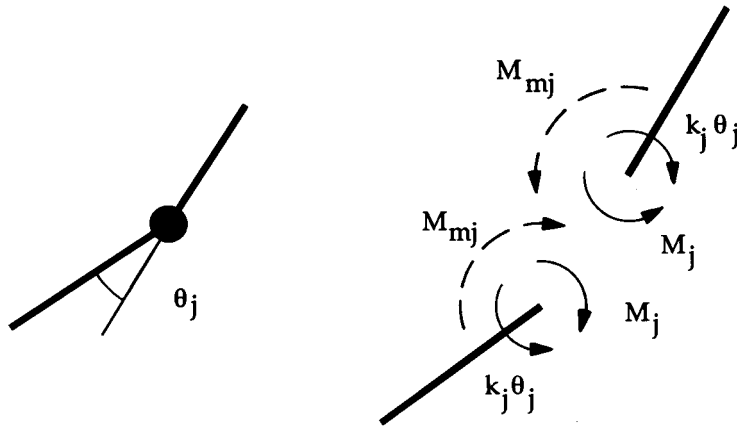


Fig. 6. Muscle torque M_{mj} , control torque M_j and spring torque $k_j \theta_j$ at joint j of the active vaulter. The torques are related by the equality $M_{mj} = M_j - k_j \theta_j$.

“Smart” behaviour of the vaulter movements is achieved through control of the vaulter muscle torques according to a given strategy. This control strategy is such that the vaulter, to the best of his ability, strives to carry through a prescribed sequence of motions, corresponding to a given style, during a vault. The prescribed motion is taken from measurements on a successful reference pole vault (by Slusarski, Olympic gold winner 1976), and described in Fig. 7 as a function of dimensionless time ξ . The variable ξ is zero when the vaulter leaves ground and is unity when the vaulter lets the pole loose.

The control strategy is such that the vaulter varies the pace of his movements during the pole vault, i.e., the variable $\xi = \xi(t)$ becomes a function of time t which is determined according to a strategy algorithm. The strategy is based on an experimental observation of the proportionality between the pole to ground angle φ and time t during the first part of the reference pole vault, see Fig. 8. The strategy is that the vaulter moves in such a pace that he will reach $\xi = \xi_v$ when the pole is standing vertically over the pole box, i.e., $\varphi = 90^\circ$. This control strategy is found to work well when simulating pole vaulting with poles of different lengths for a given vaulter.

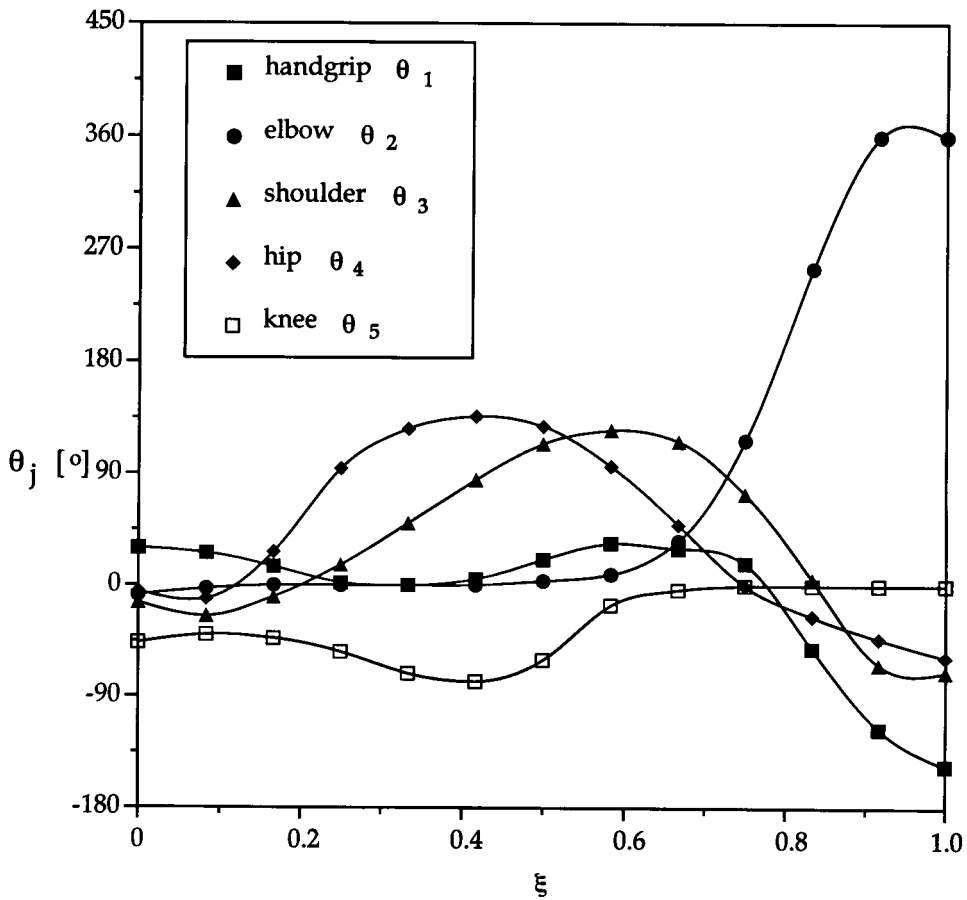


Fig. 7. Body segment angles θ_j versus dimensionless time ξ in the reference pole vault by Slusarski.

The parameter ξ_v is determined experimentally from the measured pole vault, see Fig. 8, but is tried out separately in each of the simulations with different pole lengths in order to give a realistic rotation of the vaulter at the top position. The vaulter strategy algorithm is programmed as a user subroutine linked to the finite element programme ABAQUS.

Simulations of pole vaults are made for a vaulter with body dimensions, initial velocity and muscle strength set to realistic values for an elite pole vaulter. A good pole vault for each pole length giving a realistic vaulter rotation at the top position is tried out in a sequence of simulations by varying the parameter ξ_v . A performance figure η is defined as the ratio between the maximum increase of the potential energy of the vaulter and the initial kinetic energy of the vaulter and the pole, i.e.,

$$\eta = \frac{mg(h-h_0)}{(m+m_p)V_0^2/2} \quad (3)$$

where m is the vaulter mass, m_p is the pole mass, h is the maximum height of the center of gravity of the vaulter during the vault, h_0 is the initial height of the center of gravity of the vaulter and V_0 is the initial pole and vaulter velocity.

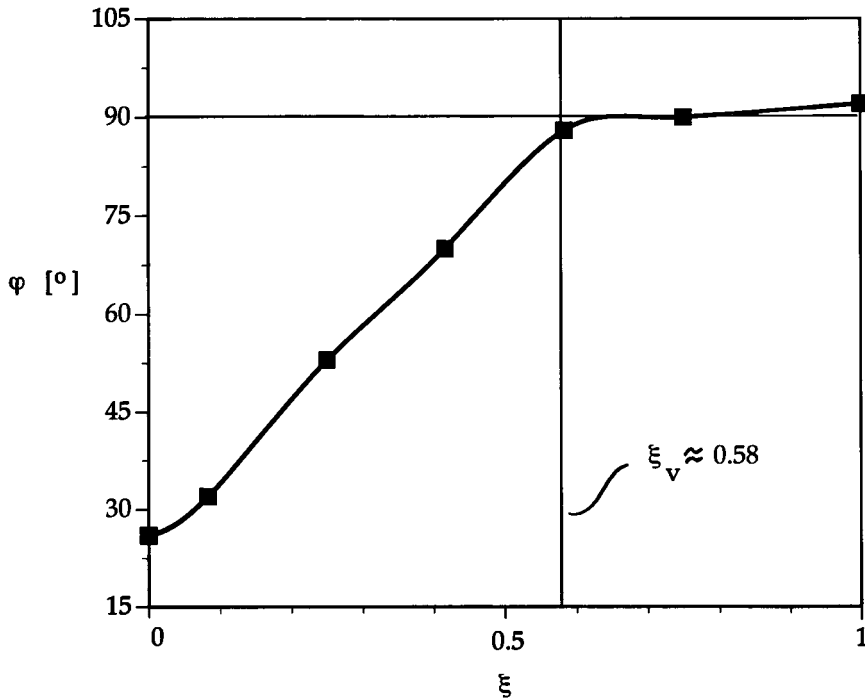


Fig. 8. Pole to ground angle φ in the reference pole vault by Slusarski.

Fig. 9 shows the maximum height of the center of gravity of the vaulter versus pole length for simulations with five different pole lengths. The optimum pole length is 4.75 m which gives a performance figure of 1.27 and a simulation of this optimum pole vault is shown in Fig. 10.

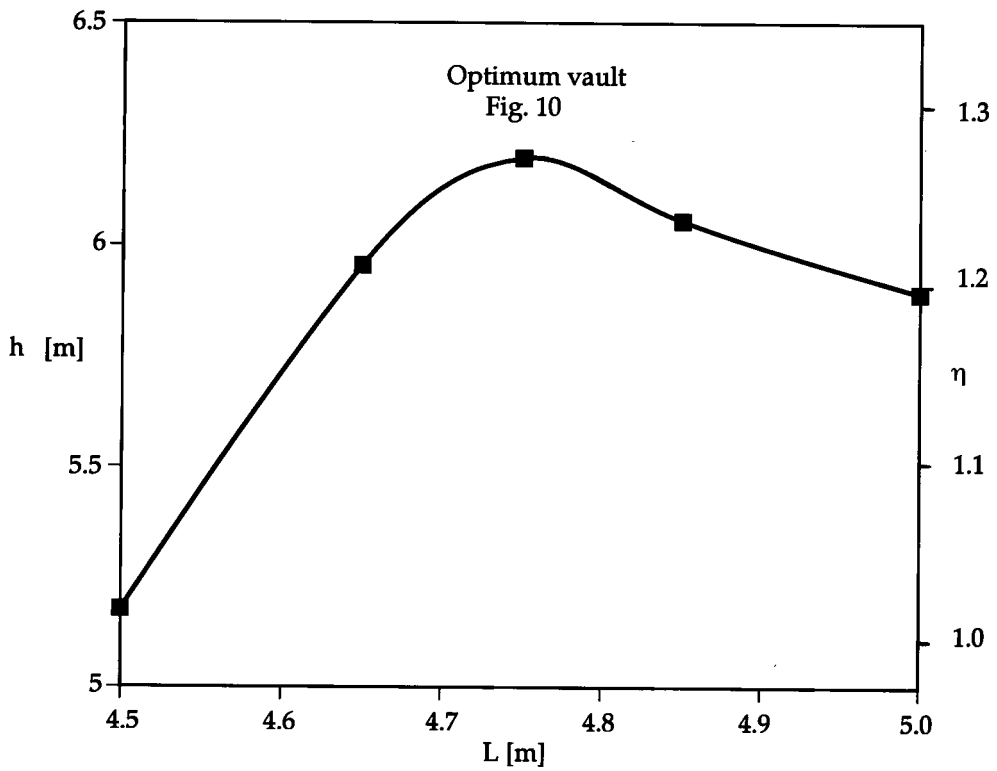


Fig. 9. Vault height h and the performance figure η versus pole length L for the active vaulter.

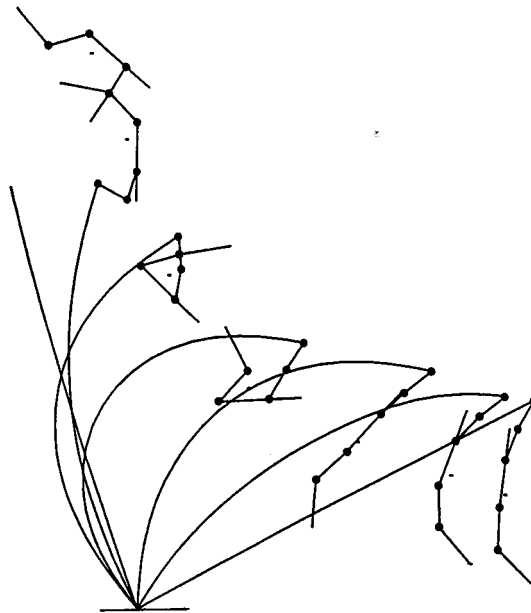


Fig. 10. Simulation of a pole vault with the optimum pole length for the active vaulter.

5. Conclusions

The simulations with the passive vaulter show that there exists an optimum combination of pole length and pole stiffness with regard to performance figure for a given vaulter. The optimum pole vault is characterized by the vaulter reaching the top position right above the pole box with a low horizontal velocity and with a nearly straight pole. Stiffer poles make the vaulter "bounce back" and never reach the position right above the pole box, and weaker poles make the vaulter reach the top position after he has passed the position right above the pole box. Longer poles do not have stiffness enough to straighten out completely and shorter poles straighten out completely but then the vaulter has an excessive vertical velocity and his maximum vertical height is restricted by the pole length. The optimum performance figure is 0.87.

The simulations with the active and "smart" pole vaulter show that the pole and the vaulter behave in realistic ways. The vaulter is capable of vaulting well when vaulting with different poles, and thus it is possible to use the simulation method to optimize pole designs. The results show that there is an optimum pole length with regard to vault height for a given vaulter and pole. The performance figure for this optimum pole vault is 1.27, which shows that the work performed by the vaulter during the vault is significant. The simulation method might also be used for optimization of vaulting style or for judging the importance of vaulter strength.

Acknowledgements

I am indebted to my supervisor and coauthor Professor Bengt Lundberg for his encouragement and support during the work. Also, I am indebted to the Industrial Development Centre, the Nordic Sport and the Swedish Board for Technical Development (STU) for their financial support.

References

ABAQUS Users manual version 4.8 (1989). Available from HKS Inc., 100 Medway Street, Providence, RI 020906, Rhode Island, USA.

Bra Böckers Lexikon (1989). Bokförlaget Bra Böcker.

Braff T. J. and Dapena J. (1985), A two-dimensional simulation method for the prediction of movements in pole vaulting. In D.A. Winter (editor) et al., *Biomechanics IX-B*, Champaign, Ill., Human Kinetics Publishers, 458-463.

Dillman C. J. and Nelson R. C., (1968), The mechanical energy transformations of pole vaulting with a fiberglass pole. *J. of Biomechanics* 1, 175-183.

Ganslen R. V. ,1973. *Mechanics of the pole vault*, 8th edition. Printed by John Swift Co., Inc. 1248 Research Blvd., St.Louis, Missouri 63132.

Hubbard M. (1980), Dynamics of the pole vault. *J. of Biomechanics* 13(11), 965-976.

Idrottsboken årets idrott (1990-1994). Strömbergs/Brunnhages förlag.

Jayasuriya S., Hubbard M. and Hvorat D. (1984), A control scheme for a pole vaulter derived from an optimal-aiming strategy. *Proceedings of the 1984 American control conference*, June 6-8, San Diego, California.

McGinnis P. M. (1984), Dynamic finite element analysis of a human-implement system in sport: *The pole vault*. Ph.D. Thesis, Univ. of Urbana-Champaign.

Walker H.S. and Kirmser P.G. (1982), Biomechanical parametric analysis of pole vaulting and optimization of performance. In D.N. Ghista (editor), *Human body dynamics: Impact, occupational, and athletics aspects*, 444 - 461. Clarendon Press: Oxford.



0021-9290(94)00168-5

SIMULATION OF 'SMART' POLE VAULTING

Mats Ekevad* and Bengt Lundberg†

*Industrial Development Centre, Skeria 1, S-931 87 Skellefteå, Sweden; and †School of Engineering, Uppsala University, Box 534, S-751 21 Uppsala, Sweden

Abstract—The process of pole vaulting is simulated using a finite element two-dimensional model of the pole and the vaulter. The pole is modelled with 20 beam elements and the vaulter with seven such elements linked together by pin joints. 'Smart' behaviour is achieved through control of limited muscle torques at the joints according to a given strategy. This control strategy is such that the vaulter strives to carry through a prescribed sequence of motions, corresponding to a given style, during a vault. The optimum pole length is determined for a vaulter with given initial velocity, strength and style. When a pole of optimum length is used, the maximum increase of the potential energy of the vaulter is 1.27 times the initial kinetic energy of the vaulter and the pole. This shows that the contribution from muscle work to the increase in potential energy during a vault may be significant. The simulation method should be a useful tool for optimization of pole design. It might also be useful for optimization of vaulting style or for judging the importance of vaulter strength.

Keywords: Pole vault; Smart; Mechanics; Biomechanics; Dynamics; Simulation.

INTRODUCTION

Pole vaulting is a discipline in which there is an extremely large influence of the sportsman's tool. The history of pole vaulting shows that the development of stronger, lighter and more flexible poles has had an extraordinary effect on the heights reached. New materials seem to have played the greatest role in this development, but also changes in geometry have greatly influenced the results. Today, the poles used are thin-walled glass-fibre pipes with varying wall thickness along their lengths. Different amounts of fibres in different directions are used in order to give desired properties to the poles.

As the rules for pole vaulting practically do not restrict the pole design, significant improvements might be achieved through optimization of geometry and materials. So far, however, poles usually have been optimized by trial and error, as there has been no way of predicting the height achievable with a given combination of vaulter and pole. Therefore, the aim of this work is to develop a computer simulation method for pole vaulting which can be used in optimization of pole design.

Several authors have simulated the pole vaulting process. Hubbard (1980) made computer simulations with an elastica pole and a three-segment vaulter controlled by internal muscle torques and studied the effect of the initial velocity of the vaulter. Walker and Kirmser (1982) used a one-segment pendulum vaulter to study the effect of pole stiffness. McGinnis (1984) made finite element simulations with different pole stiffnesses for a vaulter with a scheme of motions which, however, could not be altered during a vault. Jayasuriya *et al.* (1984) used optimal-aim control to

derive muscular controls for a simulation of a pole vault. Braff and Dapena (1985) used a ten-segment vaulter and an elastica pole to simulate pole vaulting with different pole stiffnesses.

In this paper, a computer simulation method for pole vaulting with an active and 'smart' vaulter is developed. The work completes a study (Ekevad and Lundberg 1995), where a vaulter is modelled as a point mass, and the pole has constant cross-section along its length. The pole vault is simulated using a finite element two-dimensional model of the pole and the vaulter. The pole is represented by 20 beam elements and the vaulter by seven such elements linked together by pin joints. Muscle torques at the joints, limited to realistic values, control the angles between the elements. The vaulter uses his muscles to move his body segments as closely as possible to a prescribed motion. He can do this by changing the pace during the vault in a way which is referred to as 'smart'. Thus, the vaulter adjusts his efforts to the events which take place during a vault, and in this way he is capable of vaulting successfully under different conditions. The vaulting style has been taken from photographs of a pole vault by an elite vaulter.

THEORY

Pole model

The pole is considered to be a one-dimensional beam with transverse shear, large displacements, large strains, and rotary as well as transverse inertia. It has a prebend defined by the angle

$$\beta = L/R, \quad (1)$$

where L is the length and R the constant radius of curvature of the pole. It has a variable thin-walled pipe cross-section, with three layers of linearly elastic

materials (glass fibre) as shown in Fig. 1. Pin joints connect the bottom end of the pole to the ground and the top end of the pole to the vaulter. A rotational damper in the pole-ground joint simulates the friction between the pole bottom and the pole box.

The pole is modelled using ABAQUS (1989) with 20 equally long two-node B21 beam elements. Each of these is a superposition of three uniform beam elements with pipe cross-sections, one for each layer shown in Fig. 1. The initial velocity of the pole is taken to be the same as that of the vaulter except at the box end which is simply supported.

The use of the beam model is justified in Fig. 2, where a comparison is made between beam and shell models for the pole in static axial compression. The small difference between the beam and shell models is mainly due to ovalization of the pole cross-section. Numerical data for the pole, in addition to those given in Fig. 1, are listed in Appendix A.

Vaulter model

The vaulter model consists of six segments a-f and five pin joints 1-5 as shown in Fig. 3. As the head segment c is rigidly coupled to the trunk segment d, there are only five independent segment angles θ_j . The two legs of the vaulter are modelled as one two-segment leg (thigh e and shank f), with the mass of two legs, and an intermediate position. The two arms of the vaulter are modelled as one two-segment arm (forearm a and upper arm b), with the mass of the two arms and the position of the arm with the higher hand grip. This position is chosen as the higher arm is the most important one. It exerts the largest force and is

in contact with the pole longer than the lower arm. Geometrical data and masses for the segments, representative for the human body, are taken from Winter (1979). Each vaulter segment b-f is taken to be a stiff beam element with uniformly distributed mass. The segment a is represented by one such element and another element which makes it possible for the vaulter to decouple from the pole as described below. Numerical data for the vaulter are listed in Appendix A.

Each vaulter joint j is associated with a pair of muscle torques M_{mj} which act on the two segments connected by the joint as shown in Fig. 4. The function of the muscle torques is to control the vaulter segment angles θ_j . The differences between the actual segment angles θ_j and the desired reference angles θ_{j^*} are the control errors. They give rise to the proportional muscle torques

$$M_{mj} = k_j(\theta_{j^*} - \theta_j) \quad (2)$$

which strive to eliminate the control errors. The muscle stiffnesses k_j can also be interpreted as proportional gain constants. The desired reference angles θ_{j^*} at each instant of time are determined according to the strategy algorithm described below.

A finite element realization of the proportional control system for the muscles is achieved by using, for joint j , a rotational spring with stiffnesses k_j and two control torques

$$M_j = k_j\theta_{j^*} \quad (3)$$

which act on each of the two segments of the joint as

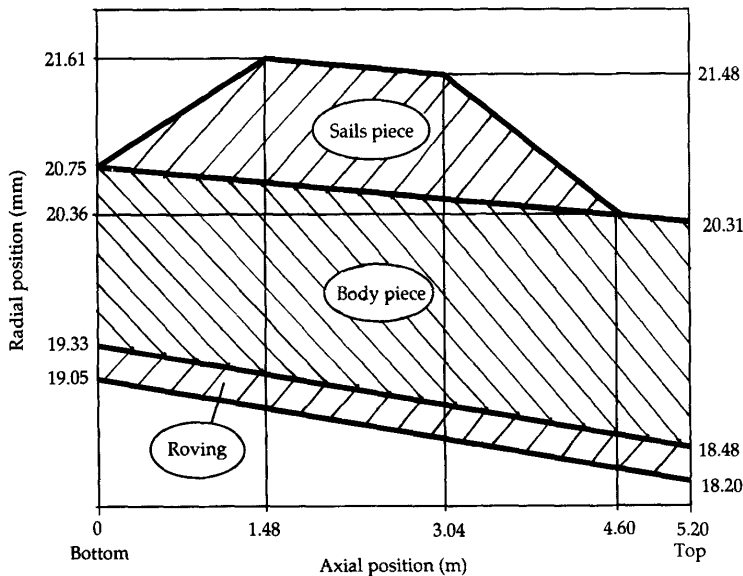


Fig. 1. Geometry of pole.

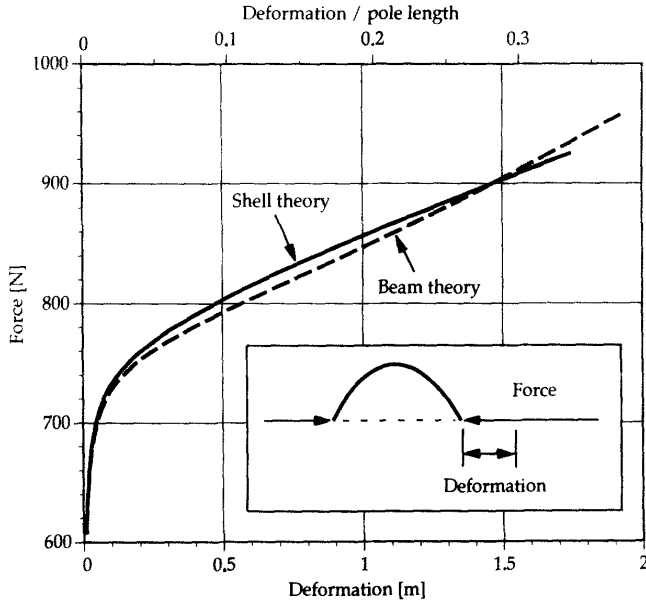


Fig. 2. Comparison of beam and shell models for the pole in static axial compression. The beam model has 20 equally spaced ABAQUS B21-elements and the shell model has $20 \times 16 = 320$ ABAQUS 8-node shell elements.

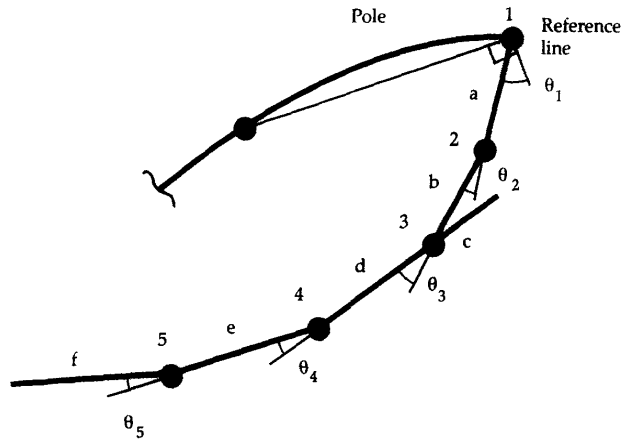


Fig. 3. Geometry of vaulter and definition of body segment angles θ_j . 1 = handgrip joint, 2 = elbow joint, 3 = shoulder joint, 4 = hip joint and 5 = knee joint; a = forearm, b = upper arm, c = head, d = trunk, e = thigh and f = shank.

shown in Fig. 4. The muscle torque, which acts on each of the two segments at the joint, is then the difference

$$M_{m_j} = M_j - k_j \theta_j \quad (4)$$

between the control torque and the spring torque. Limits for the absolute values of the muscle torques have been obtained from measurements on elite pole vaulters by McGinnis and Bergman (1986). The maximum absolute values of the muscle torques for the

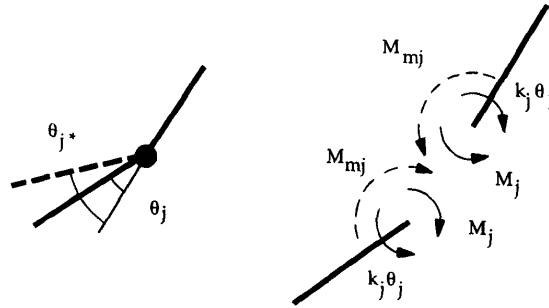


Fig. 4. Muscle torque M_{mj} , control torque M_j and spring torque $k_j\theta_j$ at vaulter joint j .

different joints are set to

$$M_{m1}^{max} = \begin{cases} 600 \text{ Nm} & \xi < 0.5, \\ (3600 - 6000 \xi) \text{ Nm}, & 0.5 < \xi < 0.6, \\ 0 \text{ Nm}, & \xi > 0.6, \end{cases}$$

$$M_{m2}^{max} = 200 \text{ Nm}, \quad M_{m3}^{max} = 500 \text{ Nm},$$

$$M_{m4}^{max} = 300 \text{ Nm}, \quad M_{m5}^{max} = 130 \text{ Nm}. \quad (5)$$

The dimensionless vault variable ξ is zero at the start of the vault and unity when the sequence of vault movements is completed. It is related to the strategy algorithm and will be defined below. The muscle torque limits are independent of ξ except that for the handgrip which is reduced to zero in the final phase of the vault where the vaulter has only one hand on the pole. Clearly, the limits are of great importance for the realism of the simulations.

The muscle stiffness constants k_j determine the characteristics of the muscle control system. In the absence of torque limits, high muscle stiffnesses result in small control errors, while low muscle stiffnesses result in large ones. High muscle stiffnesses may lead to unrealistically high and oscillating muscle torques, while low muscle stiffnesses may result in low controllability of the segment angles.

In the presence of torque limits, high muscle stiffnesses may give rise to muscle torque oscillations between the extreme values; the vaulter 'overreacts' to small control errors. Low muscle stiffnesses do not give rise to this problem. Instead, the torques may never reach their limits, even if the control errors are relatively large. Thus, in this case, the vaulter may not be able to use the maximum capacity of his muscles. Realistic values for muscle stiffnesses allow the vaulter to use his maximum muscle torques without oscillations. Such muscle stiffnesses have been found and are used in the vaulter model. Small rotational dampers in the joints of the vaulter simulate the damping in the human body and increase the stability of the movements of the vaulter. Numerical data for the muscles are given in Appendix A.

The vaulter's six segments are modelled in ABAQUS with seven B21-elements. The top of the pole and the vaulter are coupled through a short beam element which loses its stiffness when certain conditions are fulfilled. This gives the vaulter the ability to leave the pole at the end of the vault. This pole-vaulter coupling (PVC) beam element is a part of the forearm segment *a*; see Fig. 5. The torque applied at the top of the pole by the vaulter is distributed as a pair of forces to the two handgrips via a massless beam element which is placed between the position of the two handgrips as shown in Fig. 5. This force-distribution (FD) element has high stiffness in bending but low in tension, and it is coupled to the pole by pin joints.

The pole and the vaulter are shown in their initial configuration in Fig. 6(a), and at time t in Fig. 6(b). The initial velocity of the vaulter is V_0 and the initial angles α_0 and φ_0 are defined in Fig. 6(a). All segments of the vaulter have the same initial velocity at the time when the vaulter leaves the ground.

The twisting of the vaulter, which makes him have his face down when he passes the bar, is not needed in this two-dimensional simulation as the body segments can rotate in both directions.

The vaulter strategy

Vaulter movements from a series of photographs taken in Sweden in 1989 of the Polish former elite vaulter Tadeus Slusarski (gold medal in the 1976 Olympic Games in Montreal) are the basis for the reference pole vault used in this paper. The body segment angles during this vault are shown in Fig. 7. The angles θ_j have been measured and expressed as functions $\theta_j = \theta_j(\xi)$ of the dimensionless time ξ , which is taken to be zero when Slusarski leaves the ground and unity when his handgrip on the pole is released. Instantaneous body configurations for selected discrete values of ξ are shown in Fig. 8.

The strategy of the simulated vaulter is to move his body as closely as possible to the reference vault

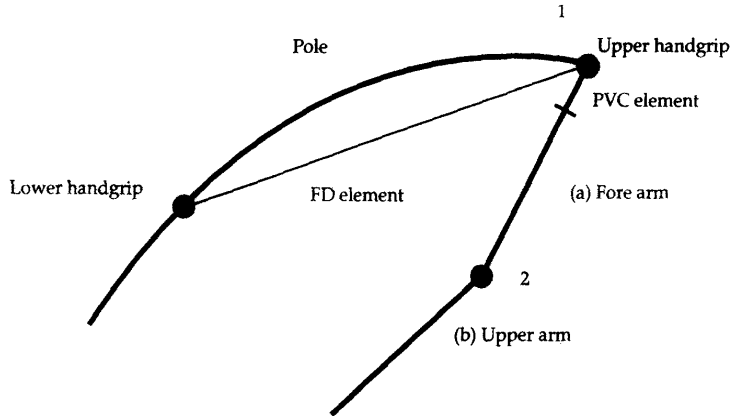


Fig. 5. Pole-vaulter coupling (PVC) and force-distribution (FD) elements

sequence of Slusarski during all phases $0 \leq \xi \leq 1$ of the pole vault. The simulated vaulter is able to change the pace of movements during the vault according to a strategy algorithm which determines the dimensionless vault variable ξ as a function of time t . Thus, in a simulated vault this variable is not proportional to time as in the reference vault by Slusarski. The capability of the simulated vaulter to change pace during a vault makes him able to react to what happens during a vault and, therefore, to adapt to different conditions. This is the restricted way in which he is 'smart'.

The strategy algorithm is based on observation of the angle φ defined in Fig. 6 during the reference pole vault by Slusarski. This angle, between a line through the ends of the pole and a horizontal line, is approximately proportional to ξ when $\xi < 0.45$ as shown in Fig. 9. In the simulations, a linear extrapolation of the angle φ to 90° , at a given time t , gives an estimation of the time t_v when the top end of the pole will be right above the pole box. This time t_v serves to determine the change in the pace variable ξ from time t^i to t^{i+1} in the first part of the vault, $0 < \xi < 0.45$, as follows:

(1) The function $\varphi(t)$ is extrapolated linearly to 90° , using its values in the time steps i and $i - 1$. This gives the preliminary estimated time t_v^i .

(2) A new estimated time t_v^{i+1} is determined on the basis of the old estimated time t_v^{i-1} and the new preliminary time t_v^i , as

$$t_v^{i+1} = (1 - C) t_v^{i-1} + C t_v^i. \tag{6}$$

The constant C was introduced and set to 0.8 in order to damp the variation in the estimated time t_v^i between two time steps.

(3) The vault variable ξ^{i+1} at time t^{i+1} is determined through linear interpolation between the

points (t^i, ξ^i) and (t_v^i, ξ_v^i) which gives

$$\xi^{i+1} = \xi^i + \frac{\xi_v^i - \xi^i}{t_v^i - t^i} (t^{i+1} - t^i). \tag{7}$$

Steps 1-3 are illustrated in Fig. 10.

The parameter ξ_v defines the desired vaulter posture when φ reaches 90° . It was varied slightly in the simulations about the value 0.58. This value was obtained from the reference pole vault by Slusarski as shown in Fig. 9. Small variations of ξ_v give slight changes of the vaulter's pace. A vaulter who is too slow will underrotate at the top position, i.e. he will not rotate his body enough during the pole vault and his body will not rise to an upside-down position at the top end of the pole. A vaulter who is too fast will overrotate, i.e. he will have a clockwise rotation of his body when he reaches the top position. This makes it impossible for him to pass the bar. Ideally, the pole vaulter should rise to a straight, upside-down position, and then rotate anticlockwise so that his body will fall over the bar.

(4) The reference joint angles

$$\theta_j^{i+1} = \theta_j(\xi^{i+1}) \tag{8}$$

are determined from the functions $\theta_j(\xi)$ shown in Fig. 7.

(5) The preliminary muscle torques

$$M_{mj}^{i+1} = k_j(\theta_j^{i+1} - \theta_j^i) \tag{9}$$

are determined from the reference joint angles θ_j^{i+1} at time t^{i+1} and the current joint angles θ_j^i . The muscle torques become

$$M_{mj}^{i+1} = \begin{cases} M_{mj}^{i+1}, & |M_{mj}^{i+1}| \leq M_{mj}^{\max} \\ \pm M_{mj}^{\max}, & |M_{mj}^{i+1}| > M_{mj}^{\max} \end{cases} \tag{10}$$

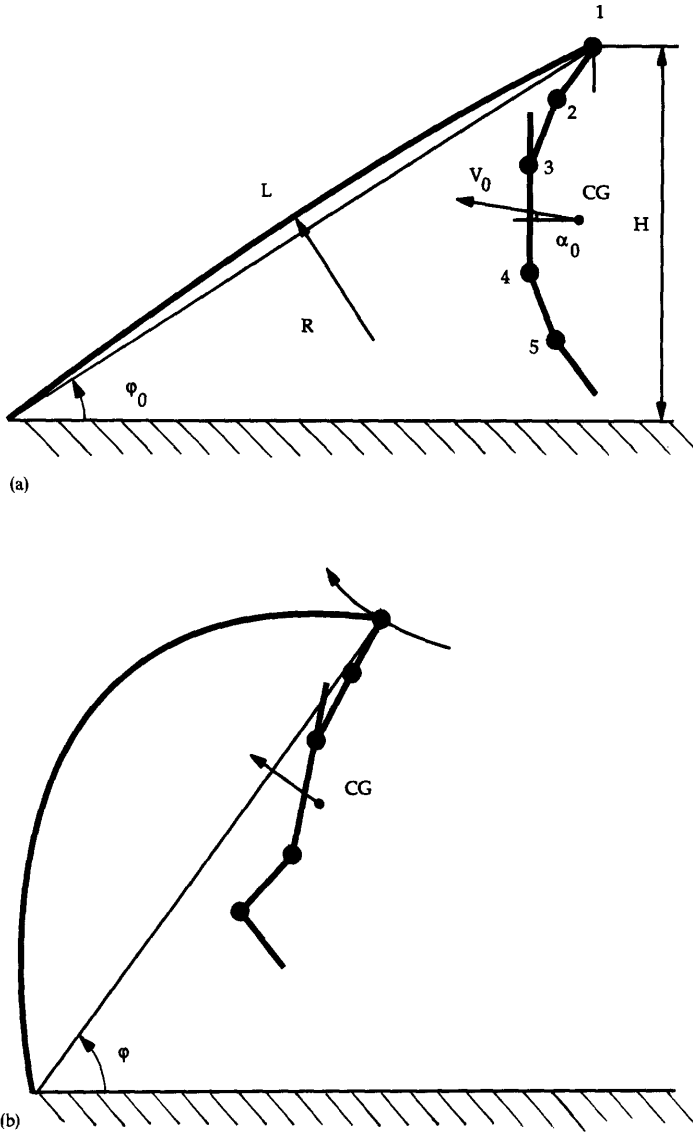


Fig. 6. (a) Pole and vaulter in initial configuration when the last foot of the vaulter leaves the ground. The leg shown is in an intermediate position between the two real legs. CG denotes the centre of gravity of the vaulter and R is the initial constant radius of curvature of the pole. (b) Pole and vaulter at time t .

(6) The control torques are determined as

$$M_j^{i+1} = M_{mj}^{i+1} + k_j \theta_j^i. \quad (11)$$

In the final part of the vault, $0.45 < \xi < 1$, the constant mean value of $d\xi/dt$ is used for determination of the vaulter pace. In this way, destabilizing variations of the vaulter pace in the critical final part of the vault are avoided. Thus, Steps 1, 2 and 3 above

are replaced by

$$\xi^{i+1} = \xi^i + \left(\frac{d\xi}{dt}\right)_M (t^{i+1} - t^i). \quad (12)$$

When $\xi = 1$, the vaulter has reached his final body configuration and the simulation continues with this body configuration kept constant. Decoupling of the pole and vaulter takes place when (i) a positive tensile

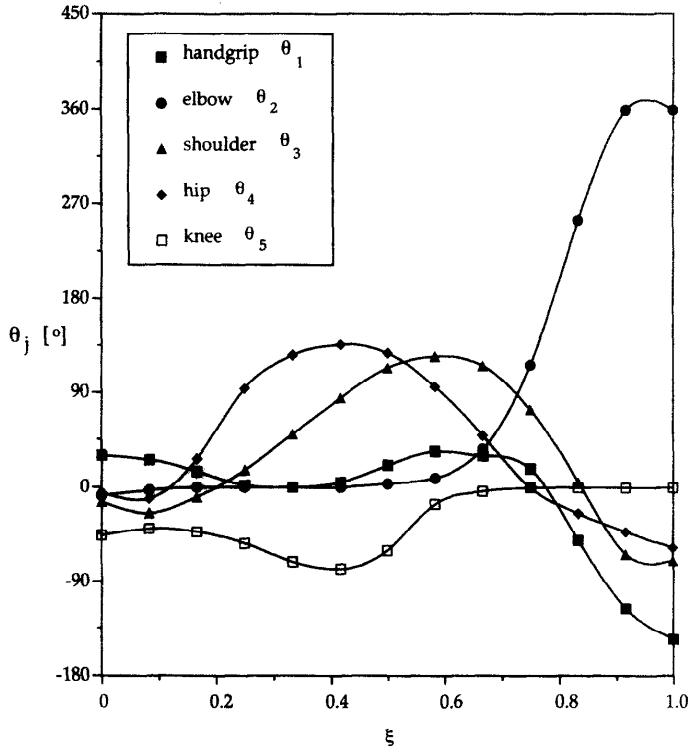


Fig. 7. Body segment angles θ_j versus dimensionless time ξ in the reference pole vault by Slusarski.

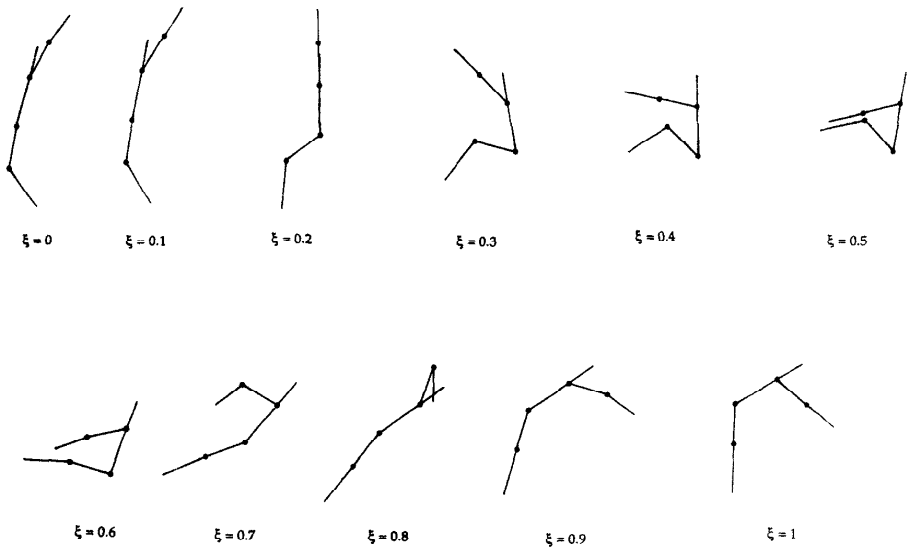


Fig. 8. Different phases of the reference pole vault by Slusarski.

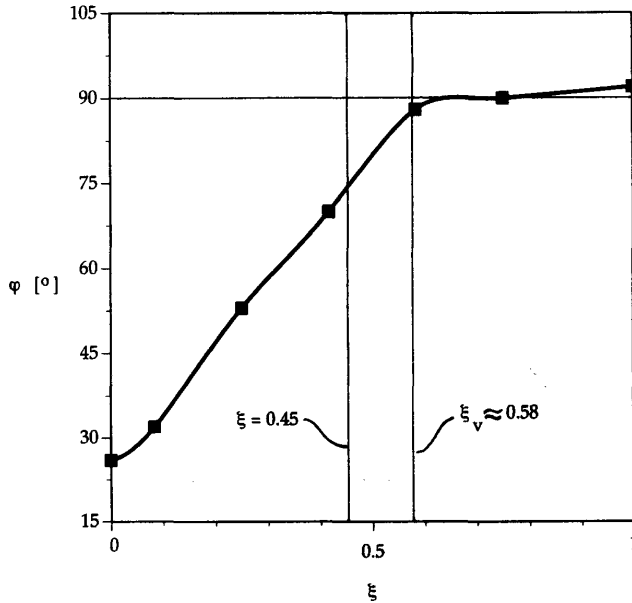


Fig. 9. Pole-to-ground angle φ in the reference pole vault by Slusarski.

force prevails in the forearm segment a, and (ii) the elbow joint 2 is higher than the handgrip joint 1. When these two conditions have been fulfilled, the vaulter and the pole are treated as separate.

The vaulter strategy algorithm was programmed in a user subroutine linked to ABAQUS. The finite element model had 126 degrees of freedom. A typical pole vault simulation takes 500–1000 time steps with 2–10 equilibrium iterations in each step.

SIMULATIONS AND RESULTS

Pole vaults with varying pole lengths were simulated in order to find the optimum pole length for a given vaulter.

The initial pole geometry is shown in Fig. 1, and the pole length L was varied by cutting the pole from the top. The parameter ξ_v was adjusted in each simulation in order to create an acceptable rotation at the top position. Vaults with an unacceptable rotation were rejected. Two or three simulations were typically needed for each pole length. Other parameters were kept constant. Numerical data used in the simulations are presented in Appendix A. The data for the pole are representative of glass-fibre poles used by elite pole vaulters today.

Vaulter and pole configurations at different phases of simulated pole vaults are shown in Fig. 11(a)–(c) for different pole lengths. The vault height h is defined as the maximum height of the centre of gravity of the vaulter in a valid vault. In such a vault the body of the

vaulter at the top position must have a slight forward (anticlockwise) rotation in order to pass the bar. Naturally, our definition of vault height does not agree with the height of the bar in a successful vault. A performance figure η is defined as the ratio between the maximum increase in potential energy of the vaulter and the initial kinetic energy of the vaulter and the pole, i.e.

$$\eta = \frac{mg(h - h_0)}{(m + m_p) V_0^2 / 2}. \quad (13)$$

The vault height h and the performance figure η versus pole length L are shown in Fig. 12. It was found that the muscle torques generally oscillate during a simulation, as mentioned above.

DISCUSSION

The pole and vaulter configurations in Fig. 11 demonstrate that the simulated vaulter behaves in a similar way as a real vaulter. Figure 12 shows that a maximum in vault height exists with respect to the pole length. Such a length is found to exist also for the simpler pole vault model used by us (Ekevad and Lundberg, 1995). Further insight into the pole vaulting process, used as a basis for the discussion below, was achieved through animations of each pole vault.

A long pole has low stiffness. If the stiffness is too low, the pole does not give appropriate support to the vaulter, especially when he uses his muscles to raise himself in the final part of the vault. As a result, the

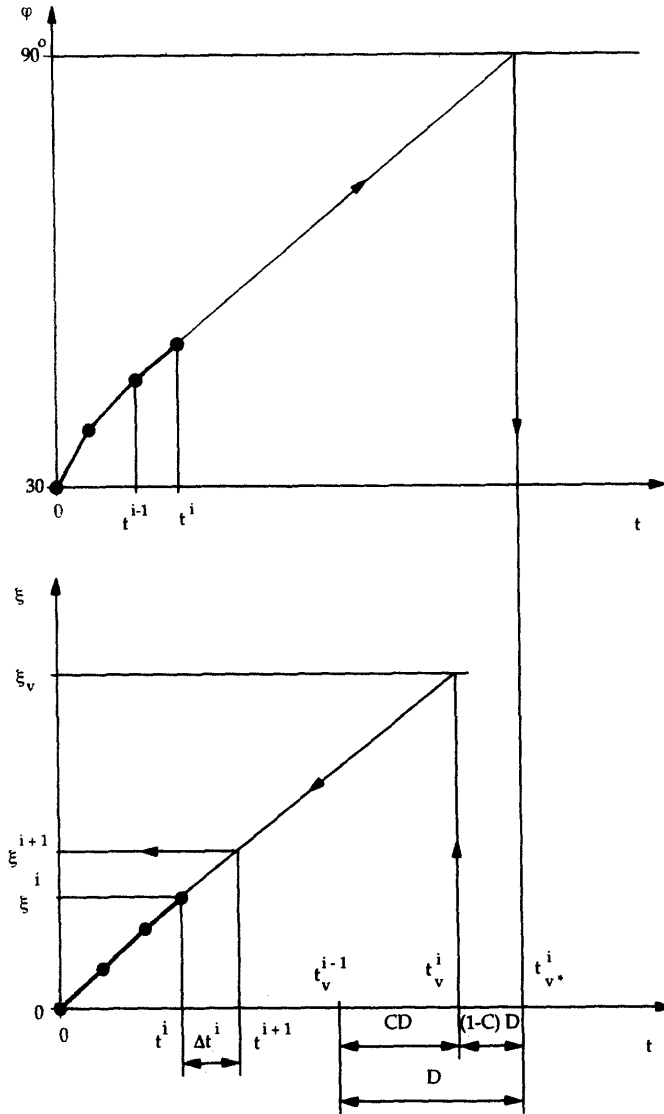


Fig. 10. Strategy algorithm for determining the function $\xi(t)$ in a simulated vault.

vault height will be low, or the vault will even become a complete failure. The result is not necessarily improved if the pole is made stiffer by changing its material or cross-section. An excessively long and stiff pole may be impossible to use as it makes the vaulter 'bounce' back. Therefore, with such a pole, he will not be able to reach the point vertically above the pole box. The same result is also obtained with the simpler pole vault model (Ekevad and Lundberg, 1995). An excessively short pole may be stiff enough to support the vaulter. Still, evidently, it is unable to bring the

vaulter to a large height. A favourable pole should be short and stiff enough to support the vaulter in all phases of the vault, and long enough to bring him to a large height.

Figure 11(a) shows a simulated vault with a relatively short pole, 4.50 m. The height reached, 5.18 m, is indicated in Fig. 12. This pole is too stiff and has too fast and strong a spring-back for the muscle strength of the vaulter. He is not able to efficiently use his muscles to lift himself at the same pace as the pole spring-back. When the vaulter pace was increased, by

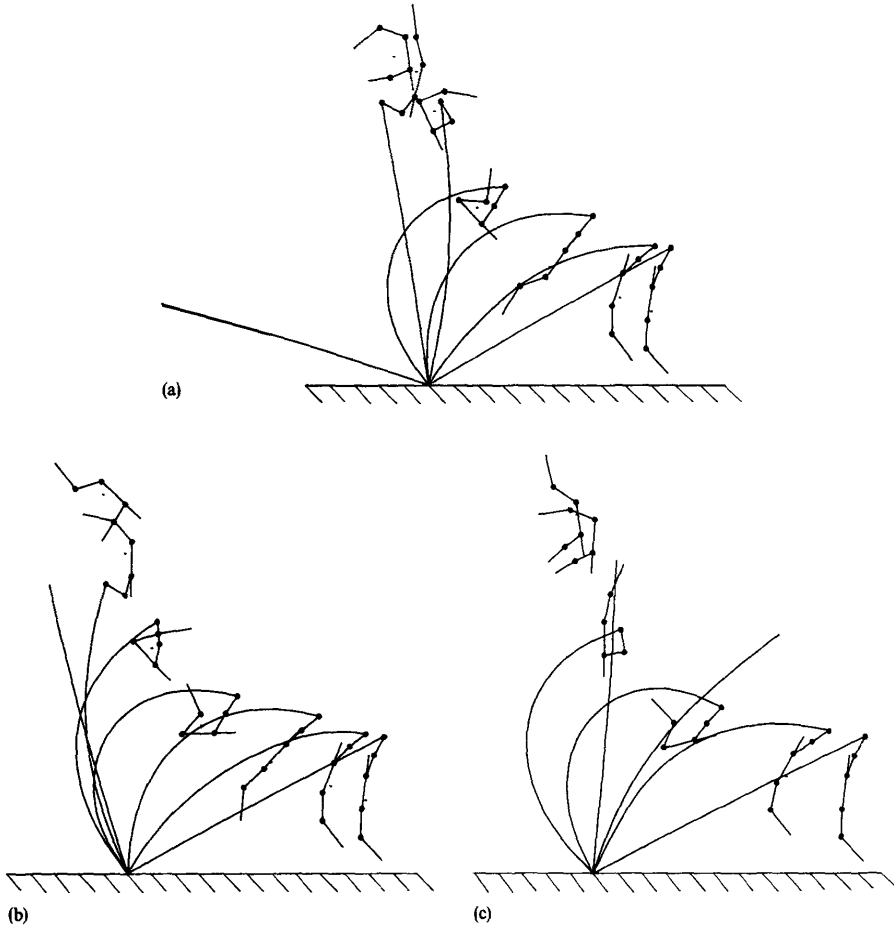


Fig. 11. Simulation of pole vaults with different pole lengths: (a) pole length 4.50 m, $\xi_v = 0.560$; (b) pole length 4.75 m, $\xi_v = 0.565$; (c) pole length 5.00 m, $\xi_v = 0.580$.

increasing ξ_v , the vaulter reached a higher position but had an inappropriate clockwise rotation of the body, a so-called overrotation, at the top.

Figure 11(c) shows a simulated vault with a relatively long pole, 5.00 m. The height reached, 5.89 m, is indicated in Fig. 12. This pole is better, but it has too little stiffness and therefore a spring-back which is too slow. The vaulter does not get sufficient support from the pole and is unable to use his muscles efficiently.

Figure 11(b) shows the simulated optimum pole vault with a pole of length 4.75 m. The height reached, 6.20 m, is indicated in Fig. 12. In this case the pole spring-back is sufficiently strong compared to the vaulter muscle strength, and the length of the pole is sufficient to bring the vaulter to a large height. The vaulter gets support from the pole during spring-back and his body is accelerated upwards. His body has

a small counterclockwise rotation at the top position, as required in a successful pole vault.

The performance figures η of the vaults in Figs 11(a)–(c) are 1.02, 1.27 and 1.20, respectively. As a comparison, the maximum performance figure for a passive point-mass vaulter was found to be 0.87 (Ekevad and Lundberg, 1995). These results show that the contribution from muscle work to the increase in potential energy during a vault may be significant.

The vaulter strategy model presented in this paper works well and creates pole vaults which seem realistic. In spite of this apparent realism, it should not be forgotten that the 'smartness' of the vaulter is restricted; the sequence of body configurations is exactly that of the reference vaulter. As seen from the examples, the vaulter strategy model should be a useful tool in the optimization of pole design. It might also be

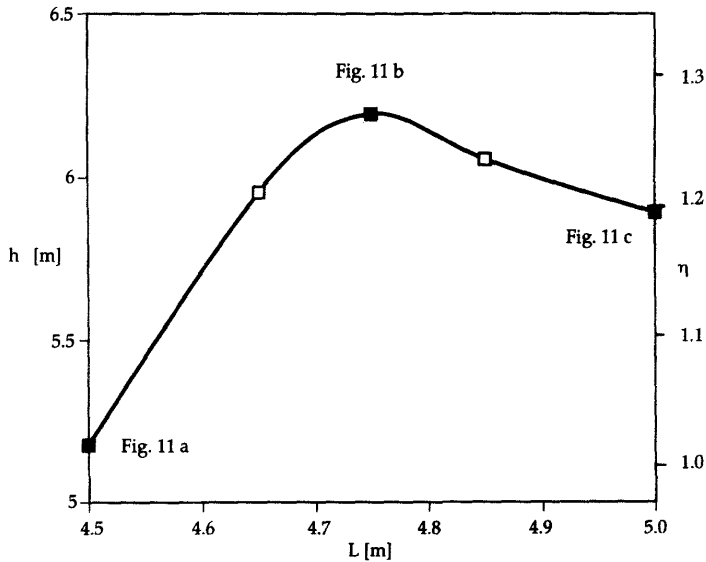


Fig. 12. Vault height h and performance figure η versus pole length L . Open squares represent $L = 4.65$ m, $\xi_v = 0.550$ and $L = 4.85$ m, $\xi_v = 0.570$. Filled squares represent the simulations shown in Fig. 11.

possible to use the model for optimization of vaulting style or for judging the importance of vaulter strength.

Acknowledgements—The authors are indebted to the Nordic Sport and the Swedish Board for Technical Development (STU) for their support.

REFERENCES

- ABAQUS Users Manual Version 4.8 (1989) Available from HKS Inc., 100 Medway Street, Providence, RI 020906, U.S.A.
- Braff, T. J. and Dapena, J. (1985) A two-dimensional simulation method for the prediction of movements in pole vaulting. In *Biomechanics IX-B* (Edited by Winter, D. A. et al.), pp. 458–463. Human Kinetics Publishers, Champaign, IL.
- Ekevad, M. and Lundberg, B. (1995) Influence of pole length and stiffness on the energy conversion in pole vaulting (submitted).
- Hubbard, M. (1980) Dynamics of the pole vault. *J. Biomechanics* 13, 965–976.
- Jayasuriya, S., Hubbard, M. and Hvorat, D. (1984) A control scheme for a pole vaulter derived from an optimal-aiming strategy. *Proc. 1984 American Control Conf.*, 6–8 June, San Diego, CA.
- McGinnis, P. M. (1984) Dynamic finite element analysis of a human-implement system in sport: The pole vault. Ph.D. thesis, University of Urbana-Champaign.
- McGinnis, P. M. and Bergman, L. A. (1986) An inverse dynamic analysis of the pole vault. *Int. J. Sport Biomechanics* 2(3), 186–201.
- Walker, H. S. and Kirmser, P. G. (1982) Biomechanical parametric analysis of pole vaulting and optimization of performance. In *Human Body Dynamics: Impact, Occupational, and Athletics Aspects* (Edited by Ghista, D. N.), pp. 444–461. Clarendon Press, Oxford.

Winter, D. A. (1979) *Biomechanics of Human Movement*. Wiley, New York.

APPENDIX A NUMERICAL DATA FOR POLE AND VAULTER

Pole

Pole length L is varied by cutting material from the top (Fig. 1)

Pole mass for $L = 5.00$ m is $m_p = 2.70$ kg
 Prebend angle $\beta = 0.05$
 Roving layer $E = 1.00$ Pa, $\nu = 0.25$
 Body piece layer $E = 44.5$ GPa, $\nu = 0.25$
 Sails piece layer $E = 44.5$ GPa, $\nu = 0.25$
 Density $\rho = 1990$ kg m⁻³ for all layers
 Box damper $c = 1.00$ Nms

Data for FD beam element

Length is $3L/20$ where L is pole length
 Bending stiffness $EI = 200$ Nm²
 Tensile stiffness $EA = 0$
 Shear stiffness $k_tGA = 2.00 \times 10^7$ N

Vaulter

Grip height $H = 2.20$ m
 Segment lengths $H_a = 0.363$, $H_b = 0.343$, $H_c = 0.332$,
 $H_d = 0.526$, $H_e = 0.447$, $H_f = 0.521$ m
 Initial height of CG $h_0 = 1.11$ m
 Vaulter mass $m = 80.0$ kg
 Segment masses $m_a = 3.52$, $m_b = 4.48$, $m_c = 6.48$, $m_d = 39.8$,
 $m_e = 16.0$, $m_f = 9.76$ kg
 Segment bending stiffness $EI = 1.67 \times 10^4$ Nm²
 Segment tension stiffness $EA = 2.00 \times 10^8$ N
 Segment shear stiffness $k_tGA = 6.54 \times 10^7$ N
 Initial angle $\alpha_0 = 20.0^\circ$
 Initial velocity $V_0 = 8.80$ m s⁻¹

Muscle stiffnesses $k_1 = 1.00 \times 10^4$, $k_2 = k_3 = k_4 = 1.00 \times 10^3$, $k_5 = 5.00 \times 10^2$ Nm

Joint dampers $c_1 = 2.40$, $c_2 = 0.800$, $c_3 = 2.00$, $c_4 = 1.20$, $c_5 = 0.800$ Nms

Data for PVC beam element

Length 0.01 m

Bending stiffness $EI = 2000$ N m² when coupled and $EI = 0$ when released

Tension stiffness $AE = 6.00 \times 10^5$ N when coupled and $AE = 0$ when released

Shear stiffness $k_s GA = 2.00 \times 10^6$ N both released and coupled

Mass 0.097 kg

APPENDIX B NOMENCLATURE

<i>A</i>	area
<i>c</i>	joint damping coefficient
<i>C</i>	damping constant
<i>E</i>	elastic modulus
<i>g</i>	acceleration of gravity
<i>G</i>	shear modulus
<i>h</i>	maximum height of vaulter CG
<i>h₀</i>	initial height of vaulter CG
<i>H</i>	vaulter grip height
<i>H_a, H_b, H_c, H_d, H_e, H_f</i>	vaulter segment lengths
<i>I</i>	second moment of area
<i>k</i>	muscle stiffness

<i>k_s</i>	shear section coefficient
<i>L</i>	length of pole
<i>m_a, m_b, m_c, m_d, m_e, m_f</i>	vaulter segment masses
<i>m_p</i>	pole mass
<i>m</i>	vaulter mass
<i>M</i>	control torque
<i>M_m</i>	muscle torque
<i>R</i>	radius of curvature for the pole
<i>t</i>	time
<i>V₀</i>	vaulter initial velocity
<i>α₀</i>	vaulter initial angle
<i>β</i>	prebend angle of pole
<i>η</i>	performance figure
<i>φ</i>	pole angle to ground
<i>ν</i>	Poisson's ratio
<i>θ</i>	body segment angle
<i>ρ</i>	density
<i>ξ</i>	dimensionless vault variable
<i>ξ_v</i>	desired value of <i>ξ</i> when $\varphi = 90^\circ$

Subscripts

<i>j</i>	number of segment
<i>v</i>	value when $\varphi = 90^\circ$
*	preliminary value, value which is estimated or desired before the actual value is known
0	initial value

Superscripts

<i>i</i>	number of time step
max	maximum value

INFLUENCE OF POLE LENGTH AND STIFFNESS ON THE ENERGY CONVERSION IN POLE-VAULTING

Mats Ekevad* and Bengt Lundberg†

*Industrial Development Centre, Skeria 1, S-931 87 Skellefteå, Sweden; and †School of Engineering, Uppsala University, Box 534, S-751 21 Uppsala, Sweden

Abstract—An impact process similar to pole-vaulting is studied, viz., the impact in a vertical plane between the bottom end of a slightly curved elastic bar (pole), with a point mass (vaulter) at the top end, and a rigid support (pole box). Before impact, the velocity of the pole and the vaulter forms a certain angle (take-off) with the horizontal ground. Finite element calculations of the trajectories of the vaulter are carried out, and a performance figure, defined as the ratio between the maximum potential energy of the vaulter and the initial kinetic energy of the vaulter and the pole, is determined as a function of dimensionless parameters. As the vaulter remains passive during the vault, in contrast to a real vaulter, this performance figure is also the efficiency of conversion of the initial kinetic energy to the achieved potential energy in the vault. It is shown that, under normal pole-vault conditions, there exists a maximum performance figure with respect to pole length and stiffness. For an initial velocity and a body mass which are representative of an elite pole-vaulter, the maximum performance figure 0.87 is obtained for a pole with length 5.5 m. © 1997 Elsevier Science Ltd. All rights reserved.

Keywords: Mechanics; Pole; Vault; Energy conversion.

NOMENCLATURE

A	cross-sectional area
E	Young's modulus
g	acceleration due to gravity
H	vaulter grip height
h	dimensionless vaulter grip height
I	area moment of inertia
L	pole length
M	vaulter mass
m	pole mass per unit length
R	prebend radius
R_i	radius of gyration
r_i	dimensionless radius of gyration
t	time
V	common initial velocity of vaulter and pole
v	dimensionless common initial velocity of vaulter and pole
X	horizontal coordinate
Y	vertical coordinate
y	dimensionless vertical coordinate
α	take-off angle
β	prebend angle
η	performance figure
ϕ	angle to ground formed by chord between ends of pole
κ	dimensionless pole stiffness
λ	dimensionless pole length
μ	dimensionless vaulter mass
ν	Poisson's ratio
τ	dimensionless time
ω	angular velocity of pole and vaulter immediately after impact

Subscripts

E	Euler buckling
L	limit due to pole length
M	maximum height, top position
R	rigid pole
0	dimensionless parameters based on reference pole length L_0 and also initial value

INTRODUCTION

Pole-vaulting is a sport in which conversion of the initial kinetic energy of a running vaulter and his pole into potential energy of the vaulter, is of primary importance. This potential energy can be directly translated into vertical height, which is the desired result of the vault. The conversion of energy is achieved in two principal phases. In the first phase, the pole is bent and a large fraction of the kinetic energy is converted into elastic strain energy. In the second phase, the pole straightens out and a large fraction of the stored elastic strain energy is converted into potential energy of the vaulter. In addition to the initial kinetic energy, the vaulter supplies muscle work during the vault which contributes to the final potential energy. Clearly, the length and stiffness of the pole are key parameters for the energy conversion and therefore also for a successful vault.

Studies of the mechanics of pole vaulting have been made by several researchers, both experimentally and theoretically. Dillman and Nelson (1968) determined experimentally kinetic and potential energies of a pole vaulter during a vault. Hubbard (1980) studied a three-segment vaulter with internal muscle forces and determined vaulter trajectories for different initial velocities of the vaulter. Walker and Kirmsler (1982) used a one-segment pendulum model of the vaulter to study the effect of pole stiffness. McGinnis (1984) made finite element simulations with different pole stiffnesses for a vaulter with a fixed scheme of motions. Braff and Dapena (1985) used a ten-segment vaulter model and an elastica pole to simulate vaulting with different pole stiffnesses. McGinnis and Bergman (1986) made an experimental study of the internal forces and moments of a vaulter during a pole vault. The effects of take-off velocity and take-off angle were considered by Linthorne (1994) for a point-mass vaulter using a massless perfectly rigid pole.

In a recent paper (Ekevad and Lundberg, 1995) we studied a six-segment (seven-element) vaulter who is 'smart' in the sense that he uses his muscles, to the best of his ability, to move his body segments as closely as possible to a prescribed motion, e.g. that which is typical of a particular elite vaulter. In this paper, in contrast, we have chosen to study a vaulter who is passive during the vault and uses the simplest possible style. We consider a simple impact process with similarity to pole vaulting, viz., the impact in a vertical plane between the bottom end of a slightly curved elastic beam (pole), with a point mass (vaulter) at the top end, and a rigid support (pole box). Before impact, the velocity of the pole and the vaulter forms a certain angle (take-off) with the horizontal ground. Finite element calculations of the trajectories of the vaulter are carried out, and we determine a performance figure as the ratio between the maximum potential energy of the vaulter and the initial kinetic energy of the vaulter and the pole, as a function of dimensionless parameters.

We focus our interest on the influence of the length and stiffness of the pole and show that under normal pole vault conditions there exists a maximum performance figure, not much below unity, with respect to pole length and stiffness. In this way we get some idea about rules for optimum pole design. Also, by comparing with results from our previous study of a more sophisticated active vaulter, we get some idea about the importance of smart behaviour and muscle work during the vault.

THEORY

Model

The pole is a prebent bar with length L , radius of curvature R , prebend angle $\beta = L/R$, cross-sectional area A , area moment of inertia I , radius of gyration $R_g = (I/A)^{1/2}$, Young's modulus E , Poisson's ratio ν , and mass per unit length m . Thus, the pole has constant properties along its length. The contact between the bottom end of the pole and the pole box is represented by a fixed pin joint, and the top end of the pole is fixed to the vaulter, who is represented by a point mass M . The vaulter grip height is H , and the common initial velocity V of the vaulter and the pole forms the take-off angle α with the horizontal ground. The acceleration due to gravity is g , and the motion of the pole and the vaulter takes place in a vertical plane; see Fig. 1.

The performance figure is defined as the ratio between the maximum potential energy of the vaulter and the initial kinetic energy of the vaulter and the pole, i.e.

$$\eta = \frac{M}{M + mL} \frac{g(Y_M - H)}{V^2/2}, \quad (1)$$

where Y_M is the maximum vertical height of the vaulter during the vault (regardless of the horizontal position where this maximum height is reached). As the vaulter here remains passive during the vault, the performance figure is also the efficiency of conversion of the initial kinetic energy to the achieved potential energy in the vault. For an elastic pole, the losses of energy which make the performance figure less than unity are the increase of potential energy of the pole in the gravitational field, the

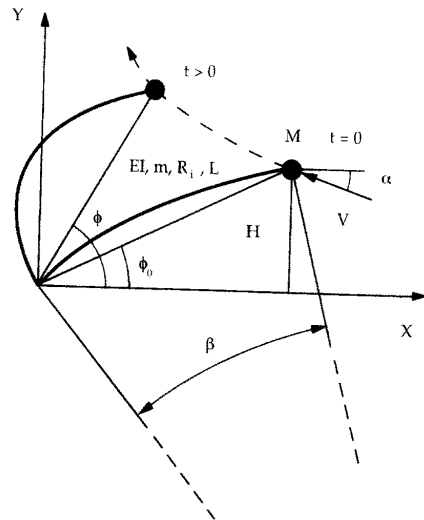


Fig. 1. Pole vault represented by point mass on a bar impacting a stiff support.

strain energy of the pole, and the kinetic energy of the vaulter and the pole when the vaulter is at maximum height.

An approximate upper limit for the vault height, due to the fact that the vaulter is attached to the pole, is $Y_M = L$. This gives the upper limit

$$\eta_U = \frac{M}{M + mL} \frac{g(L - H)}{V^2/2} \quad (2)$$

of the performance figure.

For an active (Ekevad and Lundberg, 1995) or real vaulter, who performs muscle work during the vault, the performance figure is commonly larger than unity and cannot be interpreted as an efficiency.

Rigid pole

The case of a straight rigid pole is characterized by the pole length L , the pole mass per unit length m , the vaulter mass M , the vaulter grip height H , the take-off angle α , the common initial velocity of the vaulter and the pole V , and the acceleration due to gravity g .

Just before impact between the bottom end of the pole and the pole box, the pole and the vaulter have the common translational velocity V which forms the angle α with the horizontal ground as shown in Fig. 1. At the moment of impact, there is an immediate change of the translational motion of the pole and the vaulter into a rotational motion around the fixed pole bottom pin joint. The angular velocity ω is such that the angular momentum of the pole and the vaulter with respect to the pole bottom pin joint immediately after impact is the same as that immediately before impact, i.e.

$$\omega L^2(M + mL/3) = VL \sin(\alpha + \phi_0)(M + mL/2). \quad (3)$$

where $\phi_0 = \arcsin(H/L)$ is the initial angle of the pole to the ground. The immediate change in the motion of the pole and the vaulter at impact implies a corresponding immediate loss of kinetic energy. For an elastic pole and a deformable pole box, this loss corresponds to waves generated in the pole and to work performed on the pole box.

The maximum vault height, as long as this height does not exceed the length of the pole, can be determined from the condition that the rotational kinetic energy of the pole and the vaulter immediately after impact should be completely transformed into potential energy of the pole and the vaulter, i.e.

$$(M + mL/2)g(Y_M - H) = (\omega^2 L^2/2)(M + mL/3). \quad (4)$$

The corresponding provisional performance figure, which does not take into account the limited length of the pole, can be obtained by eliminating ω from equations (3) and (4), solving for $g(Y_M - H)$, and substituting into equation (1). The result is

$$\eta_R = \frac{M}{M + mL} \frac{M + mL/2}{M + mL/3} \sin^2(\alpha + \phi_0). \quad (5)$$

This quantity is less than unity and decreases with pole length L .

Taking into account the limitation of pole length expressed by equation (2), finally, we obtain the performance figure

$$\eta = \min(\eta_R, \eta_L) \quad (6)$$

for a vault with a rigid pole.

The optimal pole length, i.e. the one which gives the maximum performance figure, is determined from the condition

$$\eta_R = \eta_L. \quad (7)$$

which means that the vaulter reaches $Y_M = L$ at $\phi = \phi_M = 90^\circ$, and with zero velocity.

Finite element model of elastic pole

Simulations with an elastic pole were carried out with the finite element programme ABAQUS Version 4-7-22 (1988). This programme uses nonlinear, large-displacement dynamic beam theory to calculate the time history of the pole and the vaulter. The 20 two-node B21 beam elements are large-displacement beams with non-deforming cross-sections and they allow for transverse shear. The elements have both mass and rotary inertia, but the vaulter has only mass. The programme uses an implicit time-stepping method to solve the equations of motion. The convergence tolerance on force is set to 0.001 times the buckling force of the straight pole. The time steps are chosen by the programme and are varied in order to give rapid convergence. The number of time steps varies from about 100 to about 500 for each simulation. Typically, about one to five load balance iterations are performed in each time step to achieve convergence within the force tolerance specified above.

Dimensionless parameters

Dimensionless parameters are taken as

$$h = H/L, \quad \beta = L/R, \quad r_i = R_i/L, \quad v, \quad \alpha, \\ v = V/(gL)^{1/2}, \quad \mu = M/mL, \quad \kappa = EI/mgL^3, \quad (8)$$

where h is the dimensionless vaulter grip height, β is the prebend angle, r_i is the dimensionless radius of gyration of the pole, v is the dimensionless common initial velocity of the vaulter and the pole, μ is the dimensionless mass of the vaulter, and κ is the dimensionless stiffness of the pole (related to its mass). For the special case of a straight rigid pole, the only dimensionless parameters are h , α , v and μ . The dimensionless time is taken to be

$$\tau = (g/L)^{1/2} t, \quad (9)$$

where t is time.

Under normal pole vault conditions, axial deformation, shear deformation and pole mass are likely to have little importance. Therefore, under such conditions, the dimensionless parameters r_i , v and μ can be expected to have little influence on the performance figure.

SIMULATIONS AND RESULTS

For the dimensionless parameters of equation (8) which involve the length L of the pole, except β , we define dimensionless parameters h_0 , r_{i0} , v_0 , μ_0 and κ_0 corresponding to a fixed length L_0 of the pole. A dimensionless pole length is then defined as

$$\lambda = L/L_0, \quad (10)$$

which gives

$$h = h_0/\lambda, \quad r_i = r_{i0}/\lambda, \quad v = v_0/(\lambda)^{1/2}, \\ \mu = \mu_0/\lambda, \quad \kappa = \kappa_0/\lambda^3. \quad (11)$$

The prebend angle β is considered to be constant, which means that the prebend radius R is proportional to the length L of the pole.

We now study the performance figure η as a function of the dimensionless pole length λ and the dimensionless pole stiffness κ_0 for constant values of the other parameters h_0 , β , r_{i0} , v_0 , α , v_0 and μ_0 . The performance figure (1) is expressed in terms of dimensionless quantities as

$$\eta = \frac{\mu_0}{\mu_0 + \lambda} \frac{y_{0M} - h_0}{v_0^2/2}, \quad (12)$$

where $y_{0M} = Y_M/L_0$. Similarly, the upper limit (2) of the performance figure is expressed as

$$\eta_L = \frac{\mu_0}{\mu_0 + \lambda} \frac{\lambda - h_0}{v_0^2/2}. \quad (13)$$

We choose a vaulter with mass $M = 75$ kg, grip height $H = 2.25$ m, take-off velocity $V = 8.5$ m s⁻¹, and take-off angle $\alpha = 20^\circ$. Also, we choose a reference pole with length $L_0 = 5.0$ m, prebend angle $\beta = 0.40$ rad, pole mass per unit length $m = 0.60$ kg m⁻¹, radius of gyration $R_i = 15$ mm and Poisson's ratio $\nu = 0.25$. These are realistic values for an experienced pole-vaulter with an appropriate pole. The acceleration due to gravity is taken to be

$g = 10 \text{ m s}^{-2}$. The resulting dimensionless parameters are: $h_0 = 0.45$, $\beta = 0.40$, $r_{i0} = 0.0030$, $v = 0.25$, $\alpha = 20^\circ$, $v_0 = 1.2$, and $\mu_0 = 25$.

Rigid pole

The performance figure (5) can be expressed as

$$\eta_R = \frac{\mu_0}{\mu_0 + \lambda} \frac{\mu_0 + \lambda/2}{\mu_0 + \lambda/3} \sin^2(\alpha + \phi_0), \quad (14)$$

where

$$\sin(\alpha + \phi_0) = [h_0 \cos(\alpha) + (\lambda^2 - h_0^2)^{1/2} \sin(\alpha)]/\lambda. \quad (15)$$

The performance figure η for a rigid pole, determined from equations (6), (13–15), is shown in Fig. 2 as a function of the dimensionless length λ of the pole. The optimal value of λ is 0.88, and the maximum performance figure is 0.59.

Elastic pole

Trajectories of the pole and the vaulter were calculated for different combinations of dimensionless pole lengths and stiffnesses. Dimensionless pole lengths λ from 0.80 to 1.25 in intervals of 0.05 were used, and about ten dimensionless pole stiffnesses κ_0 were considered for each dimensionless pole length. The maximum height of the

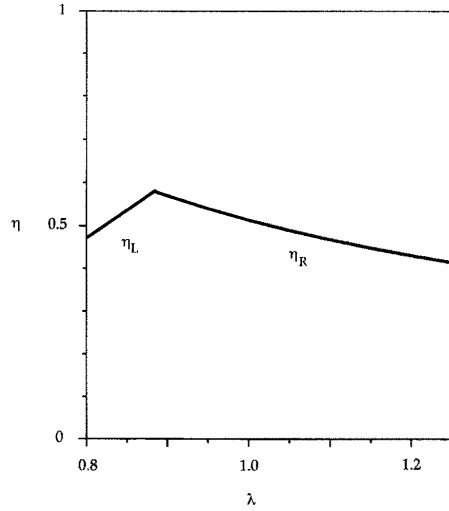


Fig. 2. Performance figure η versus dimensionless pole length λ for straight rigid pole.

vaulter for each vault was determined and used to calculate the performance figure according to equation (12).

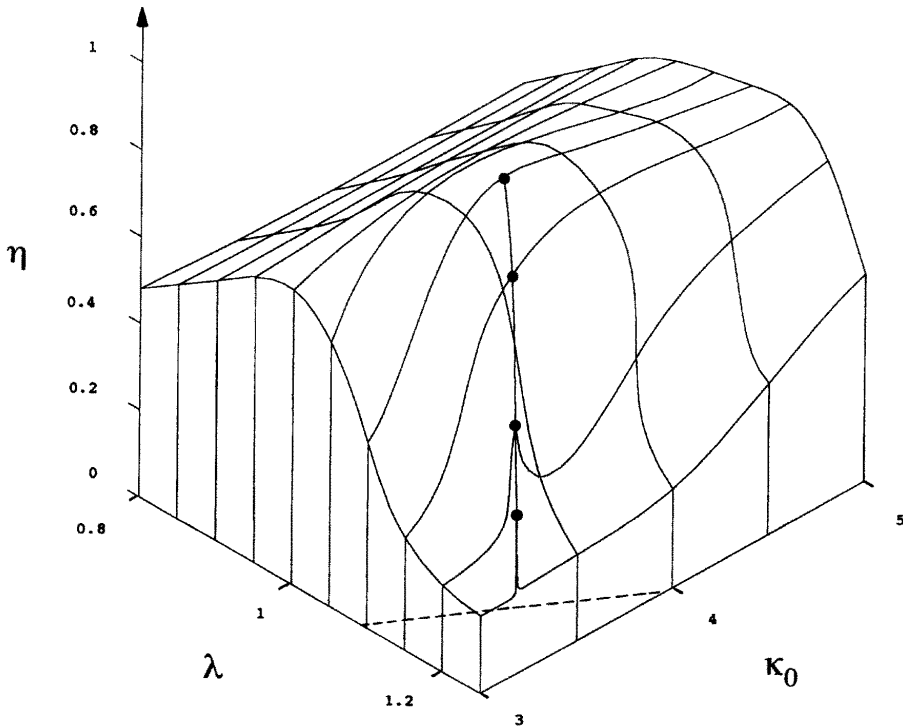


Fig. 3. Performance figure η versus dimensionless pole stiffness κ_0 and dimensionless pole length λ for elastic pole. The curve on the surface shows where the angle-to-ground at the top position ϕ_M is 90° . The dashed curve represents the condition $H_0 = \kappa_{0E}$ for Euler buckling.

Figure 3 shows the performance figure η as a function of the dimensionless pole length λ and the dimensionless pole stiffness κ_0 . Figure 4 shows the vaulter trajectories for different pole stiffnesses for a short pole with dimensionless pole length $\lambda = 0.80$, while Fig. 5 shows vaulter trajectories for different pole stiffnesses for a long pole with $\lambda = 1.21$. Figure 6 shows the vaulter trajectory for the optimal combination of pole length $\lambda = 1.1$ and pole stiffness $\kappa_0 = 3.7$.

DISCUSSION

A comparison between the weight of the vaulter and the Euler buckling load for a simply supported straight pole indicates what stiffness the pole must have in order to be able to straighten completely under the weight of the vaulter. Equality between the vaulter weight and the Euler buckling load gives the minimum pole stiffness

$$\kappa_{0E} = \mu_0 \lambda^2 / \pi^2. \tag{16}$$

The relation $\kappa_0 = \kappa_{0E}$ is represented by the dashed curve in Fig. 3. For $\kappa_0 < \kappa_{0E}$, which corresponds to the bottom corner in the figure, the pole is not able to straighten completely.

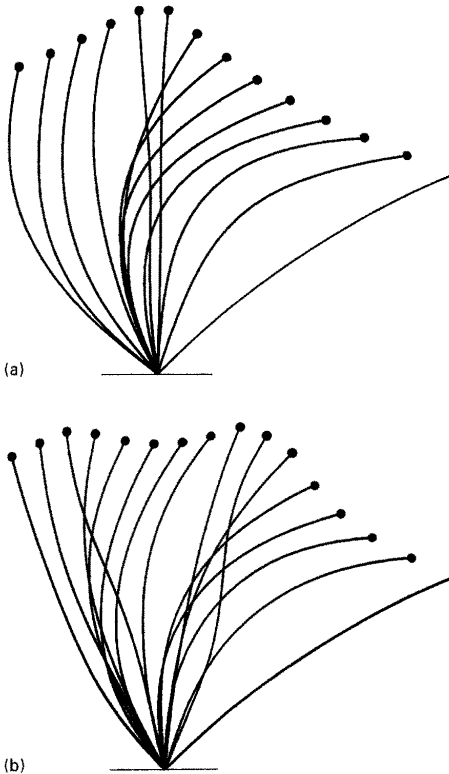


Fig. 4. Deformed configuration of pole and position of vaulter at different times with time step between two consecutive configurations $\Delta\tau = 0.10$: (a) Short pole with low stiffness, $\lambda = 0.80$ and $\kappa_0 = 3.0$; (b) short pole with high stiffness, $\lambda = 0.80$ and $\kappa_0 = 5.0$.

The performance figure shown in Fig. 3 has a global maximum of 0.87 for $\lambda = 1.1$ and $\kappa_0 = 3.7$. It can be seen that there is an increasingly narrow ridge (indicated with a curve) on the surface leading down from the global maximum through increasing λ and decreasing κ_0 . This ridge corresponds to conditions which give $\phi_M = 90^\circ$, so that the top position of the vaulter is reached vertically above the pole-ground pin joint. The narrow part of the ridge, which is in the domain $\kappa_0 < \kappa_{0E}$ where the pole is not able to straighten completely, corresponds to the slow partial straightening of long poles almost vertically from the pole-ground joint as illustrated in Fig. 5(b). The performance figure for very stiff poles ($\kappa_0 \rightarrow \infty$) approaches that shown in Fig. 2 for a rigid pole.

Relatively short and stiff poles straighten almost completely, and the vault height may be limited by the pole

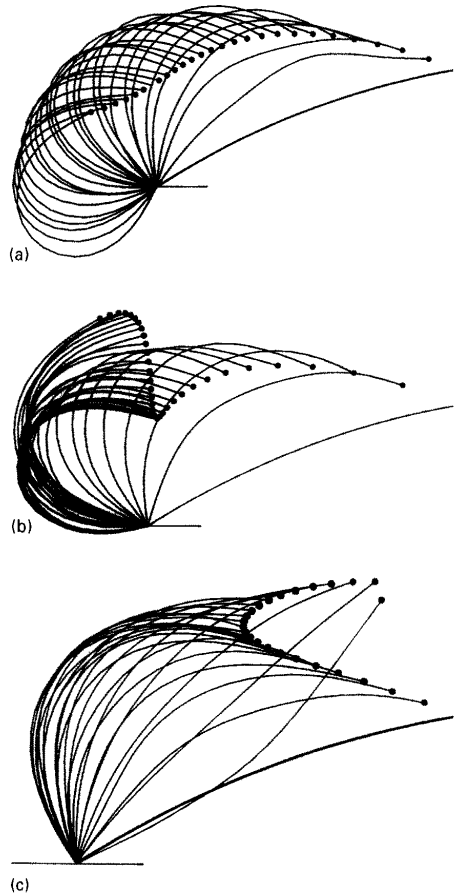


Fig. 5. Deformed configuration of pole and position of vaulter at different times. (a) Long pole with low stiffness, $\lambda = 1.21$ and $\kappa_0 = 3.0$. Time step between two consecutive configurations $\Delta\tau = 0.10$. (b) Long pole with optimal stiffness, $\lambda = 1.21$ and $\kappa_0 = 3.34$. Time step between two consecutive configurations $\Delta\tau = 0.20$. (c) Long pole with high stiffness, $\lambda = 1.21$ and $\kappa_0 = 5.0$. Time between two consecutive configurations $\Delta\tau = 0.10$.

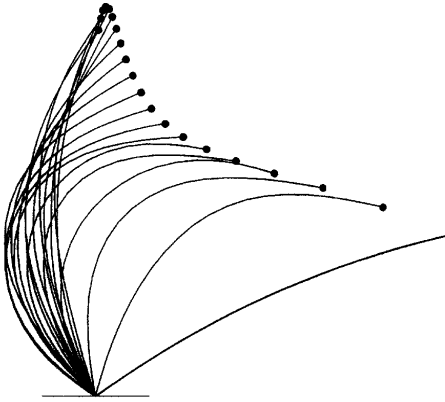


Fig. 6. Deformed configuration of pole and position of vaulter at different times with time step between two consecutive configurations $\Delta\tau = 0.20$. Pole with optimal combination of length and stiffness, $\lambda = 1.1$ and $\kappa_0 = 3.7$.

length. Thus, for $\lambda < 0.9$ and $3 < \kappa_0 < 5$ the performance figure takes on values near the limit η_1 , given by equation (13). As $\lambda \ll \mu_0$, this means that in Fig. 3 the performance figure is approximately represented by a sloping plane, parallel with the κ_0 -axis. For such poles, the stiffness κ_0 determines the angle to ground $\phi = \phi_M$ at the top position (cf. Fig. 1) as can be seen in Fig. 4 for $\lambda = 0.80$ and two different stiffnesses. Higher stiffness results in smaller angle, and vice versa.

Trajectories for the case of a long pole, $\lambda = 1.21$, are shown in Fig. 5. A pole with low stiffness, see Fig. 5(a), straightens slowly and incompletely, and the vaulter does not reach a very high level. A pole with appropriate stiffness, [see Fig. 5(b)] reduces the vaulter's horizontal speed to near zero just above the pole-ground joint and then straightens in the vertical direction. However, the force from the pole is not large enough to lift the vaulter to the full length of the pole, and the vaulter falls off horizontally. The top position in this case corresponds to the ridge in Fig. 3. A very stiff pole straightens too quickly, and the vaulter is returned horizontally and reaches his highest vertical position at an angle $\phi_M < 90^\circ$ [see Fig. 5(c)]. Again, the vaulter does not reach a very high level.

Figure 6 shows a pole-vault with a performance figure near the global maximum. The vaulter reaches the top

position at $\phi_M = 90^\circ$ with a low horizontal velocity, and the pole is almost completely straightened. A shorter pole would not allow the vaulter to reach the optimum height, and a longer pole would not give enough force to lift the vaulter to the optimum height.

We have shown for a realistic case that a maximum in performance figure with regard to dimensionless pole length λ and dimensionless pole stiffness κ_0 exists. The optimal dimensionless pole length is $\lambda = 1.1$ which corresponds to a pole length L of 5.5 m with our choice of parameters. This means a slightly longer pole than commonly used by elite pole vaulters today (about 5.2 m). The passive vaulter used in this work achieves a maximum performance figure η of 0.87, while for an active vaulter we have obtained a maximum performance figure of 1.27 (Ekevad and Lundberg, 1995). This comparison illustrates the significance of muscle work in pole vaulting and underlines that interpretations of results obtained with passive vaulters must be made with care.

Acknowledgements—The authors are indebted to Nordic Sport and the Swedish Board for Technical Development (STU) for their support.

REFERENCES

- ABAQUS Users manual and Theory manual for version 4.7–22 (1988) Available from Hibbit, Karlsson and Sorensen Inc., 100 Medway Street, Providence, RI 02906, U.S.A.
- Braff, T. J. and Dapena, J. (1985) A two-dimensional simulation method for the prediction of movements in pole vaulting. In *Biomechanics IX-B* (Edited by Winter, D. A. *et al.*), pp. 458–463. Human Kinetics Publishers, Champaign, IL.
- Dillman, C. J. and Nelson, R. C. (1968) The mechanical energy transformations of pole vaulting with a fiberglass pole. *J. Biomechanics* **1**, 175–183.
- Ekevad, M. and Lundberg, B. (1995) Simulation of smart pole vaulting. *J. Biomechanics* **28**, 1079–1090.
- Hubbard, M. (1980) Dynamics of the pole vault. *J. Biomechanics* **13**, 965–976.
- Linthorne, N. P. (1994) Mathematical model of the takeoff phase in the pole vault. *J. Appl. Biomech.* **10**, 323–334.
- McGinnis, P. M. (1984) Dynamic finite element analysis of a human-implement system in sport: The pole vault. Ph.D. thesis, Univ. of Urbana-Champaign.
- McGinnis, P. M. and Bergman, L. A. (1986) An inverse dynamic analysis of the pole vault. *Int. J. Sport Biomech.* **2**, 186–201.
- Walker, H. S. and Kirmser, P. G. (1982) Biomechanical parametric analysis of pole vaulting and optimization of performance. In *Human Body Dynamics: Impact, Occupational, and Athletics Aspects* (Edited by Ghista, D. N.) pp. 444–461. Clarendon Press, Oxford.

